Exploring Microbial Mechanisms in Arsenic Adsorption and Desorption in Iron-Manganese Binary Oxides

Sharmin Yousuf Rikta



Department of Earth Sciences

Mathematical, Physical and Life Sciences Division

St Anne's College, University of Oxford

A Thesis submitted for the degree of *Doctor of Philosophy*

Hilary 2025

Table of Contents

Table of Contents i
List of Figures iv
List of Tables vii
Statement of Originality 1
Acknowledgement 2
Abstract 3
1 Chapter One: Introduction 5
1.1 Arsenic 5
1.2 Arsenic Toxicity and Associated Health Problems 5
1.3 Arsenic in the Environment 6
1.3.1 Arsenic in Minerals and Soils 6
1.3.2 Arsenic in Groundwater 9
1.3.3 Anthropogenic Sources of Arsenic 11
1.4 Arsenic Cycling, Geochemical Behaviour and Transport 12
1.5 Arsenic Adsorption and Desorption 17
1.5.1 Arsenic Adsorption onto Minerals 17
1.5.2 Arsenic Adsorption onto Fe Oxides and Fe-Mn Binary Oxides 19
1.5.3 Adsorption- A Promising Technique of Arsenic Immobilization 22
1.5.4 Modelling Adsorption Data 23
i. Adsorption Kinetic Models 23
ii. Adsorption Isotherm Models 25
1.5.5 Arsenic Desorption and Dissolution from Minerals 26
1.6 Biofilm in the Environment 27
1.6.1 Formation of Biofilm 27
1.6.2 Significance of Biofilm in Trace Metal Cycling 28
1.7 Biogenic Minerals in the Environment 29
1.7.1 Formation of Biogenic Minerals in the Environment 29
1.7.2 Biogenic Fe Oxides, Mn Oxides, and Fe-Mn Binary Oxides 32
1.7.3 Environmental Significance of Biogenic Minerals 34
1.8 Context of this Research 35
1.8.1 Scope of Research 35
1.8.2 Research Objectives 36
1.9 Thesis Outline 37
2 Chapter Two: Assessing Arsenic(V) Adsorption Behaviours and Capacities of Abiogenic Ferrihydrite and Iron-Manganese Binary Oxides 39
Abstract 39
2.1 Introduction 40
2.2 Materials and Methods 42
2.2.1 Synthesis of Ferrihydrite and Fe-Mn Binary Oxides 42
2.2.2 Solid Phases Characterisation 42
i. Powder X-Ray Diffraction (XRD) Analysis 42
ii. Scanning Electron Microscope (SEM) Analysis 43
iii. Energy Dispersive X-ray (EDX) Analysis 43
iv. Brunauer–Emmett–Teller (BET) Analysis 43
2.2.3 As(V) Adsorption Kinetic Experiments 43
2.2.4 As(V) Adsorption Isotherm Experiments 44

2.2.5 Adsorption Kinetic and Isotherm Models....44
2.2.6 Elemental Concentration Analysis....46
2.3 Results and Discussion....47
2.3.1 Mineral Phase Identification....47
2.3.2 Morphological Characterization....49
2.3.3 Specific Surface Area....50
2.3.4 Adsorption Kinetics and Isotherms....51
2.4 Conclusion....56
3 Chapter Three: *Pseudomonas Putida*-Mediated Synthesis of Biogenic Iron-Manganese Binary Oxides Nanoparticles: Characterization Insights and Potential Environmental Implications....57
Abstract....57
3.1 Introduction....58
3.2 Materials and Methods....61
3.2.1 Synthesis of Biogenic Fe-Mn Binary Oxides....61
3.2.2 Chemical Analysis....62
i. Inductively Coupled Plasma Mass Spectrometry (ICP-MS) Analysis....62
3.2.3 Mineralogical and Morphological Characterization....63
i. X-Ray Diffraction (XRD) Analysis....63
ii. Scanning Electron Microscope (SEM) Analysis....63
iii. Scanning Transmission Electron Microscopy (STEM) and Scanning Transmission Electron Microscopy-Energy Dispersive X-ray Spectroscopy (STEM-EDX) Analyses....64
iv. Transmission Electron Microscopy (TEM)-Selected Area Electron Diffraction (SAED) Analyses....64
3.3 Results and Discussion....65
3.3.1 Biosynthesis of Biogenic Fe-Mn Binary Oxides....65
3.3.2 Mineralogical and Morphological Characterization....67
i. XRD Analysis....67
ii. SEM Analysis....69
iii. Elemental Composition and Distribution....69
iv. STEM and TEM-SAED Analyses....72
3.4 Environmental Implications of Biogenic Fe-Mn Binary Oxides Nanoparticles....75
3.5 Conclusions....79
4 Chapter Four: Unfolding the Role of *Pseudomonas putida* Biofilm in Arsenic(V) Adsorption-Desorption Dynamics on Iron-Manganese Binary Oxides....80
Abstract....80
4.1 Introduction....82
4.2 Materials and Methods....84
4.2.1 Synthesis of the Abiogenic and Biogenic Fe-Mn Binary Oxides, and Biofilm Growth....84
4.2.2 Characterization of the Abiogenic and Biogenic Fe-Mn Binary Oxides....85
i. X-Ray Diffraction (XRD) analysis....85
ii. Scanning Electron Microscope (SEM) and Scanning Electron Microscopy-Energy Dispersive X-ray Spectroscopy (SEM-EDX)....85
iii. Scanning Transmission Electron Microscopy (STEM) and Scanning Transmission Electron Microscopy-Energy Dispersive X-ray Spectroscopy (STEM-EDX)....86
4.2.3 Organic Content in Biofilm and Biogenic Fe-Mn Binary Oxides....86
i. Fluorescence Microscopy....86

ii. DNA and Polysaccharide Quantification: Nanodrop and Phenol-Sulfuric Acid Methods....87
4.2.4 As(V) Adsorption Kinetic Experiments....89
4.2.5 As(V) Desorption Experiments....89
4.2.6 Adsorption Kinetics and Desorption Isotherm Modelling....90
4.2.7 Chemical analysis....91
4.3 Results and Discussion....92
4.3.1 Morphological and Elemental Characterizations of Biogenic and Abiogenic Fe-Mn Binary Oxides....92
4.3.2 Mineralogical Characterization....95
4.3.3 Organic Content in Biofilm and Biogenic Fe-Mn Binary Oxides....96
i. Fluorescence Microscopy....96
ii. DNA and Carbohydrate Quantification....97
4.3.4 As(V) Adsorption Kinetic Experiments....98
i. Factors Affecting As(V) Adsorption on Minerals....101
ii. Role of Biofilm in As(V) Adsorption....102
4.3.5 As(V) Desorption Experiments....106
4.4 Conclusion....109
5 Chapter Five: Conclusions....110
5.1 Summary of Research Findings....110
5.2 Future Research Prospects....114
Appendices....116
Bibliography....121

List of Figures

Figure 1.1: Global distribution of countries affected by groundwater arsenic contamination (≥10 μg/L) (Guo et al., 2024).....9
Figure 1.2: Arsenic-affected areas and populations in different continents of the world (model predicted) (Podgorski and Berg, 2020).....10
Figure 1.3: Geologic arsenic cycle (Masuda, 2018) [Numbers in parenthesis correspond to the average As concentration (mg/kg) of each geological reservoir].....13
Figure 1.4: (a) Eh-pH diagram for aqueous arsenic species in the system As–O_2–H_2O at 25 °C and 1 bar total pressure, (b) Arsenite and (c) Arsenate speciation as a function of pH (ionic strength of about 0.01 M) (Smedley and Kinniburgh, 2002).....14
Figure 1.5: Adsorption of a molecule onto the internal surface of a porous adsorbent (Tan and Hameed, 2017).....17
Figure 1.6: Physisorption and chemisorption mechanisms (Berger and Bhown, 2011).....18
Figure 1.7: Outer-sphere and inner-sphere surface complexes on a metal oxide–water interface. The illustration shows uranyl ions (UO_2^{2+}) adsorption onto a silica surface as an example (Payne et al., 2013).....20
Figure 1.8: Formation of surface complexes of As(III) and As(V) on the metal oxide (M= Mn, Fe) surface (Wang and Mulligan, 2008).....21
Figure 1.9: Different stages of biofilm formation (van Hoogstraten et al., 2023).....28
Figure 1.10: The classical framework of microbial biomineralization (Cosmidis and Benzerara, 2022).....29
Figure 2.1: XRD patterns of (a) ferrihydrite and (b) Fe-Mn binary oxides with ICDD reference lines of ferrihydrite and birnessite.....47
Figure 2.2: XRD pattern of (a) ferrihydrite (Gimsing and Borggaard, 2007), (b) Fe-Mn binary oxides with biochar (Liang et al., 2020), (c) Fe-Mn binary oxides (Byanjankar et al., 2024), and (d) Fe-Mn binary oxides in different Mn/Fe mole ratios (Li et al., 2017).....48
Figure 2.3: SEM images (ferrihydrite (a, b), Fe-Mn binary oxides (c, d)) and SEM-EDX spectra of ferrihydrite and Fe-Mn binary oxides.....49
Figure 2.4: PFO kinetic models of As(V) adsorption on ferrihydrite (a) and Fe-Mn binary oxides (b).....51
Figure 2.5: Time-dependent concentrations of As(V) in solution during adsorption on ferrihydrite and Fe-Mn binary oxides (a), Mass-normalized experimental As(V) adsorption and PSO kinetic models of ferrihydrite and Fe-Mn binary oxides (b), PSO kinetic t/q_t vs reaction time (t) linear plot (c), and Specific surface area-normalized As(V) adsorption onto ferrihydrite and Fe-Mn binary oxides (d). Error bars have been calculated as the standard deviation of the different replicates.....53
Figure 2.6: Concentration-dependent As(V) adsorption on ferrihydrite and Fe-Mn binary oxides (a), Mass-normalized experimental As(V) adsorption isotherms and Langmuir isotherm models of ferrihydrite and Fe-Mn binary oxides (b), Langmuir isotherm C_e/q_e vs C_e linear plot (c), and Specific surface area-normalized As(V) adsorption of ferrihydrite and Fe-Mn binary oxides (d). Error bars have been calculated as the standard deviation of the different replicates.....54
Figure 3.1: Percentages of Mn(II) and Fe(II) mineralization over 18 days. Error bars have been calculated as the standard deviation of the different replicates.....66
Figure 3.2: (A) Raw XRD pattern of the microbial precipitates collected at 18 days, (B) Background corrected XRD spectrum with corresponding d-spacings, (C) Birnessite reference line spectrum, ICDD 00-013-0105, (D) Birnessite reference line spectrum, ICDD 01-073-7862, and (E) Ferrihydrite reference line spectrum, ICDD 00-058-0898.....67

Figure 3.3: SEM images of the biogenic precipitates showing co-localization of bacterial cells, EPS, and mineral particles. 69
Figure 3.4: (a) HAADF-STEM image of the biogenic Fe-Mn binary oxide, (b) STEM-EDX Mn map, (c) STEM-EDX Fe map, (d) STEM-EDX O map, (e) STEM-EDX P map and (f) STEM-EDX P and C overlaid map in biogenic Fe-Mn binary oxides. 70
Figure 3.5: STEM-EDX spectra of specific regions of biogenic Fe-Mn binary oxides shown on the overlaid EDX maps of Fe, Mn (spectrum 1, spectrum 2). 71
Figure 3.6: (A) BF-STEM image of the biogenic Fe-Mn-binary oxides nanoparticles mixed with bacteria cells, (B) BF-STEM image of the different morphologies of biogenic Fe-Mn binary oxides, (C) BF-STEM image of the ultrathin layered morphology of the particles, (D-E) BF-STEM image of the chain-like particle aggregates, (F) BF-STEM image of the large granular particle cluster....73
Figure 3.7: TEM images of the different areas (A, D, G) of the biogenic Fe-Mn binary oxides sample, with corresponding SAED diffraction patterns (B, E, H) and measured d-spacing (C, F, I)....74
Figure 3.8: Putative pathways of biogenic Fe-Mn binary oxides formation at the oxic-anoxic interface of a redox-stratified lake, as informed by the experimental results herein. 76
Figure 4.1: Glucose standard curve of concentration-absorbance to estimate carbohydrate concentration. 88
Figure 4.2: Schematic of As(V) desorption experiment from biogenic and abiogenic Fe-Mn binary oxides. 90
Figure 4.3: SEM images of the (a, b) biogenic and (c, d) abiogenic Fe-Mn binary oxides.....92
Figure 4.4: BF-STEM images of the biogenic Fe-Mn binary oxides. (a,b,d) Biogenic Fe-Mn binary oxides aggregation with bacterial cells, (e) Various morphologies of biogenic Fe-Mn binary oxides, (e,f) Ultra-thin plate like morphology of biogenic Fe-Mn binary oxides. 93
Figure 4.5: STEM-EDX and SEM-EDX spectra and maps of biogenic (upper) and abiogenic (lower) Fe-Mn binary oxides, respectively. 94
Figure 4.6: XRD of biogenic (a) and abiogenic (b) Fe-Mn binary oxides with ICDD reference ferrihydrite and birnessite patterns....95
Figure 4.7: Fluorescence imaging of carbohydrate (lectin- green fluorescence) and DNA (DAPI- purple fluorescence) in (a) biofilm and (b) biogenic Fe-Mn binary oxides. 96
Figure 4.8: As(V) adsorption on biofilm and biogenic Fe-Mn binary oxides (a), abiogenic Fe-Mn binary oxides, and abiogenic Fe-Mn binary oxides mixed with biofilm (b). Error bars have been calculated as the standard deviation of the different replicates. 98
Figure 4.9: PFO kinetic models of biofilm (a), biogenic Fe-Mn binary oxides (b), abiogenic Fe-Mn binary oxides (c), and abiogenic Fe-Mn binary oxides mixed with biofilm (d). 99
Figure 4.10: Experimental data plotted along with PSO As(V) adsorption kinetic models for the biofilm (a) and biogenic Fe-Mn binary oxides, abiogenic Fe-Mn binary oxides, and abiogenic Fe-Mn binary oxides mixed with biofilm (b). Error bars have been calculated as the standard deviation of the different replicates. 100
Figure 4.11: Putative mechanism of As(V) diffusion, adsorption into biofilm and onto mineral surface of the biogenic Fe-Mn binary oxides. (a) Biofilm (bacterial cells and EPS) on mineral surface and pore spaces at their interfaces, (b) Evolution of the As(V) concentration profiles across the biofilm layer over time due to diffusion, (c) Diffused As(V) adsorbed onto mineral surface passing through pore space and the diffusion flux controls the As(V) adsorption on mineral, (d) As(V) adsorption rate onto mineral will depend on how close the adsorbed concentration is to equilibrium with the pore concentration, (e) As(V) concentration in solution goes down as As(V) adsorption onto mineral progresses. 104
Figure 4.12: (A) Amount of As(V) desorbed in solution from abiogenic and biogenic Fe-Mn binary oxides during each desorption cycle, (B) Percentage of As(V) desorption in solution

from abiogenic and biogenic Fe-Mn binary oxides during each desorption cycle. Error bars have been calculated as the standard deviation of the different replicates. 107
Figure 4.13: (a) Langmuir isotherm C_e/q_e vs C_e linear plots of abiogenic and biogenic Fe-Mn binary oxides for As(V) desorption, and (b) As(V) desorption isotherms of abiogenic and biogenic Fe-Mn binary oxides. The arrow indicates the direction of reaction progress, showing that desorption decreases with each desorption cycle as As(V) concentrations on the minerals also decline.....108
Figure 3-A1: XRD pattern of the background, an empty Silicon disc.....116
Figure 3-A2: Biotic mineralization (a) and abiotic control (b) experiments after 18 days....117
Figure 3-A3: STEM-EDX elemental distribution maps of Fe (a), Mn (b), P (c) and O (e) of biogenic Fe-Mn binary oxides. Fe and Mn overlaid mapping (e) and STEM-EDX elemental distribution spectra of the whole image (f) of biogenic Fe-Mn binary oxides. 117
Figure 4-A4: Linearized Langmuir isotherm t/q_t vs t plots for As(V) adsorption on biofilm, biogenic Fe-Mn binary oxides, abiogenic Fe-Mn binary oxides and abiogenic Fe-Mn binary oxides mixed with biofilm. 119
Figure 4-A5: Images of biofilms in mineralization media (after 7days of growth).....120

List of Tables

Table 1.1: Naturally occurring major arsenic minerals (Mandal and Suzuki, 2002; WHO, 2001). 7
Table 1.2: Natural abundance of arsenic in crustal materials (Nriagu et al., 2007; Bhattacharya et al., 2002; Yudovich and Ketris, 2005). 8
Table 1.3: Examples of biogenic minerals found in various environments. 30
Table 1.4: Mn(II) oxidizing bacteria (MnOB) groups found in various environments (Cai et al., 2023). 33
Table 2.1: PFO and PSO kinetic models derived parameters for As(V) adsorption on ferrihydrite and Fe-Mn binary oxides. 52
Table 4.1: A rough estimation of the organic matter masses in biofilm and biogenic Fe-Mn binary oxides. 97
Table 4.2: PFO and PSO adsorption kinetic model parameters 101
Table 3-A1: pH changes during biomineralization experiment using *P. putida*. 118
Table 3-A2: pH changes in an abiotic control experiment. 118

Statement of Originality

I confirm this thesis I am submitting is my own original research work, and that no part of my thesis has been submitted to any educational institution as a requirement of any degree. I hereby certify that, to the best of my knowledge, my thesis does not violate anyone's copyright, and all the reference works are properly cited. Whilst this thesis is my own work, parts were written in collaboration with my advisors Don Porcelli, Julie Cosmidis and Imad Ahmed. For Chapters 2, 3 and 4, they assisted with the initial conceptualization of the study, helped to facilitate and support the laboratory work, and provided help with interpreting the data. I undertook the laboratory experiments and data collection, chemical modelling, and wrote the initial drafts of the manuscripts. My advisors provided edits to the manuscripts of all the chapters.

Acknowledgement

I express my sincere appreciation to my supervisors and academic mentors, Don Porcelli, Julie Cosmidis, and Imad Ahmed, for their invaluable guidance and constant support to conceptualize this research project, planning laboratory experiments, interpreting data, and writing this thesis. I especially thank Julie for ensuring all the laboratory facilities I needed were available in the best possible ways. I am grateful to all of them for their support during a challenging time in my life following the passing of my father.

I would like to extend my heartfelt gratitude to Professor Andreas Kappler, Verena Nikeleit, and Lars Grimm from the Geomicrobiology Laboratory at the University of Tübingen for providing me with geo-microbial training in their laboratory. I wish to thank Laura Galezowski and Feriel Panet from the Institute of Mineralogy, Physics of Materials, and Cosmochemistry at Sorbonne University for sending the *Pseudomonas putida* MnB1 strain for my experiment. I am thankful to Phil Holdship and Kris Sokol from Oxford Earth Sciences for their assistance in ICP-MS and XRD analyses. I appreciate Krisztina Sarkozi for her assistance and guidance in DNA extraction and quantification. I also appreciate the assistance of Errin Johnson and Alan Waiman from the microscopy facilities at the Sir William Dunn School of Pathology, University of Oxford, during my microscopic experiments. Additionally, I wish to thank Gerardo Martinez Alanis for his support with STEM analysis in the David Cockayne Centre for Electron Microscopy at the Department of Materials, University of Oxford.

I would also like to remember and thank my colleagues at the Oxford Microbe-Mineral Laboratory- Luke Williams, Shuo Wang, and Luca Stigliano for their constant support and companionship.

This research was made possible by the Commonwealth Scholarship Commission in the UK under the Commonwealth PhD Scholarship 2021 funding. I am sincerely thankful to the Commission for their financial support.

Finally, I am deeply grateful to my family members and friends, whose continuous encouragement, motivation, and care have been instrumental in helping me pursue and complete my DPhil.

Abstract

Arsenic (As) is a common trace metal in the environment and a global environmental concern due to its toxicity and occurrence in the groundwater of many countries in high concentrations. Understanding As adsorption and desorption mechanisms onto and from aquifer or soil minerals is important to comprehend As mobility and transport in aquatic environments. This thesis investigates As(V) adsorption and desorption dynamics onto and from iron-manganese (Fe-Mn) binary oxides formed through both biological and abiotic processes. Indeed, iron and manganese oxides often co-exist in the environment, and the roles of these binary phases in trace metal cycling are currently under-investigated. Fe-Mn binary oxides might play a significant role in As(V) adsorption dynamics in nature due to their high efficiency of As(V) adsorption. In our experiments, abiotically precipitated Fe-Mn binary oxides demonstrated higher adsorption capacity than ferrihydrite, an extensively studied potential As(V) adsorbent. Higher specific surface area and pore size might have contributed to the increased As(V) adsorption of Fe-Mn binary oxides. Both adsorption systems fitted greatly with the Pseudo-Second-Order kinetic model, indicating adsorption of As(V) onto both minerals might have been caused by chemisorption. Though abiogenic forms of Fe- and Mn oxides have been investigated a lot previously, biogenic Fe-Mn binary oxides, which in nature may be formed through the activity of metal-oxidizing bacteria, are often overlooked in terms of their role in trace metals adsorption-desorption dynamics, including As(V). In this research, we also produced biogenic Fe-Mn binary oxides using *Pseudomonas putida*, which oxidized Mn(II) to Mn oxides, followed by the oxidation of Fe(II) to Fe oxides by the Mn oxides under micro-oxic conditions. Both phases were co-precipitated as finely inter-mixed biogenic Fe-Mn binary oxides. This synthesis procedure described a potential new pathway for biogenic Fe-Mn binary oxides formation at oxic-anoxic interfaces in nature. The synthesized biogenic minerals were characterized using a suite of analytical techniques, including X-ray Diffraction, Scanning Electron Microscopy, (Scanning) Transmission Electron Microscopy, Selected Area Electron Diffraction, Energy-Dispersive X-ray Spectroscopy (EDX), and fluorescence microscopy. The biogenic minerals appeared as aggregates of fine mineral particles and bacterial cells and EPS. Ultrathin plates, long chains, and globular morphologies were commonly observed in the biogenic Fe-Mn binary oxides minerals. Mineral particles were <100 nm in size, which categorized them as nanoparticles. Mineralogical analysis revealed that the minerals' structures were amorphous or poorly crystalline and consisted of a mixture of birnessite and ferrihydrite nanocrystals. EDX analyses showed the heterogeneous distribution of Fe and Mn within the

biogenic Fe-Mn binary oxides, confirming the existence of these elements in two distinct phases. These minerals contained a significant amount of phosphorus, which might have originated from the hydrolysis of the microbial cells and is thought to be present as phosphate ions bound to the mineral surfaces.

This research also compared the As(V) adsorption-desorption dynamics of biogenic and abiogenic Fe-Mn binary oxides and revealed the role of biofilm in adsorption-desorption mechanisms. Biogenic minerals demonstrated lower As(V) adsorption capacity as compared with abiogenic Fe-Mn binary oxides due to their close association with organic matter (bacterial cells and EPS), which might cover a significant portion of the mineral surfaces. Moreover, the presence of microbial cells and EPS (biofilm) could provide net negative charges at the surface of the biogenic minerals, which might cause electrostatic repulsion to the negatively charged As(V) species, impeding As(V) adsorption. Additionally, the presence of phosphate groups at the surface of the biogenic minerals might have blocked potential surface sites for As(V) adsorption. Adsorption of As(V) on biogenic minerals was found to be controlled by As(V) diffusion through biofilm, influencing As(V) adsorption onto the biogenic minerals. As(V) desorption experiments from both biogenic and abiogenic Fe-Mn binary oxides demonstrated that, while a small fraction of the adsorbed-As(V) might desorb, the majority of As(V) is adsorbed irreversibly on both types of minerals, presumably through chemisorption. This indicates that both minerals might be expected to retain As(V) even as the concentration of As(V) in solution changes, such as in the case of flood events and groundwater level change. This research sheds light on the potential formation pathway of biogenic Fe-Mn binary oxides at the oxic-anoxic interface of the water column in nature, highlighting their environmental importance. It also provides a better understanding of the As(V) adsorption and desorption onto and from both abiogenic and biogenic Fe-Mn binary oxides in the presence of microbial biofilms, which might have great environmental significance.

1 Chapter One: Introduction

1.1 Arsenic

Arsenic (As) is a ubiquitous trace metal in the environment and a global environmental concern due to its presence at high concentrations in some groundwater. It is the 20th and 14th most abundant element in the Earth's crust and seawater, respectively (Mandal and Suzuki, 2002). Arsenic is a metalloid (semi-metal) with an atomic number of 33 and a relative atomic mass of 74.92. It has a boiling point of 613 °C and a density value of 5.75 g/cm^3 at 25 °C. Its common valence states are −3, 0, +3, and +5. It has only one stable isotope, ^{75}As. The metallic form of As is bright and silvery grey in color and brittle in texture.

1.2 Arsenic Toxicity and Associated Health Problems

Arsenic carcinogenicity and toxicity to humans are one of the primary reasons for extensive research on As adsorption, mobility, transport, and contamination remediation (Muehe et al., 2016; Guo et al., 2008). This element is considered as one of the significant global environmental issues due to its presence at a concentration higher than >10 µg/L (the World Health Organization (WHO) recommended drinking-water standard) in groundwater aquifers of many countries, especially in South Asia, including Bangladesh, India, Cambodia, Vietnam, Pakistan, Sri Lanka, Nepal, Afghanistan, and its carcinogenic effects on human health (Mukherjee et al., 2006; Benner and Fendorf, 2010; Sharma et al., 2010; Amstaetter et al., 2010; Hassan et al., 2017; Rahman et al., 2009). Consumption of As-contaminated water and food can lead to As poisoning, known as arsenicosis, a chronic health condition caused by long-term (no less than 6 months) ingestion of elevated concentrations of As, generally indicated by skin lesions (melanosis and/or keratosis), regardless of whether internal organs are affected (Ahmad and Khan, 2023; Das and Sengupta, 2008; WHO, 2003). Arsenic has been identified as a non-threshold carcinogen (class 1) for humans (Hohmann et al., 2011; WHO and IARC, 2004; Ng et al., 2003) (i.e., a carcinogen with no safe exposure level). Acute effects of As poisoning include diarrhea, abdominal pain, vomiting, and death in severe cases (WHO, 2022). Chronic exposure to As is associated with serious health conditions, including skin, lungs, liver, prostate, bladder, and hematopoietic cancers, as well as diabetes and cardiovascular and pulmonary diseases (WHO, 2022; Genchi et al., 2022; Tsuji et al., 2019; Cohen et al., 2013).

Research has also indicated that there are links between As exposure, neurotoxicity, and negative cognitive development, particularly in aspects of memory and intelligence (Tolins et al., 2014). Furthermore, As exposure has also been reported to adversely affect pregnancy outcomes, infant mortality, and child health (Quansah et al., 2015; Farzan et al., 2013). Though WHO has recommended 10 µg/L as safe As concentration in drinking water, many developing countries such as Bangladesh follow higher concentration standards, allowing up to 50 µg/L due to the inaccessibility of lower As-concentration drinking water throughout the country and available water treatment facilities (Tolins et al., 2014; Ng et al., 2003; Smedley and Kinniburgh, 2002; Frisbie et al., 2002; Smith et al., 2000).

1.3 Arsenic in the Environment

Arsenic is a naturally occurring metalloid present in soils and rocks, atmosphere, and natural waters. It is widely distributed in soil, sediment, rocks, and metal ores in the forms of oxyhydroxide or sulfide or in oxides of various metals (Aronson, 1994; Singh et al., 2007). The surface and groundwater of many countries have been reported to be contaminated with increased levels of As, primarily of natural origin or exaggerated by anthropogenic activities. Natural geological non-point sources of As pose a greater threat than point sources to global water quality (Saunders et al., 2005). Surprisingly, very high concentrations of As in groundwater, reaching several milligrams per liter, have been observed in areas with source rocks that do not necessarily contain high concentrations of As. Most of these cases occur in aquifers within relatively young materials, often consisting of alluvium or loess (Smedley and Kinniburgh, 2002). Natural processes of As contamination in surface and groundwater involve complex interactions among the hydrosphere, geosphere, and biosphere (Masuda, 2018).

1.3.1 Arsenic in Minerals and Soils

Arsenic mainly originates from geogenic sources (Smedley and Kinniburgh, 2002) and is sometimes associated with iron-containing minerals (Hohmann et al., 2011). The average concentration of total As in soil is 5 mg/kg but varies greatly among geological origins (Punshon et al., 2017; Morosini et al., 2023). The geogenic sources of As are generally As-containing minerals that are distributed in a wide variety of environments including hydrothermal and mesothermal veins. Commonly found As minerals in nature are listed in Table 1.1. Naturally, it occurs in more than 300 minerals (Drahota and Filippi, 2009). A vast majority of those minerals are arsenates, accounting for around 60%.

Approximately 20% are sulphides and sulfosalts, while the remaining 20% are comprised of arsenides, arsenites, oxides, silicates, and elemental arsenic (Mandal and Suzuki, 2002; Onishi, 1969). In the subsurface under reducing conditions, arsenopyrite (FeSAs), realgar (AsS), and orpiment (As_2S_3) are formed, which are primary mineral hosts of arsenic (Garelick et al., 2009). When exposed to oxidizing conditions, arsenite is oxidized and forms arsenates, including calcareous arsenolite and iron arsenate minerals (Nriagu et al., 2007).

Table 1.1: Naturally occurring major arsenic minerals (Mandal and Suzuki, 2002; WHO, 2001).

Mineral	Composition	Occurrence
Native arsenic	As	Hydrothermal veins
Proustite	Ag_3AsS_3	Generally one of the late Ag minerals in the sequence of primary deposition
Rammelsbergite	$NiAs_2$	Commonly in mesothermal vein deposits
Safflorite	$(Co,Fe)As_2$	Generally in mesothermal vein deposits
Seligmannite	$PbCuAsS_3$	Occurs in hydrothermal veins
Smalite	$CoAs_2$	–
Niccolite	NiAs	Vein deposits and norites
Realgar	AsS	Vein deposits, often associated with orpiment, clays and limestones, also deposits from hot springs
Orpiment	As_2S_3	Hydrothermal veins, hot springs, volcanic sublimation product
Cobaltite	CoAsS	High-temperature deposits, metamorphic rocks
Arsenopyrite	FeAsS	The most abundant As mineral, dominantly mineral veins
Tennantite	$(Cu,Fe)_{12}As_4S_{13}$	Hydrothermal veins
Enargite	Cu_3AsS_4	Hydrothermal veins
Arsenolite	As_2O_3	Secondary mineral formed by oxidation of arsenopyrite, native As and other As minerals
Claudetite	As_2O_3	Secondary mineral formed by oxidation of realgar, arsenopyrite and other As minerals
Scorodite	$FeAsO_4 \cdot 2H_2O$	Secondary mineral
Annabergrite	$(Ni,Co)_3(AsO_4)_2 \cdot 8H_2O$	Secondary mineral
Hoernesite	$Mg_3(AsO_4)_2 \cdot 8H_2O$	Secondary mineral, smelter wastes
Haematolite	$(Mn,Mg)_4Al(AsO_4)(OH)_8$	–
Conichalcite	$CaCu(AsO_4)(OH)$	Secondary mineral
Adamite	$Zn_2(OH)(AsO_4)$	Secondary mineral
Domeykite	Cu_3As	Found in vein and replacement deposits formed at moderate temperatures
Loellingite	$FeAs_2$	Found in mesothermal vein deposits
Pharmacosiderite	$Fe_3(AsO_4)_2(OH)_3 \cdot 5H_2O$	Oxidation product of arsenopyrite and other As minerals

The natural background concentration of As in soil is higher in areas overlying mineral formations with elevated As concentrations (Saxe et al., 1964). Clays and shales, which are soil-forming rocks, often contain high concentrations (0.3-490 mg/kg) of As. Clays formed in deep-sea environments but now on land particularly have elevated As content (Dragun and Chiasson, 1991). Igneous rocks also contain a wide range of As concentrations (0.2-113 mg/kg) (Jacks and Bhattacharya, 1998; Dragun and Chiasson, 1991). The natural abundance of As in crustal rocks is presented in Table 1.2 (Jacks and Bhattacharya, 1998; Nriagu et al., 2007).

Table 1.2: Natural abundance of arsenic in crustal materials (Nriagu et al., 2007; Bhattacharya et al., 2002; Yudovich and Ketris, 2005).

Rock type	Arsenic concentration range (mg/kg)
Igneous Rock	
Ultrabasics	0.3-16
Basalts	0.06–113
Andesites	0.5–5.8
Granites/silicic volcanics	0.2–13.8
Sedimentary Rock, Sediments	
Shales and clays	0.3-490
Phosphorites	0.4–188
Sandstones	0.6–120
Limestones	0.1–20
Coal	
Bituminous	9.0±0.8
Lignites	7.4±1.4
Peat	16-340

Coal has been reported as a source of elevated concentrations of As (~ 7-340 mg/kg), which occurred as both arsenite and arsenate species (Nriagu et al., 2007; Acharyya et al., 1999). Arsenic is deposited into the soil and sediment by the weathering of arsenic-bearing sedimentary and igneous rocks, aeolian and fluvial transports and redepositions (Meharg and Meharg, 2021; Masuda, 2018; Saxe et al., 1964).

1.3.2 Arsenic in Groundwater

The presence of As in groundwater is influenced by various biogeochemical and environmental factors, including aquifers geochemistry, water-rock interactions, and physical and (bio)geochemical processes for As mobilization and accumulation (Smedley and Kinniburgh, 2002). Groundwater As contamination occurs due to weathering reactions and biological activities on As-bearing rocks and minerals and leaching from those minerals and soils (Saxe et al., 1964).

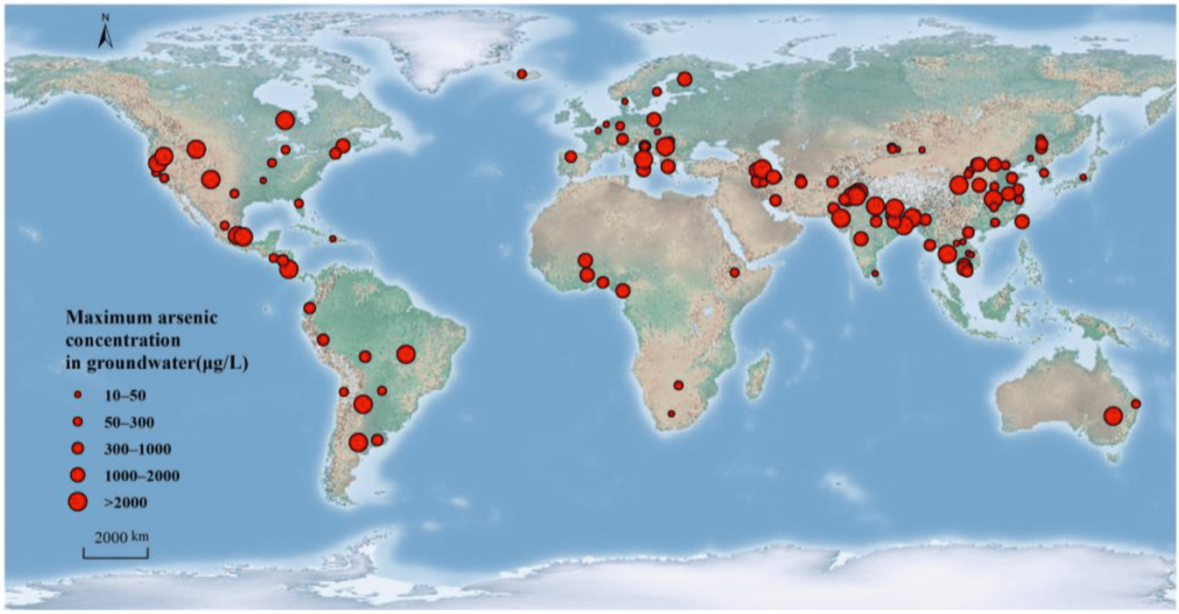


Figure 1.1: Global distribution of countries affected by groundwater arsenic contamination (≥10 μg/L) (Guo et al., 2024).

Contaminated groundwaters are often located far from sources of As, where the actual chemical weathering of As-bearing rocks and minerals happens (Saunders et al., 2005). This is because, upon weathering of the As-containing orogenic rocks by mechanical, geochemical, and geomicrobial processes, the rock fragments and sediments are river-transported across long distance to the sedimentary basin and deposited as As-containing alluvial sediments (Kumar et al., 2021; Saunders et al., 2005). Arsenic is released from alluvial aquifer sediments to the groundwater by several mechanisms, including microbial reductive dissolution of As-bearing minerals, ligand exchange, and pyrite oxidation, which are discussed in section 1.4.

Groundwater As contamination in Holocene alluvial aquifers is generally originated from natural sources and intensified by anthropogenic inputs of As (Saunders et al., 2005; Smedley and Kinniburgh, 2002). It occurs under both oxidizing and reducing groundwater conditions, as well as in both humid/temperate and arid climates (Smedley and Kinniburgh, 2002).

Though the natural background concentrations of As are less than 10 µg/L in most countries, the concentrations of As reported in the literature show a very wide range from less than 0.5 to 5000 µg/L under natural conditions (Smedley and Kinniburgh, 2002). Groundwater As contamination has been identified worldwide affecting 107 counties (Guo et al., 2024; Shaji et al., 2021). Figure 1.1 shows the global distribution of groundwater As contamination from geogenic sources. Asia has the highest number of countries and people affected by As-contaminated drinking water (Guo et al., 2024; Podgorski and Berg, 2020) as shown in Figure 1.2. Groundwater As contamination is a common natural geogenic problem in many countries, especially in Southeast Asia (McCann et al., 2018; Rahman et al., 2009), and poses a global public health threat. The presence of As above 10 µg/L has been reported in drinking water in Bangladesh, India, Pakistan, Nepal, Vietnam, Myanmar, Indonesia, Cambodia, China, Taiwan, Argentina, the USA, Chile, Hungary, Croatia, Mexico and many other countries of the world (Ahmad et al., 2018; Thakur et al., 2010; Winkel et al. 2008; Habuda-Stanić et al., 2007; Mukherjee et al. 2006) putting more than 230 million people at risk of As exposure (Shaji et al., 2021; Naujokas et al., 2013; WHO, 2011).

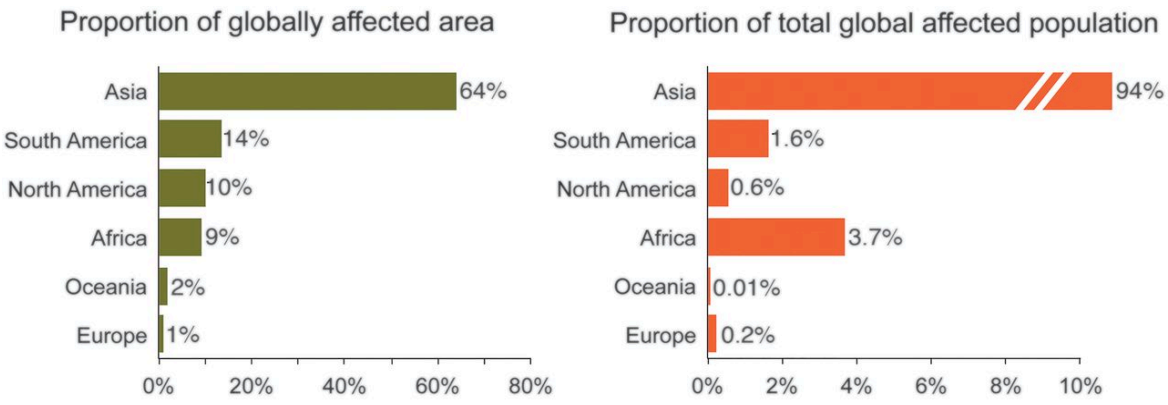


Figure 1.2: Arsenic-affected areas and populations in different continents of the world (model predicted) (Podgorski and Berg, 2020).

Bangladesh and India (West Bengal) are considered the worst As-affected countries in the world in terms of the total number of people exposed to As-contaminated drinking water. Concentrations of As in groundwaters from the affected areas of these countries range from <0.5 to ~3200 µg/L (Smedley and Kinniburgh, 2002; BGS, 2001). In Bangladesh, this situation is considered as the largest mass poisoning of a population in history because of its large As-affected population of more than 80 million (Ahmad et al., 2018; Hossain et al., 2006; Smith et al., 2000).

1.3.3 Anthropogenic Sources of Arsenic

In addition to natural processes, As is released into the environment through various anthropogenic activities (Smedley and Kinniburgh, 2002). Diverse anthropogenic sources of As have been identified that release As into the environment, including industrial and mining activities, smelting, combustion of fossil fuels, use in wood preservatives, and use of arsenical pesticides and herbicides (Smedley and Kinniburgh, 2002; Garelick et al., 2009).

Mining and smelting are the most significant anthropogenic sources of As (Garelick et al., 2009). Mine tailings and effluents often contain As in very high concentrations, posing significant concern as potential sources of As contamination. Arsenic contamination of surface and groundwater, soils, and sediments from mining sources has been reported in the UK, the USA, Australia, China, Mexico, Brazil, Taiwan, and other countries (Camm et al., 2004; Moore and Woessner, 2003; Smith et al., 2003; Zhang et al., 2002; Carillo-Cha´vez et al., 2000; Borba et al. 2003; Shih and Lin, 2003). In mine tailings, As can be found in various forms, including arsenian pyrite (As-rich FeS_2), arsenopyrite (FeAsS), and arsenates, adsorbed onto iron oxyhydroxides (Wang and Mulligan, 2006a). Arsenic concentrations can reach hundreds to thousands of mg/kg in mining tailings and effluents (Wang and Mulligan, 2004). Elevated levels of As have been found in the natural aquifers of Nova Scotia in Canada, the surface and groundwater of Cornwall in the UK, and in the soils and groundwater of northern Mexico and southwestern USA, due to leaching of mining tailings (Middleton et al., 2017; Camacho et al., 2011). Smelter, ore processing, and metal refinery facilities are also important anthropogenic sources of As contamination in soils and waters (Wang and Mulligan, 2006a). Deposition of As in soils occurs from gold, silver, and copper smelters, and the soils of Anaconda and Montana in the USA have been reported to have As concentrations as high as several hundred parts per million in areas close to the smelters (Saxe et al., 1964).

Oil and coal-burning thermal and power-generating plants are other anthropogenic contributors of As to the environment and elevated As concentrations have been detected in the vicinity of these sources (Garelick et al., 2009; Wang and Mulligan, 2006a; Saxe et al., 1964). Arsenical pesticides, insecticides, fungicides, and herbicides used in agricultural activities represent non-point anthropogenic sources of As in the environment (Wang and Mulligan, 2006a). Inorganic arsenicals such as arsenic trioxide, arsenic acid, arsenates of calcium, copper, lead, and sodium, and arsenites of sodium and potassium have been largely used as pesticides, insecticides, fungicides, and herbicides for about one hundred years. Though currently arsenical pesticides are no longer used in agricultural practices in Western countries, the remaining residues in soils are still environmental concerns (Nriagu et al., 2007; Wang and Mulligan, 2006a). Other anthropogenic sources of As include pharmaceutical substances, waste disposal and incineration, electronics industries, solar cells, colors and dyes, glassware, and ceramics manufacturing (Garelick et al., 2009).

1.4 Arsenic Cycling, Geochemical Behaviour and Transport

Arsenic concentration in any soil horizon depends on parent materials, while pedogenesis further redistributes As through weathering, leaching, and sequestration. The primary pre-anthropogenic sources of As in soils are bedrock weathering and subsequent transport of sediment or water. Arsenic also originates from atmospheric sources such as volcanic emissions, aeolian soil erosion, and microbially bio-volatilized arsines. Additionally, sediment transport contributes to mobilizing and redistributing As through aeolian, fluvial, and subduction processes (Meharg and Meharg, 2021). The geologic cycle of As is shown in Figure 1.3 and briefly described here. Volcanic and hydrothermal activities, erosion, and subsequent transportation to downstream sedimentary basins contribute to As contamination by in situ fragmentation, weathering, and dissolution of As-bearing minerals (Masuda, 2018). Arsenic is released from arc magmas enriched by hydrothermal fluids derived from metamorphic dehydration of the subducting slab and from deep continental and island-arc crust during low-temperature and high-pressure metamorphism. Hot-spring water containing arsenites (produced by oxidized As–sulfur complexes) flows out at the surface (Masuda, 2018). Arsenic can be associated with pyrite during diagenesis under strongly reducing conditions (Saunders et al., 2008).

In the geologic cycling of As, plate tectonics play an important role since steeper slopes produced by tectonics activities influence active crustal movement (Masuda, 2018; Hecht and Oguchi, 2017) and contribute to the redistributions of As in the downstream sedimentary basins and aquatic environments.

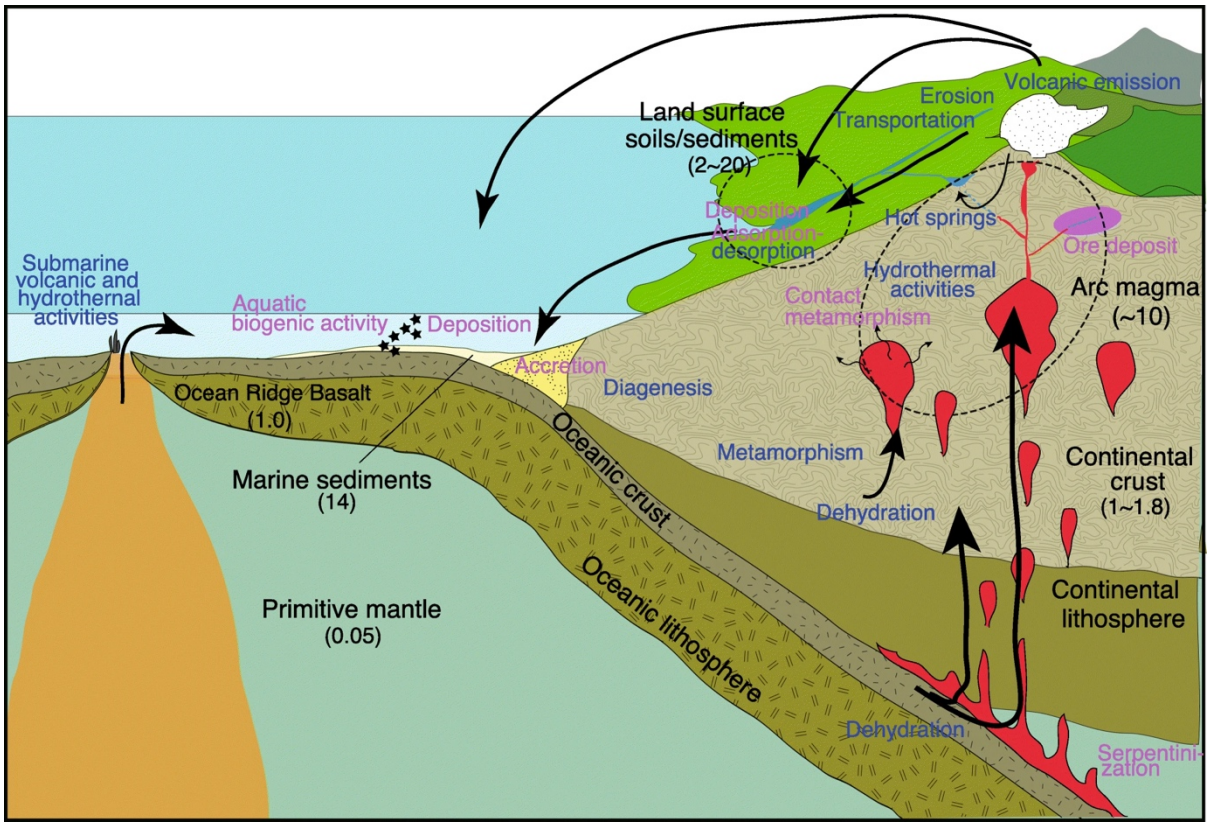


Figure 1.3: Geologic arsenic cycle (Masuda, 2018) [Numbers in parenthesis correspond to the average As concentration (mg/kg) of each geological reservoir].

Geochemical behavior and mobility of As are controlled by As speciation. Arsenic has four oxidation states; -III (arsine), 0 (elemental arsenic), +III (arsenite), and +V (arsenate), though arsine and elemental As are rare in the environment (Mandal and Suzuki, 2002). Both organic and inorganic forms of As are present in the aquatic environment, although the inorganic forms of As are more prevalent and considered more toxic than organic As species (McCarty et al., 2011; Jomova et al., 2011; Dixit and Hering, 2003; Smedley and Kinniburgh, 2002; Abbas et al., 2018; Sharma and Sohn, 2009; Smedley and Kinniburgh, 2002). Trivalent arsenite [As(III)] and pentavalent arsenate [As(V)] are the primary inorganic species in aquatic environments. As(V) is the dominant species in aerobic conditions and is generally bound with or adsorbed on mineral phases, whereas As(III) is predominant in anaerobic conditions and more mobile than As(V).

Speciation of As is primarily controlled by the pH and redox potential (Eh) of the environment (Smedley and Kinniburgh, 2002). Figure 1.4 shows the Eh-pH diagram for the distribution of aqueous As species in the As-O_2-H_2O system. At pH less than 9.2 under reducing conditions, the uncharged As(III) species $H_3AsO_3^0$ will predominate (Figure 1.4 a, b). At pH <6.9 and under oxidizing conditions, the As(V) species $H_2AsO_4^-$ is dominant, and at higher pH, the As(V) species $HAsO_4^{2-}$ becomes dominant (Figure 1.4 a, c). Arsenic can be stabilized as a series of As(V) oxyanions, H_3AsO_4, $H_2AsO_4^-$, $HAsO_4^{2-}$, and AsO_4^{3-}, under moderate or high redox potential conditions (Mandal and Suzuki, 2002). In highly acidic and alkaline conditions, $H_3AsO_4^0$ and AsO_4^{3-} can be present (Figure 1.4 a, c) (Singh et al., 2015; Smedley and Kinniburgh, 2002; Mandal and Suzuki, 2002; Lloyd and Oremland, 2006; Yan et al., 2000).

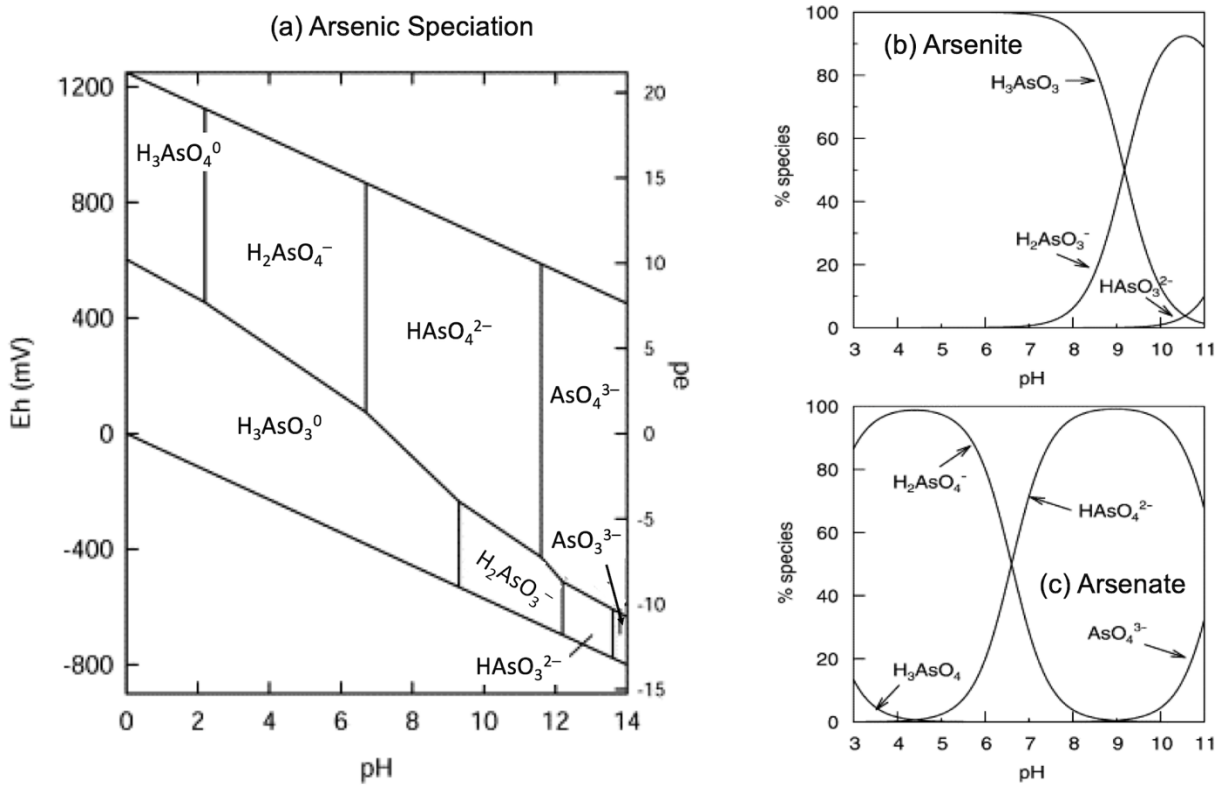


Figure 1.4: (a) Eh-pH diagram for aqueous arsenic species in the system As–O_2–H_2O at 25 °C and 1 bar total pressure, (b) Arsenite and (c) Arsenate speciation as a function of pH (ionic strength of about 0.01 M) (Smedley and Kinniburgh, 2002).

In surface and groundwater environments, redox conditions and pH are the key factors that control As release from sediments (Masuda, 2018). The major geochemical processes that control As transport and concentration in water include the oxidation of As-bearing sulfide minerals, and the reductive dissolution of As-bearing (hydro)oxides such as iron (Fe), aluminum (Al), and manganese (Mn) oxides minerals (Wang and Mulligan, 2006a; Wang and Mulligan, 2006b; Kim et al., 2000). In particular, the reductive dissolution of As-bearing Fe (hydro)oxides and oxyhydroxides has been considered as the most important mechanism of As release in groundwater.

The oxidative dissolution of As-bearing sulfide minerals is considered to be one of the major pathways of As release in groundwater aquifers. It is particularly important in dynamic aquifer systems, where groundwater levels fluctuate, and As-bearing sulfide minerals are exposed to oxygen (O_2), leading to the mobilization of As (Battistel et al., 2021). For example, arsenopyrite (FeAsS)- the most common As-bearing mineral in the subsurface- can be oxidized, releasing Fe, As, and Sulphur (S) in oxygenated aquifers following the reaction in equation 1.1.

$$FeAsS + O_2 + H_2O \rightarrow Fe^{2+} + H_3AsO_3 + SO_4^{2-} \qquad Equation\ 1.1$$

Released As(III) and Fe(II) are further oxidized to As(V) and Fe(III) respectively, by O_2, following the reactions shown in equations 1.2 and 1.3.

$$H_3AsO_3 + O_2 \rightarrow HAsO_4^{2-} + H^+ \qquad Equation\ 1.2$$

$$Fe^{2+} + O_2 + H^+ \rightarrow Fe^{3+} + H_2O \qquad Equation\ 1.3$$

Scorodite ($FeAsO_4.2H_2O$) (a ferric arsenate) is commonly observed to form during the oxidation of As-bearing sulfide minerals, following the reaction in equation 1.4. The precipitation of this secondary mineral phase ultimately results in As sequestration and surface passivation of the sulfide minerals (Battistel et al., 2021).

$$Fe^{3+} + H_3AsO_3 + O_2 + H_2O \rightarrow FeAsO_4.2H_2O + H^+ \qquad Equation\ 1.4$$

Iron (hydr)oxides and oxyhydrooxides minerals are the major hosts of As in Cenozoic aquifers. Due to the decomposition of organic matter (CH_2O), the groundwater becomes anoxic below the water table. Under reducing and alkaline conditions, As-bearing Fe minerals (e.g., goethite (FeOOH)) are reduced, which causes the desorption of As and release of Fe(II) following equation 1.5 (Masuda, 2018, Larsen et al., 2006).

$$4FeOOH + CH_2O + 7H_2CO_3 \rightarrow 4Fe^{2+} + 8HCO_3^- + 6H_2O \qquad Equation\ 1.5$$

Iron oxyhydroxides are furthermore reduced and dissolved in strongly reducing and acidic conditions, causing the release of As from the minerals (Smedley and Kinniburgh, 2002). Chemical reactions involving the reductive dissolution of FeOOH are shown in equation 1.6 (Schwertmann, 1991).

$$4FeOOH + CH_2O + 8H^+ \rightarrow 4Fe^{2+} + 7H_2O + CO_2 \qquad Equation\ 1.6$$

Polizzotto et al. (2006) proposed seasonal redox cycling of As in the surface soil layer and migration down through the sandy aquifer to explain As release to the aquifer. In a field site in Munshiganj, Bangladesh, they found reduced Fe and As in surface soil layers but interestingly, did not find Fe(III) (hydr)oxides in As-contaminated Holocene aquifer materials. Based on this field observation and laboratory experiments, they suggested that As is released via redox cycling in surface soils/sediments and then transported to well-depth through the sandy aquifer.

Additionally, microbial reduction of As-bearing minerals, As release from geothermal water, and leaching of As from sulfides by carbonates play important roles in As mobilization in soil and water environments (Wang and Mulligan, 2006a; Wang and Mulligan, 2006b; Tufano et al., 2008; Kocar et al., 2006; Bennett and Dudas, 2003; Kim et al., 2000).

1.5 Arsenic Adsorption and Desorption

Adsorption-desorption reactions are important controls of As mobility in the environment. In the following sub-sections, the theoretical backgrounds for As adsorption and desorption onto and from mineral surfaces have been described.

1.5.1 Arsenic Adsorption onto Minerals

Adsorption is a surface phenomenon, involving attraction and binding between the adsorbent (solid substance) and adsorbate (molecule) in a solution (Tan and Hameed, 2017). The adsorption process generally occurs by mass transfer (i.e., the process of moving a substance from a liquid or gas to a solid surface) and consists of three steps. In the initial step of external or film diffusion, mass transfer occurs from the bulk phase to liquid film around the adsorbent surface. In the second step, intraparticle or pore diffusion happens, where adsorbate transfers into the pores of the adsorbent. In the last step, adsorbate attaches to the surface of the adsorbent through surface reactions with active sites (Wang and Guo, 2022; Tan and Hameed, 2017; Ho et al., 2000). Figure 1.5 shows the path of a molecule during the adsorption process.

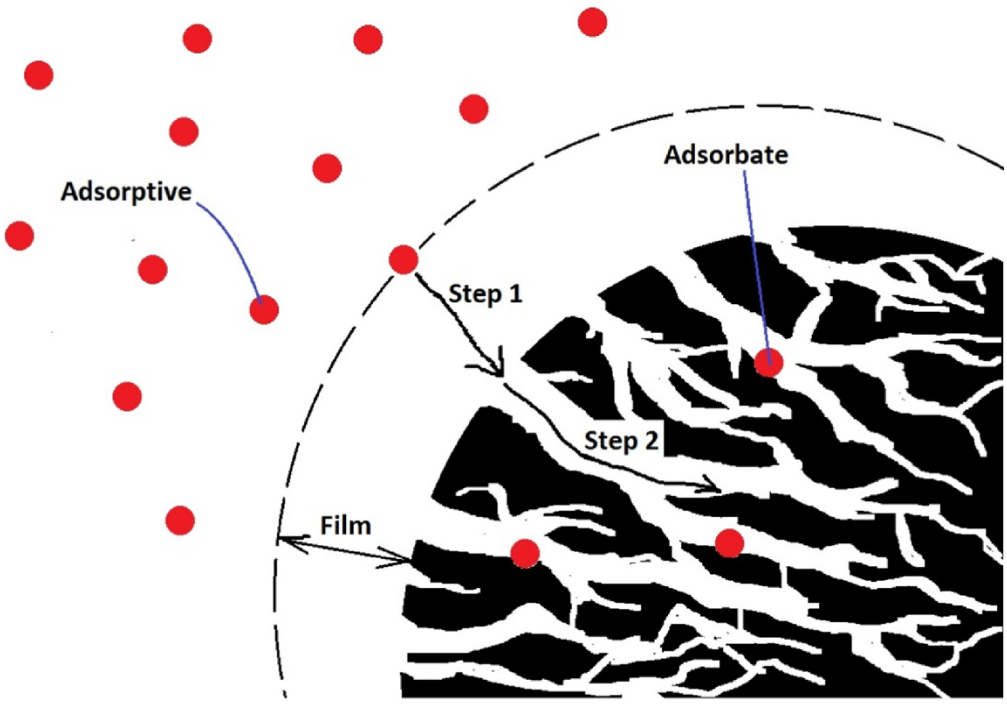


Figure 1.5: Adsorption of a molecule onto the internal surface of a porous adsorbent (Tan and Hameed, 2017).

The adsorbate concentration difference between the solution and the adsorbent surface is the main driving force of external diffusion, whereas intraparticle diffusion begins when the adsorbate jumps from one binding site to another on an adsorbent surface (Tan and Hameed, 2017; Zhang et al., 2009; Hand et al., 1983). The surface reaction is generally faster than external and intraparticle diffusions and is caused by the adsorption of the adsorbate to the binding sites on the adsorbent (Tan and Hameed, 2017; Saleh, 2022).

Adsorption on the adsorbent occurs through two possible mechanisms: physisorption and chemisorption (Figure 1.6). In physisorption, the adsorbate molecules are attached to the adsorbent surface by weak van der Waals forces. In chemisorption, the adsorbate binds to binding sites on the adsorbent, resulting in stronger covalent bonds through the sharing of electrons between adsorbent and adsorbate (Vithanage et al., 2016; Berger and Bhown, 2011; Keller and Staudt, 2005; Ruthven, 1984). Binding sites or active sites are where adsorption occurs on mineral surfaces.

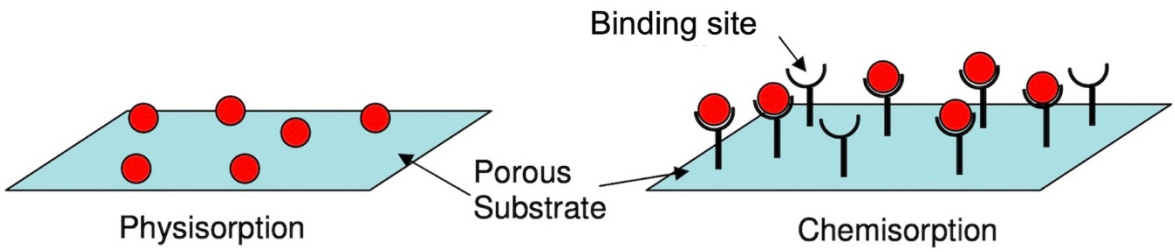


Figure 1.6: Physisorption and chemisorption mechanisms (Berger and Bhown, 2011).

Porous solid particles which are amorphous in nature with small sizes, high surface areas, and large number of surface sites, can significantly adsorb As from water (Siddiqui and Chaudhry, 2017). Many metal oxides and hydrous metal oxides contain high concentrations of As, either by adsorption on the minerals or as a constituent of the mineral structures. Arsenic adsorbs on a range of soil/sediment minerals, showing an affinity for oxides of Fe, Al, and Mn (Dixit et al., 2003; Manning et al., 2002), but particularly strong adsorption may occur on hydrous Fe oxides, reaching As weight percent concentrations (Garelick et al., 2009; Hiemstra and van Riemsdijk, 1996; Manning and Goldberg, 1996; Goldberg, 1986). While As(III) binds preferentially to Fe oxides and oxyhydroxides (Gupta et al., 1978), hydrous Al and Mn oxides can demonstrate significant As(V) adsorption when they are present in large quantities (Garelick et al., 2009; Brannon and Patrick, 1987; Peterson and Carpenter, 1983).

Arsenic has also been reported to adsorb on clay and calcite surfaces (Goldberg and Glaubig, 1988). However, As adsorption capacities for these phases are much lower than Fe oxides (Garelick et al., 2009). Adsorption reactions between As and hydrous metal oxides play a significant role in As mobility, bioavailability, and overall biogeochemical cycling of As in the aquatic environments (Zhang et al., 2014).

1.5.2 Arsenic Adsorption onto Fe Oxides and Fe-Mn Binary Oxides

Iron (oxyhydr)oxides are commonly found materials in the environment, and 16 Fe (oxyhydr)oxides have been reported so far in the literature (Siddiqui and Chaudhry, 2017). Among these, ferrihydrite ($Fe_5HO_8 \cdot 4H_2O$), magnetite (Fe_3O_4), hematite (α-Fe_2O_3), maghemite (γ-Fe_2O_3), goethite (α-FeO(OH)), lepidocrocite (γ-FeOOH), akaganeite (β-FeOOH), feroxyhyte (δ-FeOOH) and limonite ($FeO(OH) \cdot nH_2O$) are well-known oxyhydroxides minerals (Cornell and Schwertmann, 2003). They often exhibit excellent As adsorption capacity due to their small particle sizes, large surface area, and numerous active surface sites, making them good As adsorbents (Johnston et al., 2016; Sherman and Randall, 2003; Fendorf et al., 1997).

Fe-Mn binary oxides are of particular interest due to their abundance in nature and their capacity to adsorb a wide variety of trace elements, including As. Binary metal oxides contain at least one metal ion and one or more electrochemically active or inactive ions (Zhang et al., 2015). Fe-Mn binary oxides have great As adsorption efficiency primarily due to their synergistic effects combining the capacity of Mn oxides to oxidize As(III) to As(V), and the excellent As(V) adsorption capacity of Fe oxides (Chen et al., 2020; Ehlert et al., 2014; Szlachta et al., 2012). They have been reported to exhibit higher As(V) adsorption capacity compared with pure Fe oxides under experimental conditions (Zhang et al., 2014; Zhang et al., 2009; Zhang et al., 2007). Numerous research (Zhao et al., 2022; He et al., 2021; Zheng et al., 2020; Lou et al., 2017; Bai et al., 2016; Ehlert et al., 2014; Zhang et al., 2014; Zhang et al., 2012; Zhang et al., 2009; Zhang et al., 2007) have found great affinity of Fe-Mn binary oxides for As adsorption, suggesting that they might have significant roles in As biogeochemical cycling and transport within contaminated surface water and groundwater aquifer environments (Ehlert et al., 2014; Mohan and Pittman, 2007).

On polyvalent metal (hydr)oxide mineral surfaces (e.g., on Fe oxyhydroxides surface), As adsorbs by forming both inner-sphere and outer-sphere surface complexes. However, primary adsorption mechanism is the formation of inner-sphere surface complexes by ligand exchange with hydroxyl groups (Acelas and Flórez, 2017; Fendorf et al., 1997; Raven et al., 1998). An inner-sphere complex is formed when there is a direct bond between the surface site and the adsorbed molecule on the adsorbent surface, whereas in an outer-sphere complex, a molecule retains its hydration shell of co-ordinated water molecules and is attached to the adsorbent surface by electrostatic forces (Figure 1.7) (Payne et al., 2013). Therefore, inner-sphere complex bonds are much stronger than outer-sphere complex bonds (Payne et al., 2013). As anions adsorbed on minerals forming inner-sphere complex are considered not readily exchangeable (Wang and Mulligan, 2008).

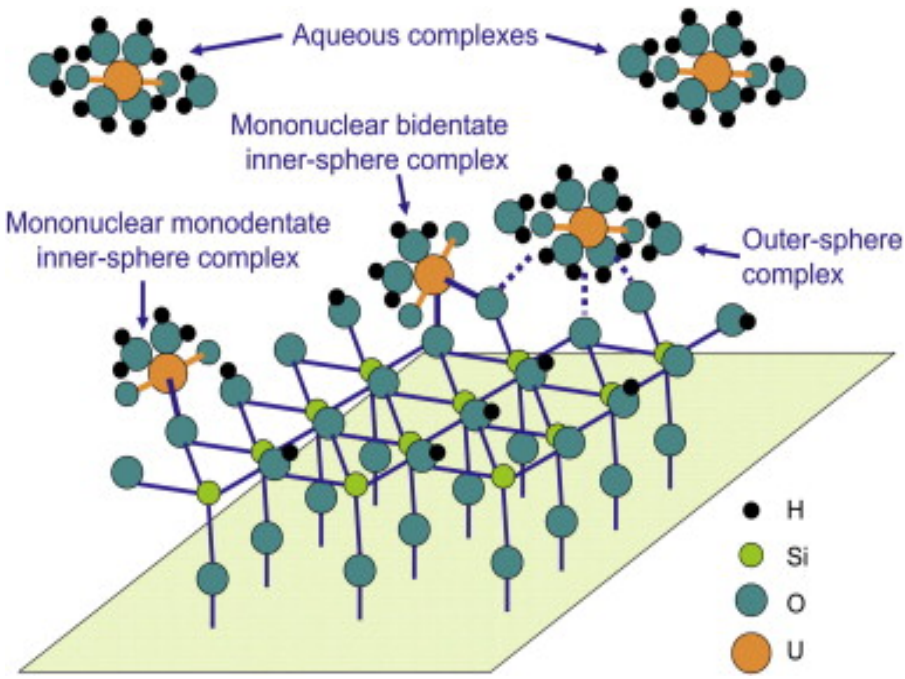


Figure 1.7: Outer-sphere and inner-sphere surface complexes on a metal oxide–water interface. The illustration shows uranyl ions (UO_2^{2+}) adsorption onto a silica surface as an example (Payne et al., 2013).

Depending on surface loading and solution chemistry, monodentate mononuclear, bidentate mononuclear, and bidentate binuclear inner-sphere complexes are formed via ligand exchange (Wu et al., 2015; Fendorf et al., 1997). In a monodentate coordination complex, a ligand binds to a central metal atom or ion through a single donor atom.

In a bidentate complex, a ligand binds to a central metal atom or ion through two donor atoms. Mononuclear complex contains one metal atom or ion in close proximity while binuclear complex contains two (Carabante, 2012; Wang and Mulligan, 2008). Figure 1.8 shows the surface complexes of As(III) and As(V) on the metal oxide (M= Mn, Fe) surface.

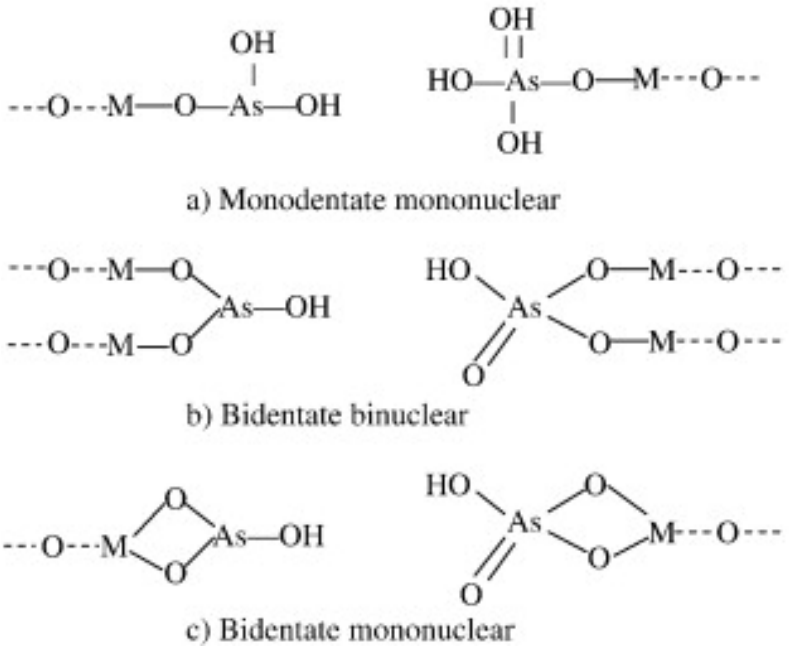


Figure 1.8: Formation of surface complexes of As(III) and As(V) on the metal oxide (M= Mn, Fe) surface (Wang and Mulligan, 2008).

Monodentate mononuclear (Figure 1.8a) and bidentate binuclear (Figure 1.8b) inner-sphere complexes are the most common adsorption modes of As(V) adsorption onto metal oxides (Fendorf et al., 1997; Fukushi and Sverjensky, 2007). Arsenic(V) adsorption as inner-sphere complexes on Fe (hydr)oxides occurs through ligand exchange between the oxygen atoms of the anion and the mineral surface functional groups. Bidentate binuclear inner-sphere complexes are formed through the exchange of two functional groups on the oxide surface, while the exchange of one functional group on the oxide surface causes monodentate mononuclear complexes formation (Acelas and Flórez, 2017). The pH of the environment controls the types of functional groups present on the mineral surfaces and complex formation (Acelas and Flórez, 2017; Farrell and Chaudhary, 2013). Under basic pH conditions, –OH will be exchanged, while under acidic pH conditions, the exchange of the $–OH_2$ ligand has been reported. At intermediate or neutral pH conditions, both the –OH functional group and $–OH_2$

ligand are exchanged, leading to the formation of monodentate complexes (Acelas and Flórez, 2017). The formation of both bidentate and monodentate complexes with As(III) and As(V) species have been reported by several researchers (Ona-Nguema et al., 2005; Manning et al., 1998; Manning et al., 2002).

Outer-sphere complex formation with As has also been reported to a small extent (Wang and Mulligan, 2008; Voegelin and Hug, 2003; Goldberg and Johnston, 2001). They are formed through nonspecific adsorption, without ligand exchange. As(V) adsorption as an outer-sphere complex occurs by intermolecular interaction (by hydrogen bonds) of the reactive oxygen atoms of As(V) species and the functional groups of the mineral surfaces (Acelas and Flórez, 2017).

1.5.3 Adsorption- A Promising Technique of Arsenic Immobilization

Arsenic transport and biogeochemistry in natural environments are controlled by its adsorption on different mineral phases along with other factors. Adsorption method is commonly used in contaminated water treatment facilities due to its flexibility, simple operating procedure, and cost effectiveness (Singh et al., 2022; Alka et al., 2021; Rashid et al., 2021; Benis et al., 2020; Almasri et al., 2018; Zhang et al., 2014; Mohan and Pittman, 2007). Selection of the proper adsorbents plays pivotal roles in determining the success of the adsorption process (Rubab et al., 2021). Various materials have been recognized as good As adsorbents including Fe-based nanoparticles, zero valent Fe, activated carbon, Fe-doped activated carbon, Mn and Al oxides and oxy(hydr)oxides, Fe-containing binary oxides, graphene oxide and graphene oxide-base adsorbents, biochar, chitosan as well as industrial and agricultural by-products such as rice husk and fly ash (Shah et al., 2024; Singh et al., 2022; Wang et al., 2020; Zeng et al., 2020; Hao et al., 2018; Wu et al., 2018; Su et al., 2017; Cope et al., 2014; Giles et al., 2011; Zhu et al., 2009; Amin et al., 2006; Diamadopoulos et al., 1993). However, due to their availability in large quantities, cost effectiveness, high specific surface area, strong redox capacity, high removal efficacy and environmental friendliness, Fe-based adsorbents are regarded as most promising (Adil and Kim, 2023; Islam et al., 2023; Gong et al., 2022; Zhang et al., 2019).

1.5.4 Modelling Adsorption Data

i. Adsorption Kinetic Models

Determining the adsorption kinetics is achieved by estimating the amount of adsorbed substances/molecules on adsorbent against time (adsorption rate). Different kinetic models are used to calculate the adsorption rate. The Pseudo-First-Order (PFO) and Pseudo-Second-Order (PSO) kinetic models are widely used and accepted empirical models to describe the kinetics of the adsorption processes at solid−liquid interfaces (Wang et al., 2024). They are called pseudo based on following assumptions: (i) in the solution, the concentration of the adsorbate is constant (considering a chemical reaction where one of the reactant species is in excess, with approximately constant concentration, it has no effect in the observed rate of the reaction), and (ii) the kinetic equation is based on adsorption capacity of adsorbents instead of the concentration in the liquid phase. The former is of course an approximation, as the adsorbate concentration in solution decreases with adsorption (Vareda, 2023).

The PFO equation, also called Lagergren's first order rate equation (Lagergren, 1898) is presented as:

$$\frac{dq_t}{dt} = k_1 (q_e - q_t) \qquad Equation\ 1.8$$

where q_e and q_t are the adsorption capacity (μmol/g) at equilibrium and at variable time t, and k_1 is the adsorption rate constant ($hour^{-1}$) for the PFO kinetic equation. Upon integrating with the boundary conditions of $q_t=0$ at t=0 and $q_t=q_t$ at t=t, the equation becomes:

$$q_t = q_e (1 - e^{-k_1 t}) \qquad Equation\ 1.9$$

The linearized form is:

$$\ln(q_e - q_t) = \ln q_e - k_1 t \qquad Equation\ 1.10$$

In this model, the $\ln(q_e-q_t)$ vs. t plot gives a straight line that intersects the origin with a slope k_1. This equation is an adaptation from reaction kinetics of homogenous systems, which means that this model is a surface reaction model, and suggests occupation of one active surface site

by the adsorbate. However, PFO is associated with the adsorption process being only dependent on the adsorbate concentration- diffusion-controlled process. The rate of direct adsorbate transfer from the bulk phase to the solid phase governs the overall rate of adsorption and the process is mainly physisorption (Vareda, 2023).

The PSO equation (Equation 1.11), also known as Ho and McKay equation (Ho and McKay, 1998), is the model that most describes the adsorption of species in solution. The equation is expressed as:

$$\frac{dq_t}{dt} = k_2\,(q_e - q_t)^2 \quad Equation\ 1.11$$

where k_2 is the adsorption rate constant (g/µmol-hour) for PSO kinetic equation and the other symbols have the same meanings as mentioned in the PFO model.

Integrating Equation (1.11) with boundary conditions of q_t=0 at t=0 and q_t=q_t at t=t, the equation becomes:

$$q_t = \frac{k_2\,q_e^2\,t}{1 + k_2\,q_e\,t} \quad Equation\ 1.12$$

The linearized form is obtained by subsequent rearrangement:

$$\frac{t}{q_t} = \frac{1}{k_2\,q_e^2} + \frac{t}{q_e} \quad Equation\ 1.13$$

The initial rate of adsorption (q(t→0)) is $k_2q_e^2$. A plot of t/q_t vs t gives a straight line for the PSO-compliant kinetics. The slope is $1/q_e$, and the intercept is $1/k_2q_e^2$. Chemisorption is the rate limiting step in the adsorption process when it follows PSO equation.

The rate constants of both PFO (k_1) and PSO (k_2) are functions of the adsorption conditions. The values of k_1 and k_2 decrease with increasing initial bulk concentration of adsorbate (Chinoune et al., 2016; Franca et al., 2009; El Haddad et al., 2013). A smaller value indicates that a longer time is required for adsorption. Experimental conditions, such as temperature and pH can influence k_1 values, and the effect on k_2 is not well studied (Tan and Hameed, 2017). Small particle size is associated with large values of k_1 and k_2 (Vincent et al., 2014).

ii. Adsorption Isotherm Models

At constant temperature and assuming equilibrium, the mathematical expression expressing the relationship between the adsorbate amount onto an adsorbent and the solution concentration of the solute is called an adsorption isotherm (Xing et al., 2022). The adsorption mechanisms are investigated by modelling the adsorption equilibrium data, characterization of the adsorbent before and after adsorption, and by other methods (Wang and Guo, 2020). Modelling adsorption data by producing an isotherm model is the most convenient and widely used technique. In addition, adsorption isotherm models can provide information on the maximum adsorption capacity, which is significant in the evaluation of the adsorbent performance. A variety of isotherms have been applied in adsorption systems, such as the Langmuir model (Langmuir, 1918), the Freundlich model (Freundlich, 1906), the Sips model (Sips, 1948), the Temkin model (Temkin and Pyzhev, 1940), and the Brunauer-Emmett-Teller (BET) model (Brunauer et al., 1938). The Langmuir model is widely used to model the adsorption isotherm of As on Fe oxides and binary oxides and shows great conformity with experimental data. Since this model is used in this thesis to describe As adsorption data, it is discussed here.

The Langmuir isotherm model is a chemical adsorption isotherm model, which assumes monolayer adsorption of the adsorbate molecules on the adsorption sites of the adsorbent (Wang and Guo, 2020). Other basic assumptions of the Langmuir isotherm are: (1) the distribution of adsorption sites is homogeneous; (2) the adsorption energy is constant; and (3) the interaction between adsorbate molecules is negligible. Surprisingly, the Langmuir isotherm, which is based on homogeneous surface sites, can describe a large number of adsorption systems, many of which possess heterogeneous surface characteristics (Foo and Hameed, 2010). Indeed, the adsorption on adsorbent materials with irregular shapes and microscopically non-uniform surfaces can also be represented by the Langmuir isotherm (Guo and Wang, 2019). The most commonly applied Langmuir isotherm model was developed to represent gas-solid adsorption (Langmuir, 1918). The nonlinear model is presented as follows:

$$q_e = \frac{q_m K_L C_e}{1 + K_L C_e} \qquad Equation\ 1.14$$

The linear Langmuir model which is used to better fit with experimental data is presented as follows:

$$\frac{C_e}{q_e} = \frac{C_e}{q_m} + \frac{1}{K_L q_m} \qquad Equation\ 1.15$$

where K_L (L/μmol) is the Langmuir constant, q_e (μmol/g) is the equilibrium adsorption capacity, C_e is the final concentration remaining in solution (μmol/L), and q_m (μmol/g) is the maximum adsorption capacity estimated by the Langmuir model. K_L indicates the affinity between adsorbent and adsorbate (Wang et al., 2018).

1.5.5 Arsenic Desorption and Dissolution from Minerals

Several hypotheses regarding As desorption and dissolution from minerals and mobilization into aquatic environments have emerged over the decades. One popular hypothesis was the competitive exchange of As with phosphate (derived from fertilizers) on mineral surfaces (Peryea and Kammereck, 1997; Acharyya et al., 1999). Phosphate competes with dissolved As for adsorption sites on mineral surfaces, enhancing the release of As in the topsoil and subsequent downward movement of As through the subsoil (Peryea and Kammereck, 1997). However, the hypothesis related to competitive exchange of As with phosphate has not been proved to be major mechanism of As contamination in groundwater aquifer. Indeed, in As contaminated groundwater aquifers of Bangladesh, concentrations of phosphorus decrease with groundwater aquifer depth and do not co-relate with As concentrations (McArthur et al., 2001).

Bicarbonate (HCO_3^-) substitution in As-bearing minerals (Anawar et al., 2004) is another theory for As desorption. Pantsar-Kallio and Manninen (1997), Appelo et al. (2002), and Anawar et al. (2004) proposed that HCO_3^- can mobilize As from Fe and Mn oxyhydroxides by substituting As and forming complexes on the mineral surface sites. Oxidation of As-containing pyrite (Chowdhury et al., 1999) and reductive dissolution of the As-bearing Fe(III) oxyhydroxides (Nickson et al., 2000; McArthur et al., 2001; Islam et al., 2004) are other popular theories of As dissolution from minerals. Among those, the reductive dissolution of As-bearing Fe(III) oxyhydroxides is the most commonly accepted (Polizzotto et al., 2006). Pyrite oxidation and reductive dissolution of As-bearing Fe(III) oxyhydroxides have been discussed in detail in section 1.4.

1.6 Biofilm in the Environment

Biofilms are ubiquitous in the environment, and more than 80% of bacterial and archaeal cells are living in biofilms (Parrilli et al., 2022; Flemming and Wuertz, 2019). They are composed of microcolonies of microorganisms that adhere to surfaces and where microbial cells are held and embedded by highly hydrated self-produced extracellular polymeric substances (EPS). Around 70-95% of biofilm is water (Flemming, 1993). Of the remainder, about 70-95% is organic matter EPS that are mainly composed of polysaccharides, proteins, extracellular DNA, uronic acids, small quantities of lipids, and many other biomolecules (Muhammad et al., 2020; Felz et al., 2019; Xiao and Zheng, 2016; Salama et al., 2016; Flemming, 1993). Biofilms are generally negatively charged. Indeed, the presence of several carboxyl, hydroxyl, and phosphate provides them with a net negative charge at circumneutral pH (Zhao et al., 2023). On Earth, almost all surfaces can be colonized by bacteria (Characklis and Marshall, 1990) and biofilms are found in a wide range of extreme environments, including very high to low temperatures, extremely acidic to alkaline environments, and high to low salinity. Biofilms are also found in radiation sources where they grow by maintaining homeostasis (Parrilli et al., 2022; Yin et al., 2019; Flemming, 1993). Overall, biofilms provide protection to cells from hostile environmental stress and toxicity and increase their resilience and survival (Yin et al., 2019; Flemming et al., 2016; Fux et al., 2005; Prakash et al., 2003).

1.6.1 Formation of Biofilm

Biofilm formation generally consists of three stages (Figure 1.9) (Arciola et al., 2018). In the primary stage, bacteria attach themselves to the surface by physical van der Waals and chemical forces. In the next maturation stage, intracellular communication is established between microbial cells by producing signaling molecules that allow cells to sense neighboring bacterial clusters (quorum-sensing). This process leads to the formation of larger cell clusters (van Hoogstraten et al., 2023; Gu et al., 2013). In this stage, the volume, size, and thickness of the biofilm increases, and the production of EPS is enhanced, embedding bacterial cells and providing stability to the biofilm structure (Khatoon et al., 2018). At the last stage- the dispersion stage, the biofilm matrix can be disrupted, and bacteria can migrate to other locations (van Hoogstraten et al., 2023).

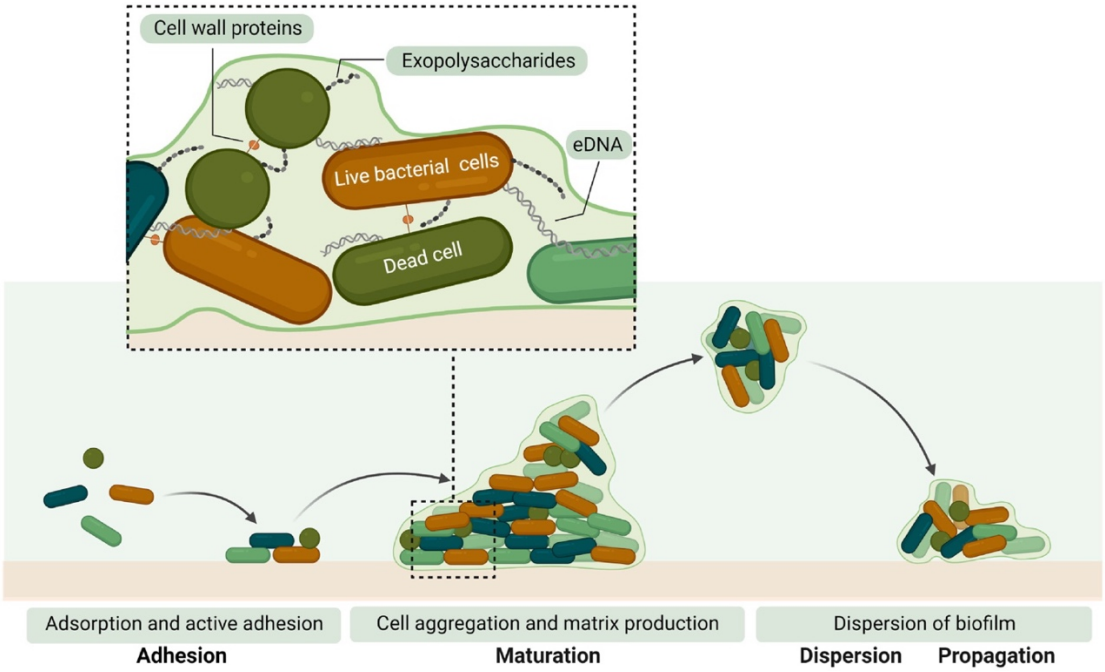


Figure 1.9: Different stages of biofilm formation (van Hoogstraten et al., 2023).

1.6.2 Significance of Biofilm in Trace Metal Cycling

Biofilms are dynamic complex biological systems (Parrilli et al., 2022; Zhou et al., 2020) and play critical roles in most global biogeochemical processes in natural and anthropogenic environments (Flemming and Wuertz, 2019). Microbes in biofilm use trace metals to meet their energy and respiratory needs. These metals can be taken up by microorganisms for use as metal centers in enzymes and cellular biomass through assimilatory processes. They can also be used in dissimilatory processes, where they are reduced or oxidized by cells to accept or provide electrons for cellular energetics (Liermann et al., 2007). This may ultimately result in the sequestration of trace metals in biofilms, sometimes with the formation of minerals containing metals, generally known as biogenic minerals or biominerals. Biofilms can produce and hold many reactive biogenic minerals (Templeton et al., 2001). Biogenic minerals are often small particles, spatially distributed on surfaces as coatings where biofilms form, and are embedded within EPS (Toner et al., 2006). Additionally, microbial cells and EPS can adsorb metals due to their surface charges and electrostatic attraction. However, it has been found that sometimes adsorption of trace metals on biofilm structures is primarily contributed by the biogenic mineral fractions present in biofilm (Guibaud et al., 2009). Microbes in biofilms are also capable of reducing metal oxide minerals, increasing the mobility of the metals. Therefore, biofilms play a significant role in trace metals biogeochemical cycling in the environment.

1.7 Biogenic Minerals in the Environment

1.7.1 Formation of Biogenic Minerals in the Environment

Biogenic minerals are formed by the biomineralization of metals or metalloids by microorganisms (Fortin, 2004; Addadi and Weiner, 2014; Lowenstam, 1981). Throughout the long co-evolutionary history of the Earth and life, some prokaryotes have gained the capability to biomineralize (Cosmidis and Benzerara, 2022; Frankel and Bazylinski, 2003). Biogenic minerals can be formed by either controlled mineralization or biologically induced and influenced mineralization. Figure 1.10 illustrates a classical framework of microbial biomineralization.

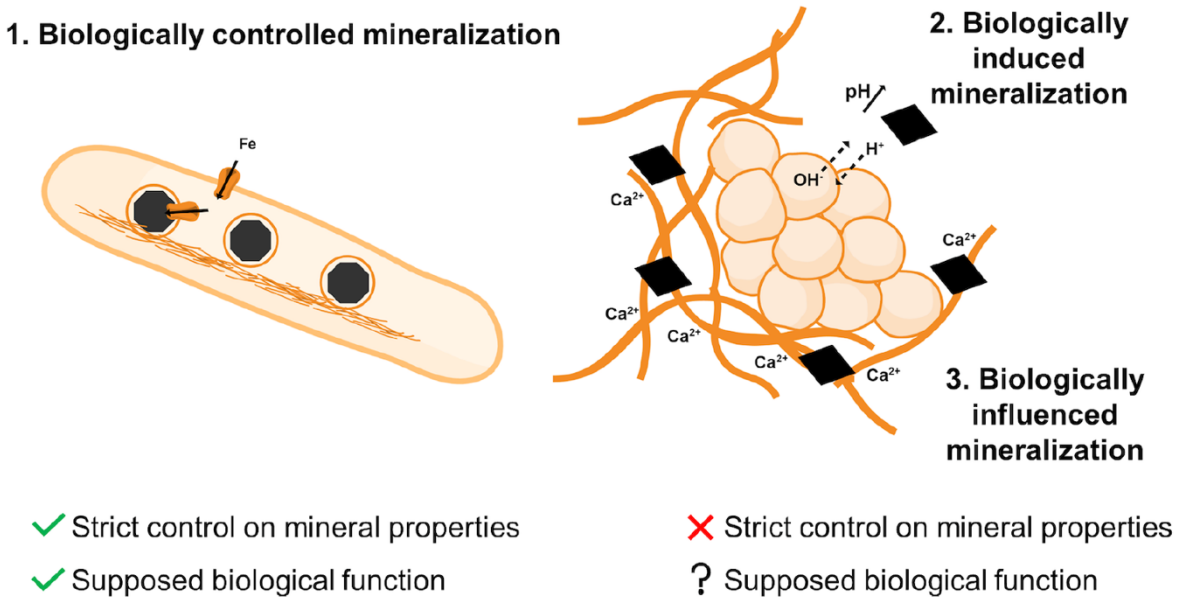
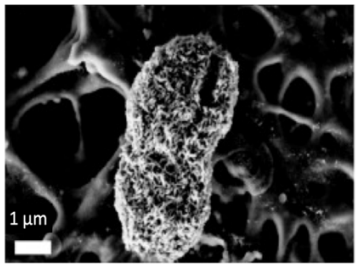
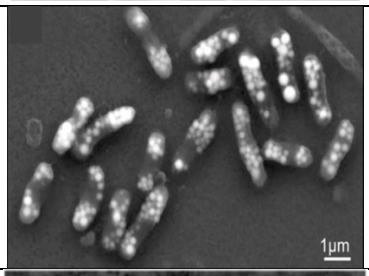
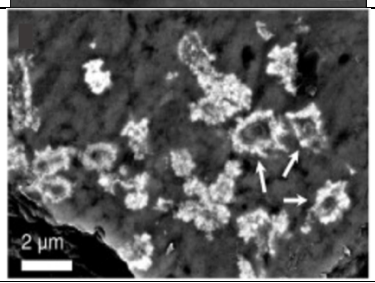
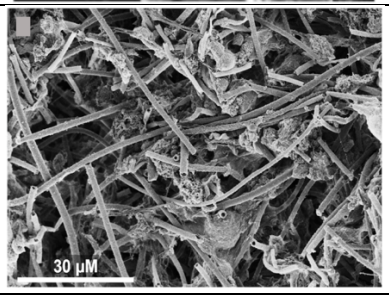


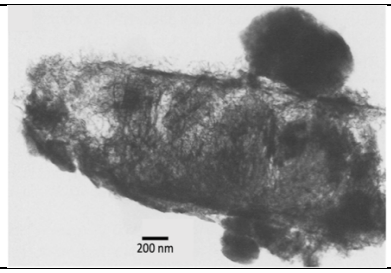
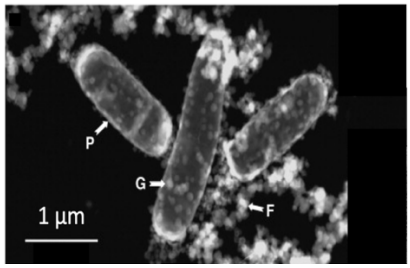
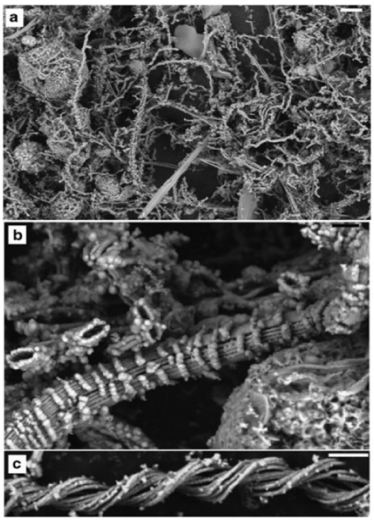
Figure 1.10: The classical framework of microbial biomineralization (Cosmidis and Benzerara, 2022).

In controlled mineralization, biogenic mineral properties (e.g., morphological, chemical, and crystallographic properties) and location are under strict genetic control, and the formation of the mineral is believed to be beneficial for the microorganism. Mineral growth generally starts intracellularly but the minerals can eventually be deposited on extracellular surfaces (Cosmidis and Benzerara, 2022; Lowenstam, 1981). In contrast, biologically induced and influenced mineralization processes typically occur extracellularly.

Both types of mineralization can occur simultaneously. Biologically induced (or indirect) mineralization (e.g., extracellular $CaCO_3$ precipitation) occurs due to local chemical changes (e.g., pH), governed by the metabolic activity of the microbial cells and enzymes (Cosmidis and Benzerara, 2022; Veis, 2003; Lowenstam, 1981), whereas in biologically influenced (or passive) mineralization, microbial cells and EPS control the locus of biogenic mineral precipitation (e.g., by electrostatic attraction between Ca^{2+} ions and OH^- groups), acting as heterogeneous nucleation surfaces in supersaturated solution. The microbe does not need to be metabolically active or alive (Cosmidis and Benzerara, 2022).

Table 1.3: Examples of biogenic minerals found in various environments.

Biogenic Minerals	**Formation Environments**	**SEM/TEM images**	**References**
Biogenic vivianite	Water column of Lake Pavin		Cosmidis et al., 2014
Biogenic carbonates	Lake Alchichica, Mexico		Couradeau et al., 2012
Pyritized cells filled by Ca-phosphates	Oxygen minimum zone of the Peru margin		Cosmidis et al., 2013
Fe-mineralized mats	Freshwater wetlands		Tothero et al., 2024

Biogenic Mn oxides	Aerobic and warm shallow-water environment		Tazaki, 2000
Biogenic iron oxide	Aerobic and warm shallow-water environment		Tazaki, 2000
Biogenic Fe-phosphates	Laboratory grown		Miot et al., 2009
Biogenic Fe-oxyhydroxide (scale: a=10 µm, b and c=1 µm)	Hydrothermal vent		Edwards et al., 2011

Biogenic minerals may be present in a wide variety of environments, often along with their abiogenic counterparts (Conley and Schelske, 2001; Ueshima and Tazaki, 2001; Fortin et al., 1998) (Table 1.3). They show diverse morphologies, chemistries, and structures (Addadi and Weiner, 2014; Fortin, 2004). Due to the frequent incorporation of organic matter (bacterial cells and EPS), biogenic minerals often possess mineralogical characteristics (small size, poor crystallinity, large surface area, redox reactivity, negatively charged surface at neutral pH) that differ from their abiogenic counterparts (Muehe et al., 2013; Kleinert et al., 2011; Posth et al., 2010; Hegler et al., 2008).

1.7.2 Biogenic Fe Oxides, Mn Oxides, and Fe-Mn Binary Oxides

In the environment at circumneutral pH biogeochemical Fe(II) oxidation is driven by concurrent microbial and chemical processes and may occur cyclically or simultaneously (Melton et al., 2014; Kappler et al., 2021). Since microbial and chemical Fe(II) oxidation might occur concurrently, the contribution of individual processes is very challenging to determine (Kappler et al., 2021). Chemical Fe(II) oxidations are generally mediated by O_2 and reactive oxygen species ($O_2^{\bullet-}$, H_2O_2, •OH), nitrogen species (NO, NO_2^-), and Mn (MnO_2) (Melton et al., 2014; Kappler et al., 2021). Fe(II) can be oxidized to FeOOH by MnO_2 as follows:

$$2Fe^{2+} + MnO_2 + 2H_2O \rightarrow Mn^{2+} + 2FeOOH + 2H^+ \quad Equation\ 1.16$$

Microbial Fe(II) oxidation is driven by microaerophiles (e.g., *Gallionella* spp., *Leptothrix* spp., *Mariprofundus* spp., *Sideroxydans* spp.), photoferrotrophs (e.g., *Rhodopseudomonas palustris* TIE-1, *Rhodobacter* sp. SW2, *Chlorobium ferrooxidans* KoFox, *Thiodictyon* sp. F4), and NO_3^- -reducing Fe(II) oxidizers (e.g., *Acidovorax* spp., *Thiobacillus denitrificans*) (Melton et al., 2014). Bio-oxidation of Fe(II) and biomineralization by microaerophiles occur through following reaction:

$$4Fe^{2+} + 10H_2O + O_2 \rightarrow 4Fe(OH)_3 + 8H^+ \quad Equation\ 1.17$$

Photoferrotrophs biomineralize Fe(II) in the presence of light as follows:

$$HCO_3^- + 4Fe^{2+} + 10H_2O \rightarrow CH_2O + 4Fe(OH)_3 + 7H^+ \quad Equation\ 1.18$$

NO_3^- -reducing Fe(II) oxidizers may biomineralize Fe(III) following Fe(II) oxidation through the following reaction:

$$10Fe^{2+} + 2NO_3^- + 24H_2O \rightarrow 10Fe(OH)_3 + N_2 + 18H^+ \quad Equation\ 1.19$$

Mn oxides can be formed through the bio-oxidation of Mn(II) (Yu and Leadbetter, 2020; Tran et al., 2018). Bio-oxidation of Mn(II) can be mediated by a wide group of microorganisms including *Pseudomonas*, *Leptothrix*, and *Bacillus* in diverse environments. Mn(II) oxidizing microbial groups found in various environments are presented in Table 1.4. Biogenic Mn oxides are generally black/brown in color and form extracellularly (Cai et al., 2023).

The mechanism of Mn(II) oxidation by Mn(II)-oxidizing bacteria is unclear. However, it has been accepted that Mn(II) bio-oxidation is an extracellular enzymatic reaction that involves several multicopper oxidase enzymes (Cai et al., 2023; Tebo et al., 2005).

Table 1.4: Mn(II) oxidizing bacteria (MnOB) groups found in various environments (Cai et al., 2023).

Environmental Conditions	**The MnOB Groups**
River	*Bacillus, Pseudomonas, Sphingomonas, Hyphomicrobium, Cyanobacteria* *Microbacterium, Agromyces, Mycobacterium, Arthrobacter, Pseudomonas, Burkholderiales* *Aurantimonas, Rhodobacter, Bacillus, Shewanella*
Lake	*Metallogenium, Leptothrix, Siderocapsa, Naumanella, Bacillus, Pseudomonas* *Bacillus, Pseudomonas, Afipia*
Well	*Acinetobacter* sp., *Bacillus, Sphingobacterium* sp. *Pseudomonas, Burkholderiales*
Mn deposits	*Bacillus, Exiguobacterium, Staphylococcus, Brevibacterium, Alcanivorax* sp. *Hyphomicrobium, Leptolyngbya* *Sphingomonas, Flavobacterium, Janthinobacterium, Acinetobacter*
Seawater	*Bacillus* sp. FF-1 *Citreicella manganoxidans* sp. nov. *Marinobacter manganoxydans* Mn17-9
Activated sludge	*Brevibacillus* *Serratia marcescens*
Biofilters	*Pseudoalteromonas* sp. *Flavobacterium, Brevundimonas, Stenotrophomonas* *Leptothrix, Pseudomonas, Methylibium*
Drinking water system	*Bacillus* *Lysinibacillus, Bacillus, Pseudomonas, Brevundimonas*

In aquatic environments, the co-precipitation of Fe oxides with Mn oxides commonly results in the formation of Fe-Mn binary oxides (Bai et al., 2016; McCann et al., 2018). The presence of Fe- and Mn-containing biogenic minerals in the environment has been demonstrated by several researchers (Abramov et al., 2020; Posth et al., 2014; Miller et al., 2012; Fortin and Langley, 2005). Fe-Mn binary oxides are often formed in situ in natural aquatic ecosystems as well as in groundwater treatment systems (Bai et al., 2013). However, the formation pathways of biogenic Fe-Mn binary oxides at various environmental conditions have not been extensively studied.

Moreover, discriminating abiogenic from biogenic Fe-Mn binary oxides in the environment is very challenging. Biogenic Fe-Mn binary oxides are generally brownish-black precipitates, and mineralogical characterization of these phases suggest that they are a combination of poorly crystalline or amorphous Fe and Mn oxides (Bai et al., 2016).

1.7.3 Environmental Significance of Biogenic Minerals

Biogenic minerals are important in environmental mineralogy and geobiology since they may store unique information on ancient environments (Benzerara and Menguy, 2009). They have been a significant reserve of organic carbon and fossils from past environments and can be used for paleoclimatic research. The formation of biogenic minerals can occur through distinct processes (De Yoreo and Vekilov, 2003) which can change the solution composition, impacting the overall chemistry of that environment (Benzerara et al., 2011). For instance, soluble Fe(II) can be oxidized to Fe(III) by Fe-oxidizing bacteria at neutral pH, forming insoluble Fe oxides. This changes the concentration of soluble Fe and other trace metals in solution because of the biomineralization of Fe and trace metal adsorption on Fe oxides, respectively (Benzerara et al., 2011; Hohmann et al., 2010). In many environments, the formation of biogenic minerals may represent an important part of elemental biogeochemical cycling (Glodowska et al., 2021; Benzerara et al., 2011). Microbial oxidation is often kinetically favored over abiotic (chemical) oxidation in the environment, consequently favoring the formation of biogenic minerals. For instance, natural Mn oxidation is primarily catalyzed by Mn-oxidizing bacteria (Tebo et al., 2005; Francis and Tebo, 2002). Biogenic Mn oxides are known for their great adsorption capacity of trace metals. Biogenic minerals exhibit small sizes, poor crystallinity, and large surface areas and are often reported as redox-active materials due to the presence of organic matter in their structures. All these properties provide them with great adsorption capacity for many trace elements, including As (Castro et al., 2021; Sowers et al., 2017), and hence, they can play a critical role in biogeochemical cycling and regulating nutrient and pollutant dynamics (Sander et al., 2015; Tebo et al., 2004; Hashimoto et al., 2014). However, elemental cycling due to biogenic mineral formation is often overlooked in biogeochemical studies. It important to understand the biogenic minerals-trace metal interactions dynamics to interpretation of trace metal cycling in different environments.

1.8 Context of this Research

1.8.1 Scope of Research

Arsenic contamination in aquatic environments represents a significant public health hazard due to its carcinogenic properties and widespread impact on millions of people dependent on As contaminated drinking water sources (Fendorf et al., 2010; Wang et al., 2007; McArthur et al., 2004; Nickson et al., 2000). Hundreds of studies have been conducted investigating the adsorption and desorption dynamics of As on aquifer materials and minerals. Much of this attention has been directed towards abiogenic minerals. Some of these minerals, such as ferrihydrite (Fe oxyhydroxides), have been extensively studied owing to their natural prevalence in soil and water, crystalline and surface properties as well as for their high capacity for As adsorption (Jain and Loeppert, 2000; Perez et al., 2019; Jiang et al., 2015). However, Fe-Mn binary oxides could be one of the potential candidates to investigate further due to the frequent co-existence of Fe with Mn in the environment. Consequently, it is important to understand the complexities of As adsorption-desorption dynamics of Fe-Mn binary oxides to comprehend the fate and biogeochemistry of As within natural environments.

Moreover, while interest is growing in biogenic minerals research, extensive research into the complexities of As adsorption and desorption onto and from biogenic Fe-Mn binary oxides remain limited. The environment harbors numerous microbes, which are capable of oxidizing Fe(II) and Mn(II). In diverse environments, bacteria typically exist within biofilms (Donlan and Costerton, 2002; Hall-Stoodley and Stoodley, 2009) and might form biogenic Fe and Mn oxide minerals. These biogenic oxides are characterized by distinct mineral structures and surface properties compared to their abiogenic counterparts. They are nano or micro-size amorphous or crystalline composite materials often closely associated with organic materials (Gilbert et al., 2005). Research supports increased surface area, reduced particle size, decreased crystallinity, incorporated bacterial biomass and other cell-derived organic matter in biogenic Fe and Mn oxides when compared with abiogenic counterparts (Hohmann et al., 2009; Cismasu et al., 2011; Muehe et al., 2013; Hao et al., 2016; Sowers et al., 2017). The inherent variations in structure and surface properties suggest potential differences in As adsorption behavior and capacity between biogenic and abiogenic Fe-Mn binary oxides.

Despite a few studies conducted on As(V) adsorption and desorption on biogenic Fe-Mn binary oxides (Si et al., 2023; Zhao et al., 2022; Xu et al., 2022; Bai et al., 2016), detailed investigations of microbial influence as well as the presence of biofilm on As(V) adsorption and desorption dynamics onto and from Fe-Mn binary oxides are lacking. This still holds significant promise for elucidating the complexities of As(V) interactions with biogenic minerals within aquatic environments since biomineralization is often associated with biofilms. Additionally, anticipating As adsorption and desorption onto and from biogenic Fe-Mn binary oxides in different environments is challenging without a deeper understanding of their formation pathways, mineralogical characteristics, and As adsorption-desorption kinetics in the presence of biofilm.

1.8.2 Research Objectives

The overall aim of the thesis is to improve the understanding of the As(V) adsorption and desorption onto and from Fe-Mn binary oxides and to investigate the microbial influence on these As(V) adsorption-desorption processes.

The specific objectives that will help to achieve this aim include: (i) the synthesis of abiogenic and biogenic Fe-Mn binary oxides and their detailed mineralogical characterizations, (ii) the evaluation of As(V) adsorption capacity and behavior of Fe-Mn binary oxides compared with single phase Fe oxide (ferrihydrite), (iii) the elucidation of the pathways for Mn(II) and Fe(II) oxidation leading to the formation of biogenic Fe-Mn binary oxides, and (iv) the investigation of the influences of *P. putida* biofilm on As(V) adsorption and desorption onto and from biogenic and abiogenic Fe-Mn binary oxides.

1.9 Thesis Outline

This thesis is structured into five chapters, in which Chapter 1 presents an introductory literature review related to this research topic. The main experiments, experimental findings, and discussions are presented in the following three chapters (Chapters 2-4) and formatted as scientific papers for future publications. Lastly, Chapter 5 gives concluding remarks, addressing the overall findings of the research and providing prospects for future research in the related fields. The chapter-wise breakdown is outlined below.

Chapter 1: Introduction

The introduction includes a literature review and describes the fundamental concepts essential for understanding this research.

Chapter 2: Assessing Arsenic(V) Adsorption Behaviours and Capacities of Abiogenic Ferrihydrite and Iron-Manganese Binary Oxides

Iron-oxides, particularly ferrihydrite, have gained considerable attention in As adsorption research due to their important adsorption capacities. Before considering biogenic Fe-Mn binary oxides, it is crucial to determine the As(V) adsorption capacity and behavior of abiogenic Fe-Mn binary oxides. This preliminary assessment is instrumental in establishing whether it possesses sufficient As(V) adsorption capacity and testing its potential as a suitable mineral candidate for subsequent biogenic experimentation. This comparison lays the groundwork for understanding potential differences or similarities in the As(V) adsorption mechanisms between abiogenic Fe-Mn binary oxides and ferrihydrite. Such insights were essential given the anticipated complexity inherent in the biogenic experiment.

Chapter 3: *Pseudomonas Putida*-Mediated Synthesis of Biogenic Iron-Manganese Binary Oxide Nanoparticles: Characterization Insights and Potential Environmental Implications

One of the significant and challenging parts of the study is to successfully synthesize biogenic Fe-Mn binary oxides. Biogenic Fe-Mn binary oxides were synthesized using *P. putida* MnB1, establishing a novel formation pathway for these phases, that could mimic Fe and Mn biogeochemical cycling at the oxic-anoxic boundary of the water column. Suites of analytical techniques were employed to characterize the synthesized biogenic Fe-Mn binary oxides.

Chapter 4: Unfolding the Role of *Pseudomonas putida* Biofilm in Arsenic(V) Adsorption-Desorption Dynamics on Iron-Manganese Binary Oxides

This chapter provides scientific evidence of the role of biofilm in As(V) adsorption-desorption dynamics by comparing As(V) adsorption-desorption dynamics for abiogenic and biogenic Fe-Mn binary oxides, mineral-free biofilm, and abiogenic Fe-Mn binary oxides mixed with biofilm. Biofilm of *P. putida* as well as Fe-Mn binary oxide biominerals produced by this microorganism were used in this study. This chapter discussed how the presence of biofilm affects As(V) adsorption kinetics and desorption capacity of biogenic and abiogenic Fe-Mn binary oxides.

Chapter 5: Conclusions and Future Research Prospects

In this section primary findings from the previous chapters are summarized, and implications of this research as well as possible future research directions are discussed.

Appendix

This section contains supplementary data, tables, STEM images, and EDX mappings.

2 Chapter Two: Assessing Arsenic(V) Adsorption Behaviours and Capacities of Abiogenic Ferrihydrite and Iron-Manganese Binary Oxides

Abstract

Arsenic (As) contamination in groundwater is one of the major environmental concerns and has become a great threat to public health due to its carcinogenic impact. Understanding As adsorption behaviours and capacities of the aquifer materials is important to comprehend its mobility in groundwater. In this research abiogenic ferrihydrite and Fe-Mn binary oxides have been synthesized and characterized by Scanning Electron Microscopy, Energy Dispersive X-ray Spectroscopy, X-Ray Diffraction, and Brunauer-Emmett-Teller analyses. Their As(V) adsorption behaviours and capacities have been investigated and compared for a better understanding of the As(V) adsorption dynamics of single-phase Fe oxide and binary oxides. As(V) adsorption kinetic data fitted best with the Pseudo-Second-Order kinetic model for both adsorbents, indicating the adsorption mechanism was primarily chemisorption. Interestingly, both adsorbents exhibited the same adsorption at equilibrium (q_e) despite ferrihydrite having higher As(V) adsorption rate constant (k_2) than Fe-Mn binary oxides. The adsorption isotherm data followed the Langmuir isotherm model, showing a 25% higher maximum As(V) adsorption capacity (q_m) of Fe-Mn binary oxides than ferrihydrite per square meter, and consistent with both having homogeneous surface sites that do not interact with one another and monolayer As(V) adsorption. The higher adsorption rate constant (k_2) and the equilibrium adsorption constant (K_L) of ferrihydrite indicate its higher As(V) adsorption rate and affinity than Fe-Mn binary oxides. The As(V) adsorption behaviour and capacity might be influenced by the solution pH, the adsorbent's specific surface area, and presumably by particle aggregation, and pore size. Higher specific surface area, less particle aggregation, and larger pore size of Fe-Mn binary oxides contributed more As(V) adsorption than ferrihydrite. Results confirm that Fe-Mn binary oxides could be a promising As(V) adsorbent and might play significant role in As(V) adsorption and mobility in aquatic environments.

Keywords: Arsenic adsorption; Adsorption kinetics; Ferrihydrite; Fe-Mn binary oxides; Pseudo-First-Order kinetic model; Pseudo-Second-Order kinetic model Langmuir isotherm, Arsenic contamination.

2.1 Introduction

Groundwater arsenic (As) contamination has been considered to be one of the major environmental concerns in many countries in the world, especially in Bangladesh, India, Vietnam, China, and Cambodia because of its potential carcinogenic impacts (Nickson et al., 2000; Wang et al., 2007; Fendorf et al., 2010; McArthur et al., 2004). During the past decade, drinking water As contamination and its adverse effects on human health have become a major concern around the world (Smedley and Kinniburgh, 2002). Worldwide, more than 230 million people are chronically exposed to As-contaminated drinking water exceeding the WHO (World Health Organization) safety standard guideline (10 μg/L), including 180 million people from Asia (Shaji et al., 2021; WHO, 2011)- reflecting the alarming situation of As contamination. Arsenic contamination in groundwater is generally naturally occurring, from aquifer materials but it has become a contaminant in surface water in many parts of the world including the UK, the USA, China, Brazil, and Colombia, because of the mining exploitation of As-containing ores in the surrounding areas (Patel et al., 2023; Wu et al., 2017). Moreover, industrial chemicals and agricultural pesticides are important anthropogenic sources of As in the environment (Chen et al., 2015; Han et al., 2003; Garelick et al., 2008). In natural water, As can exist in both organic and inorganic forms, but inorganic As was reported to be more toxic than its organic form (Su et al., 2014). Over the years, proper management and As removal techniques have been studied to tackle this problem. Such solutions have become more urgent since As pollution has started to impact food safety through bioaccumulation in grains and vegetables, especially in rice (Rauf et al., 2011; Bhattacharya et al., 2012; Rahman et al., 2008). Understanding the complex mechanisms governing As interaction with As adsorbing minerals present in the environment is vital to know about As transport and mobility and thus, to find out proper solution.

Iron (Fe) oxyhydroxides are naturally found in groundwater aquifers and widely studied due to their high affinity toward As (Huang et al., 2020; Hao et al., 2018; Jiang et al., 2013; Taylor et al., 2009). Ferrihydrite is one of the most significant and abundant Fe-containing minerals at the Earth's surface (Sassi et al., 2021; Funnell et al., 2020) and is considered to be a precursor of most Fe oxide minerals (Schwertmann et al., 1999; Funnell et al., 2020). It is widely distributed in various redox-active environments, from freshwater to marine water, and within soil and sediments at near-neutral pH conditions (Jambor and Dutrizac, 1998).

High abundances in the environment, high reactivity, and large specific surface area have made ferrihydrite an important mineral to be considered as an effective adsorbent for contaminants and trace elements, including As (Hiemstra et al., 2019; Hiemstra, 2018; Wang et al., 2013; Raven et al., 1998). It has been reported that ferrihydrite is a better As(V) adsorbent compared to other crystalline Fe oxides (Zheng et al., 2020; Perez et al., 2019; Couture et al., 2013). Ferrihydrite surface is generally positively charged at the circumneutral pH (Dublet et al., 2017), therefore, strongly attract and bind negatively charged As(V) species onto the surface. Adsorption generally occurs by electrostatic interaction (Chen et al., 2022), ligand exchange (Jia and Demopoulos, 2005), competitive ion exchange (Jain and Loeppert, 2000), or by forming inner-sphere and outer-sphere complexes at the adsorbent surface (Ouyang et al., 2022). In soil and groundwater, Fe and manganese (Mn) species are often found together (Smedley and Kinniburgh, 2002; Bai et al., 2016). Hence, the occurrence of Fe as both single-phase Fe oxide (e.g., ferrihydrite) and as binary phase (Fe-Mn binary oxides) minerals becomes pervasive in various aquatic environments.

Fe oxides are generally formed by the chemical oxidation of the soluble Fe(II) (Borch et al., 2010), whereas Mn oxides are formed by the bio-oxidation of Mn(II) (Yu and Leadbetter, 2020; Tran et al., 2018). Fe oxides co-precipitate with Mn oxides in aquatic environments to form Fe-Mn binary oxides (Bai et al., 2016; McCann et al., 2018). Shallow groundwater environments contain large quantities of Fe-Mn binary oxides and the individual Fe- and Mn oxide components of these oxides have distinct functions; Fe oxides mainly as adsorbents and Mn oxides as arsenite oxidizers (Amirbahman et al., 2006; Hou et al., 2017; Zhao et al., 2022). Single-phase Fe oxide and binary oxides form in oxidative conditions where the oxidized As(V) form is predominant. Understanding As(V) adsorption dynamics in the presence of single-phase ferrihydrite and Fe-Mn binary oxides is important since they are ubiquitous in nature and hence can control As(V) availability and transportation. This research focused on the understanding of the As(V) adsorption mechanisms of ferrihydrite and Fe-Mn binary oxides and aimed to (1) evaluate and compare the As(V) adsorption capacities of ferrihydrite and Fe-Mn binary oxides, and (2) understand the As(V) adsorption behaviours of ferrihydrite and Fe-Mn binary oxides.

2.2 Materials and Methods

2.2.1 Synthesis of Ferrihydrite and Fe-Mn Binary Oxides

Ferrihydrite was synthesized following the method described by Cornell and Schwertmann, (2003). Briefly, 40 g of ferric nitrate nonahydrate ($Fe(NO_3)_3.9H_2O$) was dissolved in 500 mL of Milli-Q water. Approximately 298 mL of 1 M NaOH was then carefully and slowly added to the solution while vigorously stirring with a magnetic stirrer until the pH of the solution reached between 7.0 to 7.5. This resulted in the formation of ferrihydrite precipitates within a few minutes. To collect the ferrihydrite, the solution was centrifuged at 5000 rpm for 15 minutes, and the supernatants were decanted. Separated precipitates were washed with Milli-Q water several times until the resistivity of the solution decreased to 20 MΩ.cm. The precipitates were collected and oven-dried at 40° C for 72 hours. The produced ferrihydrite precipitates were ground and stored at room temperature until further analyses.

Fe-Mn binary oxides were synthesized following the method described by Zhang et al. (2007a; 2007b). Briefly, 1.9 g potassium permanganate ($KMnO_4$) and 10 g ferrous sulfate heptahydrate ($FeSO_4.7H_2O$) were dissolved separately in 400 mL milli-Q water. The solution of $FeSO_4.7H_2O$ was added slowly into the $KMnO_4$ solution while continuously mixing using a magnetic stirrer. The pH of the mixed solution was adjusted between 7.0 and 7.2 by slowly adding 5M NaOH solution. The mixed solution was kept stirring for 1 hour when the Fe-Mn binary oxides started to form. The solution was then kept for aging for another 12 hours. Synthesized precipitates of the Fe-Mn binary oxides were centrifuged at 5000 rpm for 15 mins and washed with Milli-Q water until the resistivity of the solution decreased to 20 MΩ.cm. The washed precipitates were oven-dried at 105° C for 4 h and then kept at 30° C overnight. Collected precipitates of Fe-Mn binary oxides were ground and preserved at room temperature until further analyses.

2.2.2 Solid Phases Characterisation

i. Powder X-Ray Diffraction (XRD) Analysis

To identify the mineral phases, XRD analysis was conducted on the dried and ground mineral powders using a Panalytical Empyrean Series 2 diffractometer with a cobalt (Co) anode Kα radiation source, fixed slit at continuous scanning from 5° to 80° in 2θ positions, at the Department of Earth Sciences, University of Oxford.

ii. Scanning Electron Microscope (SEM) Analysis

The morphological features of the synthesized ferrihydrite and Fe-Mn binary oxides were elucidated by SEM imaging using a high-resolution Zeiss Sigma 300 Field Emission Gun Scanning Electron Microscope at the Sir William Dunn School of Pathology, University of Oxford. SEM samples were prepared by stacking finely ground ferrihydrite or Fe-Mn binary oxides on 13mm aluminum stubs covered with carbon tape. Stacked samples were then coated with a 15 nm gold layer sputtered under vacuum for 120 seconds (Quorum Q150R ES, tooling factor 2.30, sputter current 20 mA). SEM images were acquired in the secondary electron mode at a working distance of 8-9 mm with an accelerated voltage of 2 kV.

iii. Energy Dispersive X-ray (EDX) Analysis

EDX analyses were performed to reveal the elemental compositions of the ferrihydrite particles and Fe-Mn binary oxides. EDX analyses were conducted in the SEM, using an EDX detector (Ultim Xtreme X-ray detector). The EDX spectra were acquired at a working distance of 5.4 mm with an accelerated voltage of 15 kV. Data were processed using Aztec software.

iv. Brunauer–Emmett–Teller (BET) Analysis

BET analysis was performed to evaluate the specific surface areas of ferrihydrite and Fe-Mn binary oxides after degassing at 110°C for 2 hours using a multi-point BET analysis with N_2 adsorption on a Micromeritics ASAP 2020, at the Department of Chemistry, University of Oxford.

2.2.3 As(V) Adsorption Kinetic Experiments

A stock solution of 500 μM As(V) was prepared by dissolving sodium arsenate heptahydrate ($AsH_{15}Na_2O_{11}$) in Milli-Q water in a Teflon bottle. To perform As(V) adsorption kinetic experiments, 5 mL of the 500 μM As(V) solutions were taken into 150 mL polypropylene bottles, previously washed with 2% nitric acid (HNO_3), to which 95 mL of Milli-Q water was then added to make the working solution concentration 25 μM. The pH of the solutions was adjusted to approximately 6.5 using 1 M NaOH and HNO_3. In each solution, 100 mg of ferrihydrite or Fe-Mn binary oxides were added, mixed well, and then the bottles were placed on a horizontal shaker at a speed of 80 rpm at room temperature. Aliquot samples were collected from the working solutions at 0, 0.2, 0.3, 0.5, 1, 2, 4, 6, 20, 24, 30, 48, and 72 h time

intervals and filtered through 0.22 µm membrane filters (Fisherbrand). The filtrates were preserved in 2% HNO_3 for Inductively Coupled Plasma Mass Spectrometry (ICP-MS) analysis. All the experiments were performed in duplicate.

2.2.4 As(V) Adsorption Isotherm Experiments

Adsorption isotherm experiments were performed by preparing 50 ml solutions of 1, 3, 5, 10, 15, 25, 45, 65 and 125 µM As(V) by appropriate dilutions of the 500 µM As(V) stock solution. The pH of the solutions was adjusted to approximately 6.5 using 1M HNO_3 and NaOH. In each solution, 2.5 mg of adsorbent (either ferrihydrite or Fe-Mn binary oxides) were added. The solution bottles were placed on a horizontal shaker at 80 rpm at room temperature. Aliquot samples were collected from the solution at the beginning and after 48 h of reaction. The collected samples were centrifuged at 5000 rpm for 5 mins, filtered through 0.22 µm membrane filters and filtrates were preserved in 2% HNO_3 for ICP-MS analysis. The experiments were performed in duplicate.

2.2.5 Adsorption Kinetic and Isotherm Models

The time-dependent experimental data of As(V) adsorption on ferrihydrite and Fe-Mn binary oxides were tested to fit the Pseudo-First-Order (PFO) and Pseudo-Second-Order (PSO) kinetic models to find the dominant adsorption mechanism and reaction rate. The equation of the PFO kinetic model is expressed as (Lagergren, 1898; Ho and McKay, 1998):

$$\frac{dq_t}{dt} = k_1(q_e - q_t) \quad Equation\ 2.1$$

Where q_e and q_t (µmol/g) are the amounts of As(V) adsorbed at equilibrium and variable time t, respectively, and k_1 is the adsorption rate constant ($hour^{-1}$) for the PFO kinetic model.

Considering the boundary conditions q_t=0 at t=0 and q_t=q_t at t=t, after integration Equation 2.1 can be written as:

$$q_t = q_e(1 - e^{-k_1 t}) \quad Equation\ 2.2$$

The linearized form of this equation has been given by Ho and McKay (1999) as follows:

$$\ln(q_e - q_t) = \ln q_e - k_1 t \quad Equation\ 2.3$$

The equation of the PSO kinetic model is expressed as (Ho and McKay, 1998):

$$\frac{dq_t}{dt} = k_2\,(q_e - q_t)^2 \quad Equation\ 2.4$$

Considering the boundary condition q_t=0 at t=0 and q_t=q_t at t=t, after integration Equation 2.4 can be written as:

$$q_t = \frac{k_2\,q_e^2\,t}{1 + k_2\,q_e\,t} \quad Equation\ 2.5$$

The linearized form expressed as:

$$\frac{t}{q_t} = \frac{1}{k_2\,q_e^2} + \frac{t}{q_e} \quad Equation\ 2.6$$

Where q_e and q_t represent the same as in the PFO equation and k_2 is the adsorption rate constant (g/µmol-hour) for the PSO kinetic model. The conformity between experimental data and the model-predicted values was evaluated by calculating the coefficient of determination (R^2) for both models.

A Langmuir isotherm model was employed to determine the maximum As(V) adsorption capacities onto ferrihydrite and Fe-Mn binary oxides and their surface properties. The Langmuir isotherm is mainly applicable for the chemisorption process (Ghosal and Gupta, 2017). This is one of the simplest models, widely used to interpret As adsorption isotherm data of ferrihydrite and Fe-Mn binary oxides (Raven et al., 1998; Lafferty and Loeppert, 2005; Zhang et al., 2007). In 1916, Irving Langmuir first published the Langmuir equation for a gas-solid phase adsorption system assuming monolayer adsorption of adsorbate onto an adsorbent surface with homogeneous adsorption sites. Adsorption can only occur at a finite number of definite adsorption sites, with no interaction between the adsorbed molecules (Alafnan et al., 2021; Guo and Wang, 2019; Foo and Hameed, 2010). The isotherm model is expressed using the following equation (Kalam et al., 2021; Ayawei et al., 2017):

$$q_e = \frac{q_m\,K_L C_e}{1 + K_L C_e} \quad Equation\ 2.7$$

where q_e is the amount of As(V) adsorbed on the adsorbent (ferrihydrite or Fe-Mn binary oxides) (µmol/g), C_e is the equilibrium concentration of As(V) in the solution (µmol/L), K_L is the equilibrium adsorption constant related to the affinity of binding sites (L/µmol), and q_m is the maximum amount of As(V) adsorbed on adsorbent (µmol/g).

The linearized equation is expressed as:

$$\frac{C_e}{q_e} = \frac{1}{q_m K_L} + \frac{C_e}{q_m} \quad Equation\ 2.8$$

A plot between C_e/q_e versus C_e will generate a straight line with a slope of $1/q_m$ and an intercept equal to $1/ q_m K_L$.

2.2.6 Elemental Concentration Analysis

The concentrations of As, Fe, and Mn in experimental solutions were determined by ICP-MS analysis using a PerkinElmer Nex-ION 350D ICP-MS at the Department of Earth Sciences, University of Oxford, using a River water reference material for trace metals (SLRS-5) from the National Research Council Canada and rhodium as an internal standard.

2.3 Results and Discussion

2.3.1 Mineral Phase Identification

Mineral phases of the synthesized ferrihydrite and Fe-Mn binary oxides were identified using XRD analysis. The XRD patterns of the ferrihydrite and Fe-Mn binary oxides are shown in Figure 2.1. The observed XRD patterns shapes with broad spectra without defined peaks suggest the mineral phases might be highly amorphous or poorly crystalline in structures. Synthesized ferrihydrite showed two broad bands at 40°, and 74° 2θ positions in the XRD pattern (Figure 2.1a), which mostly resemble the International Centre for Diffraction Data (ICDD) 00-058-0898 reference line spectrum of hexagonal ferrihydrite. Fe-Mn binary oxides showed (Figure 2.1b) most intensive broad peaks around 22° and 42° 2θ positions and best match with ICDD 00-018-0802 and ICDD 01-073-8408 reference lines of hexagonal birnessite and ferrihydrite, respectively.

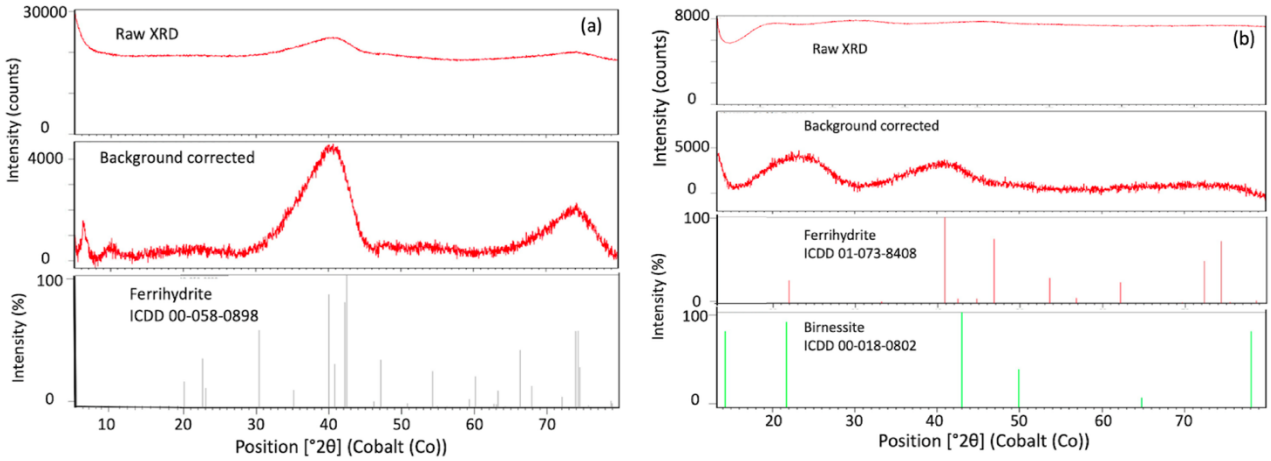


Figure 2.1: XRD patterns of (a) ferrihydrite and (b) Fe-Mn binary oxides with ICDD reference lines of ferrihydrite and birnessite.

Previous studies have found XRD patterns of ferrihydrite and Fe-Mn binary oxides with similar shapes and peak positions (Gimsing and Borggaard, 2007; Yang et al., 2019; Liang et al., 2020; Jiang et al., 2015). Gimsing and Borggaard (2007) and Dzieniszewska et al. (2020) identified the ferrihydrite phase by XRD patterns identical to the pattern found in this study with the shape and peak positions (Figure 2.2a) though the synthesis methods they have used are different from this study.

Varieties of shapes and peak positions in the XRD patterns of Fe-Mn binary oxides have been reported in the literature, mainly due to the presence of different Fe and Mn phases in different studies and different Mn/Fe mole ratios (Figure 2.2 b, c, d) (Granados-Correa and Bulbulian, 2012; Yang et al., 2019; Liang et al., 2020; Li et al., 2017).

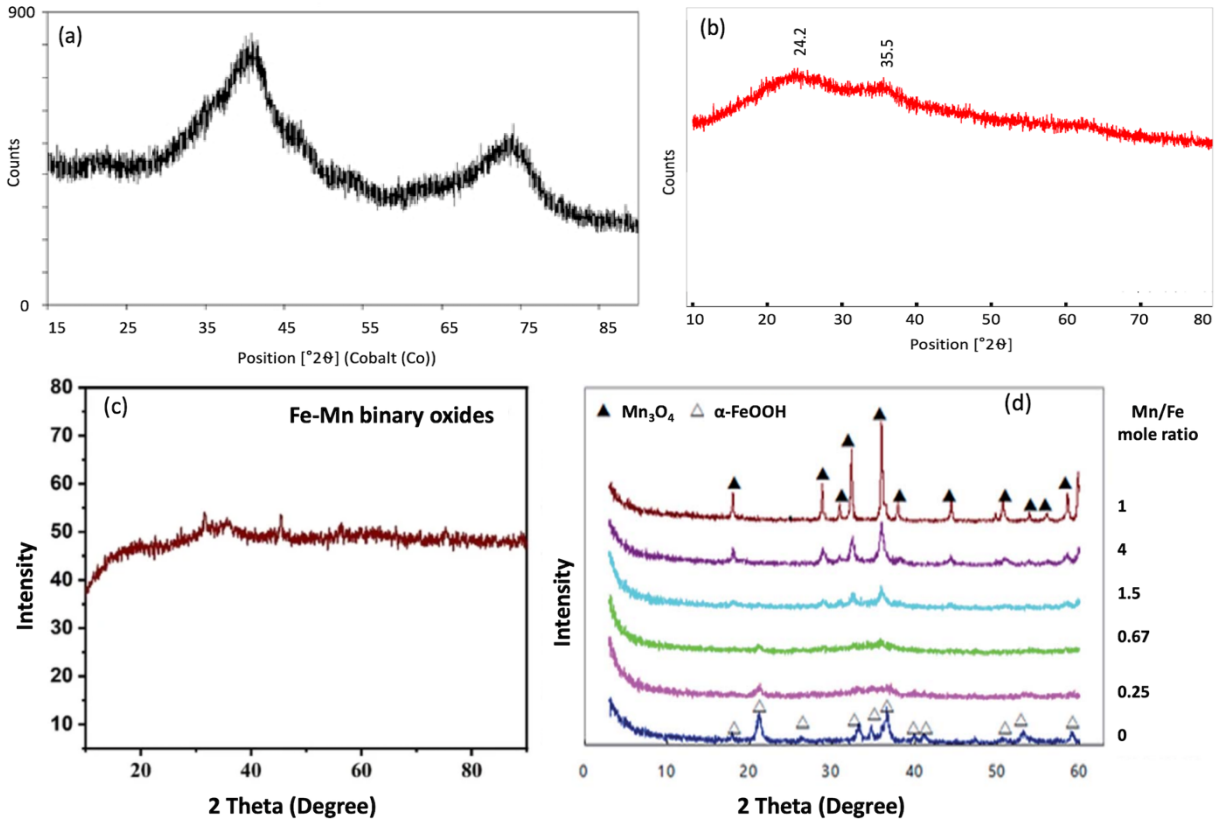


Figure 2.2: XRD pattern of (a) ferrihydrite (Gimsing and Borggaard, 2007), (b) Fe-Mn binary oxides with biochar (Liang et al., 2020), (c) Fe-Mn binary oxides (Byanjankar et al., 2024), and (d) Fe-Mn binary oxides in different Mn/Fe mole ratios (Li et al., 2017).

Sometimes absence of Mn oxides peaks was reported due to the high amorphization of Fe-Mn binary oxides (Liang et al., 2020). XRD pattern of Fe-Mn binary oxides found in this study matches the XRD pattern of Fe-Mn binary oxides mixed biochar identified by Liang et al. (2020) (Figure 2.2b). Li et al. (2017) reported various shapes and peak positions of Fe-Mn binary oxides based on different Mn/Fe mole ratios (Figure 2.2d). Though the mineral synthesis and XRD procedures vary, the overall shapes of the Fe-Mn binary oxides shown in those studies support the result of this research.

2.3.2 Morphological Characterization

The SEM images of ferrihydrite and Fe-Mn binary oxides are shown in Figure 2.3. The SEM images of both ferrihydrite (Figure 2.3a, b) and Fe-Mn binary oxides (Figure 2.3c, d) indicated they were the aggregates of many fine particles.

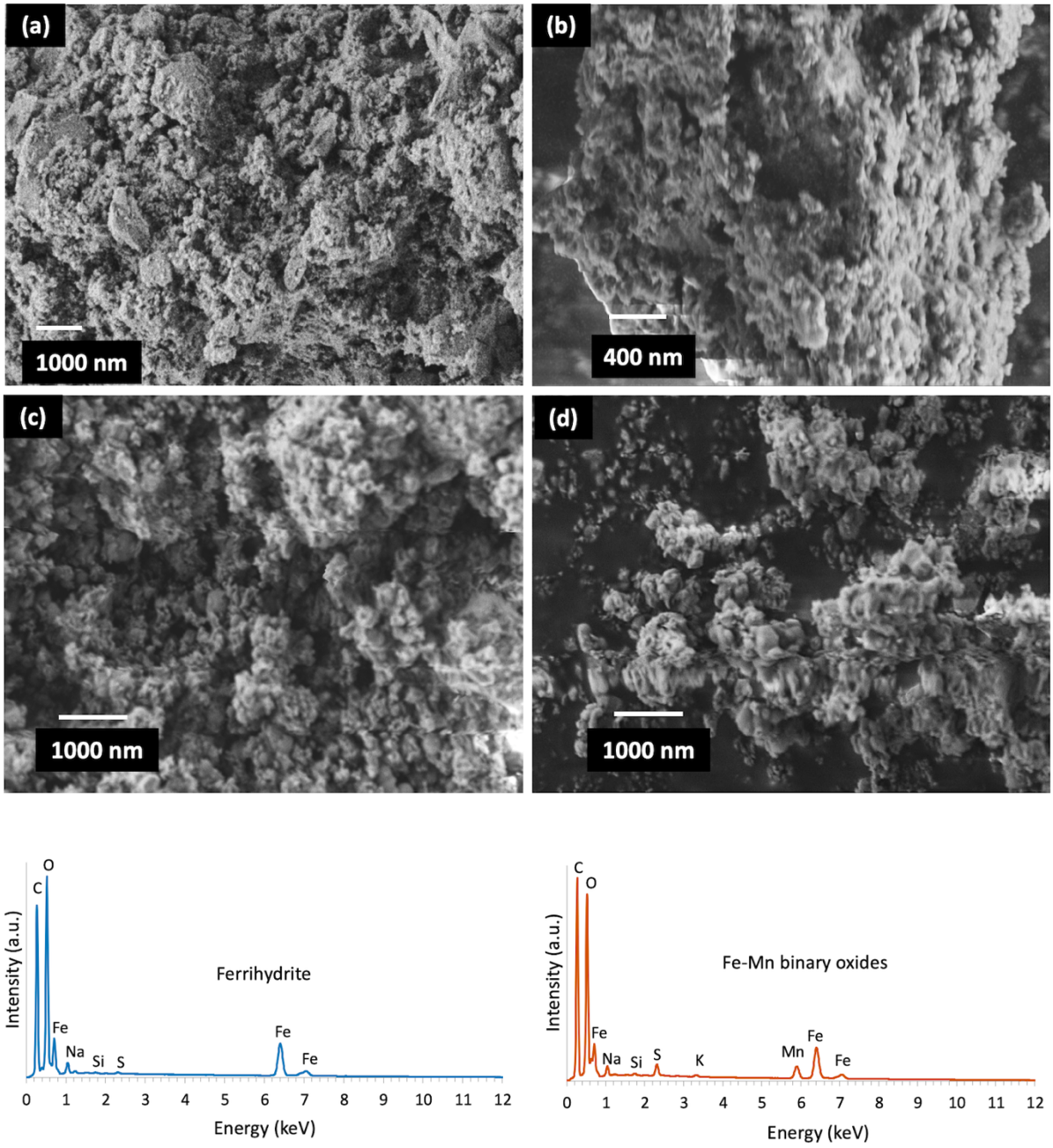


Figure 2.3: SEM images (ferrihydrite (a, b), Fe-Mn binary oxides (c, d)) and SEM-EDX spectra of ferrihydrite and Fe-Mn binary oxides.

Due to extensive particle aggregation, it is difficult to see the sizes of individual particles, but the SEM images indicate they could be categorized as nanoparticles (<100 nm). Similar morphologies of ferrihydrite and Fe-Mn binary oxides have been found in previous studies (Zheng et al., 2023; Abdus-Salam and M'civer, 2012; Hu et al., 2022).

The SEM-EDX spectra in Figure 2.3 show the elemental compositions of synthesized ferrihydrite and Fe-Mn binary oxides. Ferrihydrite EDX spectra showed the presence of Fe and oxygen (O). The SEM-EDX spectra of the Fe-Mn binary oxides confirmed the presence of Fe and Mn. The Potassium (K) peak might have originated from residual $KMnO_4$ used for Fe-Mn binary oxides synthesis. The presence of sulfur (S), sodium (Na), and silicon (Si) in both ferrihydrite and binary oxides spectra might arise from the residues of $FeSO_4.7H_2O$, NaOH, and Si glass bottles. Sharp carbon (C) peaks in both spectra resulted from the carbon tape on which samples were stacked. The elemental composition of ferrihydrite is similar to the ferrihydrite synthesized by Abdus-Salam and M'civer, (2012). The SEM-EDX spectrum of Fe-Mn binary oxides presented in this study is consistent with the SEM-EDX of Fe-Mn binary oxides reported by Zhang et al. (2023).

2.3.3 Specific Surface Area

The specific surface area plays a significant role in determining active surface sites, surface charge density, or electrostatic field in mineral particles (Mendez and Hiemstra, 2020), which ultimately control the adsorption of metals or charged species. BET analysis revealed that the specific surface areas of ferrihydrite and Fe-Mn binary oxides were 248 m^2/g and 278 m^2/g, respectively. The pore size of ferrihydrite was 2 nm to 3 nm, consistent with the results reported by Weidler and Stanjek (1998) and the total pore volume was 0.1 cm^3/g. Whereas the pore size of Fe-Mn binary oxides ranged from 5 nm to 8 nm and the total pore volume was 0.3 cm^3/g. The smaller specific surface area of ferrihydrite compared to Fe-Mn binary oxides might have resulted from the aggregation of particles as shown in the SEM image (Figure 2.3) (Hiemstra, 2018; Dzombak and Morel, 1991), and poor dispersion. However, the measured specific surface area of ferrihydrite was close to the values (223.6 m^2/g, 292 m^2/g, 180 m^2/g) reported by several studies (Zheng et al., 2023; Lan et al., 2018; Zhu et al., 2011). Since ferrihydrite is thermodynamically metastable, and its particles can grow over time, the specific surface area may change too (Hiemstra et al., 2019; Dehouck et al., 2017; Mao et al., 2012; Burleson and Penn, 2006).

Several studies have reported significant changes in the specific surface area of the ferrihydrite controlled by a few factors such as pH, temperature, and aging (Hiemstra et al., 2019; Antelo et al., 2010). In particular, aging and particle aggregation resulted in the reduction of the specific surface area of the ferrihydrite. It has been known that the ferrihydrite nanoparticles can attach or bind themselves irreversibly to form larger porous aggregates, especially when dried and as a result of aging, which significantly decreases reactive surface area (Hiemstra et al., 2019; Antelo et al., 2010; Hiemstra et al., 2009). Moreover, He et al. (2021) mentioned that the co-existence of Mn and Fe in the binary oxide particles would prevent particle aggregation compared to monometallic Fe oxide, providing Fe-Mn binary oxides with a larger surface area. A close specific surface area value (231 m^2/g) for Fe-Mn binary oxides was observed by Wu et al. (2011).

2.3.4 Adsorption Kinetics and Isotherms

PFO kinetic models of As(V) adsorption onto ferrihydrite and Fe-Mn binary oxides clearly exhibited two phases of adsorption; the first linear phase up to 10 hours and then another semi-linear phase between 10-72h (Figure 2.4). Interestingly, both adsorbents showed the similar characteristics. The sharp slope at start indicates fast adsorption, perhaps dominated by film diffusion and the second phase was slower, perhaps due to pore diffusion. As the adsorbent became more saturated with adsorbates, fewer sites were available, and the adsorption rate decreased.

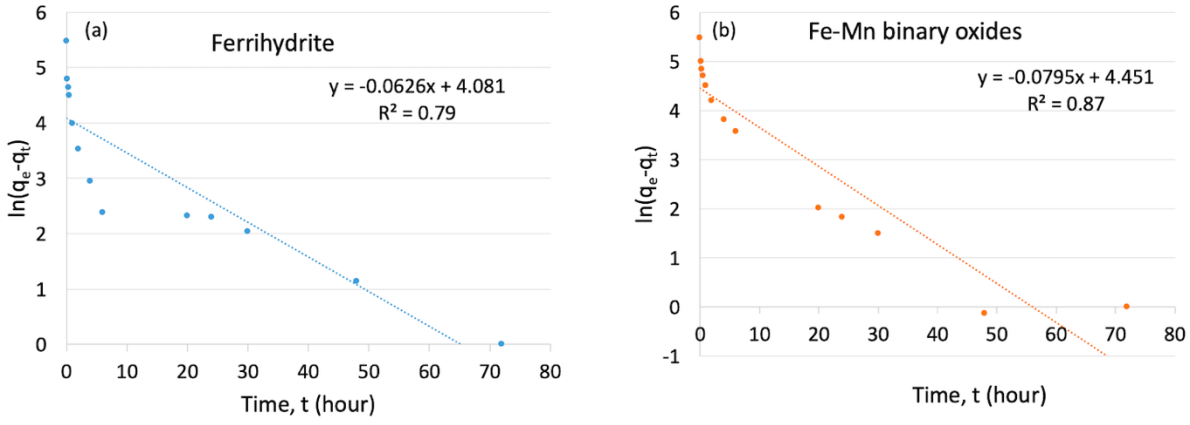


Figure 2.4: PFO kinetic models of As(V) adsorption on ferrihydrite (a) and Fe-Mn binary oxides (b).

As(V) adsorption kinetic studies indicated rapid As(V) adsorption onto both ferrihydrite and Fe-Mn binary oxides from experimental solutions at the beginning of the reactions (Figure 2.5a). In the first 6 hours of reactions, As(V) adsorption rate on ferrihydrite was higher than on Fe-Mn binary oxides. From approximately 20 hours, the As(V) adsorption rate on both adsorbents slowed down considerably, and the concentration of As(V) in solutions remained steady until the end of the reaction period.

The PSO kinetic model provided a good fit to As(V) adsorption experimental data of ferrihydrite and Fe-Mn binary oxides. PFO and PSO kinetic models derived parameters for As(V) adsorption on ferrihydrite and Fe-Mn binary oxides are provided in Table 2.1. Conformity to As(V) adsorption experimental data with the PSO kinetic models (Figure 2.5b) was confirmed by high R^2 values (R^2= 0.999) in t/q_t versus reaction time (t) linear plot (Figure 2.5c). Interestingly, the models provided the same calculated As(V) adsorption at equilibrium (q_e) for both ferrihydrite and Fe-Mn binary oxides, 238 µmol/g, which is close to the experimental adsorption at equilibrium of both adsorbents (238 µmol/g and 239 µmol/g, respectively) (Figure 2.5b). The k_2 values of ferrihydrite and Fe-Mn binary oxides were found to be 0.01 g/µmol-hour and 0.007 g/µmol-hour, respectively. At the very beginning of the adsorption process, the calculated adsorption rates ($k_2q_e^2$) of As(V) onto ferrihydrite and Fe-Mn binary oxides were 625 µmol/g-hour and 400 µmol/g-hour, respectively.

Table 2.1: PFO and PSO kinetic models derived parameters for As(V) adsorption on ferrihydrite and Fe-Mn binary oxides.

Kinetic Model	PFO			PSO		
	R^2	k_1 (per hour)	q_e (µmol/g)	R^2	k_2 (g/µmol-hour)	q_e (µmol/g)
Ferrihydrite	0.79	0.06	59	0.99	0.01	238
Fe-Mn binary oxides	0.87	0.08	86	0.99	0.007	238

The specific surface area-normalized As(V) adsorption onto ferrihydrite was higher than for Fe-Mn binary oxides at equilibrium and throughout the reactions approaching equilibrium (Figure 2.5d). Ferrihydrite exhibited specific surface area-normalized equilibrium adsorption of 0.96 µmol/m^2, while Fe-Mn binary oxides demonstrated an equilibrium adsorption of 0.86 µmol/m^2 at the end of the 72 hour of adsorption period.

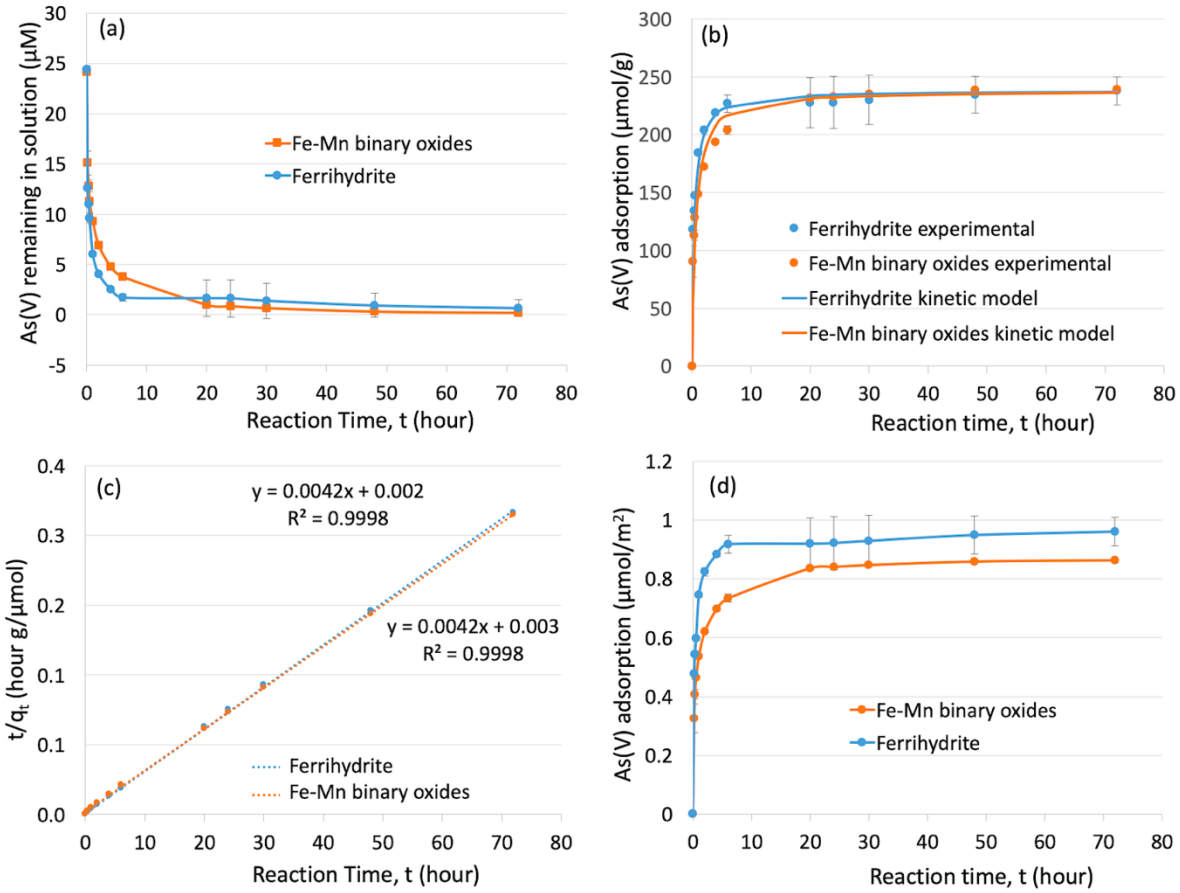


Figure 2.5: Time-dependent concentrations of As(V) in solution during adsorption on ferrihydrite and Fe-Mn binary oxides (a), Mass-normalized experimental As(V) adsorption and PSO kinetic models of ferrihydrite and Fe-Mn binary oxides (b), PSO kinetic t/q_t vs reaction time (t) linear plot (c), and Specific surface area-normalized As(V) adsorption onto ferrihydrite and Fe-Mn binary oxides (d). Error bars have been calculated as the standard deviation of the different replicates.

In As(V) adsorption kinetic experiments, the best fitting with PSO kinetic models suggested that the dominant process of As(V) adsorption onto both ferrihydrite and Fe-Mn binary oxides was mainly driven by chemisorption. These indicated that inner-sphere surface complexes formation by ligand exchange might be the predominant mechanism of As(V) adsorption. This result is consistent with the findings reported by Wang et al. (2022). A higher k_2 value of As(V) adsorption onto ferrihydrite than Fe-Mn binary oxides indicated faster adsorption and higher affinity of ferrihydrite to As(V) than Fe-Mn binary oxides (Wang et al., 2022; Zhu et al., 2011). Almost complete adsorption of As(V) by both adsorbents indicates that the specific surface areas of ferrihydrite and Fe-Mn binary oxides contained sufficient surface sites to adsorb this low concentration (25 µM) of As(V) from the solution.

The concentration-dependent As(V) adsorptions on ferrihydrite and Fe-Mn binary oxides were determined by batch experiments using several As(V) solutions with concentrations ranging from 1 to 125 µM at a pH value of 6.5. Figure 2.6a shows that the As(V) adsorption on Fe-Mn binary oxides was higher than ferrihydrite. Mass-normalized As(V) adsorption demonstrated higher adsorption ability of Fe-Mn binary oxides than ferrihydrite after 48 h of adsorption reaction (Figure 2.6b). The experimental maximum adsorption capacities of ferrihydrite and Fe-Mn binary oxides were 289 µmol/g and 431 µmol/g, respectively.

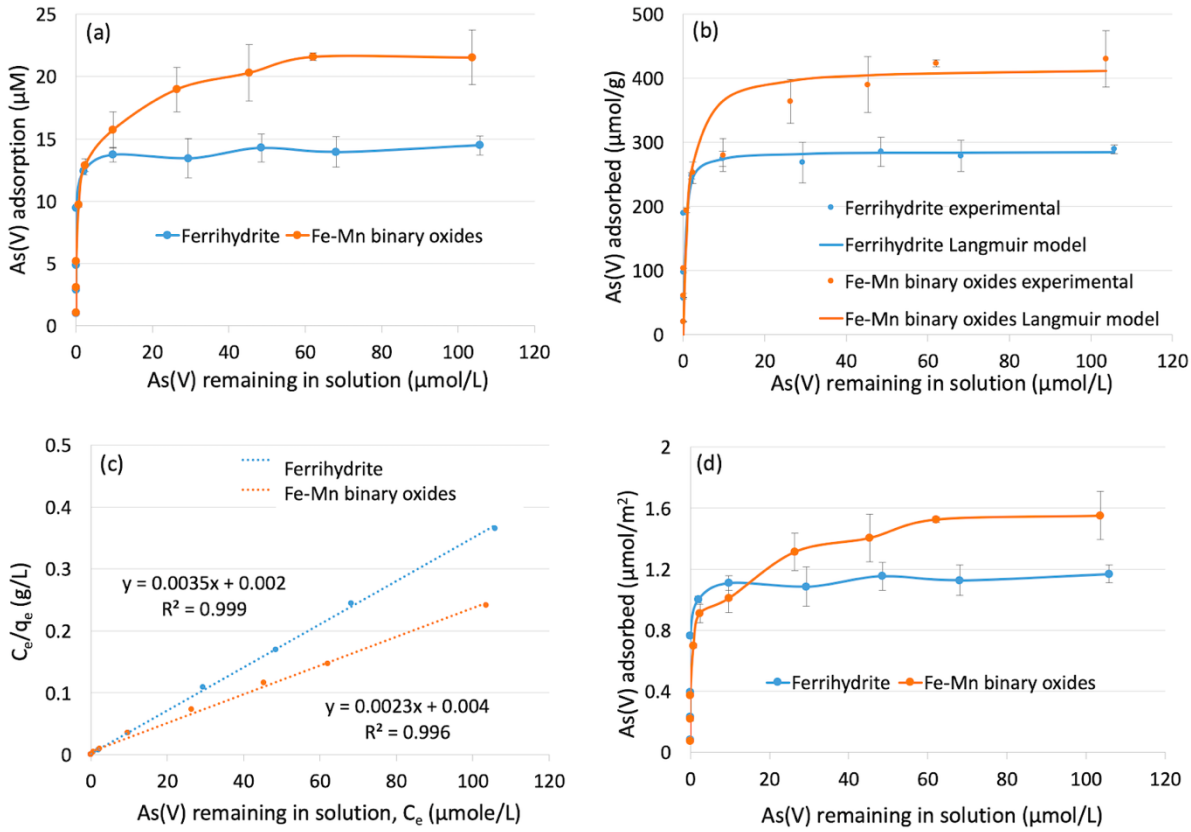


Figure 2.6: Concentration-dependent As(V) adsorption on ferrihydrite and Fe-Mn binary oxides (a), Mass-normalized experimental As(V) adsorption isotherms and Langmuir isotherm models of ferrihydrite and Fe-Mn binary oxides (b), Langmuir isotherm C_e/q_e vs C_e linear plot (c), and Specific surface area-normalized As(V) adsorption of ferrihydrite and Fe-Mn binary oxides (d). Error bars have been calculated as the standard deviation of the different replicates.

The As(V) adsorption experimental data were fitted using the linear Langmuir adsorption isotherms (Figure 2.6c) with R^2 values of 0.999 and 0.996 for ferrihydrite and Fe-Mn binary oxides, respectively. Several researchers have also demonstrated Langmuir isotherm for explaining adsorption systems (Zheng et al., 2023; Das et al., 2013; Zhu et al., 2011; Poinern

et al., 2010; Foo and Hameed, 2010; Masue et al., 2007; Lafferty and Loeppert, 2005). The Langmuir adsorption isotherm of ferrihydrite provided a calculated maximum adsorption capacity (q_m) of 286 μmol/g and an equilibrium adsorption constant (K_L) of 2.5 L/μmol. The Langmuir adsorption isotherm of Fe-Mn binary oxides showed a q_m value of 435 μmol/g and a K_L value of 0.5 L/μmol.

The Langmuir As(V) adsorption isotherm of both adsorbents suggested strong agreements between the models and the experimental adsorption data. This indicated that the surfaces of the adsorbents likely had homogeneous adsorption sites and that the adsorption energies of As(V) adsorption on the surfaces of the adsorbents were the same. The adsorption occurred onto the monolayers of the ferrihydrite and Fe-Mn binary oxides and there were no interactions between adsorbed As(V) species. A higher K_L value for ferrihydrite suggested a higher affinity of ferrihydrite for As(V) compared to Fe-Mn binary oxides. Previous research also supported the use of the Langmuir isotherm equation for describing As(V) adsorption on ferrihydrite and Fe-Mn binary oxides (Raven et al., 1998; Lafferty and Loeppert, 2005; Zhang et al., 2007). However, the applicability of Freundlich isotherm is also common in describing and it generally depends on the solution chemistry and the pH (Raven et al., 1998; Zhu et al., 2011; Zhang et al., 2007). Since the Langmuir isotherm well described the As(V) adsorption onto ferrihydrite and Fe-Mn binary oxides, and there were high conformities between experimental data and model predicted values ($R^2 > 0.99$), no other model was employed.

The specific surface area normalized results of adsorption isotherm experiments indicated that Fe-Mn binary oxides generally had a 25% higher capacity for As(V) adsorption per square meter than ferrihydrite (Figure 2.6d). Ferrihydrite reached the highest adsorption capacity of 1.2 μmol/m^2, whereas Fe-Mn binary oxides achieved a maximum capacity of 1.6 μmol/m^2. On the contrary, in adsorption kinetic experiments, surface area normalized result showed higher adsorption capacity of ferrihydrite than Fe-Mn binary oxides at equilibrium (Figure 2.5d), which might be only applicable in low As(V) concentration solution (25 μM).

However, higher As(V) adsorption capacity of Fe-Mn binary oxides might be due to the larger specific surface areas of Fe-Mn binary oxides than ferrihydrite. Nonetheless, Fe-Mn binary oxides had an 11% larger specific surface area than ferrihydrite but a 34% higher adsorption capacity per gram. Hence, specific surface area may not be the only key factor controlling As(V) adsorption capacity. Surface site densities and morphologies of the adsorbents (e.g., aggregation, pore size) might also affect their As(V) adsorption capacities.

Adsorption of As(V) onto both adsorbents could be controlled by the solution's pH, the adsorbent's mineralogy, and specific surface area. In natural environments, at neutral pH, As remains as oxyanion. The As(V) is a charged oxygen anion ($H_2AsO_4^-$, $HAsO_4^{2-}$) at pH 6.5 and forms molecules of a large hydrated ionic radius after combining with water (Zheng et al., 2023). Because of having higher pore volume and larger pore size than ferrihydrite, monolayer adsorption might occur onto the external surface areas as well as in pores insides of the binary oxides by external diffusion, surface reaction, and intraparticle diffusion (Wang and Guo, 2020). On the contrary, agglomeration of ferrihydrite could change the pore structure and reduce pore size, decreasing As(V) adsorption capacity (Wang et al., 2022; Das and Bezbaruah, 2021; Hofmann et al., 2004). Particle aggregation of ferrihydrite might affect the adsorption of larger hydrated As(V) molecules onto all effective surface sites, reducing adsorption capacity of ferrihydrite.

2.4 Conclusion

This study reveals that synthesized ferrihydrite and Fe-Mn binary oxides were aggregates of very small particles and poorly crystalline or amorphous in nature. Fe-Mn binary oxides had larger specific surface areas, larger pore size, and higher total pore volume than ferrihydrite. Adsorption of As(V) onto both ferrihydrite and Fe-Mn binary oxides was mainly driven by the chemisorption process and the reactions followed the PSO kinetic equations. Ferrihydrite exhibited a higher adsorption rate and affinity towards As(V) than Fe-Mn binary oxides. Despite these, Fe-Mn binary oxides showed a 25% higher maximum As(V) adsorption capacity per square meter than ferrihydrite. Adsorption isotherm data followed the Langmuir equation suggesting monolayer adsorption onto the homogeneous surface sites of both adsorbents. The adsorption capacity of the adsorbents might have been influenced by the solution pH, the specific surface areas, and the morphologies of these minerals. The larger specific surface area and pore size of the Fe-Mn binary oxides might have contributed more As(V) adsorption than ferrihydrite. Aggregation of ferrihydrite particles and smaller pore size might have resulted in adsorption only on the external surface, potentially reducing the adsorption capacity (per square meter). The findings indicate the Fe-Mn binary oxides are excellent in As(V) adsorption and might have a significant role in controlling As(V) transport and bioavailability in aquatic environments.

3 Chapter Three: *Pseudomonas Putida*-Mediated Synthesis of Biogenic Iron-Manganese Binary Oxides Nanoparticles: Characterization Insights and Potential Environmental Implications

Abstract

Biogenic iron-manganese (Fe-Mn) binary oxides are thought to be of significant environmental importance due to their strong reactivity and frequent occurrence in natural settings. Despite their critical role, their formation pathways in different environmental conditions and detailed characterization remain underexplored. This research presents an in-depth investigation into the synthesis of biogenic Fe-Mn binary oxides, mediated by the Mn-oxidizing bacterium *Pseudomonas putida* MnB1 (*P. putida*), under conditions mimicking the oxic-anoxic interface of a water column, a potential pathway described here for the first time. Synthesis of biogenic Fe-Mn binary oxides was performed in laboratory experiments consisting of three successive steps: (i) culturing *P. putida*, (ii) bio-oxidation of Mn(II) to produce biogenic Mn oxide, and (iii) oxidation of Fe(II) by biogenic Mn oxides. Advanced analytical techniques, including XRD, SEM, STEM, STEM-EDX, TEM-SAED, and ICP-MS revealed the formation of heterogeneously distributed distinct phases of Fe and Mn oxide minerals. The minerals were identified as poorly crystalline birnessite and ferrihydrite nanocrystals closely associated with bacterial cells and extracellular polymeric substances (EPS). Synthesized biogenic Fe-Mn binary oxides showed diverse morphologies, including large granules, long chains, and ultrathin sheets, produced extracellularly on the bacterial cell surfaces. The synthesis process of biogenic Fe-Mn binary oxides described in this study provides a better understanding of one of the possible pathways of Mn and Fe cycling at the oxic-anoxic interface of the water column. Potential environmental implications of the formation of these phases have also been discussed, including trace metals transport dynamics in aquatic environments.

Keywords: Biogenic Fe-Mn binary oxides, *Pseudomonas putida* MnB1, Nanoparticles, Bio-mineralization, Mn(II) oxidizer, Oxic-anoxic interface.

3.1 Introduction

Microbes play a pivotal role in global geochemical cycling, biotransformations, biodegradation, bioavailability, and the transport of contaminants and nutrients in natural environments (Zheng et al., 2018; Borch et al., 2010). Their metabolic activities significantly influence the mineralogy of surface environments by driving the formation of biogenic minerals, often while using transition metals to meet energy requirements or to adapt to environmental stress (Cosmidis and Benzerara, 2022; Soldatova et al., 2017; Rajkumar and Freitas, 2008). Biogenic minerals form in close association with bacteria as either internal or external precipitates. They often exhibit distinct characteristics compared to abiogenic phases, such as smaller sizes, poorer crystallinity, higher reactivity, and larger surface area. As a result, they tend to be more reactive and can control the biogeochemical cycling of contaminants in natural environments (Glodowska et al., 2021; Piepenbrock et al., 2014; Muehe et al., 2013; Posth et al., 2014). They also have significant roles in contamination remediation in different built environments, including wastewater treatment plants and sites contaminated by industry and mining (Staicu et al., 2021).

Manganese (Mn) is a vital trace element necessary for intracellular functions in humans, animals, and plants, primarily due to its role as a cofactor for several enzymes and its involvement in various metabolic and physiological processes (Chen et al., 2018; Li and Yang, 2018; Lucchini et al., 2015). Many bacteria utilize Mn for growth and protection against oxidative stress (Waters, 2020; Culotta and Daly, 2013). Enzymes with Mn cofactors catalyze nucleic acid and carbohydrate metabolism (Martin et al., 2017; Juttukonda and Skaar, 2015). Some bacteria are known to oxidize Mn(II) to generate energy and form Mn(III,IV) oxide minerals (Yu and Leadbetter, 2020; Tebo et al., 2004). The predominant mechanism for bacterial Mn(II) oxidation is enzymatic, and although Mn(II)-oxidizing bacteria are phylogenetically diverse, they all rely on a multicopper oxidase-like enzyme to carry out this process. The oxidation of Mn(II) to Mn(IV) proceeds through a Mn(III) intermediate, which may be either soluble or enzyme-bound (Webb et al., 2005; Tebo et al., 2004). Abiotic Mn(II) oxidation is kinetically limited and microbial Mn oxidation processes play a critical role in the biological formation of Mn oxides and regulate Mn cycling in natural systems (Handley and Lloyd, 2013; Tebo et al., 2005; Nealson et al., 1988). This process is influenced by a range of environmental factors, including temperature, salinity, and oxygen (O_2) levels (Hansel, 2017).

While Mn(II) oxidation by O_2 is thermodynamically favorable (Diem and Stumm, 1984), it is kinetically limited without the presence of a catalyst. In the environment, microbial Mn(II) oxidation is widespread across different microbial phylogenetic domains, including bacteria, archaea, and eukarya (Hansel, 2017). *Pseudomonas putida* MnB1 (*P. putida*), a Gram-negative Gammaproteobacterium, is ubiquitous in soil and freshwater, and is a well-known model organism for the laboratory study of microbial Mn(II) oxidation (Tong et al., 2022; Galezowski et al., 2020; Zheng et al., 2018; Toner et al., 2005; Villalobos et al., 2003; Caspi et al., 1998). This strain can survive under diverse environmental stresses, including heavy metal contamination. The biochemical mechanism of direct oxidation and acquisition of Mn(II) by *P. putida* is thought to involve a multicopper oxidase enzyme complex (Francis and Tebo, 2001; Tebo et al., 2005; Miller et al., 2012) and Mn transporters (Courville et al., 2006; Nevo and Nelson, 2006). Additionally, the involvement of extracellular superoxide radicals has been identified as an indirect Mn(II) oxidation pathway in *P. putida* (Miller et al., 2012; Learman et al., 2011). Despite progress, the exact mechanisms underlying Mn(II) oxidation and extracellular Mn oxides deposition remain incompletely understood (Webb et al., 2005; Miyata et al., 2006; Learman et al., 2011). However, microbial Mn oxidation occurs at rates several orders of magnitude greater than abiotic oxidation by O_2 (Tebo et al., 2004), emphasizing the significance of the formation of biogenic Mn oxides in natural aquatic systems.

The geochemistry of Mn is interlinked with iron (Fe), as these two metals often co-exist in various forms, including as hydrated ions, in soluble complexes, and in particles across diverse environments such as waters, soils, and sediments (Kappler et al., 2021; Liu et al., 2022; Bai et al., 2016). Iron, the most abundant transition metal in the Earth's crust, is ubiquitous in surface and groundwater environments. Fe oxides form through the oxidative precipitation of Fe(II) under aerated conditions, primarily via chemical oxidation, although microbial processes can also facilitate the oxidation of Fe(II) to Fe(III) under anoxic conditions, particularly via nitrate-reducing and photoautotrophic bacteria (Kappler et al., 2021; Kappler and Straub, 2005; Straub and Kappler, 2005). Moreover, microorganisms can also passively sorb Fe onto their cell walls, leading to Fe oxides nucleation on the cell surface. Microbial extracellular polymeric substances (EPS) can also act as templates for Fe oxides nucleation (Fortin and Langley, 2005). Fe- and Mn oxides often co-exist in environments and co-precipitate as Fe-Mn binary oxides. Understanding the formation of biogenic Fe-Mn binary oxides is critical, as these minerals play essential roles in controlling the speciation, transport, and fate of several redox-sensitive metals, thereby regulating their biogeochemical cycles (Zheng et al., 2024).

This research focuses on the interplay between Fe and Mn in a microbial system that mimics the geochemical dynamics at the oxic-anoxic interface, and which has rarely been investigated. While numerous studies have focused on the chemical synthesis of binary or mixed Fe- and Mn oxides (Hu et al., 2022; Chen et al., 2020; Zheng et al., 2021; Zheng 2020; Yang et al., 2018; Zhang et al., 2014; Liu et al., 2012; Xu et al., 2011; Chang et al., 2009; Zhang et al., 2007), investigations into the synthesis of microbially mediated Fe-Mn binary oxides, along with a detailed characterization of these minerals, are limited. The *in-situ* formation of biogenic Fe-Mn binary oxides was investigated by Bai et al. (2016) in aerobic conditions using *Pseudomonas* sp. QJX-1 for Mn(II) oxidation. Tong et al. (2022) investigated the effect of Fe(II) oxidation by O_2 on Mn(II) oxidation by *P. putida*. However, neither study addressed the redox behavior of biogenic Mn oxides in the presence of Fe(II) in micro-oxic conditions.

This research describes a novel pathway for the microbial formation of biogenic Fe-Mn binary oxides under the conditions of an oxic-anoxic boundary in the water column: first, the formation of biogenic Mn oxide nanoparticles through the bio-oxidation of Mn(II) by *P. putida* in oxic conditions, followed by the synthesis of Fe oxide nanoparticles through *in situ* oxidation of Fe(II) by biogenic Mn-oxide in a micro-oxic environment, in a laboratory setting. Additionally, the study offers a detailed characterization of the synthesized biogenic Fe-Mn binary oxides. Finally, environmental implications of this new microbial synthesis pathway have been discussed.

3.2 Materials and Methods

3.2.1 Synthesis of Biogenic Fe-Mn Binary Oxides

Biogenic Fe-Mn binary oxides were produced in a three-step process: (i) culturing of *P. putida* MnB1, (ii) synthesis of biogenic Mn oxide, and (iii) synthesis of biogenic Fe-Mn binary oxides. Culturing and synthesis of biogenic Mn oxide were performed following a protocol slightly modified after Galezowski et al., (2020). All the solutions prepared and used in this experiment were sterilized either by autoclaving or filtering through 0.22 μm filters. To culture the bacteria, a growth medium was prepared by dissolving nutrient broth (Sigma-Aldrich) in MilliQ water (8 g/L). The nutrient broth was composed of 3 g/L beef extract, 5 g/L peptone, and 50 μM $MnSO_4.H_2O$ (manganese sulfate monohydrate). Cells of *P. putida* strain MnB1 (ATCC 23483) were inoculated in the growth medium and cultured overnight under aerobic conditions on a horizontal shaker at a speed of 120 rpm at 30 °C and a pH 6.8. On the next day, the cells were separated from the growth medium by centrifuging at 5000 rpm for 5 mins. Cells were then washed with 10 mM HEPES (4-(2-Hydroxyethyl)piperazine-1-ethane-sulfonic acid) and 10 mM NaCl (sodium chloride) three times to rinse off any growth medium from the separated cells.

In the second step, a mineralization medium composed of 10 mM HEPES, 2 mM $(NH_4)_2SO_4$ (ammonium sulfate), 0.7 mM NaCl and 1 mM glucose was prepared, and the pH was buffered at 7.4. Then, the rinsed *P. putida* cells were transferred at a cell density of 2.3 x 10^8 cells/mL to several 250 mL Schott bottles, each containing 150 mL of mineralization medium. After this, 5 mL of a 5.58 mM Mn(II) ($MnSO_4.H_2O$) solution was added to each bottle to achieve a Mn(II) concentration of 180 μM. After that, the bottle lids were loosely closed, and bottles were placed on a horizontal shaker at a speed of 120 rpm at 30 °C. Blackish-grey precipitates were observed to form in the experimental media from the second day of the experiment, interpreted as the bio-oxidation of Mn(II) to insoluble Mn(III)/(IV) by *P. putida.* In order to assess spontaneous chemical formation of Mn oxide, an abiotic control was prepared by introducing Mn (II) at 180 μM in the same mineralization medium, without inoculation with *P. putida*, and under the same experimental conditions mentioned above.

Finally, after 12 days of Mn(II) bio-oxidation and mineralization, each Schott bottle was sparged with nitrogen (N_2) gas for 5 minutes to establish micro-oxic conditions, and Fe(II) ($FeSO_4.7H_2O$) was added to the solution at a final concentration of 200 μM. The experiment was then continued for 6 days at 30 °C, with agitation at a speed of 120 rpm.

All solutions and cell handling were performed in a biosafety hood to prevent microbial contamination and maintain sterile conditions. After synthesis, minerals were separated from the mineralization media by centrifuging at 8000 rpm for 10 minutes and then washed with milli-Q water five times for further analyses.

3.2.2 Chemical Analysis

i. Inductively Coupled Plasma Mass Spectrometry (ICP-MS) Analysis

The concentrations of Fe and Mn in experimental solutions were determined by ICP-MS analysis using a PerkinElmer NexION 350D ICP-MS. A river water standard for trace metals (SLRS-5) from the National Research Council Canada was used as reference material for Fe and Mn concentrations, using rhodium as the internal standard. For the analysis, 200 μL aliquots were collected from the experimental solution immediately after the addition and mixing of Mn(II) in the solution, filtered through 0.22 μm, and preserved in 2% nitric acid (HNO_3) to determine the initial concentration of Mn(II) added for bio-mineralization. Sample aliquots were also collected from the experimental solutions before and immediately after the addition and mixing of Fe(II) and also after 6 days of Fe(II) oxidation. The samples were filtered through 0.22 μm filters and dissolved in 2% HNO_3 for ICP-MS analysis to determine the initial concentration of Fe(II) added and concentrations of Fe(II) and Mn(II) remaining in the solution after reaction. Concentrations of Mn and Fe in particulates were found by subtracting the concentrations of Mn and Fe remaining in the mineralization media from the concentrations of Mn and Fe initially added.

3.2.3 Mineralogical and Morphological Characterization

i. X-Ray Diffraction (XRD) Analysis

XRD analysis was employed to identify the crystalline mineral phases composing the biogenic precipitates. A portion of the separated biogenic sample was suspended in 3 mL of Milli-Q water. This suspension was then pipetted onto the center of a silicon crystal low-background disk (Appendix, Figure 3-A1), evenly spread over a 10-15 mm circular area ensuring complete coverage, secured in a holder with a spring, and left to air dry overnight. The XRD analysis was performed the next day at the University of Oxford's Department of Earth Sciences using a Panalytical Empyrean Series 2 diffractometer with a cobalt (Co) anode Kα radiation source (Kα1=1.78901 Å and Kα2=1.79290 Å). The diffractometer was set up in a standard reflection geometry using a fixed slit at continuous scanning from 4 to 80º over a total estimated duration of 6.5 h in 2θ position with a spinning holder (4 seconds per revolution) and a step size of 0.026º. Background noise was subtracted by manual fitting to aid the accuracy of XRD peak identification.

ii. Scanning Electron Microscope (SEM) Analysis

SEM imaging was performed to elucidate the morphological features of the produced biogenic Fe-Mn binary oxides using a high-resolution Zeiss Sigma 300 Field Emission Gun Scanning Electron Microscope at the Sir William Dunn School of Pathology, University of Oxford. For SEM analysis, samples were prepared by filtering 2 ml of the homogeneously mixed mineralization medium containing biogenic Fe-Mn binary oxides through a 0.22 μm filter to retain the minerals. The filter was then rinsed with approximately 5 ml of Milli-Q water to remove residual salts and ions. A small section of the filter containing biogenic minerals was affixed to a 13 mm aluminum stub covered with carbon tape. The stub was allowed to air dry overnight before being gold-coated for imaging. For gold coating, the aluminum stub was sputtered under vacuum for 120 seconds with a 15 nm thick gold layer (Quorum Q150R ES, sputter current 20 mA, tooling factor 2.30). Images were acquired by the electron microscope operating in the secondary electron mode with an acceleration voltage of 2 kV and at a working distance of 8−9 mm.

iii. Scanning Transmission Electron Microscopy (STEM) and Scanning Transmission Electron Microscopy-Energy Dispersive X-ray Spectroscopy (STEM-EDX) Analyses

STEM and STEM-EDX analyses of the biogenic Fe-Mn binary oxides were performed at the David Cockayne Centre for Electron Microscopy of the Department of Materials at the University of Oxford. STEM images were acquired with a JEOL ARM200F, equipped with a cold field emission source and Caesium (Cs) probe corrector, and operating at 200 kV. The imaging conditions were set up to acquire high-angle annular dark field (HAADF) and bright field (BF) STEM images simultaneously. STEM-EDX was performed in the same instrument, equipped with a 100 mm^2 Centurion EDX detector. For the analyses, the separated particulate samples were diluted into Milli-Q water and a drop of the suspension (~3 μL) was placed on a 3 mm copper (Cu) TEM grid with formvar support. The grids were allowed to air dry overnight before analysis.

iv. Transmission Electron Microscopy (TEM)-Selected Area Electron Diffraction (SAED) Analyses

TEM-SAED was performed in a JEOL JEM-2100, 200 kV analytical electron microscope equipped with a LaB_6 electron gun in combination with SAED. The SAED patterns were processed using ImageJ software (version 2.9.0/1.53t). Samples for TEM-SAED analysis were prepared in the same way as for STEM analysis (section 2.3.3) but lacey carbon film supported TEM grids were used instead of formvar supported grids.

3.3 Results and Discussion

3.3.1 Biosynthesis of Biogenic Fe-Mn Binary Oxides

Bio-mineralization of Mn oxides by *P. putida* was conducted for 12 days, during which mineral particles formation began as early as the second day. A characteristic blackish-grey mineral deposit appeared at the bottom of the Schott bottles, indicative of the bio-oxidation of Mn(II) to Mn(III) or Mn(IV). The initial concentration of Mn(II) introduced into the mineralization medium was 187.5 μM. After 12-days, the concentration of soluble Mn remaining in the solution was measured at 60.8 (±0.6) μM, indicating that 67.6 % of the added Mn had been bio-oxidized. The formation of Mn oxides was not observed in the abiotic control experiment (Appendix, Figure 3-A2).

Following the 12 days of the Mn(II) bio-mineralization, Fe(II) was added to the solution resulting in a concentration of 210.4 (±0.8) μM. The timing of Fe(II) addition was strategically chosen after the biosynthesis of biogenic Mn oxide particles to prevent any potential toxic effect of Fe(II) on *P. putida* that could have retarded biogenic Mn oxide formation (Tong et al., 2022). The media were furthermore sparged with N_2 gas for 5 minutes before Fe(II) addition to minimize the chemical oxidation of Fe(II) by O_2 and instead maximize Fe(II) oxidation by the biogenic Mn oxides. Biogenic Mn oxides are known to be among the strongest oxidants with high redox reactivity (Fischel et al., 2024; Tebo et al., 2004). Previous research has also provided evidence that at low O_2 concentrations, the chemical oxidation of Fe(II) by O_2 is very slow (Emerson, 2000). It was thus expected that Fe(II) would be primarily oxidized by Mn oxides under these micro-oxic conditions. The Fe(II) oxidation and mineralization process was then continued for an additional 6 days, extending the total experimental period to 18 days (Figure 3.1). In the oxidation process of Fe(II) to Fe(III), biogenic Fe-Mn binary oxides are expected to form, following the reaction below:

$$MnO_2 + 2Fe^{2+} + 2H_2O \rightarrow Mn^{2+} + 2FeOOH + 2H^+ \qquad \textit{Equation 3.1}$$

where MnO_2 represents Mn(III, IV) oxides, such as pyrolusite or birnessite, and FeOOH represents the possible Fe(III) oxyhydroxides, such as ferrihydrite or goethite (exact stoichiometry would thus vary accordingly) (Liu et al., 2022).

After 18 days of mineralization, more than 99% (186.2 (±1.8) µM) of Mn mineralization was achieved. A much higher percentage of Mn bio-oxidation after 18 days compared to 12 days indicated that *P. putida* would have survived in the micro-oxic condition and promoted Mn oxides formation through bio-oxidation or through passive biomineralization. More than 81% (171.6 (±2.3) µM) of Fe(II) was precipitated, making the Fe to Mn ratio in the synthesized biogenic Fe-Mn binary oxides approximately 0.9:1. A micro-oxic environment in the experimental mineralization medium was indicated by the survival of the aerobic bacterium *P. putida* even after N_2 sparging, which supported the continuous bioxidation of Mn(II). The incomplete oxidation of Fe(II) (>80%) by the end of the reaction implies that the solution lacked sufficient amount of O_2 to oxidize Fe(II) completely.

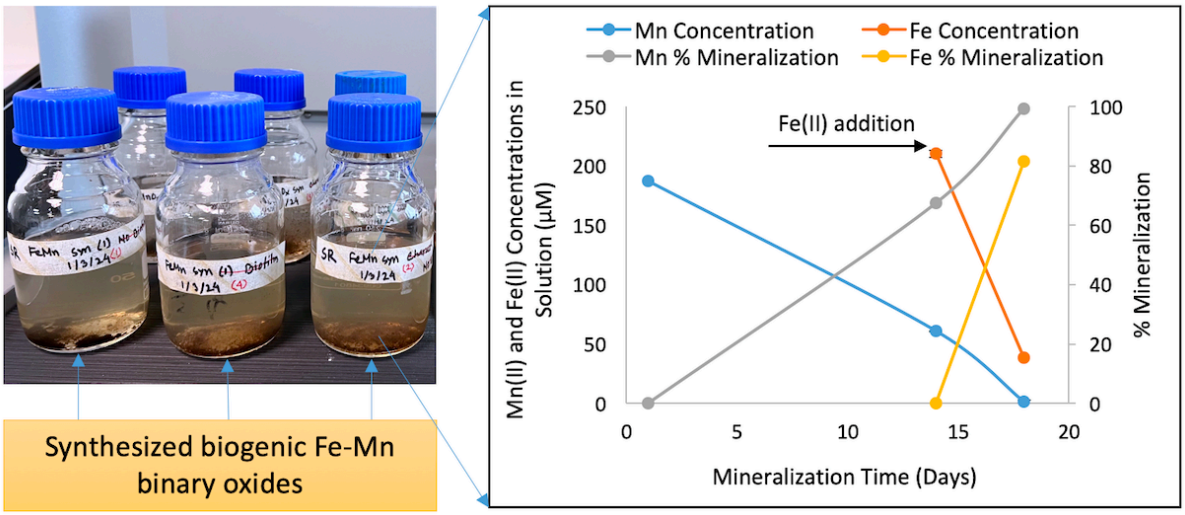


Figure 3.1: Percentages of Mn(II) and Fe(II) mineralization over 18 days. Error bars have been calculated as the standard deviation of the different replicates.

Throughout the mineralization process, the pH of the solution remained relatively stable (Appendix, Table 3-A1). Indeed, after 12 days of Mn(II) mineralization, the pH decreased from 7.4 to 7.3 (±0.2). A slight decrease in the pH might be due to the production of organic acids (e.g., uronic acids) by bacterial cells and EPS (Behbahani et al., 2022). Heterogeneity in pH among different bio-mineralization replicates was also observed, which could be explained by the heterogeneous acid production rates and O_2 consumption by bacterial microcolonies in each replicate (Behbahani et al., 2022). The pH further dropped to 7.15 (±0.2) after the addition of Fe(II) into the mineralization media. This could be due to the release of protons following Fe(II) addition (Equation 3.1), and the formation and degradation of bacterial cells and EPS. However, at the end of the 18 days of mineralization, the pH was found to be 7.2 (±0.2). Since

the changes of pH in all steps were relatively small, no further pH adjustments were performed. On the other hand, in the abiotic controls, the pH remained stable between 7.39 and 7.41 (Appendix, Table 3-A2) since no Fe(II) was added to the solution.

3.3.2 Mineralogical and Morphological Characterization

i. XRD Analysis

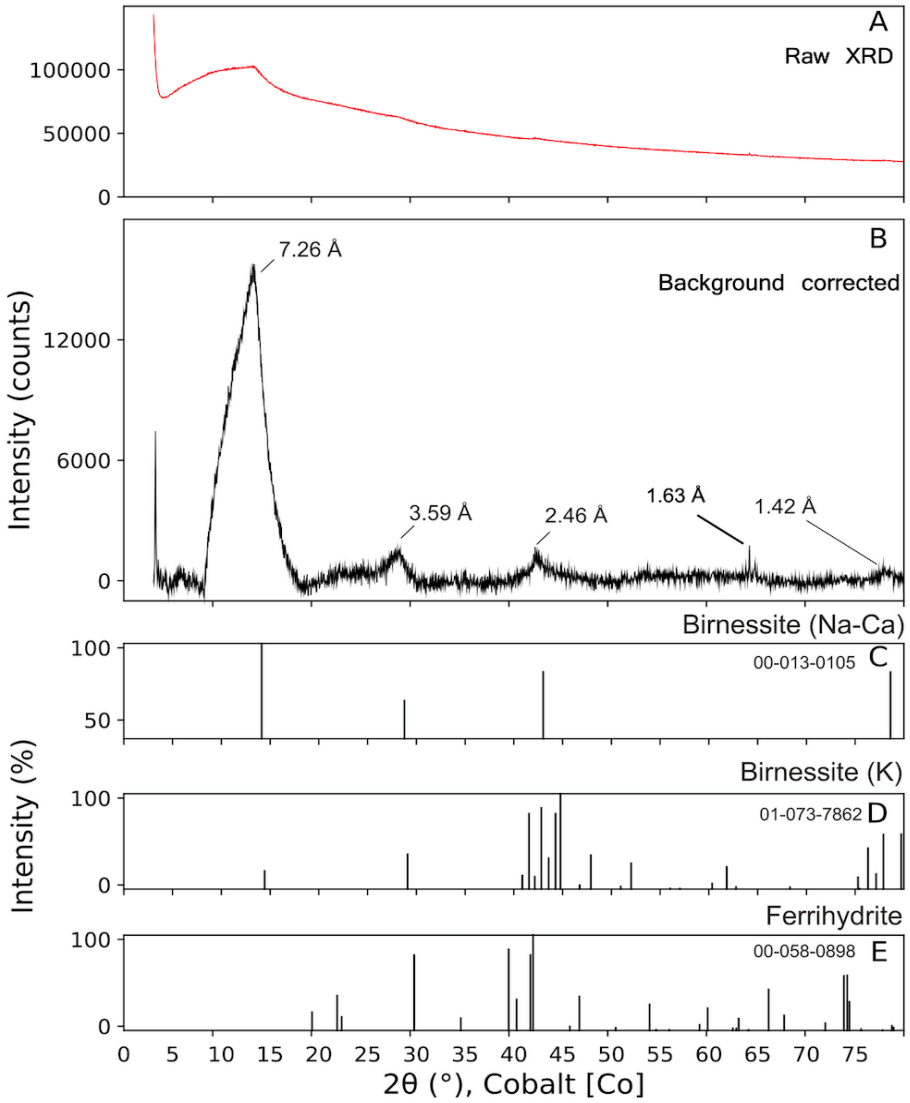


Figure 3.2: (A) Raw XRD pattern of the microbial precipitates collected at 18 days, (B) Background corrected XRD spectrum with corresponding d-spacings, (C) Birnessite reference line spectrum, ICDD 00-013-0105, (D) Birnessite reference line spectrum, ICDD 01-073-7862, and (E) Ferrihydrite reference line spectrum, ICDD 00-058-0898.

The XRD pattern for the biogenic particles collected from the experimental medium after 18 days is shown in Figure 3.2. The lack of well-defined diffraction peaks suggests the biogenic precipitates were either poorly- or nano-crystalline (Post, 1999; Billinge and Levin, 2007) though, the measured data showed a plausible match with several entries from the International Centre for Diffraction Data (ICDD).

The background corrected diffractogram (Figure 3.2B) shows a broad peak at the 14.2° 2θ position (d-spacing 7.26 Å) and weak peaks at the 28.7° 2θ (d-spacing 3.59 Å), 43° 2θ (d-spacing 2.46 Å), and 78.6° 2θ (1.42 Å) positions matching d-spacing of ICDD entries (00-013-0105, Figure 3.2C; 01-073-7862, Figure 3.2D) suggesting the presence of poorly crystalline birnessite, similar to previously published data (Cieschi et al., 2021; Bondar and Alekseev, 2020; Gao et al., 2015). The patterns closely resemble the measurements of poorly ordered birnessite produced using *P. putida* (Villalobos et al., 2003; Galezowski et al., 2020). The XRD diffractogram also shows a reasonable match with the ICDD ferrihydrite patterns (i.e. 00-058-0898; Figure 3.2E) in line with the evidence for poorly crystalline ferrihydrite found by other researchers (Valášková et al., 2022; Schwertmann et al., 1999).

ii. SEM Analysis

SEM imaging provides insights into the morphology and texture of the biogenic precipitates collected on day 18 of the experiment (Figure 3.3a-d). The images in Figure 3.3 indicate that these minerals were complexly interwoven with bacterial cells and EPS.

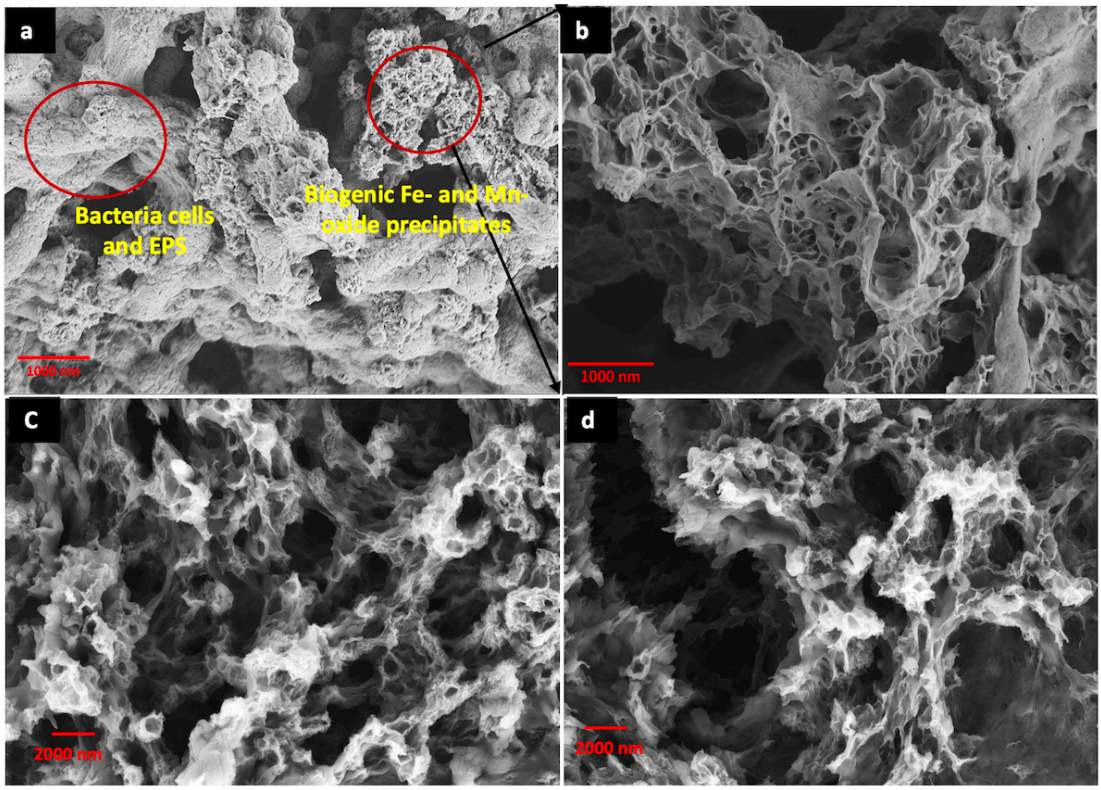


Figure 3.3: SEM images of the biogenic precipitates showing co-localization of bacterial cells, EPS, and mineral particles.

EPS are produced during the growth of bacteria and include polysaccharides, humic acids, proteins, nucleic acids, and lipids (Wingender et al., 1999; Ras et al., 2008; Guibaud et al., 2009; Tebo et al., 2004). The SEM images show that the minerals, mixed with the EPS components, are located extracellularly or on the cell surface.

iii. Elemental Composition and Distribution

STEM-EDX analysis of the biogenic mineral precipitates collected at 18 days revealed a heterogeneous distribution of Fe and Mn within the particles. Elemental mapping across the investigated mineral area of interest indicated that Mn oxides and Fe oxides exist as distinct separate mineral phases (Figure 4 b, c, d), heterogeneously distributed relative to one another

rather than forming a homogeneous mixture (Figure 3.4). Several studies (Zheng et al., 2020; Li et al., 2017; Zheng et al., 2021; Zhang et al., 2014) have demonstrated the synthesis of abiogenic Fe-Mn binary oxides typically resulting in similar elemental distributions. The heterogeneous distribution of Fe and Mn might be caused by the sequential oxidation of Mn(II) and Fe(II) in two separate steps.

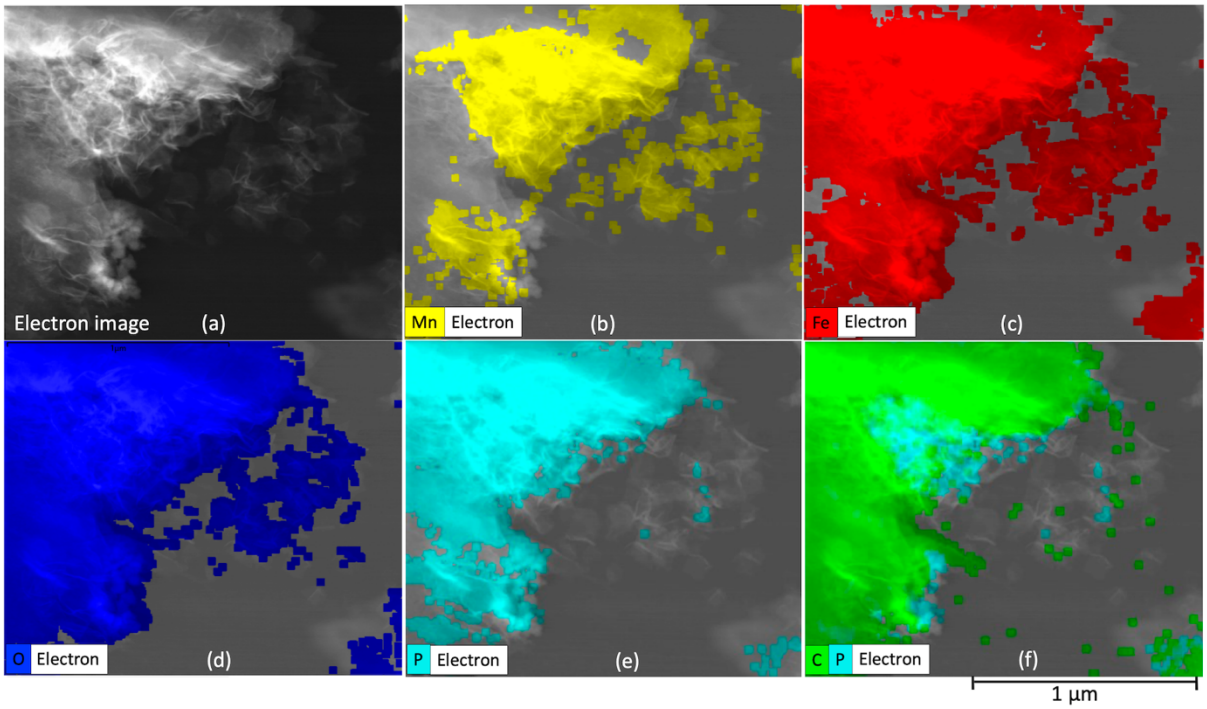


Figure 3.4: (a) HAADF-STEM image of the biogenic Fe-Mn binary oxide, (b) STEM-EDX Mn map, (c) STEM-EDX Fe map, (d) STEM-EDX O map, (e) STEM-EDX P map and (f) STEM-EDX P and C overlaid map in biogenic Fe-Mn binary oxides.

The heterogeneity of Fe and Mn distributions was further investigated by analyzing the elemental compositions of specific areas within the sample (Figure 3.5). For instance, in Figure 3.5, the EDX maps and spectra indicate that the distribution and concentration of Fe and Mn were different in areas 1 and 2, with Spectrum 1 showing mainly Fe-oxide composition, and Spectrum 2 showing both Fe and Mn-oxide compositions.

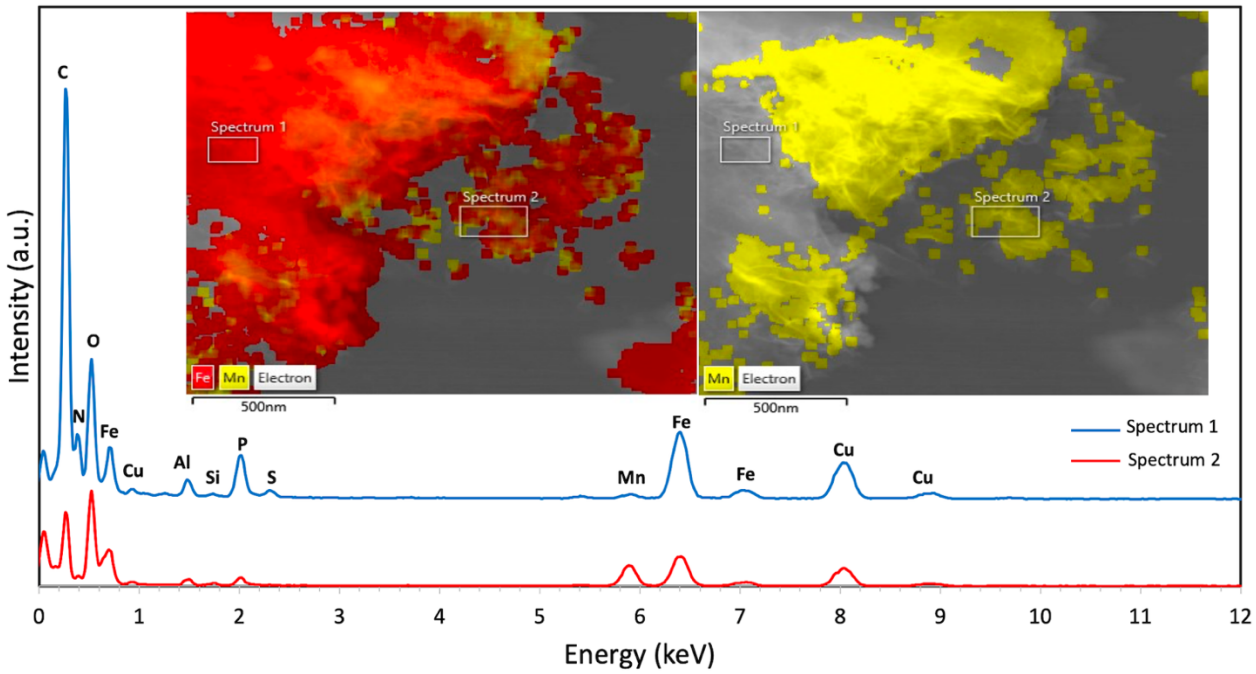


Figure 3.5: STEM-EDX spectra of specific regions of biogenic Fe-Mn binary oxides shown on the overlaid EDX maps of Fe, Mn (spectrum 1, spectrum 2).

The presence of phosphorus (P) associated with the biogenic minerals was observed in the EDX maps and spectra (Figure 3.4e, 3.5). The detected carbon (C) distribution in the EDX maps closely correlated to the P distribution, suggesting that P and C likely originated from the bacterial cells and EPS. Although some of the carbon signal might also come from the formvar coating of the TEM grid itself. In Figure 3.5, EDX spectra show higher P and C signals in area 1 compared to area 2, supporting the claim that the presence of P is mainly associated with organic carbon (bacteria cells and EPS). The co-distribution of P and C was evident in the STEM-EDX P and C overlaid map in Figure 3.4(f). In addition, some of the P signal may be explained by the formation of Mn phosphates, although such phases were not identified in our experiments by XRD.

Indeed, it has been reported that inorganic phosphate may originate from the hydrolysis of cells, increasing concentration in the extracellular environment, which could promote its reaction with Mn adsorbed on the bacterial cell surfaces and the formation of manganese phosphate precipitates close to the cells (Parikh and Chorover, 2005; Galezowski et al., 2020). A similar finding was demonstrated by Galezowski et al. (2020) in biogenic Mn oxides produced by *P. putida*.

The EDX analysis identified other elements such as nitrogen (N), sulfur (S), aluminum (Al), silicon (Si), and negligible amounts of calcium (Ca), and potassium (K), consistent with findings reported by Morales et al. (2024) for biogenic Mn oxides produced by *P. putida*. Miller et al. (2012) also reported the presence of Al, Si, Ca, and P in biogenic Mn oxide. These elements likely originate from borosilicate bottles, and chemicals used for preparation of the experimental media. The Cu signal likely originates from the TEM grid. Additional EDX maps have been provided in Appendix (Figure 3-A3).

iv. STEM and TEM-SAED Analyses

The STEM images provide insights into the relative sizes, crystalline properties, morphology, and phases of the biogenic Fe-Mn binary oxides. While it was difficult to precisely determine the actual size of the particles due to their tendency to form aggregates, the characteristic size observed from the images was less than 100 nm (Figure 3.6A-F) corresponding to the nanoparticle size range.

Bright-field scanning transmission electron microscopy (BF-STEM) was performed to evaluate the morphology and crystalline properties of the biogenic Fe-Mn binary oxides. The BF-STEM image in Figure 3.6(A) shows the presence of rod-shaped *P. putida* cells associated with Fe and Mn oxide particles. The BF-STEM images reveal morphological differences of the binary oxides across the measured area (Figure 3.6B). The biogenic particles tend to exhibit an ultrathin layered morphology with individual layers folded at various angles or stacked atop one another (Figure 3.6C). This characteristic morphology of biogenic Mn oxide has also been documented in previous research (Villalobos et al., 2003; Miller et al., 2012; Galezowski et al., 2020). In addition, the particles exhibit greater morphological diversity. They were found to form chain-like morphology, likely due to the aggregation of the nanoparticles mediated by bacterial cells and EPS, which might have connected individual particles (Figure 3.6D, E). Nanoparticles also formed large aggregates or clusters forming many granular structures (Figure 3.6F). The underlying mechanism responsible for the formation of long chain-like structures and clusters of large aggregates is unclear but the electrostatic interaction or biding of mineral surface with charged functional groups at the surface of the bacteria cell walls and EPS may promote particle aggregation and formation of these diverse morphologies (Fortin and Langley, 2005).

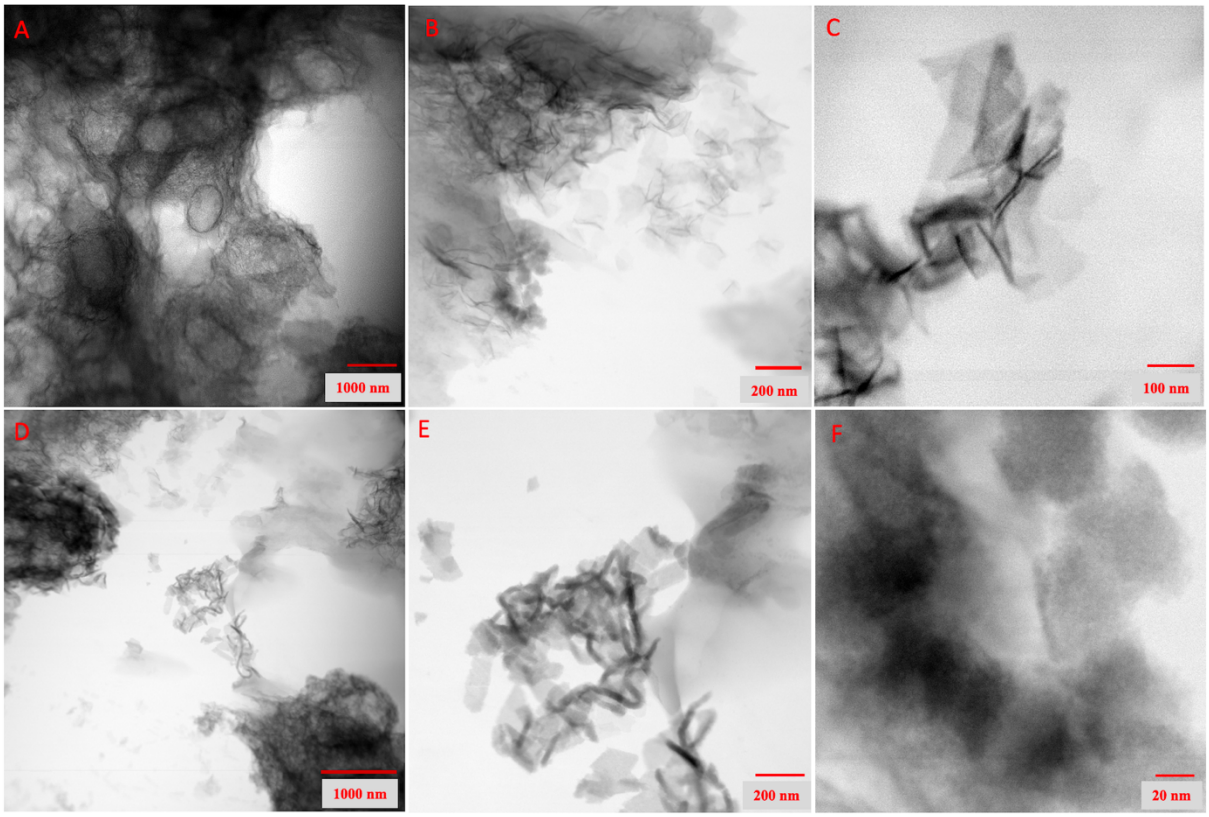


Figure 3.6: (A) BF-STEM image of the biogenic Fe-Mn-binary oxides nanoparticles mixed with bacteria cells, (B) BF-STEM image of the different morphologies of biogenic Fe-Mn binary oxides, (C) BF-STEM image of the ultrathin layered morphology of the particles, (D-E) BF-STEM image of the chain-like particle aggregates, (F) BF-STEM image of the large granular particle cluster.

High-resolution STEM imaging failed to reveal consistent lattice fringes in the biogenic Fe-Mn binary oxides. This could be due to the highly disordered structure of the minerals. Moreover, the presence of organic matter may have obscured the particle surface or scattered electrons, reducing the contrast and clarity of lattice fringes. Also, Galezowski et al. (2020) found that radiation damage during imaging can lead to Mn(III)/Mn(IV) reduction to Mn(II) species. Toner et al. (2005) have found that organic matter associated with biogenic Mn oxides can generate free-radical species when exposed to radiation beams, leading to the photo-reduction of Mn(IV) /Mn(III). The high electron acceleration voltage used for STEM in this study might therefore have contributed to the radiation-induced damage of the mineral phases causing difficulty in clearly observing crystal lattice fringes.

Additionally, biogenic minerals have been reported to display lattice distortions compared to their synthetic or naturally occurring abiogenic counterparts (Deng et al., 2022).

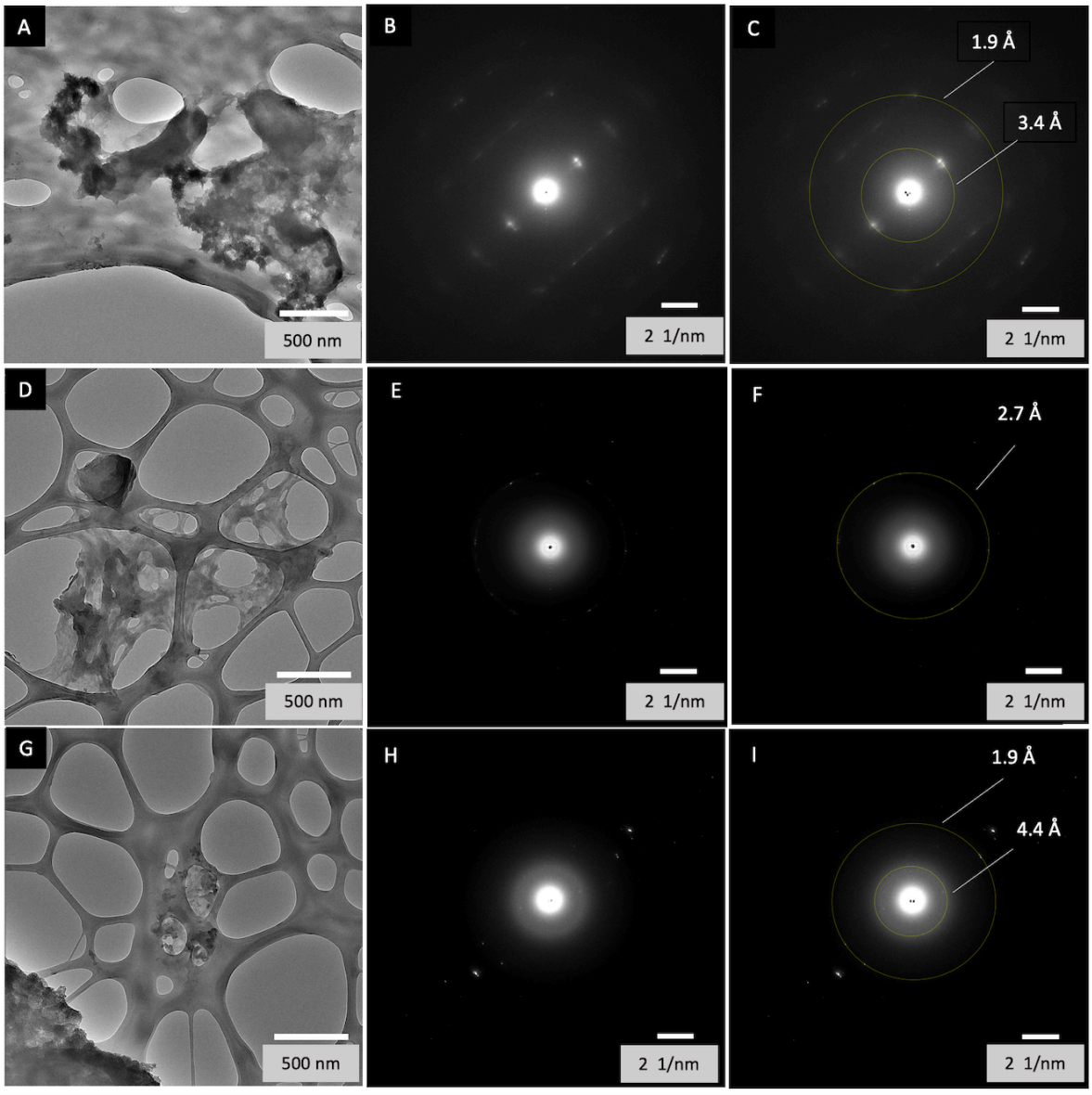


Figure 3.7: TEM images of the different areas (A, D, G) of the biogenic Fe-Mn binary oxides sample, with corresponding SAED diffraction patterns (B, E, H) and measured d-spacing (C, F, I).

Nonetheless, the TEM-SAED analysis provided valuable evidence regarding the crystalline properties of these biogenic minerals. As shown in Figure 3.7, TEM images and corresponding SAED diffraction patterns of the biogenic Fe-Mn binary oxides display variations across different measured areas. The SAED diffraction pattern in Figure 3.7 (B, C) of a specific region (Figure 3.7A) exhibits an amorphous halo alongside several weak diffraction speckles (Figure

3.7B). These speckles suggest the presence of nano-sized polycrystals sharing a common orientation within the measured area. Another SAED diffraction pattern (Figure 3.7E, F) from a different region (Figure 3.7D) shows an amorphous halo with a very weak diffraction ring (Figure 3.7E) indicating randomly oriented polycrystals. SAED diffraction pattern in Figure 3.7 (H, I) of another measured area of the sample (Figure 3.7G) also exhibits several diffraction speckles indicative of the nano-sized crystals. The diffraction speckles and all the d-spacing values (3.4 Å, 4.4 Å, 2.7 Å, and 1.9 Å) in the SAED diffraction patterns from the different sample areas closely resemble nano-sized birnessite and ferrihydrite polycrystals (Lee and Xu, 2019; Arias et al., 2019; Powell et al., 2014), consistent with the XRD results. The presence of amorphous halos in all the SAED diffraction patterns is believed to originate from the organic carbon (bacterial cells and EPS) present in the samples (Shi et al., 2024; Galezowski et al., 2020).

3.4 Environmental Implications of Biogenic Fe-Mn Binary Oxides Nanoparticles

Biogenic Fe and Mn oxides are commonly found across various environmental systems (Glodowska et al., 2021; Estes et al., 2017; Tebo et al., 2004; Villalobos et al., 2003; Sowers et al., 2017). In natural aquatic environments, mixtures of Fe and Mn oxides often arise through various mechanisms depending on the redox environment (see below). Fe- and Mn-rich sediment layers at oxic-anoxic interfaces have been found in various environments ranging from groundwater aquifers to marine environments. For instance, a few hundred microns of Fe- and Mn-rich laminae have been reported by Bábek et al. (2023) in a groundwater aquifer and are believed to be partly microbial in origin. Globally, Mn- and Fe-enriched layers have been discovered in both shallow and deep marine water environments and freshwater sediments in aerobic conditions as well as at oxic-anoxic interface (Tazaki, 2000; Palermo and Dittrich, 2016).

Mn(II) bio-oxidation followed by abiotic Fe(II) oxidation, as described below, might represent a potential pathway for forming biogenic Fe-Mn binary oxide precipitates at the oxic-anoxic interface in natural aquatic environments. In redox-stratified aquatic environments such as in stratified lakes, the cycling of Fe and Mn largely depends on the presence of O_2 (Rincón-Tomás et al., 2016) and the formation of Fe and Mn oxides arise through several pathways based on the redox environment (Nelson et al., 2002). Simplified putative pathways of Fe and Mn cycling, and biogenic Fe-Mn binary oxides formation at the oxic-anoxic interface of a redox

stratified lake have been shown in Figure 3.8. In the O_2-rich upper layer of the oxic-anoxic interface, Fe(II) can be easily oxidized by O_2 abiotically (1). Biotic oxidation of Fe(II) by microaerophilic Fe(II)-oxidizing bacteria can outcompete abiotic oxidation at low O_2 concentrations in redox boundary forming biogenic Fe(III) oxides (Emerson et al., 2010) (2). Though the abiotic oxidation of Mn(II) by O_2 is kinetically limited (3), microbial Mn oxidation by Mn-oxidizing bacteria (e.g., *P. putida*) and fungi, and the formation of biogenic Mn(III,IV) oxides is known to be predominant (4) (Madison et al. 2013; Tebo et al. 2004).

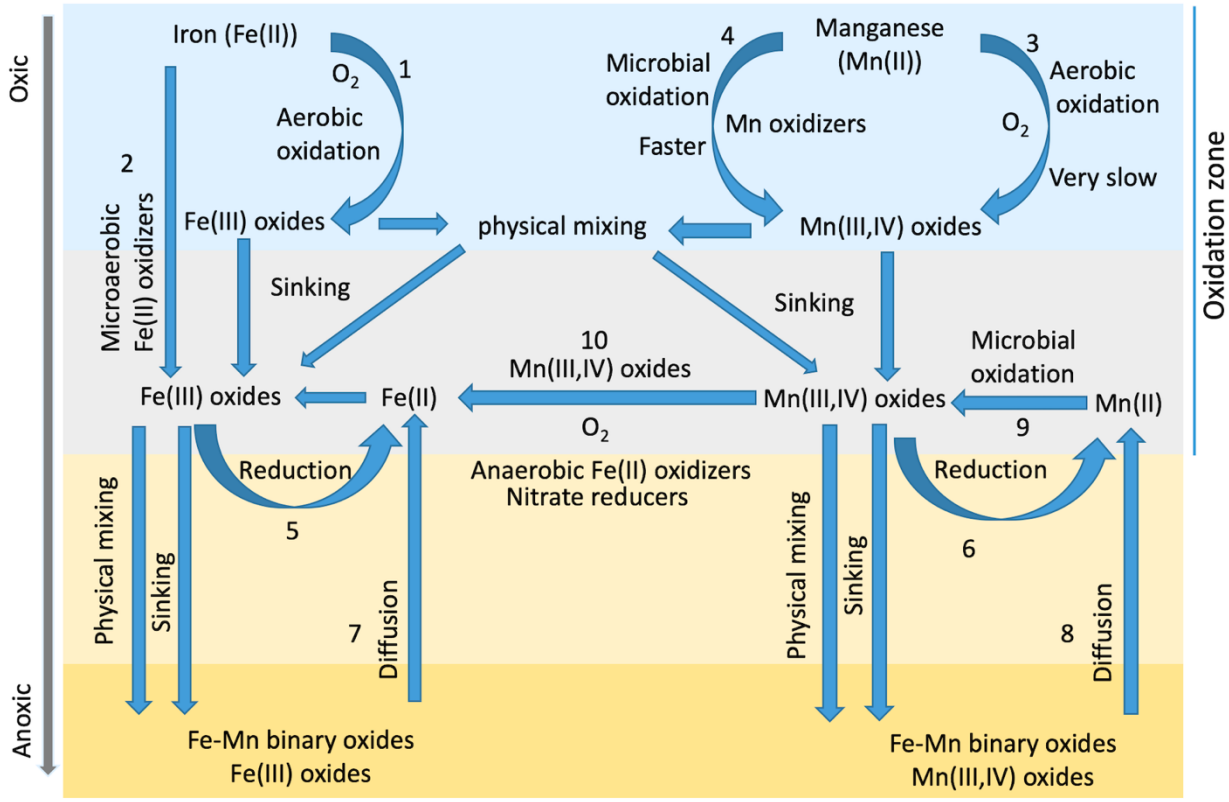


Figure 3.8: Putative pathways of biogenic Fe-Mn binary oxides formation at the oxic-anoxic interface of a redox-stratified lake, as informed by the experimental results herein.

Microbial Mn(II) oxidation at oxic-anoxic interfaces has been evidenced by many researchers (Oldham et al., 2017; Jones et al., 2018; Clement et al., 2009) in natural environments. These Fe and Mn oxides can physically mix to form biogenic Fe-Mn binary oxides. The formation of binary oxides is dependent on the relative concentrations of Fe(II) and Mn(II), along with the presence of Fe and Mn-oxidizing microorganisms within the redox gradient (Nelson et al., 2002). Fe oxides surfaces can be coated with Mn-oxidizing microbes and then subsequently with biogenic Mn oxides, or microbial extracellular Mn oxide surfaces can be coated with Fe

oxides to form biogenic Fe-Mn binary oxides (Nelson et al., 2002). These Fe and Mn oxides and biogenic Fe-Mn binary oxides sink to the oxygen-deficient (micro-oxic) lower water column where Fe and Mn oxides can be reduced to Fe(II) and Mn(II) through microbial or chemical Fe and Mn reduction (5, 6). Additionally, Fe(II) and Mn(II) can be diffused back to the upper micro-oxic or oxic water columns from the deeper anoxic water columns or sediments containing Fe(III) oxides and Mn(III,IV) oxides, which are reduced in the reducing conditions (7, 8). Mn(II) diffusing back to the micro-oxic water column can be oxidized again by Mn(II)-oxidizers and form Mn(III,IV) oxides (9). In this water column, biogenic Mn(III,IV) oxides can facilitate Fe(II) oxidation, leading to the formation of Fe(III) oxides (10). However, the biogenic Mn oxide might not be the sole oxidizer of Fe(II), but there might be competition between Mn oxide, nitrite, O_2 (very low concentration), and anaerobic Fe(II)-oxidizing phototrophic and nitrate-reducing bacteria to facilitate the oxidation process (10) (Kappler and Straub, 2005; Kappler and Newman, 2004; Straub et al., 2004; Hafenbradl et al. 1996; Myers and Nealson, 1988).

Overall, depending on environmental conditions such as the steepness of the redox gradient, we may have two distinct situations: (i) either Fe(II) oxidation and Mn(II) bio-oxidation occur separately and the distinctly formed Fe(III) and Mn(III,IV) minerals physically mix during sedimentation processes, (ii) or Mn oxides form first, oxidize Fe(II), and form finely intermixed phase of biogenic Fe-Mn binary oxides, similar to what is observed in our experiments. In the proposed second pathway, Fe and Mn oxidation, and the formation of biogenic binary oxides mostly occur in the oxic to micro-oxic zone of the redox stratified water column. The present study highlights one of the possible pathways of the natural biogeochemical cycling of Fe and Mn at the oxic-anoxic interface of a redox stratified water column under specific conditions (e.g., pH, Fe: Mn ratio, microbial strain, temperature, etc.), and provides a better understanding of the mechanisms of Fe-Mn binary oxide formation in the environment.

Previous studies have also reported the formation of biogenic Fe-Mn binary oxides which follow very different pathways from this proposed pathway of biogenic Fe-Mn binary oxides formation. For instance, Bai et al. (2016) investigated the formation of biogenic Fe-Mn binary oxides produced through aerobic Fe(II) oxidation and biotic Mn(II) oxidation by *Pseudomonas* sp. QJX- 1. Produced Fe and Mn phases were identified as lepidocrocite and birnessite respectively. Yang et al. (2023) also reported biogenic Fe-Mn binary oxides formation through aerobic Fe(II) oxidation and Mn(II) bio-oxidation. Both studies found amorphous structure of the minerals, but the formation pathways mostly applied for the oxic environment.

In past studies, several researchers have investigated and demonstrated a wide range of applications of similar mineral phases. For instance, biogenic Fe-Mn binary oxide nanoparticles are widely known to effectively remove and adsorb a wide variety of heavy metals from water and wastewater (Tebo et al., 2004; Cieschi et al., 2021). Biogenic Mn oxides are known for their superior oxidative activity and enhanced adsorption capacities compared to their abiogenic counterparts (Liu et al., 2009; Post, 1999; Manceau et al., 2007). Mn oxide is among the strongest natural oxidizing agents and the presence of organic matter associated with biogenic Mn oxide has been reported to play a significant role in improving its reactivity. The organic material in biogenic minerals not only contributes to their structural complexity, for instance, disorder and small-scale porosity, but also facilitates higher surface area and provides more active sites for redox reactions and adsorption processes (Feng et al., 2010; Tebo et al., 2004). As a result, biogenic Mn oxide has been considered a more effective candidate for various environmental applications compared to its abiogenic form (Nelson et al., 2002). Similarly, biogenic Fe oxides are reported to be more reactive than abiogenic counterparts, with larger surface area, lower degree of crystallinity, and smaller particle sizes (Xu et al., 2022; Posth et al., 2010; Miot et al., 2009; Roden, 2004). The binary phase of biogenic Fe and Mn oxides is also known as highly disordered, poorly crystalline reactive material (Bai et al., 2016).

Along with the implications in natural environmental systems, synthesized biogenic Fe-Mn binary oxides presented in this study could be a cost-effective foundation for environmental contamination remediation strategies, and for developing various metal removal and recovery technologies. They might hold significant potential for use in low-cost, low-maintenance household water filtration systems and for scaling up to pilot-scale applications. For example, similar phases were found to be effective for the simultaneous removal of As, Fe, and Mn from

contaminated water (Bai et al., 2016). Kleinert et al. (2011) reported the formation of biogenic Fe-Mn binary oxides and the adsorption of As in water filtration systems at the household level. This study advances the understanding of a potential mechanism for biogenic Fe-Mn binary oxides formation in the natural aquatic environments which could be considered for large-scale applications in heavy metals-contaminated redox-stratified environments (e.g., groundwater aquifers, tailings ponds) with high Fe and Mn concentrations by controlling specific biogeochemical factors.

3.5 Conclusions

The study proposed one of the pathways for forming biogenic Fe-Mn binary oxides at the oxic-anoxic interface of the water column, a process mediated by *P. putida*. A suite of analytical approaches, including XRD, SEM, STEM, STEM-EDX, and TEM-SAED, was implemented to provide comprehensive insights into the mineralogical properties, morphological characteristics, and microbial associations of the biogenic minerals. XRD analysis identified the biogenic Fe-Mn binary oxides as poorly crystalline birnessite and ferrihydrite nanocrystals. SEM revealed the co-existence of bacterial cells and EPS (organic carbon) with the biogenic Fe-Mn binary oxides and the extracellular deposition of the minerals. STEM-EDX mapping showed a heterogeneous distribution of Fe and Mn, while STEM demonstrated morphological diversity, such as granular, long-chain, and ultrathin plate-like folded mineral structures. TEM-SAED further confirmed the presence of nano-sized, poorly crystalline birnessite and ferrihydrite, with amorphous halos originating from organic carbon (bacterial cells and EPS). These features suggest that these phases could act as highly efficient adsorbents and redox-active materials, making them promising minerals for controlling the geochemical cycling of various contaminants and nutrients in aquatic environments.This study contributes to expanding the understanding of biogenic Fe-Mn binary oxides formation at the oxic-anoxic interface of the water column, while also providing a better understanding of microbially driven Fe and Mn biogeochemistry in such environments. Additionally, the research lays the foundation for future studies into the environmental applications of biogenic Fe-Mn binary oxides by providing detailed characterization of these phases.

4 Chapter Four: Unfolding the Role of *Pseudomonas putida* Biofilm in Arsenic(V) Adsorption-Desorption Dynamics on Iron-Manganese Binary Oxides

Abstract

Biogenic and abiogenic Fe-Mn binary oxides are well-known for their As(V) adsorption efficiencies. Previous studies have focused on the As(V) adsorption and desorption dynamics of biogenic and abiogenic Fe-Mn binary oxides but failed to consider the passive role of organic materials (e.g., bacterial cells and EPS) that are generally associated with biogenic minerals. This research reveals the role of biofilms of *Pseudomonas putida* (*P. putida*) in As(V) adsorption and desorption dynamics onto and from biogenic and abiogenic Fe-Mn binary oxides for the first time. As(V) adsorption experiments were conducted using mineral-free *P. putida* biofilm, biogenic Fe-Mn binary oxides, abiogenic Fe-Mn binary oxides and abiogenic Fe-Mn binary oxides mixed with biofilm as adsorbents. All the adsorbent systems fitted well with PFO kinetic model except mineral-free biofilm, and all showed good conformity with PSO kinetic model, indicating that As(V) adsorption on biogenic and abiogenic Fe-Mn binary oxides might have been mostly dominated by chemisorption and partly by physisorption mechanisms. Mineral-free biofilm demonstrated lower As(V) adsorption capacity at equilibrium than that of biogenic and abiogenic Fe-Mn binary oxides. Biogenic Fe-Mn binary oxides demonstrated ~45% smaller adsorption capacity compared with abiogenic Fe-Mn binary oxides at equilibrium. Weak As(V) adsorption on the biofilm might have resulted due to the presence of fewer positively charged and mostly negatively charged functional groups in biofilm. The electrostatic repulsions between negatively charged As(V) species and negatively charged functional groups in biofilm restricted higher adsorption. Weaker As(V) adsorption onto biogenic Fe-Mn binary oxides compared with abiogenic Fe-Mn binary oxides may result from several factors. Electrostatic repulsions of biogenic minerals to As(V) caused by closely associated organic matter in biogenic minerals, coverage of the effective binding sites on mineral surface by the bacterial cells, EPS and negatively charged functional groups, and the presence of a significant amount of phosphate in the biogenic oxides are important factors contributing less As(V) by biogenic minerals. As(V) diffusion into biofilm likely plays an important role in kinetically controlling As(V) adsorption onto biogenic minerals. The As(V) desorption mechanism was investigated for the As(V)-adsorbed biogenic and abiogenic Fe-Mn binary oxides by perturbing equilibrium through multiple desorption cycles.

Experimental data indicated that most of As(V) were irreversibly bound onto the both mineral surfaces, possibly through chemisorption. A small fraction of surface adsorbed As(V) might be desorbed that were weakly bound by physisorption. The desorption result implies that Fe-Mn binary oxides-sorbed As(V) would not be released easily even if they are in the less diluted solution. This research sheds light on the role of biofilms of *P. putida* in As(V) adsorption and desorption dynamics on and from biogenic and abiogenic Fe-Mn binary oxides which deepens the understanding of environmental As(V) mobility.

Keywords: Biogenic Fe-Mn binary oxides, abiogenic Fe-Mn binary oxides, Biofilm, Arsenic Adsorption Desorption, *Pseudomonas putida* MnB1.

4.1 Introduction

Arsenic (As) is a ubiquitously present metalloid in the environment (Lv et al., 2024; Prieto et al., 2013) and is widely studied due to its public health concern (Xie et al., 2018; Muehe et al., 2016; Guo et al., 2008). Inorganic As in natural water mainly exists either as arsenate (As(V)) or arsenite (As(III)). Arsenate is a thermodynamically stable form that predominates in oxic water and tends to exhibit higher adsorption affinity onto minerals. Arsenite is more toxic and mobile than As(V) and is the dominant species in reducing and low pH environments (He et al., 2019; Anderson and Bruland, 1991; Hao et al., 2018; Lv et al., 2024; Genç-Fuhrman et al., 2004). Anionic arsenate species ($H_2AsO_4^-$ and $HAsO_4^{2-}$) and neutral arsenite ($As(OH)_3^0$) are the primary aqueous species in natural water at neutral pH (Anderson and Bruland, 1991). Understanding As adsorption-desorption dynamics is vital to predict As transport, transformation and bioavailability, and to control contamination in the environment.

Recently, iron-manganese (Fe-Mn) binary oxides have attracted much attention for As adsorption due to their adsorption capacity (Zhao et al., 2022; Zheng et al., 2020; Zhang et al., 2014; Bai et al., 2016). They have been reported as more effective in adsorbing arsenic than Fe oxides or Mn oxides alone (Zhang et al., 2014), playing a significant role in governing As(V) adsorption-desorption dynamics in natural water (Zhao et al., 2022). In the environment, Fe and Mn frequently co-exist (Bai et al., 2016; McCann et al., 2018). Dissolved Fe(II) undergoes chemical oxidation to form Fe oxyhydroxides (Borch et al., 2010) and Mn(II) forms Mn oxides primarily through bio-oxidation (Yu and Leadbetter, 2020; Learman et al., 2011). These Fe oxyhydroxides and Mn oxides can co-precipitate to form Fe-Mn binary oxides (Bai et al., 2016). However, many Fe and Mn phases do not form through direct precipitation of aqueous species from solution but are formed as secondary phases during incongruent weathering. Moreover, formation of biogenic Fe and Mn oxides is common and associated with biofilm (Larasati et al., 2024; Li et al., 2016; Toner et al., 2005) in the environment.

Biofilm is widely distributed in natural aquatic systems, rivers and streams, as well as in water distribution systems, and consists of various microorganisms (Donlan, 2002; Mahto et al., 2022) within a hydrated matrix of extracellular polymeric substances (EPS) that they produce (Flemming and Wingender, 2010). EPS are composed of polysaccharides, proteins, extracellular DNA, uronic acids, and lipids (Flemming and Wingender, 2010; Flemming et al., 2000; Donlan, 2002; Branda et al., 2005; Vázquez-Sánchez and Rodríguez-López, 2018;

Mahto et al., 2022). Biofilm is a highly complex and dynamic system, heterogeneous in time and space (Flemming and Wingender, 2010; Donlan, 2002). In natural water at neutral pH, they are negatively charged (Kurniawan and Fukuda, 2023; Alhariri et al., 2017; Jansen and Kohnen, 1995) and can bind a wide variety of contaminants and nutrients due to the presence of active binding sites (Fathollahi and Coupe, 2021; Mahto et al., 2022). On the other hand, some microorganisms in biofilms have metal oxidizing or reducing properties which affect the formation or degradation of the many minerals, thereby affecting the biofilms' adsorption capacities for these elements. *Pseudomonas putida* (*P. putida*) is an example of a gram-negative bacterium, widely distributed in the environment and known to form biofilms (Zheng et al., 2018). *P. putida* cells can oxidize Mn(II) to form biogenic Mn(III,IV) oxides, which can adsorb a wide variety of metals (Zhou et al., 2015).

Biofilm has also been reported to remove As from water due to the activity of As(III)-oxidizing bacteria (*Burkholderiaceae*, *Comamonadaceae*, *Rhodobacteraceae*, *Xanthomonadaceae*) (Chen et al., 2023; Crognale et al., 2019; Battaglia-Brunet et al., 2002). However, these studies focused on the metabolic activity of the bacterial cells rather than the passive effect of the EPS and cell materials on adsorption by minerals such as Fe-Mn binary oxides. Previous studies have also investigated the effect of pH, ionic strength, competing ions, salinity, organic matter, concentration of As, the presence of oxidizing or reducing microbes, reductive dissolution or microbially mediated reductive dissolution of As-bearing minerals, and many other factors that influence As adsorption-desorption dynamics on Fe-Mn binary oxides and Fe oxyhydroxides minerals (Shipley et al., 2009; Mamindy-Pajany et al., 2011; Liu et al., 2001; Antelo et al., 2005; Payne and Abdel-Fattah, 2005; Gupta and Chen , 1978; Jackson and Miller, 2000; Tufano and Fendorf, 2008; Pedersen et al., 2006; Campbell et al., 2006; Kocar et al., 2006; Langner and Inskeep, 2000; Bauer and Blodau, 2006). Though the As(V) adsorption properties of Fe-Mn binary oxides have been well investigated, there has been no study focusing on As(V) adsorption and desorption dynamics on and from these minerals when they occur within biofilms, as they are often found in the environment. This research works with a model organism, *P. putida,* that produces biogenic Fe-Mn binary oxides. These biominerals occur within a biofilm, which might have impacts on As(V) adsorption-desorption mechanisms. In this research a series of experiments has been designed to test the respective roles of Fe-Mn binary oxides minerals and biofilm in the As(V) adsorption-desorption dynamics.

4.2 Materials and Methods

4.2.1 Synthesis of the Abiogenic and Biogenic Fe-Mn Binary Oxides, and Biofilm Growth

Abiogenic Fe-Mn binary oxides were synthesized according to the methods outlined by Zhang et al. (2007a; 2007b) and Zhao et al. (2022). Briefly, 1.9 g potassium permanganate ($KMnO_4$) was dissolved in 400 mL Milli-Q water. Then, 10 g ferrous sulfate heptahydrate ($FeSO_4.7H_2O$) was added to 400 mL Milli-Q water. The $FeSO_4.7H_2O$ solution was added slowly into the $KMnO_4$ solution while stirring with a magnetic stirrer. The pH of the mixed solution was adjusted to 7.00 by adding 5M NaOH solution. The mixed solution was kept stirring for 1 h and then aged for another 12 h. The Fe-Mn oxide precipitates produced were concentrated by centrifugation at 5000 rpm for 5 mins and washed with Milli-Q water until to solution resistivity became 20 MΩ.cm. The precipitates were dried at 105° C for 4 h and then kept at 30° C overnight. Finally, the abiogenic Fe-Mn binary oxide precipitates were ground and preserved at room temperature for further use.

Biogenic Fe-Mn binary oxides were prepared in a three-step procedure. First, *P. putida* strain MnB1 (ATCC 23483) was cultured in a nutrient broth (Sigma-Aldrich) medium, composed of 3 g/L beef extract, 5 g/L peptone, and 50 μM $MnSO_4.H_2O$. Cells were cultured overnight at 30° C on a horizontal shaker at 120 rpm. Cells were centrifuged at 5000 rpm for 5 mins and washed with 10 mM HEPES and 10 mM NaCl to separate cells from the culture medium. In the second step, 2.3 x 10^8 cells/mL were added to the 150 mL mineralization medium composed of 10 mM HEPES, 2 mM $(NH_4)_2SO_4$, 0.7 mM NaCl, and 1 mM glucose at pH 7.4. After inoculation, $MnSO_4.H_2O$ solution was added to the mineralization media at a final concentration of 180 μM, and mineralization of Mn(II) was allowed to proceed for 12 days at 30° C, while shaking at 120 rpm to produce biogenic Mn oxides. After that period, the solution was purged with N_2 gas for 5 minutes and Fe(II) ($FeSO_4.7H_2O$) was added at a final concentration of 200 μM, and mineralization was continued for 6 days at the same temperature and rate of agitation. The produced biogenic Fe-Mn binary oxide precipitates were collected by centrifugation at 8000 rpm for 10 minutes, washed with milli-Q water five times and dried at 30°C for 48 hours, ground and preserved for further analyses.

Synthesis of a mineral-free biofilm of *P. putida* strain MnB1 followed a two-step procedure. In the first step, *P. putida* was cultured and then washed following the same culture protocol as above. In the second step, 2.3 x 10^8 cells/mL were added to the 150 mL mineralization media with a composition identical to mentioned above, but without addition of Mn(II) or Fe(II). The cells were then grown for 7 days while shaking at 120 rpm at 30° C. Biofilm pellets were collected by centrifuging at 6000 rpm for 5 minutes and washed with 10 mM HEPES and 10 mM NaCl for further analysis. *P. putida* biofilms were grown in mineralization media instead of nutrient broth to provide bacteria with a similar chemical environment to that in the biogenic Fe-Mn oxides synthesis experiment, so that similar mass production of cells in biogenic binary oxides and in biofilm could be expected. Images of biofilms in mineralization media have been provided in Appendix (Figure 4-A5).

4.2.2 Characterization of the Abiogenic and Biogenic Fe-Mn Binary Oxides

i. X-Ray Diffraction (XRD) analysis

XRD was performed to identify the crystalline mineral phases composing the biogenic and abiogenic Fe-Mn binary oxides. The finely ground solid abiogenic sample was loaded onto a silicon crystal low background disk covering a 10-15 mm circular area. For the biogenic sample, a portion of the liquid sample was suspended in 3 mL of Milli-Q water. The sample was then loaded and spread over a 10-15 mm circular area of a silicon crystal low background disk and air-dried overnight. The XRD analysis was performed using a Panalytical Empyrean Series 2 diffractometer with a cobalt (Co) anode Kα radiation source (Kα1=1.78901 Å and Kα2=1.79290 Å) scanning from 4 to 80º in 2θ position and a step size of 0.026º. Background noise was subtracted by manual fitting to aid the accuracy of XRD peak identification.

ii. Scanning Electron Microscope (SEM) and Scanning Electron Microscopy-Energy Dispersive X-ray Spectroscopy (SEM-EDX)

SEM imaging was performed to characterize the morphologies of the biogenic and abiogenic Fe-Mn binary oxides. A high-resolution Zeiss Sigma 300 Field Emission Gun Scanning Electron Microscope was used, operating in the secondary electron mode with an acceleration voltage of 2 kV and at a working distance of 8−9 mm. Biogenic samples were prepared by filtering 2 ml of the homogeneously mixed mineralization medium containing biogenic Fe-Mn binary oxides through a 0.22 μm filter to retain the minerals. The filter was then rinsed with

approximately 5 ml of Milli-Q water to remove residual salts and ions. A small section of the filter supporting biogenic minerals was affixed to a 13 mm aluminum stub covered with carbon tape. The stub was allowed to air dry overnight before being gold-coated for imaging. Abiogenic samples were prepared by stacking finely ground Fe-Mn binary oxides on 13mm aluminum stubs covered with carbon tape. Samples were gold coated for 120 seconds with a 15 nm thick gold layer using Quorum Q150R ES. SEM-EDX analysis of the abiogenic Fe-Mn binary oxides was performed to know the elemental composition and distribution using Zeiss Sigma 300 Field Emission Gun Scanning Electron Microscope (FEG-SEM) equipped with an Electron Dispersive X-ray Spectroscopy (EDX) detector. For EDX analyses, with the acceleration voltage set to 15 keV and the working distance set to 5.4 mm.

iii. Scanning Transmission Electron Microscopy (STEM) and Scanning Transmission Electron Microscopy-Energy Dispersive X-ray Spectroscopy (STEM-EDX)

For STEM analysis, particulate biogenic samples were suspended in Milli-Q water, and a drop of the suspension (~3 µL) was placed on a 3 mm copper (Cu) TEM grid with formvar support. The grids were allowed to air dry overnight before analysis. A JEOL ARM200F (Scanning) Transmission Electron Microscope (STEM), was used to observe the morphology of biogenic samples; it was equipped with a cold field emission source and Caesium probe corrector. The equipment was operated at 200 kV and set up to acquire bright field (BF) and high-angle annular dark field (HAADF) STEM images at the same time. STEM-EDX analysis was performed to determine the elemental compositions and distribution of the biogenic Fe-Mn binary oxides, using a 100 mm^2 Centurion EDX detector.

4.2.3 Organic Content in Biofilm and Biogenic Fe-Mn Binary Oxides

i. Fluorescence Microscopy

Fluorescence imaging was performed to visualize the distribution of DNA and carbohydrates associated with the biogenic Fe-Mn binary oxides formed by *P. putida*, as proxies for the presence of bacteria cells and EPS, respectively. For this, 1 mL aliquot of sample was collected from the homogeneously mixed mineralization medium containing biogenic Fe-Mn binary oxides. This sample was then centrifuged at 6000 rpm for 5 minutes, and the supernatant was decanted, while the separated pellet was collected for subsequent imaging. Fluorescence imaging was conducted using an Olympus Fluoview FV1000 confocal microscope with a UPlanSApo lens (60x/1.35NA Oil Objective).

The imaging was performed on the sample pellet suspended and stained with 3 µg/mL of 4',6-diamidino-2-phenylindole (DAPI) and Alexa Fluor 488 (lectin) fluorophores. DAPI was used to visualize DNA and was excited with a 405 nm laser line, while the lectin, which labels carbohydrates, was excited with a 488 nm laser line. Mineral-free *P. putida* biofilm samples were also analyzed following the same protocol. 3D fluorescence images were captured using Olympus Fluoview software (version 4.2).

ii. DNA and Polysaccharide Quantification: Nanodrop and Phenol-Sulfuric Acid Methods

DNA and carbohydrates in the mineral-free biofilm and biogenic Fe-Mn binary oxide samples were quantified using nanodrop and phenol-sulfuric acid methods, respectively. DNA quantification used as a proxy for estimating bacterial cells in both the biofilm and biogenic minerals. To determine the DNA concentrations, DNA samples were extracted following the DNeasy PowerWater Kit (cat. nos. 14900-50-NF and 14900-100-NF) Quick-Start Protocol. Briefly, 5 mL of the homogeneously mixed samples were collected from each of the mineralization media containing biogenic Fe-Mn binary oxides and biofilm culture. The collected samples were centrifuged at 6000 rpm for 5 minutes to separate the pellets from the supernatants. The sample pellets were then transferred to the 5 ml PowerWater Bead Pro Tubes and 1 ml of guanidinium thiocyanate solution was added to each tube before vortexing for 5 min. After centrifuging the tubes at 4000 x g for 1 min, the supernatants from the tubes were collected. Collected samples were centrifuged again at 13,000 x g for 1 min to remove any solid material, and clean supernatants were collected. In each sample 200 µL IRS (AAS-12) was added, vortexed briefly to mix, and incubated at 5 °C for 5 min. Then after centrifuging at 13,000 x g for 1 min, supernatants were collected and 650 µL of guanidinium thiocyanate and ethanol mixture solution was added to each collected sample, and vortexed briefly to mix. Samples were then loaded onto the membrane (MB) Spin Columns and centrifuged at 13,000 x g for 1 min. The flowthroughs were discarded, and the process was repeated until all the samples had been processed. After that, 650 µL isopropanol was loaded onto each MB column, centrifuged at 13,000 x g for 1 min, and the flow-through was discarded. At this stage, 650 µL ethanol was loaded onto each MB column, centrifuged at the same speed for 1 min, and centrifugation was repeated for another 2 min to ensure complete removal of ethanol.

At last, 100 µL elution buffer (10 mM Tris) was added to the center of each MB column, and after 1 min centrifugation at 13,000 x g for 1 min was performed, and eluted DNA samples were collected. The DNA concentrations in the collected samples were measured in a NanoDrop Spectrometer (NanoDrop, ND-1000 Spectrophotometer, with a lower detection limit of 2 ng/µL) using molecular grade water as blank.

To determine the total carbohydrate content in the biogenic Fe-Mn binary oxides and mineral-free biofilm samples, the phenol-sulfuric acid method was employed following Nelson (2010), using a glucose standard curve. For this, 5 ml of the homogeneously mixed samples were collected from each mineralization medium containing either biogenic Fe-Mn oxides or *P. putida* biofilm. Then 50 µL 80% phenol was added to each tube and the tubes were vortexed briefly. Again, to each tube, 5 mL of concentrated sulfuric acid (H_2SO_4) was added, and the tubes were vortexed briefly. After 10 min, the tubes were then placed in a 25 °C water bath for 10 min to cool down the heat generated by H_2SO_4 to room temperature. The principle of the phenol-sulfuric acid method is that carbohydrates in the samples react in the presence of H_2SO_4 and heat to generate furan derivatives that condense with phenol to form stable yellow-gold compounds, that can be measured spectrophotometrically at 490 nm. To do this, a Hach DR 2800 spectrophotometer was used. Absorbance at 490 nm were recorded to determine carbohydrate concentrations against a standard curve (Figure 4.1), prepared using glucose solutions of different concentrations. A blank was prepared using Milli-Q water.

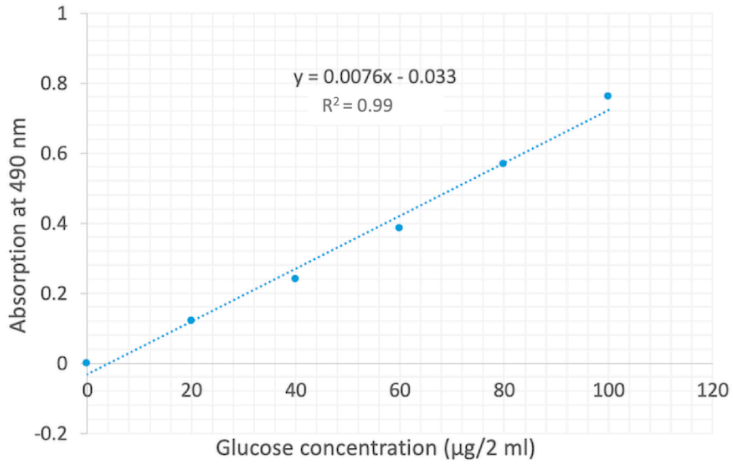


Figure 4.1: Glucose standard curve of concentration-absorbance to estimate carbohydrate concentration.

4.2.4 As(V) Adsorption Kinetic Experiments

As(V) adsorption kinetic experiments were performed over 144 h on mineral-free *P. putida* biofilm, biogenic Fe-Mn binary oxides, abiogenic Fe-Mn binary oxides, and abiogenic Fe-Mn binary oxides mixed with *P. putida* biofilm at an initial As(V) concentration of 195 µM at pH 7.0 (±0.5). To set up the adsorption experiment with biofilm, biofilm grown in a Schott bottle was separated by centrifuging at 5000 rpm for 10 min and added to 150 ml of a 0.001 M sodium nitrate ($NaNO_3$) solution with an As(V) concentration of 195 µM. For the experiments with biogenic and abiogenic Fe-Mn binary oxides, 9.5 mg of each mineral was added to 150 ml of a 0.001 M $NaNO_3$ solution with an As(V) concentration of 195 µM. For the experiment with abiogenic Fe-Mn binary oxides mixed with biofilm, 9.5 mg each of the mineral (dry weight) and biofilm separated from a Schott bottle (wet weight) was added to 150 ml of a 0.001 M $NaNO_3$ solution with an As(V) concentration of 195 µM and mixed well by shaking. Adsorption experiments were performed on a horizontal shaker at 120 rpm and 25°C for 144h. Aliquots were collected from each experimental solution after adding As(V) and at different time intervals throughout the experiments. After centrifuging at 5000 rpm for 5 min and filtering through 0.22 µm filters, collected samples were preserved in 2% HNO_3 for Inductively Coupled Plasma Mass Spectrometry (ICP-MS) analysis. Experiments were repeated twice for abiogenic and biogenic Fe-Mn binary oxides as well as abiogenic Fe-Mn binary oxides mixed with biofilm, and 4 times for the mineral-free biofilm.

4.2.5 As(V) Desorption Experiments

As(V) desorption from abiogenic and biogenic Fe-Mn binary oxides was investigated at pH 7.1 (±0.1). To set up the As(V) desorption experiments for abiogenic and biogenic Fe-Mn binary oxides, adsorption was first conducted over 120 h using 9.5 mg abiogenic and biogenic Fe-Mn binary oxides in 150 ml of solutions under the same experimental conditions described in section 4.2.4 (As(V) adsorption experiments). The initial As(V) concentrations for adsorption on abiogenic and biogenic minerals were 193 (±0.6) µM and 234 (±2) µM, respectively. After 120 h of adsorption, the experimental solutions were centrifuged at 8000 rpm for 10 min. Then, 5 ml of supernatant from each solution was collected and filtered through 0.22 µm filters for ICP-MS analysis, and the rest were carefully decanted without touching the bottom sediment containing the minerals. To avoid any accidental removal of the minerals, 5 ml of solutions at the bottom of the bottles were kept and then diluted by adding 45 ml 0.001 M $NaNO_3$ solution to start the desorption experiment. About 200 µL sample from each solution

was collected immediately after dilution, filtered through 0.22 µm filter and preserved for ICP-MS analysis. The diluted solutions were placed on a rotary shaker at 120 rpm at 25°C for 24 h. The next day the solutions were centrifuged at 8000 rpm for 10 min and 5 ml sample was collected from the solution after filtering through 0.22 µm filters for ICP-MS analysis. The remaining solutions were carefully decanted again, keeping 5 ml of solution at the bottom of the bottles without disturbing the minerals. The same procedure was repeated for up to 6 dilution cycles. Experiments were replicated 4 times for biogenic, and twice for abiogenic, Fe-Mn binary oxides. A schematic of the As(V) desorption experiment has been provided in Figure 4.2.

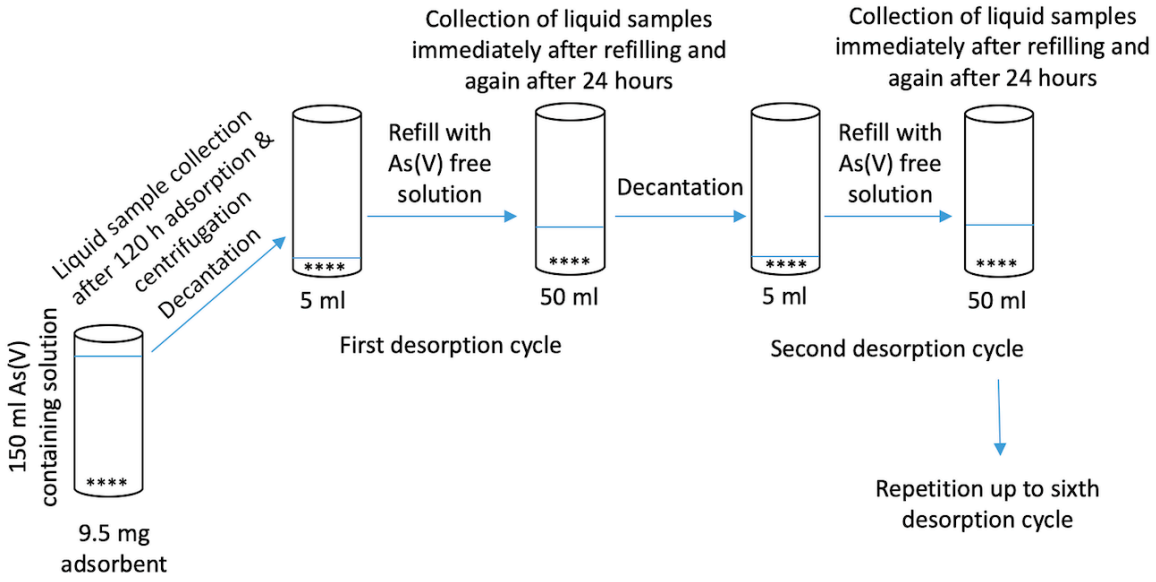


Figure 4.2: Schematic of As(V) desorption experiment from biogenic and abiogenic Fe-Mn binary oxides.

4.2.6 Adsorption Kinetics and Desorption Isotherm Modelling

Adsorbed As(V) concentration was calculated using equation 4.1 (Yang et al., 2022).

$$q_e = (C_0 - C_e) \times \frac{V}{m} \qquad Equation\ 4.1$$

Where q_e is the adsorbed concentration of As(V) on minerals (µmol/g), C_0 and C_e are the As(V) concentration in solution before and after the adsorption, V is the volume of solution (L), and m is the mass of the adsorbent minerals (g).

As(V) adsorption kinetics of biogenic and abiogenic Fe-Mn binary oxides were modelled using Pseudo-First-Order (PFO) and Pseudo-Second-Order (PSO) kinetic models (previously described in Chapter 1 and 2) following the equations 4.2 and 4.3 (Ho and McKay, 1998).

$$\ln(q_e - q_t) = \ln q_e - k_1 t \qquad Equation\ 4.2$$

$$\frac{t}{q_t} = \frac{1}{k_2\, q_e^2} + \frac{t}{q_e} \qquad Equation\ 4.3$$

Where q_e and q_t (µmol/g) are the amounts of As(V) adsorbed at equilibrium and variable time t, respectively, k_1 is the adsorption rate constant ($hour^{-1}$) for the PFO kinetic model, and k_2 is the adsorption rate constant (g/µmol-hour) for the PSO kinetic model.

For As(V) desorption isotherm, a linear Langmuir isotherm (described in Chapter 1 and 2) was plotted for desorption from biogenic and abiogenic Fe-Mn binary oxides by plotting each individual desorption cycle data using equation 4.4 (Kalam et al., 2021; Ayawei et al., 2017).

$$\frac{C_e}{q_e} = \frac{1}{q_m\, K_L} + \frac{C_e}{q_m} \qquad Equation\ 4.4$$

where q_e is the amount of As(V) adsorbed on the adsorbent (abiogenic or biogenic Fe-Mn binary oxides) (µmol/g), C_e is the concentration of As(V) in the solution (µmol/L), K_L is the equilibrium adsorption constant (L/µmol), and q_m is the maximum surface capacilty for As(V) adsorption on adsorbent (µmol/g) or the amount of As(V) adsorbed on minerals. A plot between C_e/q_e versus C_e will generate a straight line with a slope of $1/q_m$ and an intercept equal to $1/ q_m K_L$. If an adsorption reaction is completely reversible, then the amount of desorption would be equal to the maximum surface capacilty for adsorption.

4.2.7 Chemical analysis

The concentrations of As, Fe, and Mn in experimental solutions were determined by ICP-MS analysis using a PerkinElmer NexION 350D ICP-MS with rhodium internal standard and using a river water reference material for trace metals (SLRS-5) for As, Fe, and Mn concentrations. For the dilution of the samples, 2% HNO_3 was always used.

4.3 Results and Discussion

4.3.1 Morphological and Elemental Characterizations of Biogenic and Abiogenic Fe-Mn Binary Oxides

SEM images of the biogenic Fe-Mn binary oxides showed aggregations of the mineral particles with bacterial cells and EPS (Figure 4.3a, b). Both biogenic and abiogenic Fe-Mn binary oxides were aggregates of many fine particles (Figure 4.3).

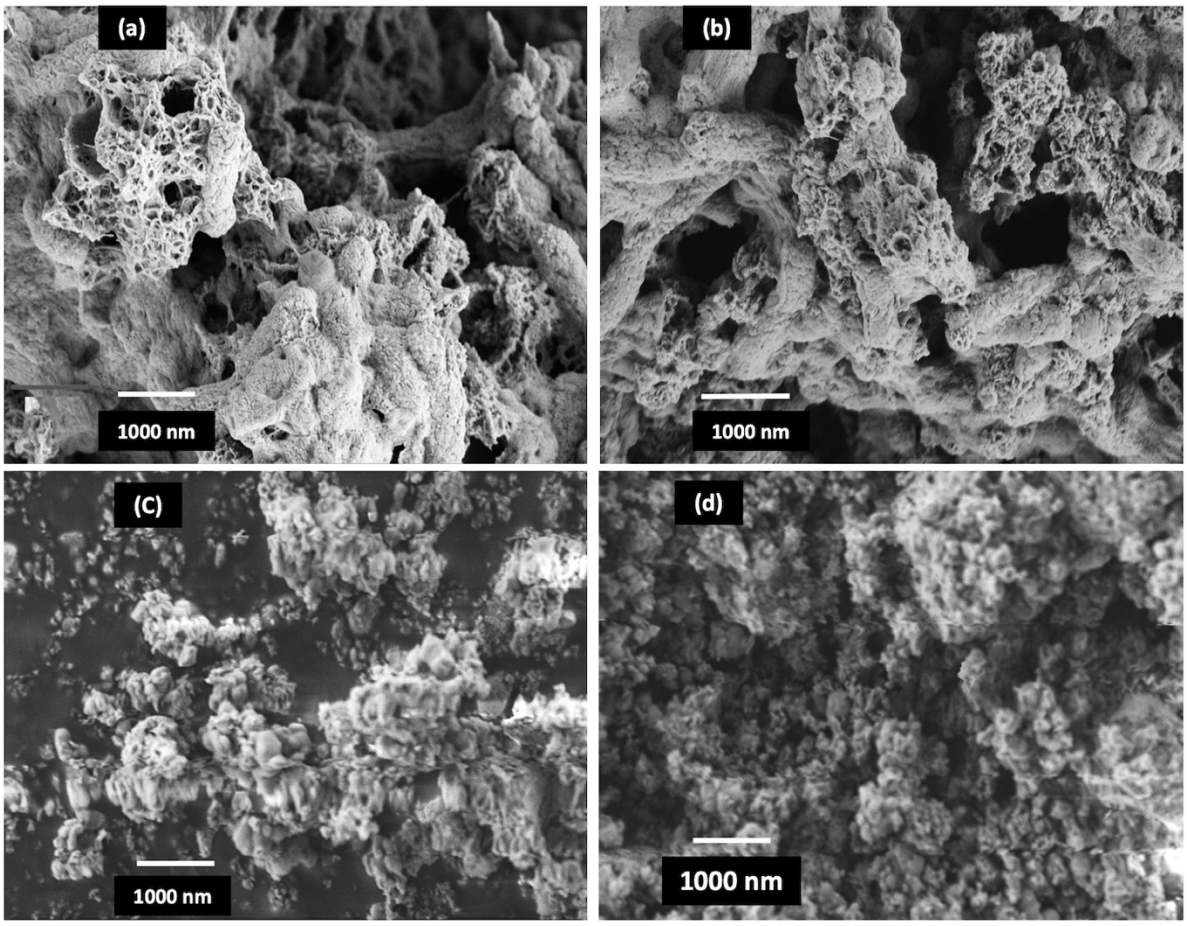


Figure 4.3: SEM images of the (a, b) biogenic and (c, d) abiogenic Fe-Mn binary oxides.

BF-STEM images of the biogenic Fe-Mn binary oxides also showed the presence of bacterial cells, with minerals produced extracellularly on the cell surfaces (Figure 4.4a, b, d). Minerals displayed mainly ultrathin plates-like morphologies (Figure 4.4e, f), but other morphologies were also observed (details in Chapter 3, Figure 3.6). Aggregation of the particles also formed granular mineral structures (Figure 4.4c), with particles probably joined by EPS. No BF-STEM imaging was performed on the abiogenic Fe-Mn binary oxides.

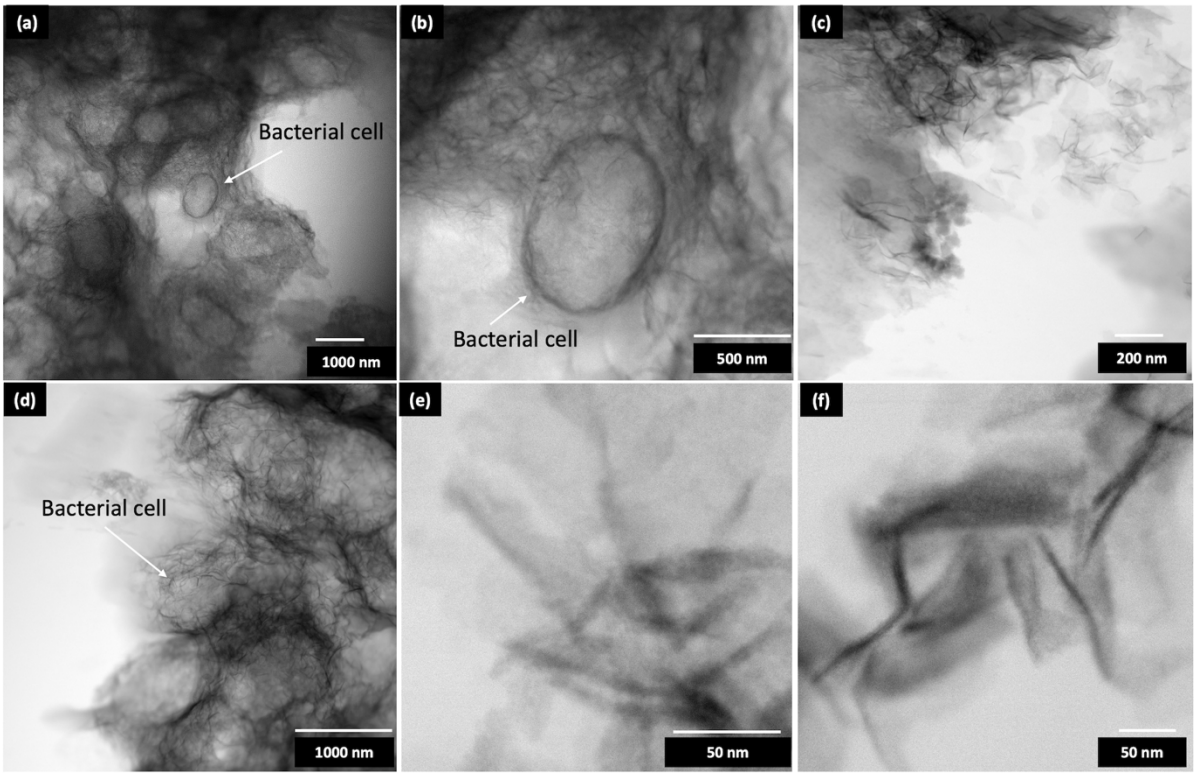


Figure 4.4: BF-STEM images of the biogenic Fe-Mn binary oxides. (a,b,d) Biogenic Fe-Mn binary oxides aggregation with bacterial cells, (e) Various morphologies of biogenic Fe-Mn binary oxides, (e,f) Ultra-thin plate like morphology of biogenic Fe-Mn binary oxides.

The elemental compositions of the biogenic and abiogenic minerals were revealed using STEM-EDX and SEM-EDX analysis, respectively. STEM-EDX and SEM-EDX spectra were extracted from the whole image fields of the biogenic and abiogenic minerals (Figure 4.5). Biogenic binary oxides exhibited a heterogeneous distribution of Fe and Mn. In contrast, abiogenic minerals exhibited a relatively homogeneous co-distribution of Fe and Mn in the areas of the analyzed samples (Figure 4.5). The homogeneous distribution of Fe and Mn in abiogenic minerals might be due to the good dispersion and their synthesis process: Fe and Mn were co-precipitated simultaneously to form the abiogenic Fe-Mn binary oxides. On the other hand, in the biogenic binary oxide synthesis process, Fe and Mn were oxidized and precipitated in two distinct steps. The presence of bacterial cells and EPS might also have caused poor dispersion of Fe and Mn.

In addition to Fe, Mn and O in the biogenic Fe-Mn binary oxides (Figure 4.5) phosphorus (P) was found to be co-distributed with carbon (C), and is thus thought to originate from organic matter. The presence of copper (Cu) peaks in the EDX spectra was believed to originate from the STEM grid. More details of the elemental composition and distribution in biogenic Fe-Mn binary oxides have been discussed in the previous chapter (Chapter 3).

Abiogenic Fe-Mn binary oxides showed the presence in small amounts of sodium (Na), potassium (K), and sulphur (S). They might have originated from the residuals of chemicals (NaOH, $KMnO_4$, and $FeSO_4.7H_2O$) used in mineral synthesis. The presence of silicon (Si), present in relatively minor amounts, might orinigate from the glass beaker.

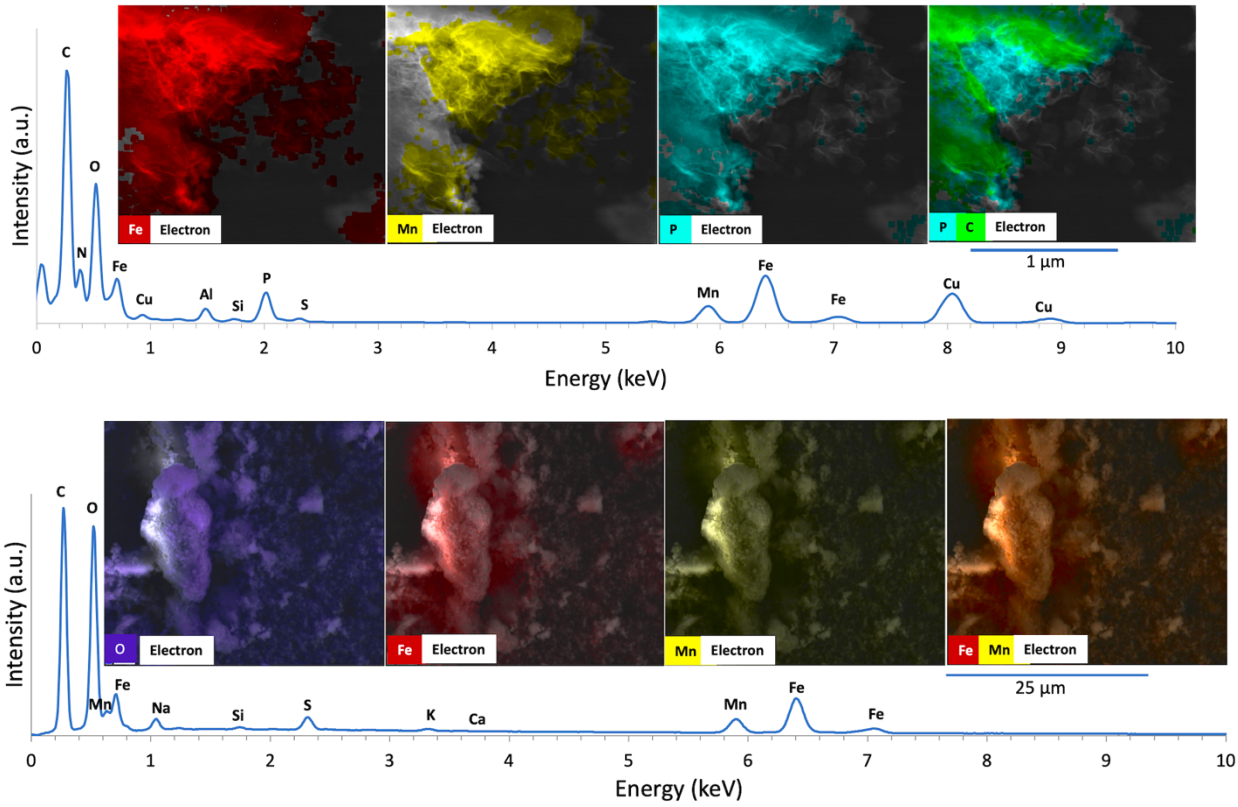


Figure 4.5: STEM-EDX and SEM-EDX spectra and maps of biogenic (upper) and abiogenic (lower) Fe-Mn binary oxides, respectively.

Physical and structural morphology and mineralogical composition are important factors that influence metal adsorption/desorption onto/from minerals (Gunawardana et al., 2014; Violante and Pigna, 2008).

4.3.2 Mineralogical Characterization

Crystalline mineral phases in the synthesized biogenic and abiogenic Fe-Mn binary oxides were identified by XRD analysis. Diffractograms of abiogenic and biogenic Fe-Mn binary oxide showed broad XRD peaks and have been identified as mixtures of poorly crystalline birnessite and ferrihydrite based on comparison with the XRD database of the International Centre for Diffraction Data (ICDD) (Figure 4.6). The background corrected XRD diffractogram (Figure 4.6a, B) of biogenic Fe-Mn binary oxides closely matches that of the reference ICDD 00-013-0105 (Figure 4.6a, C) and ICDD 01-073-7862 (Figure 4.6a, D) birnessite patterns as well as that of the ICDD 00-058-0898 (Figure 4.6a, E) ferrihydrite pattern. The XRD diffractogram of abiogenic Fe-Mn oxides matches the ICDD 01-073-8408 (Figure 4.6b, C) ferrihydrite reference pattern and ICCD 00-018-0802 (Figure 4.6b, D) birnessite reference pattern.

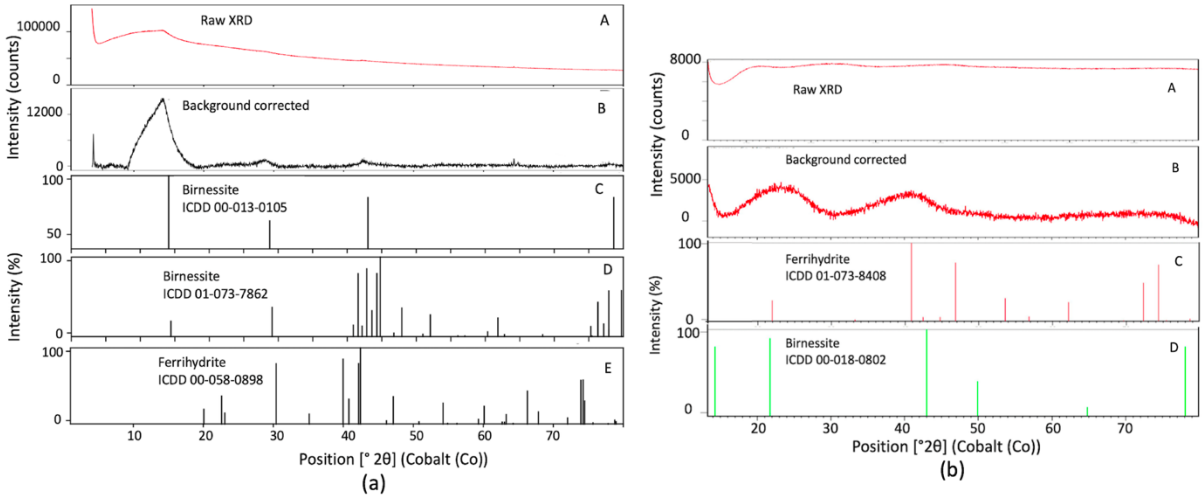


Figure 4.6: XRD of biogenic (a) and abiogenic (b) Fe-Mn binary oxides with ICDD reference ferrihydrite and birnessite patterns.

4.3.3 Organic Content in Biofilm and Biogenic Fe-Mn Binary Oxides

i. Fluorescence Microscopy

Fluorescence microscopy was employed to visualize bacterial cells and their associated EPS within the mineral-free *P. putida* biofilm and the biogenic Fe-Mn binary oxides. The distributions of DNA visualized using DAPI (purple fluorescence) and carbohydrates, detected with a lectin (green fluorescence), within both the mineral-free biofilm and the biogenic Fe-Mn binary oxide samples are shown in Figure 4.7. In Figure 4.7a, the image clearly showed cell shapes with DAPI, confirming that DAPI fluorescence is a good proxy for bacterial cells. Green fluorescence extracellularly, confirming the presence of abundant EPS around the cells. These fluorescence signals were also detected within the structures of the biogenic Fe-Mn binary oxides, suggesting that the minerals were forming within a matrix of cells and EPS (Figure 4.7b). Furthermore, higher fluorescence intensities for both DAPI and lectin were observed in the biofilm samples compared to the biogenic Fe-Mn binary oxides. This observation suggests a greater concentration of organic biomass, comprising DNA and carbohydrates, within the biofilm compared to the biogenic mineral sample.

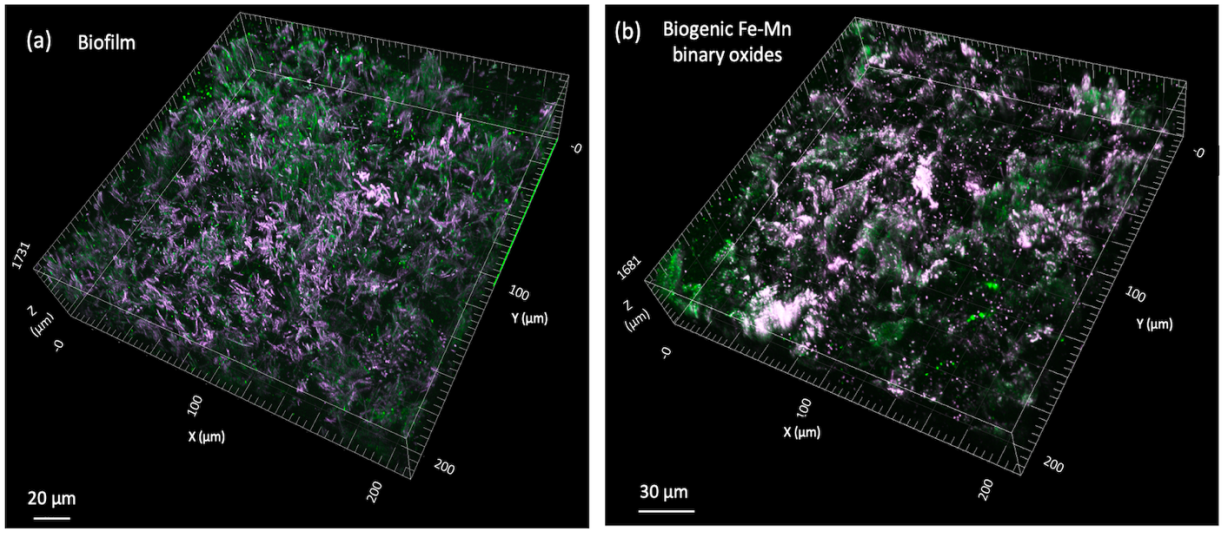


Figure 4.7: Fluorescence imaging of carbohydrate (lectin- green fluorescence) and DNA (DAPI- purple fluorescence) in (a) biofilm and (b) biogenic Fe-Mn binary oxides.

ii. DNA and Carbohydrate Quantification

The carbohydrate concentration within the mineral-free biofilm was 22 µg/ml, whereas the biogenic Fe-Mn binary oxides showed a lower carbohydrate concentration of 9 µg/ml. DNA quantification, used as a proxy for estimating bacterial cells in both the biofilm and biogenic Fe-Mn binary oxides, revealed a DNA concentration of 5 µg/ml in the biofilm and 3 µg/ml in the biogenic Fe-Mn binary oxides. From these measurements, the total biofilm mass was calculated to be 4.05 mg (Table 4.1) which made up the bulk of the organic material (carbohydrates + DNA). In the biogenic Fe-Mn binary oxides, the total organic matter mass was determined to be 1.8 mg. Given that the total mass of the biogenic mineral was 9.5 mg, the remaining (9.5-1.8 mg) 7.7 mg was attributed to the mineral fractions composed of Fe and Mn oxides. Organic contents in biofilm and biogenic Fe-Mn binary oxides are given in Table 4.1.

Table 4.1: A rough estimation of the organic matter masses in biofilm and biogenic Fe-Mn binary oxides.

Organic containing substances	Total volume (ml), V	Carbohydrate (µg/ml), C	DNA (µg/ml), D	Total mass of organic (mg) $\frac{(C+D)\times V}{1000}$
Biofilm	150	22 µg/ml	5	4.05
Biogenic Fe-Mn binary oxides	150	9 µg/ml	3	1.8

While this analysis suggests the concentrations of DNA present in biofilm and biogenic Fe-Mn binary oxides, it is important to remember that it is a rough estimation and there is a caveat to consider: not all DNA from the samples might get extracted and the measured DNA concentrations might not fully represent the true amount of biological material in the samples, so the findings may not be generalizable.

4.3.4 As(V) Adsorption Kinetic Experiments

As(V) adsorption experiments with mineral-free *P. putida* biofilm, abiogenic Fe-Mn binary oxides mixed with biofilm, as well as biogenic and abiogenic Fe-Mn binary oxides over 144h demonstrated varying As(V) adsorptions from experimental solutions. The adsorption experiment with biofilm showed a decreased As(V) concentration in solution, from 207.9 (±3.3) µM to 205.3 (±2.6) µM, over 144 h, whereas in the experiment with biogenic Fe-Mn binary oxides As(V) decreased from 195.2 (±1.4) µM to 181.2 (±0.5) µM (Figure 4.8a), indicating minimal As(V) adsorption by the mineral free-biofilm. A slightly higher As(V) adsorption by abiogenic Fe-Mn binary oxides was observed compared to abiogenic Fe-Mn binary oxides mixed with biofilm (Figure 4.8b). The concentration of As(V) decreased to 166.4 (± 2.6) µM from 193.6 (± 2.6) µM during the adsorption experiment with abiogenic Fe-Mn binary oxides, while a concentration decrease of 167.6 (±1.6) µM from 193 (±0.6) µM was observed for As(V) adsorption onto the abiogenic Fe-Mn binary oxides mixed with biofilm (Figure 4.8b).

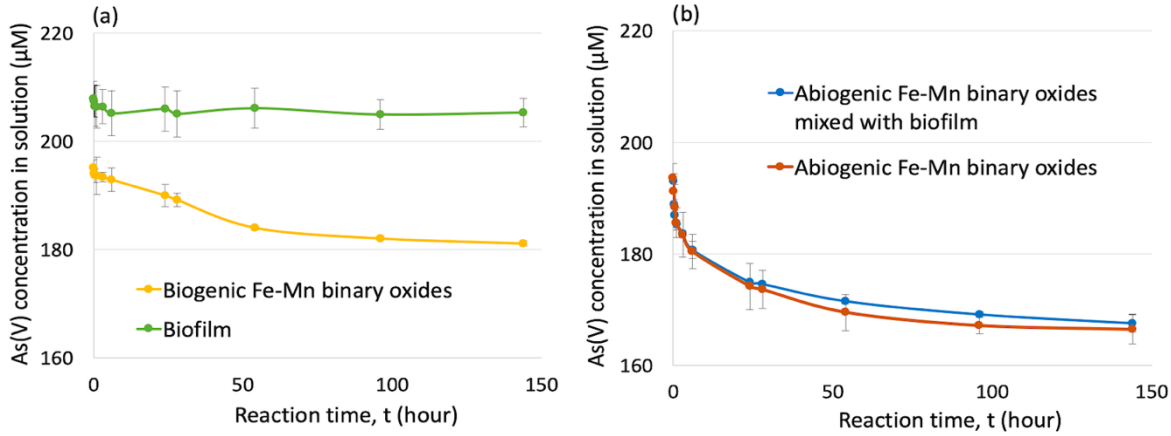


Figure 4.8: As(V) adsorption on biofilm and biogenic Fe-Mn binary oxides (a), abiogenic Fe-Mn binary oxides, and abiogenic Fe-Mn binary oxides mixed with biofilm (b). Error bars have been calculated as the standard deviation of the different replicates.

PFO kinetic models of As(V) on the mineral-free biofilm showed poor conformity with experimental data indicated by a R^2 value of 0.362. On the other hand, As(V) adsorption data of biogenic Fe-Mn binary oxides, abiogenic binary oxides and abiogenic Fe-Mn binary oxides mixed with biofilm showed good model conformities (Figure 4.9) suggesting adsorption of As(V) was due to the film diffusion and pore diffusion. As the adsorbents became more saturated with adsorbates, the adsorption rates decreased because fewer sites were available.

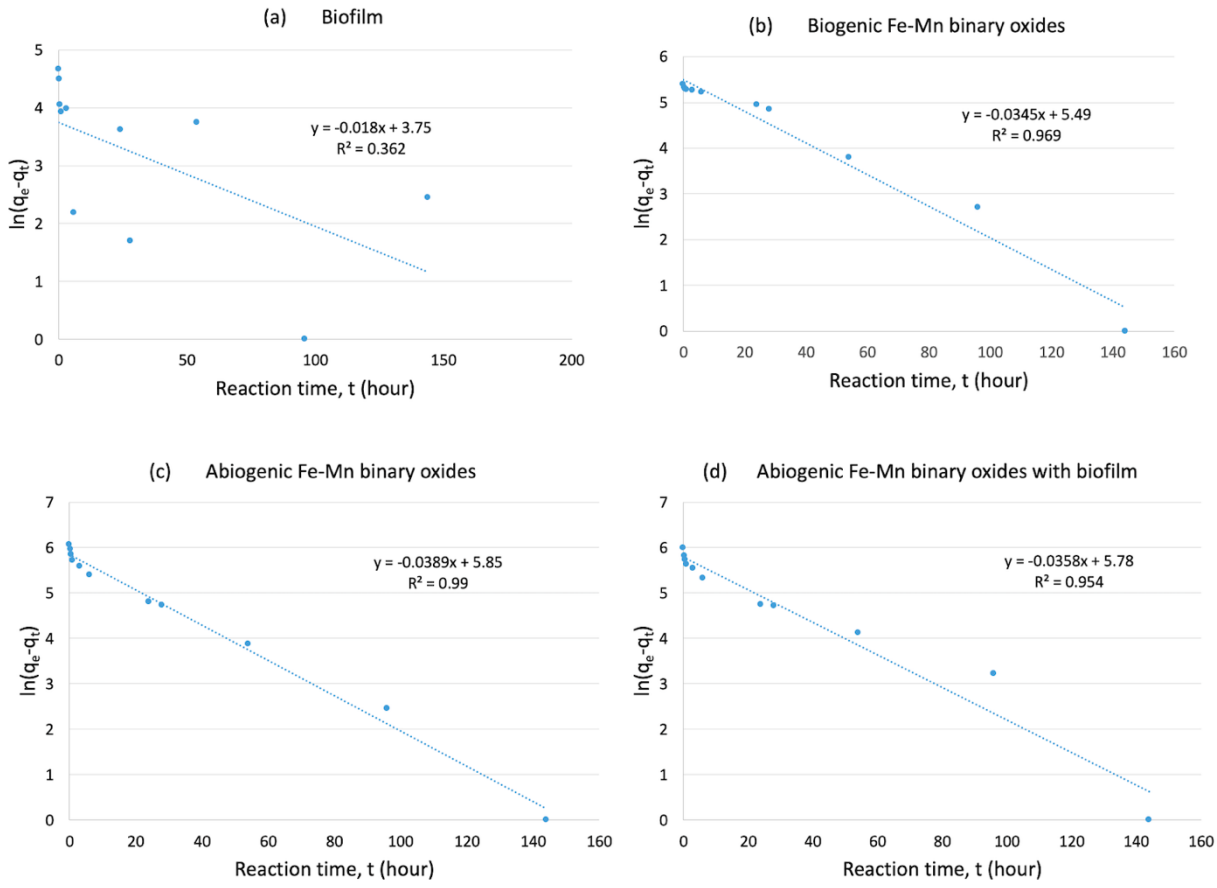


Figure 4.9: PFO kinetic models of biofilm (a), biogenic Fe-Mn binary oxides (b), abiogenic Fe-Mn binary oxides (c), and abiogenic Fe-Mn binary oxides mixed with biofilm (d).

Data from all the adsorption experiments could also be fitted with PSO kinetic model (Figure 4.10), assuming that adsorption process was controlled by chemisorption or surface reaction. However, biogenic Fe-Mn binary oxides exhibited greater conformity with PFO (R^2= 0.968) than PSO (R^2= 0.897) model that suggests film and pore diffusions might have great importance on As(V) adsorption onto their surface.

In the PSO kinetic model, the equilibrium adsorption capacity (q_e) of mineral-free *P. Putida* biofilm was 96 µmol/g, calculated from the slope of the linearized PSO model (t/q_t vs t) (Appendix, Figure 4-A4) and it was similar to the experimental value (96 µmol/g), calculated using equation 4.1 (Table 4.2).

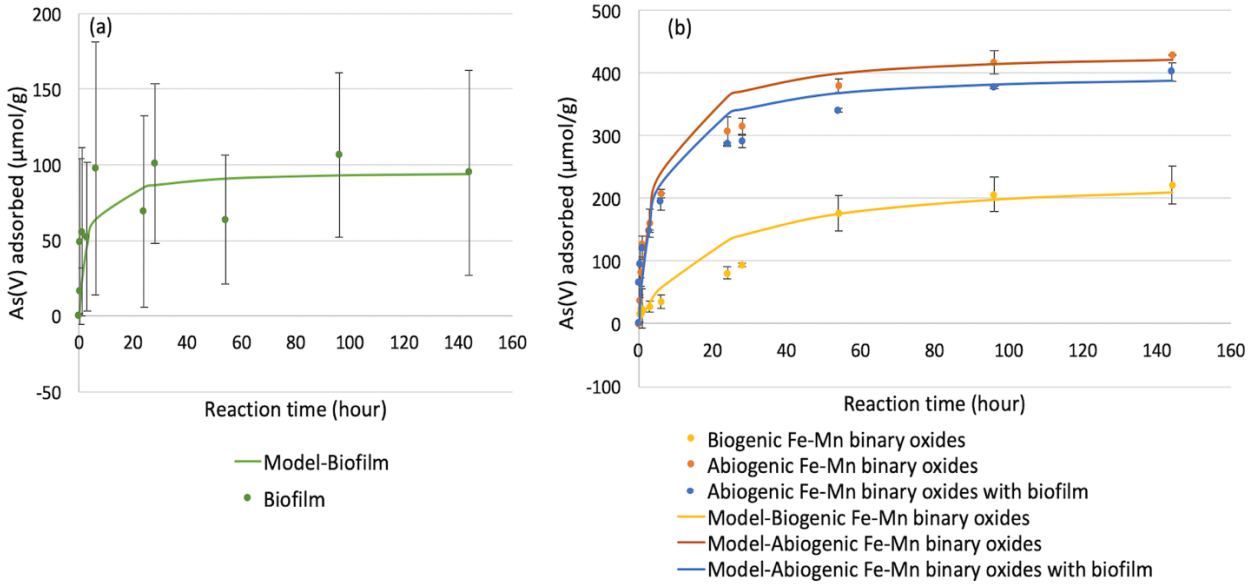


Figure 4.10: Experimental data plotted along with PSO As(V) adsorption kinetic models for the biofilm (a) and biogenic Fe-Mn binary oxides, abiogenic Fe-Mn binary oxides, and abiogenic Fe-Mn binary oxides mixed with biofilm (b). Error bars have been calculated as the standard deviation of the different replicates.

The PSO model showed increased As(V) adsorption up to 20 hours, after which it remained constant for the remainder of the reaction time (Figure 4.10a). As(V) adsorption experimental data plot of the mineral-free biofilm showed inconsistency over time (Figure 4.10a) but they would fit a consistent line. Very high standard deviation values (represented as large error bars) in the amount of As(V) adsorbed by mineral-free biofilm sample quadruplicates (Figure 4.10a) indicated the variability in As(V) adsorption by *P. putida* biofilm. Biogenic Fe-Mn binary oxide showed a q_e value of 238 µmol/g. Abiogenic Fe-Mn binary oxides had a q_e value of 435 µmol/g. In comparison, the experiment with abiogenic Fe-Mn binary oxides mixed with biofilm showed an ~8% reduced q_e value (400 µmol/g) (Figure 4.10b).

Table 4.2: PFO and PSO adsorption kinetic model parameters.

Kinetic Model	PFO			PSO		
	R^2	k_1 (per hour)	q_e (μmol/g)	R^2	k_2 (g/μmol-hour)	q_e (μmol/g)
Biofilm	0.362	0.018	42	0.964	0.0034	96
Biogenic Fe-Mn binary oxides	0.968	0.0345	242	0.897	0.0002	238
Abiogenic Fe-Mn binary oxides	0.99	0.0389	346	0.995	0.0005	435
Abiogenic Fe-Mn binary oxides with biofilm	0.954	0.0358	325	0.993	0.0005	400

The calculated As(V) adsorption rate ($k_2q_e^2$) of *P. putida* biofilm at the beginning of the adsorption process was 32 μmol/g-hour. Biogenic Fe-Mn binary oxides showed a value of 12.5 μmol/g-hour. Abiogenic Fe-Mn binary oxides, and abiogenic Fe-Mn binary oxides mixed with biofilm demonstrated adsorption rates of 89 μmol/g-hour and 83 μmol/g-hour, respectively.

i. Factors Affecting As(V) Adsorption on Minerals

The equilibrium As(V) adsorption concentrations varied between the experiments, with the highest adsorption concentrations found in the abiogenic Fe-Mn binary oxides (q_e = 435 μmol/g) which was similar to the abiogenic Fe-Mn binary oxides mixed with biofilm (q_e = 400 μmol/g). The biogenic Fe-Mn binary oxides adsorbed less As(V) (q_e = 238 μmol/g) followed by the biofilm (q_e = 96 μmol/g). This suggests that the association with bacterial cells and EPS (biofilm) reduced As(V) adsorption onto Fe-Mn binary oxide minerals. The As(V) adsorption capacity of biogenic Fe-Mn binary oxides was significantly lower than that of abiogenic Fe-Mn binary oxides and abiogenic Fe-Mn binary oxides mixed with biofilms. Compared with abiogenic Fe-Mn binary oxides, biogenic Fe-Mn binary oxides demonstrated ~45% less As(V) adsorption at equilibrium. SEM and STEM images (Figures 4.3 and 4.4) reveal that biogenic Fe-Mn binary oxides form aggregates of minerals, complexly associated with bacterial cells and EPS, indicating an abundance of negatively charged functional groups.

Although ferrihydrite carries a positive charge at pH levels below its point of zero charge (pH_{PZC} 8.1) (Parks and de Bruyn, 1962; Campos-Pereira et al., 2020; Zaia et al., 2020), and birnessite is negatively charged above pH 2–2.5 (Yang et al., 2020; Villalobos, 2015; Villalobos et al., 2014), the bacterial cells-EPS-mineral aggregates result in a net negative surface charge on biogenic Fe-Mn binary oxides (Tadanier et al., 2005; Posth et al., 2010). This overall negative surface charge likely caused electrostatic repulsion between the biogenic minerals and the negatively charged As(V) species, which may have reduced the adsorption efficiency of biogenic Fe-Mn binary oxides compared to the abiogenic minerals. A similar finding was reported by Kleinert et al. (2011), where they investigated As(V) adsorption by various abiogenic and biogenic minerals in commercial water filters and observed a reduced As(V) adsorption efficiency in biogenic Fe(III)-mineral-containing filters compared to those containing abiogenic Fe(III) oxyhydroxides.

Additionally, in the biogenic Fe-Mn binary oxide samples, phosphate (PO_4^{3-}) and other charged species derived from organic matter may occupy binding sites on the minerals, thereby reducing the As(V) adsorption capacity. Phosphate is recognized as a strong competitor with As(V) for surface sites, inhibiting its adsorption onto Fe-oxides (Liu et al., 2001; Manning and Goldberg, 1996). However, phosphate also has certain adsorption sites that are uniquely specific to it (Liu et al., 2001). The presence of significant amounts of phosphorus within the biogenic minerals (Figure 4.5) is thus another mechanism that could further explain their observed reduced As(V) adsorption capacity compared with the abiogenic Fe-Mn binary oxides.

ii. Role of Biofilm in As(V) Adsorption

In *P. putida* biofilm, cells are negatively charged due to the presence of functional groups in cell wall constituents, such as carboxyl, hydroxyl, and phosphate groups in proteins and carbohydrates (Rochex et al, 2004). Additionally, cells are mixed and bonded with EPS, which are polyfunctional heterogeneous large molecules displaying carboxyl, phenolic, phosphoric, sulfhydryl, pheaffectnol, hydroxyl, and many other functional groups, that are mostly negatively charged at neutral pH (Huang et al., 2022; Guibaud et al., 2009). Such negatively charged groups in the *P. putida* biofilm samples likely resulted in electrostatic repulsion with the negatively charged As(V) species ($H_2AsO_4^-$, $HAsO_4^{2-}$), resulting in minimal equilibrium As(V) adsorption of 96 µmol/g.

The small As(V) adsorption observed could be due to the presence of some positively charged functional groups such as amino groups, coexisting with the negatively charged groups at neutral pH (Feher, 2017). Biofilms are inherently dynamic systems, whose surface characteristics, including protein, EPS coverage, lipopolysaccharide composition, hydrophobicity, and surface charges may fluctuate depending on the bacterial growth phase (Xu et al., 2014; Flemming and Wingender, 2010). These changes in surface charges and chemical heterogeneity might have induced the continuous processes of adsorption, desorption, and re-adsorption of As(V), influencing the overall adsorption kinetics of As(V) on the biofilm, and exhibiting an inconsistent adsorption pattern over time. However, this variation in adsorption with the biofilm may not be real, since the values were consistent within the error bars (Figure 4.10a), but it was not resolvable given the precision of the measurements in this experiment.

In the case of biogenic Fe-Mn binary oxides, the close association between the minerals and both bacterial cells and EPS may be a key factor influencing the efficiency of As(V) adsorption by these biogenic oxides. As shown in electron microscopy observations (Figure 4.3, 4.4), bacterial cells and EPS may cover a significant portion of the surface area of the biogenic minerals, potentially acting as a barrier to the active binding sites necessary for As(V) adsorption. Based on the data presented here, the mineral fraction (7.7 mg) within the bacteria-EPS-mineral aggregate might have played a primary role in As(V) adsorption, showing an equilibrium adsorption of 238 μmol/g. As(V) diffusion flux into the biofilm (cells and EPS) was presumed to act as an initial controlling factor of the As(V) adsorption rate onto biogenic Fe-Mn binary oxides. The putative mechanism of As(V) diffusion, adsorption into biofilm and onto mineral surface of the biogenic mineral is described below (Figure 4.11). Initially, As(V) starts diffusing into the biofilm. Due to the presence of biofilm layer on the mineral surface As(V) cannot directly adsorbed onto the minerals, rather diffuse through the biofilm first (Figure 4.11a). The diffusion flux depends on the As(V) concentration gradient, which initially is the steepest. Since As(V) moves into the biofilm layer, the As(V) concentration profile across the biofilm layer evolves (curves 1, 2, 3 in Figure 4.11b). The rapid observed initial adsorption could reflect this diffusion into the biofilm (and adsorption onto uncovered mineral). When curve 3 is reached the flux of As(V) into the biofilm is the same along the profile and out of the biofilm and onto the underlying mineral surface. This flux is constant as long as the concentration at both ends doesn't change much so that the concentration gradient across the biofilm does not change significantly.

From the pore space immediately adjacent to the mineral, As(V) will be adsorbed onto the mineral surface. The As(V) concentration in this pore space will increase if diffusion coming in is faster than the rate of adsorption (Figure 4.11c).

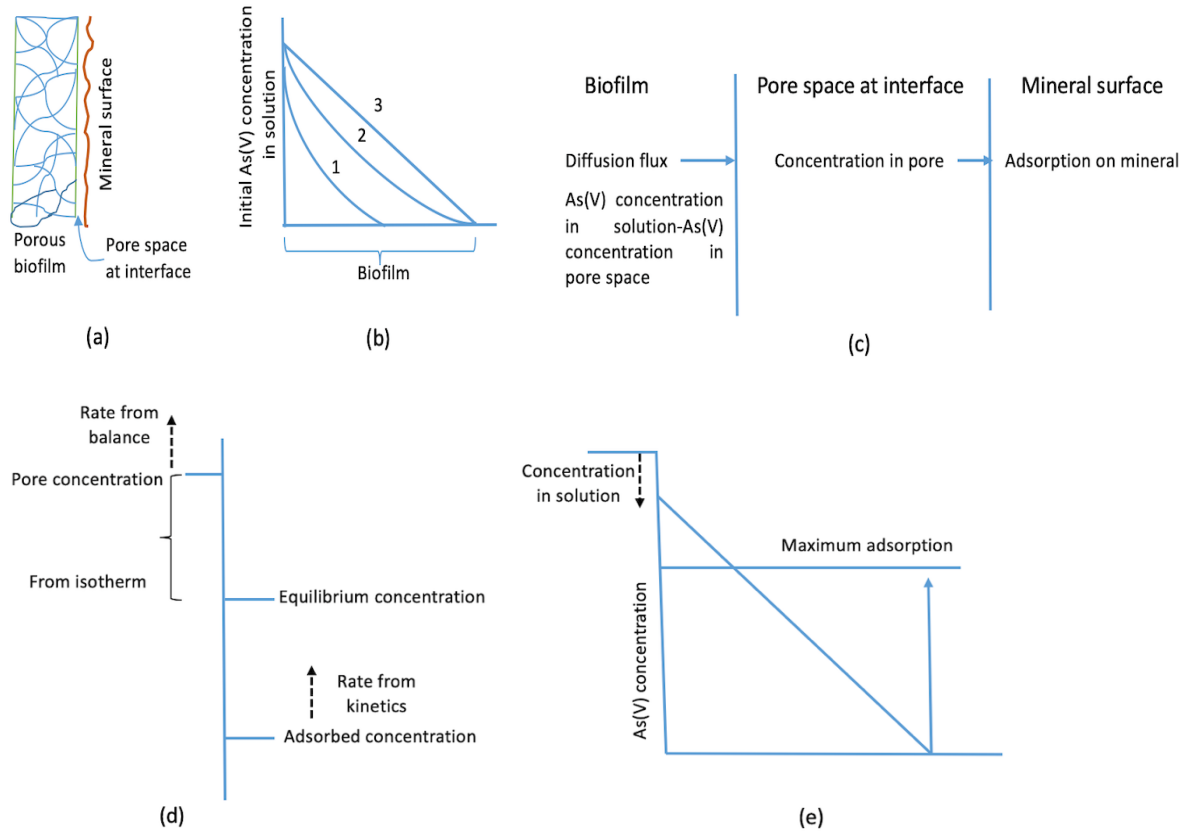


Figure 4.11: Putative mechanism of As(V) diffusion, adsorption into biofilm and onto mineral surface of the biogenic Fe-Mn binary oxides. (a) Biofilm (bacterial cells and EPS) on mineral surface and pore spaces at their interfaces, (b) Evolution of the As(V) concentration profiles across the biofilm layer over time due to diffusion, (c) Diffused As(V) adsorbed onto mineral surface passing through pore space and the diffusion flux controls the As(V) adsorption on mineral, (d) As(V) adsorption rate onto mineral will depend on how close the adsorbed concentration is to equilibrium with the pore concentration, (e) As(V) concentration in solution goes down as As(V) adsorption onto mineral progresses.

In turn, the adsorption rate onto mineral will depend on how close the adsorbed concentration is to equilibrium with the pore concentration and it will follow the kinetic rate law to establish equilibrium (Figure 4.11d). In this case, the adsorption rate is greater the further out of equilibrium the two are. At first, there is no adsorbed As(V) until As(V) begins to reach the mineral surface through the biofilm.

As the pore concentration climbs from diffusion in, the mineral surface concentration will be low compared to equilibrium and As(V) will adsorb faster if it is further behind (Figure 4.11d). If adsorption is faster, diffusion supplying As(V) to the interface will be the rate controlling step for As(V) adsorption. As As(V) adsorption progresses the solution concentration goes down and the interface concentration goes up so that the gradient decreases and the flux decreases. The rate of adsorption at the interface will drop as the equilibrium value is approached (Figure 4.11e).

These explain the As(V) adsorption curve of the biogenic Fe-Mn binary oxides (Figure 4.10b, yellow line). While As(V) was rapidly adsorbed when there was not much on the mineral surface, the rate at which As(V) adsorbed on the surface might have been controlled by diffusion through biofilm- leading to a different kinetic curve (Figure 4.10b, yellow line) than the curve seen for the abiogenic Fe-Mn binary oxides without biofilm (Figure 4.10b, brown line). When the As(V) reached the mineral surface, then adsorption followed the adsorption rules seen in the experiment without biofilm (abiogenic Fe-Mn binary oxides).

A more detailed, mathematical model of the diffusion and adsorption mechanisms would require constraints on the thickness of the biofilm (and extent of coverage over the minerals) at the mineral surface. Moreover, diffusion coefficients and diffusive fluxes within the biofilm are heterogeneous and may vary with time. Finally, the diffusion profile will not remain linear both due to changes affecting diffusion rates and as the concentration of As(V) in solution approaches the equilibrium concentration in the pore space at the mineral surface. Such a quantitative model incorporating these factors would be complicated and very underconstrained, and so was not pursued in this study.

The concentrations of Fe and Mn within the mineral structure play a critical role in determining the overall As(V) adsorption capacity of the Fe-Mn binary oxides, as it is well-established that iron oxides have higher As(V) adsorption capacity than Mn oxides (Zheng et al., 2020; Suda and Makino, 2016; Li et al., 2015). In this study, a direct comparison between As(V) adsorption by biogenic and abiogenic Fe-Mn binary oxides was challenging due to the differing Fe-to-Mn ratios in the biogenic (0.9:1) and abiogenic (3:1) samples (Zhang et al., 2007). For a deeper understanding of the impact of biofilm on As(V) adsorption by abiogenic Fe-Mn binary oxides, experiments were conducted comparing As(V) adsorption by abiogenic Fe-Mn binary oxides alone and those mixed with biofilm with the same Fe-to Mn ratios in both cases. As(V)

adsorption at equilibrium was 8% lower on the abiogenic Fe-Mn binary oxides mixed with biofilm relative to those without biofilm. This reduction in adsorption might be attributed to similar factors discussed earlier for biogenic Fe-Mn oxides. However, the effect was less pronounced, as the biofilm in this case was easily dispersed in the solution and not as finely intermixed with the Fe-Mn binary oxides, and additional ionic species such as phosphate (PO_4^{3-}), which might have been present at the surface of the biogenic minerals, were absent from the abiogenic minerals (Figure 4.5). Nevertheless, the biofilm (bacterial cells and EPS) could have blocked some active binding sites on the Fe-Mn oxides, and the negatively charged functional groups might have occupied positively charged sites on the mineral surfaces, thereby slightly reducing the adsorption of As(V) species.

4.3.5 As(V) Desorption Experiments

Studying the desorption kinetics of As(V) is crucial in understanding how quickly or slowly As(V) can be released from mineral surfaces. Understanding the reversibility of As(V) uptake is important in environmental and contaminant treatment systems. This is because As(V) may initially be taken up by materials and subsequently released into less contaminated water, such as during seasonal changes in groundwater levels, flooding events, or within treatment systems operating under diluted water conditions. As(V) adsorption reversibility of biogenic and abiogenic Fe-Mn binary oxides was tested through desorption experiments. Before conducting the desorption experiments, As(V) adsorption onto both biogenic and abiogenic Fe-Mn binary oxides was performed. The biogenic Fe-Mn binary oxides adsorbed 146 (± 16) µmol/g of As(V), reducing As(V) concentration from 234 µmol/L to 225 µmol/L in a solution, while the abiogenic Fe-Mn binary oxides adsorbed 470 (± 13) µmol/g of As(V) from solution, reducing As(V) concentration from 193 µmol/L to 163 µmol/L over a 120 h experimental period. These As(V)-adsorbed biogenic and abiogenic minerals were used for subsequent desorption experiments, enabling the assessment of As(V) adsorption reversibility of these minerals.

The desorption isotherms of As(V) from abiogenic and biogenic Fe-Mn binary oxides were investigated by perturbing the equilibrium between As(V)-adsorbed minerals and As(V) in solution. Unlike previous studies, which primarily focused on As(V) desorption from Fe minerals through mineral-destructive processes, such as abiotic or microbial reductive dissolution (Cai et al., 2020; Tong et al., 2020; Jiang et al., 2013; Huang, 2018; Liu et al., 2020; Tian et al., 2015), or in the presence of competing anions and cations (Lv et al., 2024), this study employed a non-destructive approach. By systematically altering the equilibrium via a series of dilutions, this work aimed to assess As(V) adsorption reversibility of abiogenic and biogenic Fe-Mn binary oxides.

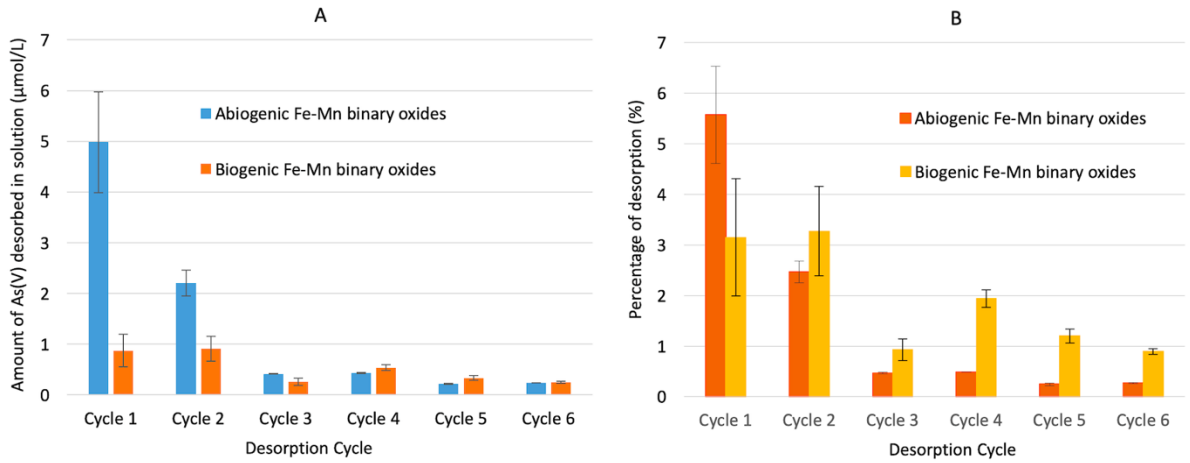


Figure 4.12: (A) Amount of As(V) desorbed in solution from abiogenic and biogenic Fe-Mn binary oxides during each desorption cycle, (B) Percentage of As(V) desorption in solution from abiogenic and biogenic Fe-Mn binary oxides during each desorption cycle. Error bars have been calculated as the standard deviation of the different replicates.

Figure 4.12A showed the amount of As(V) desorbed in solution in each desorption cycle for both abiogenic and biogenic Fe-Mn binary oxides. Desorption from both minerals were higher in fisrt two desorption cycles and then remained ≤ 0.5 µmol/L in the rest of the desorption cycles. In camparison with biogenic Fe-Mn binary oxides, abiogenic Fe-Mn binary oxides desorbed higher amounts of As(V) during first two desorption cycles. Percentages of As(V) desorption from biogenic Fe-Mn binary oxides were higher than abiogenic Fe-Mn binary oxides in each cycle expept first desorption cycle (Figure 4.12B). However, the percentage of desorption was less than 6% during any cycle for both minerals.

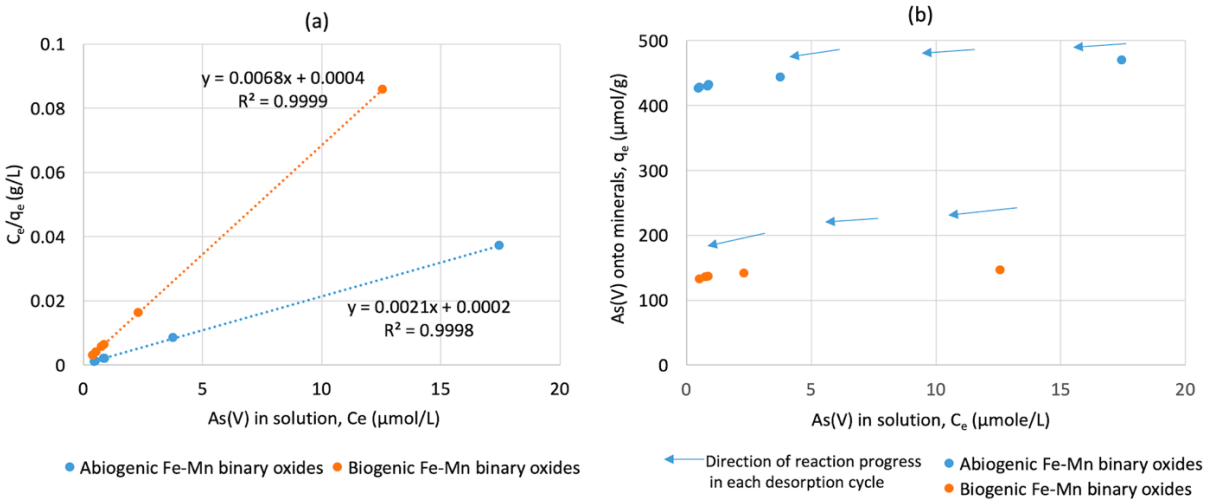


Figure 4.13: (a) Langmuir isotherm C_e/q_e vs C_e linear plots of abiogenic and biogenic Fe-Mn binary oxides for As(V) desorption, and (b) As(V) desorption isotherms of abiogenic and biogenic Fe-Mn binary oxides. The arrow indicates the direction of reaction progress, showing that desorption decreases with each desorption cycle as As(V) concentrations on the minerals also decline.

A Langmuir isotherm model was adopted to describe equilibrium states in both minerals systems. Langmuir isotherm is the most intuitive and simplest approach, with assumptions of monolayer adsorption on homogeneous adsorption sites, constant adsorption energy, and no or negligible interaction between adsorbate molecules on different adsorption sites. Linearized Langmuir isotherm plots of both minerals fitted well as indicated by R^2 values (Figure 4.13a). In abiogenic Fe-Mn binary oxides system the calculated maximum surface capacity (q_m) from the desorption Langmuir plot (476 µmol/g) was also very close to the As(V) initially adsorbed on the abiogenic Fe-Mn binary oxides (470 µmol/g) for this desorption experiment. In biogenic Fe-Mn binary oxides, the As(V) desorption Langmuir plot provided a gradient value of 0.0068 with q_m value of 147 µmol/g/. The As(V) initially adsorbed on the biogenic Fe-Mn binary oxides was 180.5 µmol/g for this desorption experiment. However, the amounts of As(V) desorbed in solutions by both minerals differ from the As(V) concentrations remaining in solutions at equilibria during initial adsorption experiments (225 µmol/L and 163 µmol/L for biogenic and abiogenic minerals, respectively). These variations indicated that a small fraction of As(V) might be released from both minerals, but the majority was irreversibly bound to the mineral surfaces, possibly by chemisorption.

The implication of this is that both minerals might be expected to hold As(V) even if the concentration of As(V) in solution changes (e.g., if relatively high As(V) concentrations in contaminated waters are followed by As(V)-free conditions in clean waters, either in the environment or in a remediation system).

The role of biofilm or organic fraction in As(V) desorption from biogenic Fe-Mn binary oxides was not clear. Further investigation involving other factors such as different pH, and organic content is required to fully understand and confirm these findings.

4.4 Conclusion

This research investigated how biofilm affects the As(V) adsorption-desorption dynamics of biogenic and abiogenic Fe-Mn binary oxides. PFO and PSO kinetic modelling of As(V) adsorption experimental data indicated that As(V) adsorption on both minerals might have been dominated by chemisorption, with a minor contribution of physisorption. Biogenic Fe-Mn binary oxides showed ~45% lower equilibrium As(V) adsorption compared to abiogenic Fe-Mn binary oxides. While abiogenic Fe-Mn binary oxides showed higher adsorption capacity at equilibrium, abiogenic Fe-Mn binary oxides mixed with biofilm revealed a slightly lower (~8%) As(V) adsorption capacity at equilibrium than the abiogenic Fe-Mn binary oxides alone. The As(V) desorption experimental data of both minerals indicated that As(V) adsorption on biogenic and abiogenic Fe-Mn binary oxides were not reversible, though a small fraction of the weakly bound As(V) might desorb. Results reveal that the adsorption-desorption dynamics of biogenic and abiogenic Fe-Mn binary oxides in the presence of biofilm were influenced by As(V) diffusion into biofilm (when present with the mineral fraction), electrostatic forces generated by the functional groups of the biofilm/organic matter present at the surface of the minerals, and the presence of PO_4^{3-} gorups. The As(V) desorption isotherms of both adsorbents suggested that most of the As(V) species were possibly bound by chemisorption, making them less likely to be desorbed.

5 Chapter Five: Conclusions

5.1 Summary of Research Findings

Chapter 2 (Arsenic(V) adsorption behaviours and capacities of abiogenic ferrihydrite and Fe-Mn binary oxides) major findings:

This chapter compared the adsorption dynamics of As(V) onto abiogenic Fe oxides and Fe-Mn binary oxides. Abiogenic Fe oxide and Fe-Mn binary oxides were synthesized. Synthesized abiogenic Fe oxide was identified as poorly crystalline ferrihydrite and abiogenic Fe-Mn binary oxides were identified as a mixture of poorly crystalline birnessite and ferrihydrite using XRD analysis. EDX analysis of the ferrihydrite sample showed the co-distribution of Fe and O. Abiogenic Fe-Mn binary oxides exhibited heterogeneous distribution of Fe and Mn in the sample. SEM analysis identified the ferrihydrite and abiogenic Fe-Mn binary oxide samples as aggregates of nanoparticles. BET analysis revealed higher specific surface area and larger pore size for the Fe-Mn binary oxides as compared with ferrihydrite. Smaller surface area of ferrihydrite might have been caused by particle aggregation. Fe-Mn binary oxides demonstrated higher maximum As(V) adsorption capacity than ferrihydrite though ferrihydrite showed higher initial As(V) adsorption rate and affinity. Both adsorbents showed fast initial adsorption due to film diffusion, followed by slower adsorption due to pore diffusion, as indicated by PFO kinetic models. Adsorption on both sample types showed good conformities with a PSO kinetic model suggesting that As(V) adsorption on both minerals was dominated by chemisorption. Langmuir isotherm model suggested the presence of non-interactive homogeneous surface sites on the mineral surfaces and monolayer adsorption. The higher surface area of the Fe-Mn binary oxides as compared with ferrihydrite might provide more surface sites for binding As(V). Moreover, the larger pore size of the Fe-Mn binary oxides facilitated As(V) adsorption on the surface of internal pores within the mineral, providing more adsorption capacity.

Chapter 3 (*Pseudomonas Putida*-Mediated Synthesis of Biogenic Iron-Manganese Binary Oxides Nanoparticles: Characterization Insights and Potential Environmental Implications) major findings:

This chapter proposed a novel pathway for the formation of biogenic Fe-Mn binary oxides at water column of the oxic-anoxic interfaces. To produce biogenic Fe-Mn binary oxides, synthesis of biogenic Mn oxides was performed as a first step mediated by *P. putida* MnB1 under aerobic condition. More than 99 % of the initial Mn (II) was oxidized and precipitated as biogenic Mn oxides. Biogenic Mn oxides oxidized Fe(II) under micro-aerobic condition, resulting in the precipitation of Fe oxides and formation of biogenic Fe-Mn binary oxides. Mineralogical identification using XRD and TEM-SAED confirmed that poorly crystalline birnessite and ferrihydrite nanocrystals phases composed the biogenic Fe-Mn binary oxides. Elemental composition by STEM-EDX analysis revealed the presence of Fe and Mn colocalized with C and O, but heterogeneous distribution of Fe and Mn. Significant amount of P was identified in the biogenic minerals. SEM analysis demonstrated that the biogenic minerals formed aggregates with *P. putida* cells and EPS. STEM also showed that the minerals were formed extracellularly and precipitated on the bacterial cell surfaces. The biogenic Fe-Mn binary oxides particles were identified as nanoparticles with typical dimensions smaller than 100 nm. Diverse morphological features of the biogenic minerals such as plates/sheets like features, long elongated chains of particle aggregates, and aggregations of the particles into granular morphologies, were also identified using STEM imaging. This research proposed a pathway for biogenic Fe-Mn binary oxides formation at oxic-anoxic interfaces of the water columns, involving microbial Mn(II) bio-oxidation, followed by Fe(II) oxidation by Mn oxides, to form finely intermixed Fe- and Mn-oxide phases.

Chapter 4 (Unfolding the role of *Pseudomonas putida* biofilm in Arsenic(V) adsorption-desorption dynamics on Iron-Manganese binary oxides) major findings:

This chapter investigated the role of biofilm on As(V) adsorption and desorption onto and from Fe-Mn binary oxides. Fluorescence microscopy combined with quantification of carbohydrates and DNA revealed the presence and concentration of organic matter (cells and EPS) associated with the biogenic Fe-Mn binary oxide minerals. Higher concentrations of organics were present in mineral-free *P. putida* biofilm than in the biogenic Fe-Mn binary oxides. As(V) adsorption kinetics experiments on the mineral-free biofilm, abiogenic and biogenic Fe-Mn binary oxides, and abiogenic Fe-Mn binary oxides mixed with biofilm were performed over 144h. The mineral-free biofilm showed the least adsorption capacity as well as fluctuating adsorption rates over time. The low As(V) adsorption capacity of the biofilm likely result from the fact that most of the organic functional groups present on the cell surfaces and EPS are negatively charged at neutral pH, which might confer electrostatic repulsion to negatively charged As(V) species. Biogenic Fe-Mn binary oxides showed higher adsorption capacity than the mineral-free biofilm due to lower amount of organic matter, corresponding to a lower content in negatively charged functional groups. The As(V) adsorption capacity of the biogenic Fe-Mn oxides was higher than that of the biofilm but significantly lower than that of abiogenic Fe-Mn binary oxides. This is interpreted as the presence of cells and EPS within the biofilm blocking the As(V) binding sites at the surface of the Fe oxides, providing a net negative charge to the biogenic minerals. Based on electron microscopy observations, bacterial cells and EPS might indeed have covered a good portion of the specific surface area of the biogenic minerals. In biogenic Fe-Mn binary oxides As(V) diffusion into biofilm also played important role in As(V) adsorption on the mineral surfaces. Moreover, the presence of PO_4^{3-} groups in the biogenic minerals might have inhibited the adsorption of As(V). All these factors contributed to the reduced As(V) adsorption onto biogenic Fe-Mn binary oxides as compared to abiogenic Fe-Mn binary oxides. As(V) desorption experiments were performed on As(V) adsorbed biogenic and abiogenic Fe-Mn binary oxides. The As(V) desorption experiments of both biogenic and abiogenic Fe-Mn binary oxides demonstrated that most of the As(V) were irreversibly bound onto the mineral surfaces.

Overall, this research provides a holistic understanding of the As(V) adsorption-desorption dynamics of Fe-Mn binary oxides, of both biogenic and abiogenic origins. Fe-Mn binary oxides might play a significant role in As(V) adsorption dynamics in nature due to their high efficiency of As(V) adsorption. Fe-Mn binary oxides are often overlooked in terms of their role in trace metals adsorption-desorption dynamics, including As(V). This research also provides new information on the impact of the presence of microbial biofilms in reducing the adsorption capacity of Fe-Mn binary oxides, which might be also true for the adsorption-desorption dynamics of other important trace metals. This research unfolds a potential pathway for biogenic Fe-Mn binary oxides formation at the oxic-anoxic interface of stratified water columns. This research also deepens our understanding of the As(V) adsorption-desorption dynamics of environmentally common mineral phases, which may thus impact As(V) transport in the aquatic environments.

5.2 Future Research Prospects

There is significant potential to further extend research involving biogenic Fe-Mn binary oxides and As adsorption-desorption dynamics. In particular, future research efforts could further address why and how the presence of bacterial cells and EPS can reduce their As(V) adsorption capacity and affect desorption mechanism. A deep investigation into the organic matter compositions and concentrations of biogenic Fe-Mn binary oxides could be insightful in determining more accurate adsorption-desorption dynamics of many trace elements including As.

Moreover, the effect of the significant amount of microbially derived PO_4^{3-} in the biogenic minerals on As(V) adsorption mechanisms and dynamics could be investigated more thoroughly. Separation of the organic fraction and removal of PO_4^{3-} from the biogenic minerals could for instance be performed to test their effects on As(V) adsorption-desorption. However, this approach could be challenging because further chemical treatment to remove organic matter and PO_4^{3-} might change the structure of the biogenic minerals. There is also a possibility of the significant loss of mineral mass during the treatment procedure.

This research focused on the biofilm of a model organism, *P. putida* and its influences on As(V) adsorption-desorption dynamics. Biofilm of different microbial communities might play different roles based on their metabolic activities and As oxidation-reduction capabilities. Moreover, the natural environment harbors a great diversity of microbes, natural biofilms consist of complex microbial communities. Therefore, more realistic experiments could be using complex community-biofilms instead of single species-biofilms. However, identifying the specific roles of each microbial strain within the community would bear significant challenges. Additionally, As cycling within natural biofilm samples could be studied to gain a better understanding of the complex biogeochemical cycle of this element.

Current research addressed the As(V) adsorption-desorption of Fe-Mn binary oxides in the presence of biofilm. However, As(III) species might have shown different behaviors since they are more mobile, unstable and subject to oxidation. A detailed investigation of the As(III) adsorption-desorption dynamics of biogenic Fe-Mn binary oxides within biofilms is needed for a complete understanding of the impact of Fe-Mn binary oxides-As-biofilm interactions on As speciation, mobility, and transport in the aquatic environment.

Finally, further investigations including long term desorption experiments with continual sampling, monitoring changes in organic content in biogenic Fe-Mn oxides during desorption, studying how changes in pH might matter, and how the minerals and any associated organic matter might evolve with time, can deepen our understanding of the As desorption behaviour of these abiogenic and biogenic minerals in perturbed equilibria.

Appendices

XRD Analysis:

The accuracy of the XRD measurement was constrained by testing the XRD background of an empty Silicon disk. The disk returned to a peak at 3.1360 angstroms which is close to the known value for that silicon peak.

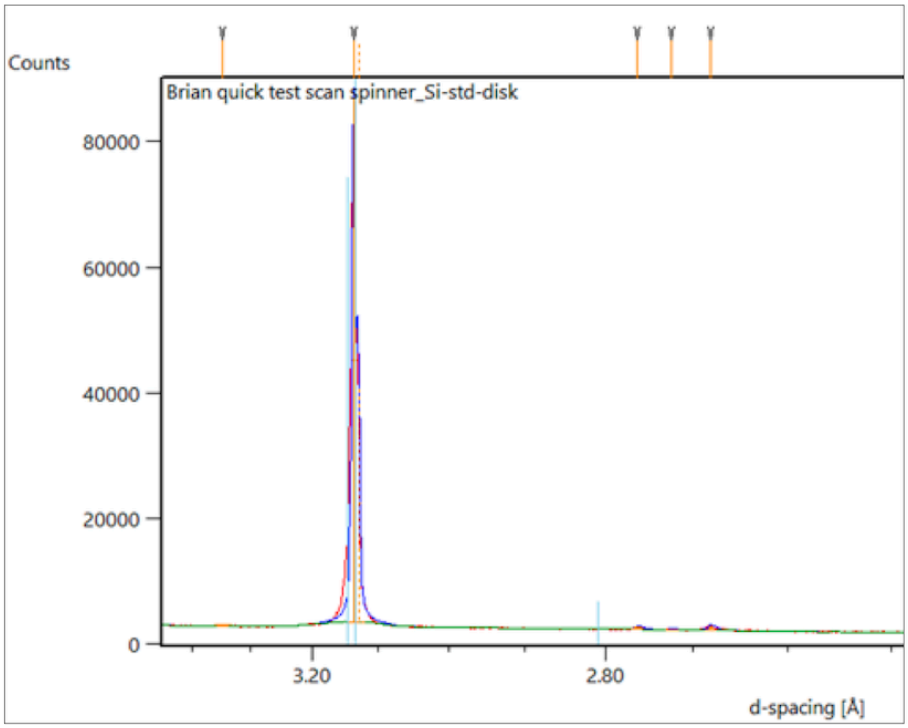
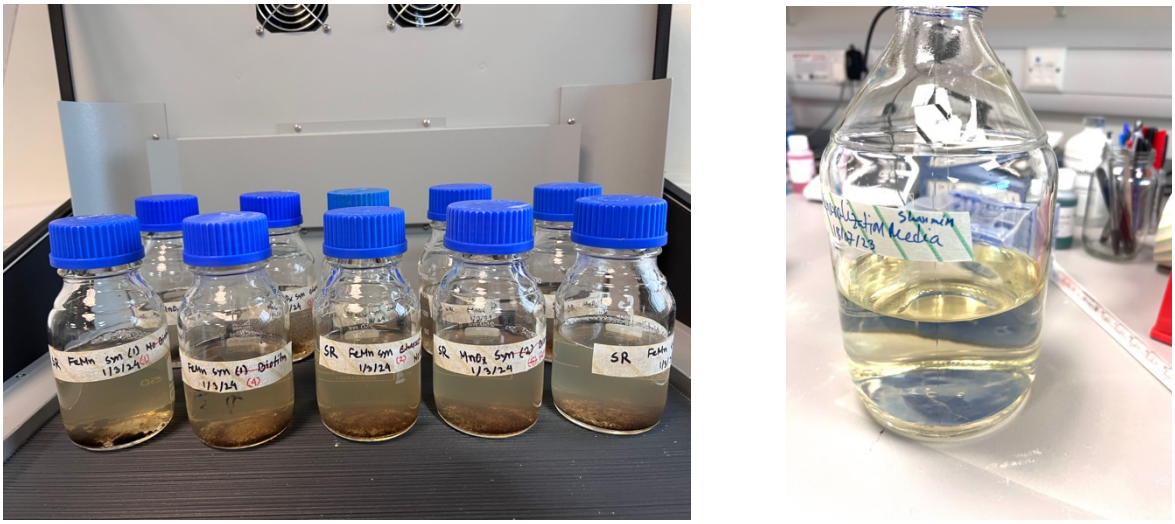


Figure 3-A1: XRD pattern of the background, an empty Silicon disc.

Mn(II) Biomineralization:

No biogenic Mn oxides formation in abiotic control (Figure 3-A2b).



(a) (b)

Figure 3-A2: Biotic mineralization (a) and abiotic control (b) experiments after 18 days.

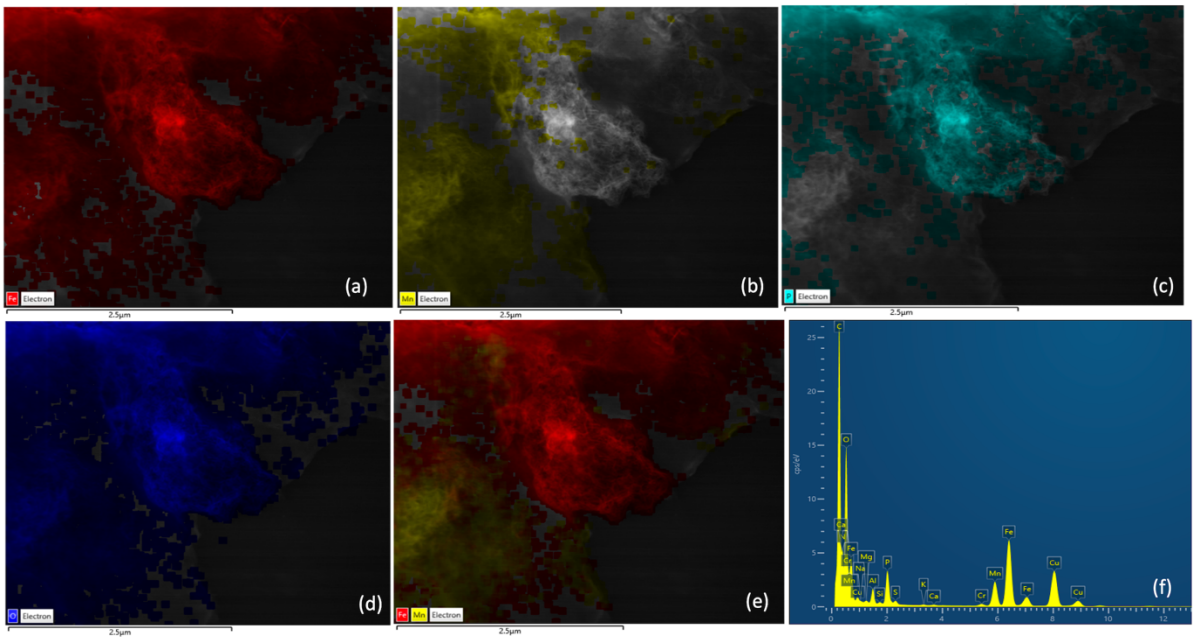


Figure 3-A3: STEM-EDX elemental distribution maps of Fe (a), Mn (b), P (c) and O (e) of biogenic Fe-Mn binary oxides. Fe and Mn overlaid mapping (e) and STEM-EDX elemental distribution spectra of the whole image (f) of biogenic Fe-Mn binary oxides.

Table 3-A1: pH changes during biomineralization experiment using *P. putida*.

Replication	**pH changes over time**			
	Day 1 (Initial)	Day 12	Day 12 after Fe(II) addition	Day 18
Replicate 1	7.4	7.31	7.2	7.22
Replicate 2	7.4	7.42	7.34	7.5
Replicate 3	7.4	6.98	6.9	7.1
Replicate 4	7.4	7.29	7.15	6.99
Average	7.4	7.25	7.15	7.2
Standard deviation	±0	±0.2	±0.2	±0.2

Table 3-A2: pH changes in an abiotic control experiment.

Day	pH
Initial- Day 1	7.4
Day 12	7.39
Day 18	7.41

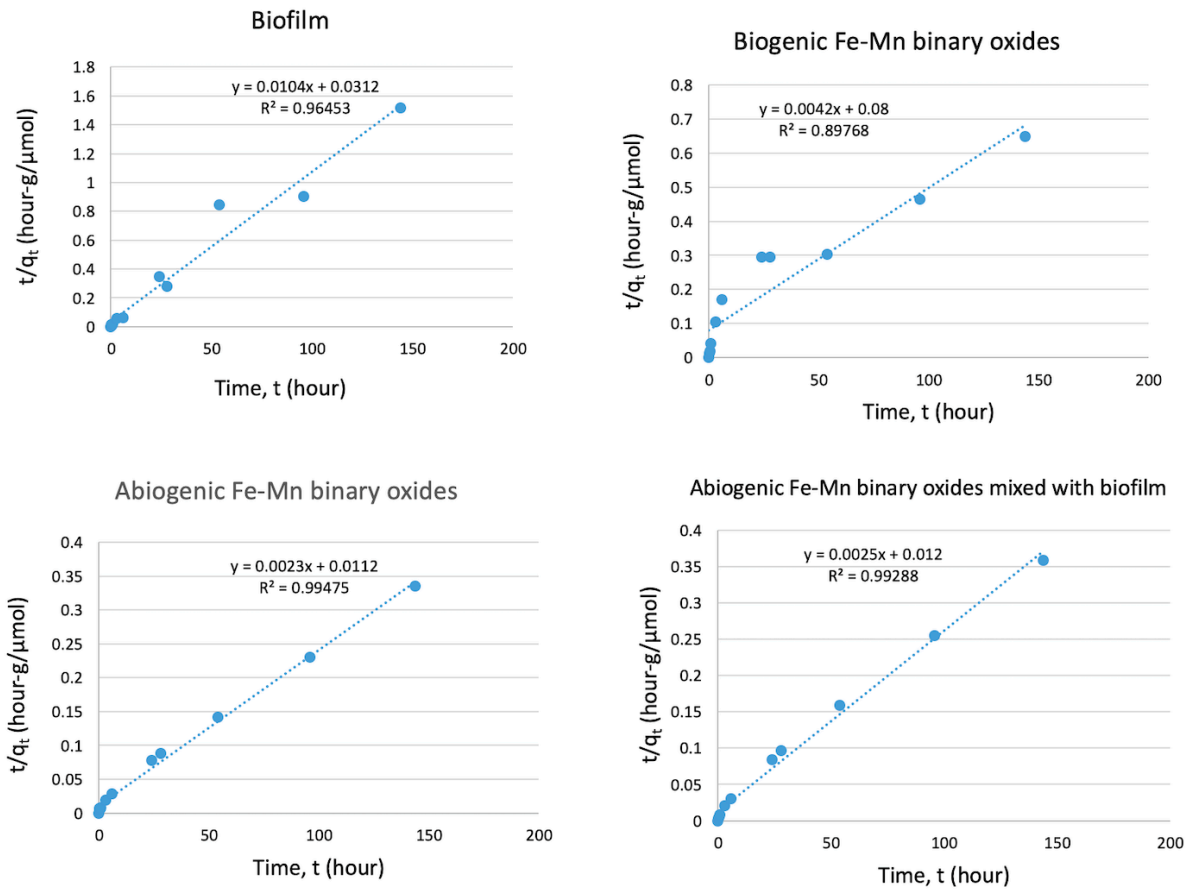


Figure 4-A4: Linearized Langmuir isotherm t/q_t vs t plots for As(V) adsorption on biofilm, biogenic Fe-Mn binary oxides, abiogenic Fe-Mn binary oxides and abiogenic Fe-Mn binary oxides mixed with biofilm.



Figure 4-A5: Images of biofilms in mineralization media (after 7days of growth).

Bibliography

Abbas, G., Murtaza, B., Bibi, I., Shahid, M., Niazi, N.K., Khan, M.I., Amjad, M., Hussain, M. and Natasha, 2018. Arsenic uptake, toxicity, detoxification, and speciation in plants: physiological, biochemical, and molecular aspects. International journal of environmental research and public health, 15(1), p.59.

Abdus-Salam, N. and M'civer, F.A., 2012. Synthesis, characterization and application of 2-Line and 6-Line ferrihydrite to Pb (II) removal from aqueous solution. Journal of Applied Sciences and Environmental Management, 16(4).

Acelas, N.Y. and Flórez, E., 2017, December. Adsorption of arsenate on Fe-(hydr) oxide. In Journal of Physics: Conference Series (Vol. 935, No. 1, p. 012074). IOP Publishing.

Acharyya, S.K., Chakraborty, P., Lahiri, S., Raymahashay, B.C., Guha, S. and Bhowmik, A., 1999. Arsenic poisoning in the Ganges delta. Nature, 401(6753), pp.545-545.

Ahmad, S.A. and Khan, M.H., 2023. Groundwater arsenic contamination and its health effects in Bangladesh. In Handbook of Arsenic Toxicology (pp. 51-77). Academic Press.

Alafnan, S., Awotunde, A., Glatz, G., Adjei, S., Alrumaih, I. and Gowida, A., 2021. Langmuir adsorption isotherm in unconventional resources: Applicability and limitations. Journal of Petroleum Science and Engineering, 207, p.109172.

Alhariri, M., Majrashi, M.A., Bahkali, A.H., Almajed, F.S., Azghani, A.O., Khiyami, M.A., Alyamani, E.J., Aljohani, S.M. and Halwani, M.A., 2017. Efficacy of neutral and negatively charged liposome-loaded gentamicin on planktonic bacteria and biofilm communities. International journal of nanomedicine, pp.6949-6961.

Alka, S., Shahir, S., Ibrahim, N., Ndejiko, M.J., Vo, D.V.N. and Abd Manan, F., 2021. Arsenic removal technologies and future trends: A mini review. Journal of cleaner production, 278, p.123805.

Amirbahman, A., Kent, D.B., Curtis, G.P. and Davis, J.A., 2006. Kinetics of sorption and abiotic oxidation of arsenic (III) by aquifer materials. Geochimica et Cosmochimica Acta, 70(3), pp.533-547.

Amstaetter, K., Borch, T., Larese-Casanova, P. and Kappler, A., 2010. Redox transformation of arsenic by Fe (II)-activated goethite (α-FeOOH). Environmental science & technology, 44(1), pp.102-108.

Anawar, H.M., Akai, J. and Sakugawa, H., 2004. Mobilization of arsenic from subsurface sediments by effect of bicarbonate ions in groundwater. Chemosphere, 54(6), pp.753-762.

Anderson, L.C. and Bruland, K.W., 1991. Biogeochemistry of arsenic in natural waters: the importance of methylated species. Environmental science & technology, 25(3), pp.420-427.

Antelo, J., Avena, M., Fiol, S., López, R. and Arce, F., 2005. Effects of pH and ionic strength on the adsorption of phosphate and arsenate at the goethite–water interface. Journal of colloid and interface science, 285(2), pp.476-486.

Antelo, J., Fiol, S., Pérez, C., Mariño, S., Arce, F., Gondar, D. and López, R., 2010. Analysis of phosphate adsorption onto ferrihydrite using the CD-MUSIC model. Journal of Colloid and Interface Science, 347(1), pp.112-119.

Appelo, C.A.J., Van der Weiden, M.J.J., Tournassat, C. and Charlet, L., 2002. Surface complexation of ferrous iron and carbonate on ferrihydrite and the mobilization of arsenic. Environmental Science & Technology, 36(14), pp.3096-3103.

Arias, N.P., Becerra, M.E. and Giraldo, O., 2019. Structural and electrical studies for birnessite-type materials synthesized by solid-state reactions. Nanomaterials, 9(8), p.1156.

Aronson, S.M., 1994. Arsenic and old myths. RI Med., 77, pp.233-234.

ATSDR. 2000. Toxicological Profile for Manganese. U.S. Department of Health and Human Services, Public Health Service, Agency for Toxic Substances and Disease Registry, Atlanta, GA.

Ayawei, N., Ebelegi, A.N. and Wankasi, D., 2017. Modelling and interpretation of adsorption isotherms. Journal of chemistry, 2017(1), p.3039817.

Bábek, O., Sracek, O., Všianský, D. and Holá, M., 2023. Groundwater red beds in Holocene fluvial sediments as a product of iron and manganese redox cycling; Morava River, Czechia. Sedimentology, 70(7), pp.2220-2240.

Bai, Y., Liu, R., Liang, J. and Qu, J., 2013. Integrated metagenomic and physiochemical analyses to evaluate the potential role of microbes in the sand filter of a drinking water treatment system. PLoS One, 8(4), p.e61011.

Bai, Y., Yang, T., Liang, J. and Qu, J., 2016. The role of biogenic Fe-Mn oxides formed in situ for arsenic oxidation and adsorption in aquatic ecosystems. Water research, 98, pp.119-127.

Barceloux, D.G., 1999. Manganese. Clinical Toxicology, 37, pp.293-307.

Battaglia-Brunet, F., Dictor, M.C., Garrido, F., Crouzet, C., Morin, D., Dekeyser, K., Clarens, M. and Baranger, P., 2002. An arsenic (III)-oxidizing bacterial population: selection, characterization, and performance in reactors. Journal of applied microbiology, 93(4), pp.656-667.

Battistel, M., Stolze, L., Muniruzzaman, M. and Rolle, M., 2021. Arsenic release and transport during oxidative dissolution of spatially-distributed sulfide minerals. Journal of Hazardous Materials, 409, p.124651.

Bauer, M. and Blodau, C., 2006. Mobilization of arsenic by dissolved organic matter from iron oxides, soils and sediments. Science of the Total Environment, 354(2-3), pp.179-190.

Behbahani, S.B., Kiridena, S.D., Wijayaratna, U.N., Taylor, C., Anker, J.N. and Tzeng, T.R.J., 2022. pH variation in medical implant biofilms: Causes, measurements, and its implications for antibiotic resistance. Frontiers in Microbiology, 13, p.1028560.

Benis, K.Z., Damuchali, A.M., Soltan, J. and McPhedran, K.N., 2020. Treatment of aqueous arsenic–A review of biochar modification methods. Science of The Total Environment, 739, p.139750.

Benner, S.G. and Fendorf, S., 2010. Arsenic in south Asia groundwater. Geography Compass, 4(10), pp.1532-1552.

Bennett, B. and Dudas, M.J., 2003. Release of arsenic and molybdenum by reductive dissolution of iron oxides in a soil with enriched levels of native arsenic. Journal of Environmental Engineering and Science, 2(4), pp.265-272.

Benzerara, K. and Menguy, N., 2009. Looking for traces of life in minerals. Comptes Rendus Palevol, 8(7), pp.617-628.

Benzerara, K., Miot, J., Morin, G., Ona-Nguema, G., Skouri-Panet, F. and Férard, C., 2011. Significance, mechanisms and environmental implications of microbial biomineralization. Comptes Rendus. Géoscience, 343(2-3), pp.160-167.

Berger, A.H. and Bhown, A.S., 2011. Comparing physisorption and chemisorption solid sorbents for use separating CO2 from flue gas using temperature swing adsorption. Energy Procedia, 4, pp.562-567.

BGS (British Geological Survey), 2001. Arsenic contamination of groundwater in Bangladesh, D.G. Kinniburgh, P.L. Smedley (Eds.), Technical Report, WC/00/19, volumes 4.

Bhattacharya, S., Gupta, K., Debnath, S., Ghosh, U.C., Chattopadhyay, D. and Mukhopadhyay, A., 2012. Arsenic bioaccumulation in rice and edible plants and subsequent transmission through food chain in Bengal basin: a review of the perspectives for environmental health. Toxicological & Environmental Chemistry, 94(3), pp.429-441.

Billinge, S.J., & Levin, I. (2007). The Problem with Determining Atomic Structure at the Nanoscale. Science, 316, 561 - 565.

Bondar, Y.V. and Alekseev, S.A., 2020. Synthesis and evaluation of manganese dioxide with layered structure as an adsorbent for selective removal of strontium ions from aqueous solution. SN Applied Sciences, 2(8), p.1379.

Borch, T., Kretzschmar, R., Kappler, A., Cappellen, P.V., Ginder-Vogel, M., Voegelin, A. and Campbell, K., 2010. Biogeochemical redox processes and their impact on contaminant dynamics. Environmental science & technology, 44(1), pp.15-23.

Branda, S.S., Vik, Å., Friedman, L. and Kolter, R., 2005. Biofilms: the matrix revisited. Trends in microbiology, 13(1), pp.20-26.

Brunauer, S., Emmett, P.H. and Teller, E., 1938. Adsorption of gases in multimolecular layers. Journal of the American chemical society, 60(2), pp.309-319.

Burleson, D.J. and Penn, R.L., 2006. Two-step growth of goethite from ferrihydrite. Langmuir, 22(1), pp.402-409.

Byanjankar, N., Joshi, T.P., Dhakal, A., Joshi, D.R., Koju, R., Qi, Z., Hu, C. and Liu, R., 2024. Removal of Dimethyl Arsenic Acid from Aqueous Solution by Ferric Manganese Binary Oxide. Water, Air, & Soil Pollution, 235(3), p.196.

Cai, X., ThomasArrigo, L.K., Fang, X., Bouchet, S., Cui, Y. and Kretzschmar, R., 2020. Impact of organic matter on microbially-mediated reduction and mobilization of arsenic and iron in arsenic (V)-bearing ferrihydrite. Environmental Science & Technology, 55(2), pp.1319-1328.

Cai, Y., Yang, K., Qiu, C., Bi, Y., Tian, B. and Bi, X., 2023. A review of manganese-oxidizing bacteria (MnOB): Applications, future concerns, and challenges. International Journal of Environmental Research and Public Health, 20(2), p.1272.

Camacho, L.M., Gutiérrez, M., Alarcón-Herrera, M.T., de Lourdes Villalba, M. and Deng, S., 2011. Occurrence and treatment of arsenic in groundwater and soil in northern Mexico and southwestern USA. Chemosphere, 83(3), pp.211-225.

Campbell, K.M., Malasarn, D., Saltikov, C.W., Newman, D.K. and Hering, J.G., 2006. Simultaneous microbial reduction of iron (III) and arsenic (V) in suspensions of hydrous ferric oxide. Environmental science & technology, 40(19), pp.5950-5955.

Campos-Pereira, H., Kleja, D.B., Sjöstedt, C., Ahrens, L., Klysubun, W. and Gustafsson, J.P., 2020. The adsorption of per-and polyfluoroalkyl substances (PFASs) onto ferrihydrite is governed by surface charge. Environmental science & technology, 54(24), pp.15722-15730.

Cannon, W.F., Jr., 2014. Manganese—It turns iron into steel (and does so much more): US Geological Survey Fact Sheet 2014–3087, 2 p., https://dx.doi.org/10.3133/fs20143087.

Carabante, I., 2012. Arsenic (V) adsorption on iron oxide: implications for soil remediation and water purification (Doctoral dissertation, Luleå tekniska universitet).

Caspi, R., Tebo, B.M. and Haygood, M.G., 1998. c-type cytochromes and manganese oxidation in Pseudomonas putida MnB1. Applied and environmental Microbiology, 64(10), pp.3549-3555.

Chang, F., Qu, J., Liu, H., Liu, R. and Zhao, X., 2009. Fe–Mn binary oxide incorporated into diatomite as an adsorbent for arsenite removal: preparation and evaluation. Journal of Colloid and Interface Science, 338(2), pp.353-358.

Chen P, Bornhorst J, Aschner M., 2018. Manganese metabolism in humans. Frontiers in Bioscience (Landmark Ed), 23(9), pp.1655-1679. doi: 10.2741/4665. PMID: 29293455.

Chen, C., Wang, G., Li, M., Chen, X., Chen, D., Feng, Z., Jiang, Y., Yu, H., Chao, Y., Tang, Y. and Qiu, R., 2023. Mechanism of arsenic immobilization and biotransformation in the biological aqua crust of mine drainage. Science of The Total Environment, 892, p.164230.

Chen, G., Shi, H., Tao, J., Chen, L., Liu, Y., Lei, G., Liu, X. and Smol, J.P., 2015. Industrial arsenic contamination causes catastrophic changes in freshwater ecosystems. Scientific reports, 5(1), p.17419.

Chen, M., Xie, Z., Yang, Y., Gao, B. and Wang, J., 2022. Effects of calcium on arsenate adsorption and arsenate/iron bioreduction of ferrihydrite in stimulated groundwater. International Journal of Environmental Research and Public Health, 19(6), p.3465.

Chen, Y., Liu, Y., Li, Y., Wu, Y., Chen, Y., Liu, Y., Zhang, J., Xu, F., Li, M. and Li, L., 2020. Synthesis, application and mechanisms of Ferro-Manganese binary oxide in water remediation: A review. Chemical Engineering Journal, 388, p.124313.

Chinoune, K., Bentaleb, K., Bouberka, Z., Nadim, A. and Maschke, U., 2016. Adsorption of reactive dyes from aqueous solution by dirty bentonite. Applied Clay Science, 123, pp.64-75.

Chowdhury, T.R., Basu, G.K., Samanta, G., Chanda, C.R., Mandal, B.K., Dhar, R.K., et al., 1999. Arsenic poisoning of Bangladesh groundwater. Nature, 401, pp.545–546.

Cieschi, M.T., de Francisco, M., Herrero, P., Sánchez-Marcos, J., Cuevas, J., Esteban, E., Lucena, J.J. and Yunta, F., 2021. Synthesis and characterization of nano Fe and Mn (hydr)

oxides to be used as natural sorbents and micronutrient fertilizers. Agronomy, 11(9), p.1876.

Cismasu, AC, Michel, FM, Tcaciuc, AP, Tyliszczak, T. and Brown Jr, GE, 2011. Composition and structural aspects of naturally occurring ferrihydrite. Reports. Geoscience, 343 (2-3), pp.210-218.

Clement, B.G., Luther III, G.W. and Tebo, B.M., 2009. Rapid, oxygen-dependent microbial Mn (II) oxidation kinetics at sub-micromolar oxygen concentrations in the Black Sea suboxic zone. Geochimica et Cosmochimica Acta, 73(7), pp.1878-1889.

Cohen, S.M., Arnold, L.L. and Tsuji, J.S., 2019. Inorganic arsenic: a nongenotoxic threshold carcinogen. Current Opinion in Toxicology, 14, pp.8-13.

Cohen, S.M., Arnold, L.L., Beck, B.D., Lewis, A.S. and Eldan, M., 2013. Evaluation of the carcinogenicity of inorganic arsenic. Critical reviews in toxicology, 43(9), pp.711-752.

Cornell, R.M. and Schwertmann, U., 2003. The iron oxides: structure, properties, reactions, occurrences, and uses (Vol. 664). Weinheim: Wiley-vch.

Cosmidis, J., Benzerara, K., Menguy, N. and Arning, E., 2013. Microscopy evidence of bacterial microfossils in phosphorite crusts of the Peruvian shelf: Implications for phosphogenesis mechanisms. Chemical Geology, 359, pp.10-22.

Cosmidis, J., Benzerara, K., Morin, G., Busigny, V., Lebeau, O., Jézéquel, D., Noël, V., Dublet, G. and Othmane, G., 2014. Biomineralization of iron-phosphates in the water column of Lake Pavin (Massif Central, France). Geochimica et Cosmochimica Acta, 126, pp.78-96.

Cosmidis, J. and Benzerara, K., 2022. Why do microbes make minerals?. Comptes Rendus. Géoscience, 354, pp.1-39.

Couradeau, E., Benzerara, K., Gérard, E., Moreira, D., Bernard, S., Brown Jr, G.E. and López-García, P., 2012. An early-branching microbialite cyanobacterium forms intracellular carbonates. Science, 336(6080), pp.459-462.

Courville, P., Chaloupka, R. and Cellier, M.F.M., 2006. Recent progress in structure–function analyses of Nramp proton-dependent metal-ion transporters. Biochemistry and Cell Biology, 84(6), pp.960-978.

Couture, R.M., Rose, J., Kumar, N., Mitchell, K., Wallschlager, D. and Van Cappellen, P., 2013. Sorption of arsenite, arsenate, and thioarsenates to iron oxides and iron sulfides: a kinetic and spectroscopic investigation. Environmental science & technology, 47(11), pp.5652-5659.

Crognale, S., Casentini, B., Amalfitano, S., Fazi, S., Petruccioli, M. and Rossetti, S., 2019. Biological As (III) oxidation in biofilters by using native groundwater microorganisms. Science of the Total Environment, 651, pp.93-102.

Culotta, V.C. and Daly, M.J., 2013. Manganese complexes: diverse metabolic routes to oxidative stress resistance in prokaryotes and yeast. Antioxidants & redox signaling, 19(9), pp.933-944.

Das, N.K. and Sengupta, S.R., 2008. Arsenicosis: diagnosis and treatment. Indian journal of dermatology, venereology and leprology, 74, p.571.

Das, S., Hendry, M.J. and Essilfie-Dughan, J., 2013. Adsorption of selenate onto ferrihydrite, goethite, and lepidocrocite under neutral pH conditions. Applied geochemistry, 28, pp.185-193.

Das, T.K. and Bezbaruah, A.N., 2021. Comparative study of arsenic removal by iron-based nanomaterials: Potential candidates for field applications. Science of the Total Environment, 764, p.142914.

De Yoreo, J.J. and Vekilov, P.G., 2003. Principles of crystal nucleation and growth. Reviews in mineralogy and geochemistry, 54(1), pp.57-93.

Dehouck, E., McLennan, S.M., Sklute, E.C. and Dyar, M.D., 2017. Stability and fate of ferrihydrite during episodes of water/rock interactions on early Mars: An experimental approach. Journal of Geophysical Research: Planets, 122(2), pp.358-382.

Deng, Z., Jia, Z. and Li, L., 2022. Biomineralized materials as model systems for structural composites: Intracrystalline structural features and their strengthening and toughening mechanisms. Advanced Science, 9(14), p.2103524.

Diem D. and Stumm W. (1984) Is dissolved Mn^{2+} being oxidized by O_2 in absence of Mn-bacteria or surface catalysts. Geochimica Et Cosmochimica Acta 48, 1571–1573.

Dixit, S., Hering, J. G., 2003. Comparison of Arsenic(V) and Arsenic(III) sorption onto iron oxide minerals: implications for arsenic mobility. Environmental Science & Technology, 37, pp.4182-4189.

Donlan, R.M. and Costerton, J.W., 2002. Biofilms: survival mechanisms of clinically relevant microorganisms. Clinical microbiology reviews, 15(2), pp.167-193.

Donlan, R.M., 2002. Biofilms: microbial life on surfaces. Emerging infectious diseases, 8(9), p.881.

Dragun J., Chiasson A., 1991. Elements in North American Soils, Hazardous Materials Control Resources Institute, Greenbelt, Maryland.

Dublet, G., Pacheco, J.L., Bargar, J.R., Fendorf, S., Kumar, N., Lowry, G.V. and Brown Jr, G.E., 2017. Partitioning of uranyl between ferrihydrite and humic substances at acidic and circum-neutral pH. Geochimica et Cosmochimica Acta, 215, pp.122-140.

Dzieniszewska, A., Kyziol-Komosinska, J. and Pająk, M., 2020. Adsorption and bonding strength of chromium species by ferrihydrite from acidic aqueous solutions. PeerJ, 8, p.e9324.

Dzombak, D.A. and Morel, F.M., 1991. Surface complexation modeling: hydrous ferric oxide. John Wiley & Sons.

Edwards, K.J., Glazer, B.T., Rouxel, O.J., Bach, W., Emerson, D., Davis, R.E., Toner, B.M., Chan, C.S., Tebo, B.M., Staudigel, H. and Moyer, C.L., 2011. Ultra-diffuse hydrothermal venting supports Fe-oxidizing bacteria and massive umber deposition at 5000 m off Hawaii. The ISME Journal, 5(11), pp.1748-1758.

Ehlert, K., Mikutta, C. and Kretzschmar, R., 2014. Impact of birnessite on arsenic and iron speciation during microbial reduction of arsenic-bearing ferrihydrite. Environmental science & technology, 48(19), pp.11320-11329.

El Haddad, M., Slimani, R., Mamouni, R., ElAntri, S. and Lazar, S., 2013. Removal of two textile dyes from aqueous solutions onto calcined bones. Journal of the Association of Arab Universities for Basic and Applied Sciences, 14(1), pp.51-59.

Emerson, D., 2000. Microbial oxidation of Fe(ll) and Mn(ll) at circumneutral pH. In: Environmental Microbemineral Interactions. Lovley DR (ed) ASM Press, Washington D.C., p 53-78.

Emerson, D., Fleming, E.J. and McBeth, J.M., 2010. Iron-oxidizing bacteria: an environmental and genomic perspective. Annual review of microbiology, 64(1), pp.561-583.

EPA. 1984. Health assessment document for manganese. Final draft. Cincinnati, OH: U.S. Environmental Protection Agency, Office of Research and Development. EPA600883013F.

Estes, E.R., Andeer, P.F., Nordlund, D., Wankel, S.D. and Hansel, C.M., 2017. Biogenic manganese oxides as reservoirs of organic carbon and proteins in terrestrial and marine environments. Geobiology, 15(1), pp.158-172.

Farrell, J. and Chaudhary, B.K., 2013. Understanding arsenate reaction kinetics with ferric hydroxides. Environmental science & technology, 47(15), pp.8342-8347.

Farzan, S.F., Karagas, M.R. and Chen, Y., 2013. In utero and early life arsenic exposure in relation to long-term health and disease. Toxicology and applied pharmacology, 272(2), pp.384-390.

Fathollahi, A. and Coupe, S.J., 2021. Effect of environmental and nutritional conditions on the formation of single and mixed-species biofilms and their efficiency in cadmium removal. Chemosphere, 283, p.131152.

Feher, J. 2017. Protein Structure In Quantitative Human Physiology. Editor(s): Joseph Feher, Second Edition, Academic Press, pp.130-141. ISBN 9780128008836, https://doi.org/10.1016/B978-0-12-800883-6.00012-4.

Fendorf, S., Eick, M.J., Grossl, P. and Sparks, D.L., 1997. Arsenate and chromate retention mechanisms on goethite. 1. Surface structure. Environmental science & technology, 31(2), pp.315-320.

Fendorf, S., Michael H.A., van Geen, A., 2010. Spatial and temporal variations of groundwater arsenic in South and Southeast Asia. Science, 328, pp. 1123–1127.

Feng, X.H., Zhu, M., Ginder-Vogel, M., Ni, C., Parikh, S.J. and Sparks, D.L., 2010. Formation of nano-crystalline todorokite from biogenic Mn oxides. Geochimica et Cosmochimica Acta, 74(11), pp.3232-3245.

Fischel, M.H., Clarke, C.E. and Sparks, D.L., 2024. Arsenic sorption and oxidation by natural manganese-oxide-enriched soils: Reaction kinetics respond to varying environmental conditions. Geoderma, 441, p.116715.

Flemming, H.C., Wingender J., Griegbe, Mayer, C., 2000. Physico-chemical properties of biofilms In: Evans LV, editor. Biofilms: recent advances in their study and control. Harwood Academic Publishers, Amsterdam, p.19–34.

Flemming, H.C. and Wingender, J., 2010. The biofilm matrix. Nature reviews microbiology, 8(9), pp.623-633.

Foo, K.Y. and Hameed, B.H., 2010. Insights into the modeling of adsorption isotherm systems. Chemical engineering journal, 156(1), pp.2-10.

Fortin, D. and Langley, S., 2005. Formation and occurrence of biogenic iron-rich minerals. Earth-Science Reviews, 72(1-2), pp.1-19.

Franca, A.S., Oliveira, L.S. and Ferreira, M.E., 2009. Kinetics and equilibrium studies of methylene blue adsorption by spent coffee grounds. Desalination, 249(1), pp.267-272.

Francis, C.A. and Tebo, B.M., 2001. cumA multicopper oxidase genes from diverse Mn (II)-oxidizing and non-Mn (II)-oxidizing Pseudomonas strains. Applied and Environmental Microbiology, 67(9), pp.4272-4278.

Francis, C.A. and Tebo, B.M., 2002. Enzymatic manganese (II) oxidation by metabolically dormant spores of diverse Bacillus species. Applied and Environmental Microbiology, 68(2), pp.874-880.

Freundlich, H., 1907. Über die adsorption in lösungen. Zeitschrift für physikalische Chemie, 57(1), pp.385-470.

Frisbie, S.H., Ortega, R., Maynard, D.M. and Sarkar, B., 2002. The concentrations of arsenic and other toxic elements in Bangladesh's drinking water. Environmental Health Perspectives, 110(11), pp.1147-1153.

Fukushi, K. and Sverjensky, D.A., 2007. A predictive model (ETLM) for arsenate adsorption and surface speciation on oxides consistent with spectroscopic and theoretical molecular evidence. Geochimica et cosmochimica acta, 71(15), pp.3717-3745.

Funnell, N.P., Fulford, M.F., Inoué, S. et al., 2020. Nanocomposite structure of two-line ferrihydrite powder from total scattering. Communications Chemistry, 3, p.22. https://doi.org/10.1038/s42004-020-0269-2.

Galezowski, L., Recham, N., Larcher, D., Miot, J., Skouri-Panet, F. and Guyot, F., 2020. Microbially induced mineralization of layered Mn oxides electroactive in Li batteries. Frontiers in microbiology, 11, p.2031.

Gao, T., Shen, Y., Jia, Z., Qiu, G., Liu, F., Zhang, Y., Feng, X. and Cai, C., 2015. Interaction mechanisms and kinetics of ferrous ion and hexagonal birnessite in aqueous systems. Geochemical transactions, 16, pp.1-14.

Garelick, H., Jones, H., Dybowska, A. and Valsami-Jones, E., 2008. Arsenic pollution sources. Reviews of environmental contamination volume 197: International perspectives on arsenic pollution and remediation, pp.17-60.

Genç-Fuhrman, H., Tjell, J.C. and McConchie, D., 2004. Adsorption of arsenic from water using activated neutralized red mud. Environmental Science & Technology, 38(8), pp.2428-2434

Genchi, G., Lauria, G., Catalano, A., Carocci, A. and Sinicropi, M.S., 2022. Arsenic: a review on a great health issue worldwide. Applied Sciences, 12(12), p.6184.

Ghosal, P.S. and Gupta, A.K., 2017. Development of a generalized adsorption isotherm model at solid-liquid interface: A novel approach. Journal of Molecular Liquids, 240, pp.21-24.

Gilbert, P.U.P.A., Abrecht, M. and Frazer, B.H., 2005. The organic-mineral interface in biominerals. Reviews in Mineralogy and Geochemistry, 59(1), pp.157-185.

Gimsing, A.L. and Borggaard, O.K., 2007. Phosphate and glyphosate adsorption by hematite and ferrihydrite and comparison with other variable-charge minerals. Clays and Clay Minerals, 55(1), pp.108-114.

Glodowska, M., Schneider, M., Eiche, E., Kontny, A., Neumann, T., Straub, D., Kleindienst, S., Kappler, A., 2021. Microbial transformation of biogenic and abiogenic Fe minerals followed by in-situ incubations in an As-contaminated vs. non-contaminated aquifer. Environmental Pollution, 281, p.117012.

Goldberg, S. and Johnston, C.T., 2001. Mechanisms of arsenic adsorption on amorphous oxides evaluated using macroscopic measurements, vibrational spectroscopy, and surface complexation modeling. Journal of colloid and Interface Science, 234(1), pp.204-216.

Granados-Correa, F. and Bulbulian, S., 2012. Co (II) adsorption in aqueous media by a synthetic Fe–Mn binary oxide adsorbent. Water, Air, & Soil Pollution, 223, pp.4089-4100.

Guibaud, G., van Hullebusch, E., Bordas, F., d'Abzac, P. and Joussein, E., 2009. Sorption of Cd (II) and Pb (II) by exopolymeric substances (EPS) extracted from activated sludges and pure bacterial strains: modeling of the metal/ligand ratio effect and role of the mineral fraction. Bioresource Technology, 100(12), pp.2959-2968.

Gunawardana, C., Egodawatta, P. and Goonetilleke, A., 2014. Role of particle size and composition in metal adsorption by solids deposited on urban road surfaces. Environmental pollution, 184, pp.44-53.

Guo, H.M., Yang, S.Z., Tang, X.H., Li, Y., Shen, Z.L., 2008. Groundwater geochemistry and its implications for arsenic mobilization in shallow aquifers of the Hetao Basin, Inner Mongolia. Science of The Total Environment, 393 (1), pp.131–144.

Guo, X. and Wang, J., 2019. Comparison of linearization methods for modeling the Langmuir adsorption isotherm. Journal of Molecular Liquids, 296, p.111850.

Gupta, S.K. and Chen, K.Y., 1978. Arsenic removal by adsorption. Journal (Water Pollution Control Federation), pp.493-506.

Hafenbradl, D., Keller, M., Dirmeier, R., Rachel, R., Roßnagel, P., Burggraf, S., Huber, H. and Stetter, K.O., 1996. Ferroglobus placidus gen. nov., sp. nov., a novel hyperthermophilic archaeum that oxidizes Fe^{2+} at neutral pH under anoxic conditions. Archives of microbiology, 166, pp.308-314.

Hall-Stoodley, L. and Stoodley, P., 2009. Evolving concepts in biofilm infections. Cellular microbiology, 11(7), pp.1034-1043.

Han, F.X., Su, Y., Monts, D.L., Plodinec, M.J., Banin, A. and Triplett, G.E., 2003. Assessment of global industrial-age anthropogenic arsenic contamination. Naturwissenschaften, 90, pp.395-401.

Hand, D.W., Crittenden, J.C. and Thacker, W.E., 1983. User-oriented batch reactor solutions to the homogeneous surface diffusion model. Journal of Environmental Engineering, 109(1), pp.82-101.

Handley, K.M. and Lloyd, J.R., 2013. Biogeochemical implications of the ubiquitous colonization of marine habitats and redox gradients by Marinobacter species. Frontiers in microbiology, 4, p.136.

Hansel, C.M., 2017. Manganese in marine microbiology. Advances in microbial physiology, 70, pp.37-83.

Hao, L., Guo, Y., Byrne, J.M., Zeitvogel, F., Schmid, G., Ingino, P., Li, J., Neu, T.R., Swanner, E.D., Kappler, A. and Obst, M., 2016. Binding of heavy metal ions in aggregates of microbial cells, EPS and biogenic iron minerals measured in-situ using metal-and glycoconjugates-specific fluorophores. Geochimica et Cosmochimica Acta, 180, pp.66-96.

Hao, L., Liu, M., Wang, N. and Li, G., 2018. A critical review on arsenic removal from water using iron-based adsorbents. RSC advances, 8(69), pp.39545-39560.

Harben, P.W. and Bates, R.L., 1990. Industrial Minerals - Geology and World Deposits. Industrial Minerals Division, Metal Bulletin Plc, London.

Hashimoto, H., Kobayashi, G., Sakuma, R., Fujii, T., Hayashi, N., Suzuki, T., Kanno, R., Takano, M. and Takada, J., 2014. Bacterial nanometric amorphous Fe-based oxide: a potential lithium-ion battery anode material. ACS applied materials & interfaces, 6(8), pp.5374-5378.

Hassan, F.I., Niaz, K., Khan, F., Maqbool, F. and Abdollahi, M., 2017. The relation between rice consumption, arsenic contamination, and prevalence of diabetes in South Asia. EXCLI journal, 16, p.1132.

He, K.Q., Yuan, C.G., Jiang, Y.H., Duan, X.L., Li, Y. and Shi, M.D., 2021. Synergistic effects of Fe-Mn binary oxide for gaseous arsenic removal in flue gas. Ecotoxicology and Environmental Safety, 207, p.111491.

He, Z., Zhang, Q., Wei, Z., Wang, S. and Pan, X., 2019. Multiple-pathway arsenic oxidation and removal from wastewater by a novel manganese-oxidizing aerobic granular sludge. Water Research, 157, pp.83-93.

Hecht, H. and Oguchi, T., 2017. Global evaluation of erosion rates in relation to tectonics. Progress in Earth and Planetary Science, 4, pp.1-9.

Hiemstra, T. and Van Riemsdijk, W.H., 2009. A surface structural model for ferrihydrite I: Sites related to primary charge, molar mass, and mass density. Geochimica et Cosmochimica Acta, 73(15), pp.4423-4436.

Hiemstra, T., 2018. Ferrihydrite interaction with silicate and competing oxyanions: geometry and hydrogen bonding of surface species. Geochimica et Cosmochimica Acta, 238, pp.453-476.

Hiemstra, T., Mendez, J.C. and Li, J., 2019. Evolution of the reactive surface area of ferrihydrite: time, pH, and temperature dependency of growth by Ostwald ripening. Environmental Science: Nano, 6(3), pp.820-833.

Ho, Y.S. and McKay, G., 1998. A comparison of chemisorption kinetic models applied to pollutant removal on various sorbents. Process safety and environmental protection, 76(4), pp.332-340.

Ho, Y.S. and McKay, G., 1999. Pseudo-second order model for sorption processes. Process biochemistry, 34(5), pp.451-465.

Ho, Y.S., Ng, J.C.Y. and McKay, G., 2000. Kinetics of pollutant sorption by biosorbents. Separation and purification methods, 29(2), pp.189-232.

Hofmann, A., Pelletier, M., Michot, L., Stradner, A., Schurtenberger, P. and Kretzschmar, R., 2004. Characterization of the pores in hydrous ferric oxide aggregates formed by freezing and thawing. Journal of colloid and interface science, 271(1), pp.163-173.

Hohmann, C., Morin, G., Ona-Nguema, G., Guigner, J.M., Brown Jr, G.E. and Kappler, A., 2011. Molecular-level modes of As binding to Fe (III)(oxyhydr) oxides precipitated by the anaerobic nitrate-reducing Fe (II)-oxidizing Acidovorax sp. strain BoFeN1. Geochimica et Cosmochimica Acta, 75(17), pp.4699-4712.

Hohmann, C., Winkler, E., Morin, G. and Kappler, A., 2010. Anaerobic Fe (II)-oxidizing bacteria show As resistance and immobilize As during Fe (III) mineral precipitation. Environmental science & technology, 44(1), pp.94-101.

Hou, J., Xiang, Y., Zheng, D., Li, Y., Xue, S., Wu, C., Hartley, W. and Tan, W., 2017. Morphology-dependent enhancement of arsenite oxidation to arsenate on birnessite-type manganese oxide. Chemical Engineering Journal, 327, pp.235-243.

Hu, H., Zhang, Q., Wang, C., Chen, M. and Chen, M., 2022. Mechanochemically synthesized Fe-Mn binary oxides for efficient As (III) removal: insight into the origin of synergy action from mutual Fe and Mn doping. Journal of Hazardous Materials, 424, p.127708.

Huang, L., Jin, Y., Zhou, D., Liu, L., Huang, S., Zhao, Y. and Chen, Y., 2022. A review of the role of extracellular polymeric substances (EPS) in wastewater treatment systems. International journal of environmental research and public health, 19(19), p.12191.

Huang, J.H., 2018. Characterising microbial reduction of arsenate sorbed to ferrihydrite and its concurrence with iron reduction. Chemosphere, 194, pp.49-56.

Huang, Y., Gao, M., Deng, Y., Khan, Z.H., Liu, X., Song, Z. and Qiu, W., 2020. Efficient oxidation and adsorption of As (III) and As (V) in water using a Fenton-like reagent,(ferrihydrite)-loaded biochar. Science of the total environment, 715, p.136957.

Islam, F.S., Gault, A.G., Boothman, C., Polya, D.A., Chatterjee, D. and Lloyd, J.R., 2004. Direct evidence of arsenic release from Bengali sediments due to metal-reducing bacteria. Nature, 430, pp.68-71.

Jacks, G. and Bhattacharya, P., 1998. Arsenic contamination in the environment due to the use of CCA-wood preservatives. Arsenic in Wood Preservatives. Part, 1(7), p.75.

Jackson, B.P. and Miller, W.P., 2000. Effectiveness of phosphate and hydroxide for desorption of arsenic and selenium species from iron oxides. Soil Science Society of America Journal, 64(5), pp.1616-1622.

Jain, A. and Loeppert, R.H., 2000. Effect of competing anions on the adsorption of arsenate and arsenite by ferrihydrite (Vol. 29, No. 5, pp. 1422-1430). American Society of Agronomy, Crop Science Society of America, and Soil Science Society of America.

Jain, A. and Loeppert, R.H., 2000. Effect of competing anions on the adsorption of arsenate and arsenite by ferrihydrite. Journal of Environmental Quality, 29(5), pp.1422-1430.

Jambor, J.L. and Dutrizac, J.E., 1998. Occurrence and constitution of natural and synthetic ferrihydrite, a widespread iron oxyhydroxide. Chemical reviews, 98(7), pp.2549-2586.

Jansen, B. and Kohnen, W., 1995. Prevention of biofilm formation by polymer modification. Journal of industrial microbiology and biotechnology, 15(4), pp.391-396.

Jia, Y. and Demopoulos, G.P., 2005. Adsorption of arsenate onto ferrihydrite from aqueous solution: influence of media (sulfate vs nitrate), added gypsum, and pH alteration. Environmental Science & Technology, 39(24), pp.9523-9527.

Jiang, L., Xiao, S. and Chen, J., 2015. Removal behavior and mechanism of Co (II) on the surface of Fe–Mn binary oxide adsorbent. Colloids and Surfaces A: Physicochemical and Engineering Aspects, 479, pp.1-10.

Jiang, S., Lee, J.H., Kim, D., Kanaly, R.A., Kim, M.G. and Hur, H.G., 2013. Differential arsenic mobilization from As-bearing ferrihydrite by iron-respiring Shewanella strains with different arsenic-reducing activities. Environmental science & technology, 47(15), pp.8616-8623.

Jiang, W., Lv, J., Luo, L., Yang, K., Lin, Y., Hu, F., Zhang, J. and Zhang, S., 2013. Arsenate and cadmium co-adsorption and co-precipitation on goethite. Journal of Hazardous Materials, 262, pp.55-63.

Jiang, X., Peng, C., Fu, D., Chen, Z., Shen, L., Li, Q., Ouyang, T. and Wang, Y., 2015. Removal of arsenate by ferrihydrite via surface complexation and surface precipitation. Applied Surface Science, 353, pp.1087-1094.

Johnston, S.G., Burton, E.D. and Moon, E.M., 2016. Arsenic mobilization is enhanced by thermal transformation of schwertmannite. Environmental Science & Technology, 50(15), pp.8010-8019.

Jomova, K., Jenisova, Z., Feszterova, M., Baros, S., Liska, J., Hudecova, D., Rhodes, C.J. and Valko, M., 2011. Arsenic: toxicity, oxidative stress and human disease. Journal of applied toxicology, 31(2), pp.95-107.

Jones, M.E., Nico, P.S., Ying, S., Regier, T., Thieme, J. and Keiluweit, M., 2018. Manganese-driven carbon oxidation at oxic–anoxic interfaces. Environmental science & technology, 52(21), pp.12349-12357.

Juttukonda, L.J. and Skaar, E.P., 2015. Manganese homeostasis and utilization in pathogenic bacteria. Molecular microbiology, 97(2), pp.216-228.

Kalam, S., Abu-Khamsin, S.A., Kamal, M.S. and Patil, S., 2021. Surfactant adsorption isotherms: A review. ACS omega, 6(48), pp.32342-32348.

Kappler, A. and Newman, D.K., 2004. Formation of Fe (III)-minerals by Fe (II)-oxidizing photoautotrophic bacteria. Geochimica et Cosmochimica Acta, 68(6), pp.1217-1226.

Kappler, A. and Straub, K.L., 2005. Geomicrobiological cycling of iron. Reviews in Mineralogy and Geochemistry, 59(1), pp.85-108.

Kappler, A., Bryce, C., Mansor, M., Lueder, U., Byrne, J.M. and Swanner, E.D., 2021. An evolving view on biogeochemical cycling of iron. Nature Reviews Microbiology, 19(6), pp.360-374.

Keller, J.U. and Staudt, R., 2005. Gas adsorption equilibria: experimental methods and adsorptive isotherms. Springer Science & Business Media.

Kim, M.J., Nriagu, J. and Haack, S., 2000. Carbonate ions and arsenic dissolution by groundwater. Environmental Science & Technology, 34(15), pp.3094-3100.

Kleinert, S., Muehe, E.M., Posth, N.R., Dippon, U., Daus, B. and Kappler, A., 2011. Biogenic Fe (III) minerals lower the efficiency of iron-mineral-based commercial filter systems for arsenic removal. Environmental science & technology, 45(17), pp.7533-7541.

Kocar, B.D., Herbel, M.J., Tufano, K.J. and Fendorf, S., 2006. Contrasting effects of dissimilatory iron (III) and arsenic (V) reduction on arsenic retention and transport. Environmental science & technology, 40(21), pp.6715-6721.

Kumar, S., Ghosh, D., Donselaar, M.E., Burgers, F. and Ghosh, A.K., 2021. Clay-plug sediment as the locus of arsenic pollution in Holocene alluvial-plain aquifers. Catena, 202, p.105255.

Kurniawan, A. and Fukuda, Y., 2023. Analysis of the electric charge properties of biofilm for the development of biofilm matrices as biosorbents for water pollutant. Energy, Ecology and Environment, 8(1), pp.62-68.

Lafferty, B.J. and Loeppert, R.H., 2005. Methyl arsenic adsorption and desorption behavior on iron oxides. Environmental science & technology, 39(7), pp.2120-2127.

Lagergren, S., 1898, About the theory of so-called adsorption of soluble substances, Kungliga Svenska Vetenskapsakademiens. Handlingar, 24 (4), pp.1-39.

Lan, S., Ying, H., Wang, X., Liu, F., Tan, W., Huang, Q., Zhang, J. and Feng, X., 2018. Efficient catalytic As (III) oxidation on the surface of ferrihydrite in the presence of aqueous Mn (II). Water research, 128, pp.92-101.

Langmuir, I., 1918. The adsorption of gases on plane surfaces of glass, mica and platinum. Journal of the American Chemical society, 40(9), pp.1361-1403.

Langner, H.W. and Inskeep, W.P., 2000. Microbial reduction of arsenate in the presence of ferrihydrite. Environmental Science & Technology, 34(15), pp.3131-3136.

Larasati, A., Bernadet, O., Euverink, G.J.W., van Veelen, H.P.J. and Gagliano, M.C., 2024. Production of birnessite-type manganese oxides by biofilms from oxygen-supplemented biological activated carbon (BAC) filters. Environmental Science: Water Research & Technology, 10(11), pp.2844-2857.

Larsen, O., Postma, D. and Jakobsen, R., 2006. The reactivity of iron oxides towards reductive dissolution with ascorbic acid in a shallow sandy aquifer (Rømø, Denmark). Geochimica et Cosmochimica Acta, 70(19), pp.4827-4835.

Le, A.V., Muehe, E.M., Bone, S., Drabesch, S., Fischer, S. and Kappler, A., 2023. Field and Laboratory Evidence for Manganese Redox Cycling Controlling Iron and Arsenic Retention in Household Sand Filters. ACS ES&T Water, 4(1), pp.33-43.

Learman, D.R., Voelker, B.M., Vazquez-Rodriguez, A.I. and Hansel, C.M., 2011. Formation of manganese oxides by bacterially generated superoxide. Nature Geoscience, 4(2), pp.95-98.

Lee, S. and Xu, H., 2019. One-step route synthesis of siliceous six-line ferrihydrite: Implication for the formation of natural ferrihydrite. ACS Earth and Space Chemistry, 3(4), pp.503-509.

Li, C., Wang, S., Du, X., Cheng, X., Fu, M., Hou, N. and Li, D., 2016. Immobilization of iron- and manganese-oxidizing bacteria with a biofilm-forming bacterium for the effective removal of iron and manganese from groundwater. Bioresource technology, 220, pp.76-84.

Li, F., Geng, D. and Cao, Q., 2015. Adsorption of As (V) on aluminum-, iron-, and manganese-(oxyhydr) oxides: equilibrium and kinetics. Desalination and Water Treatment, 56(7), pp.1829-1838.

Li, J., Gyoten, H., Sonoda, A., Feng, Q. and Xue, M., 2017. Removal of trace arsenic to below drinking water standards using a Mn–Fe binary oxide. RSC Advances, 7(3), pp.1490-1497.

Li, L. and Yang, X., 2018. The essential element manganese, oxidative stress, and metabolic diseases: links and interactions. Oxidative medicine and cellular longevity, 2018(1), p.7580707.

Liang, M., Xu, S., Zhu, Y., Chen, X., Deng, Z., Yan, L. and He, H., 2020. Preparation and characterization of Fe-Mn binary oxide/mulberry stem biochar composite adsorbent and adsorption of Cr (VI) from aqueous solution. International Journal of Environmental Research and Public Health, 17(3), p.676.

Liermann, L.J., Hausrath, E.M., Anbar, A.D. and Brantley, S.L., 2007. Assimilatory and dissimilatory processes of microorganisms affecting metals in the environment. Journal of Analytical Atomic Spectrometry, 22(8), pp.867-877.

Liu, C., Zhang, L., Li, F., Wang, Y., Gao, Y., Li, X., Cao, W., Feng, C., Dong, J. and Sun, L., 2009. Dependence of sulfadiazine oxidative degradation on physicochemical properties of manganese dioxides. Industrial & engineering chemistry research, 48(23), pp.10408-10413.

Liu, F., De Cristofaro, A. and Violante, A., 2001. Effect of pH, phosphate and oxalate on the adsorption/desorption of arsenate on/from goethite. Soil Science, 166(3), pp.197-208.

Liu, H., Li, P., Wang, H., Qing, C., Tan, T., Shi, B., Zhang, G., Jiang, Z., Wang, Y. and Hasan, S.Z., 2020. Arsenic mobilization affected by extracellular polymeric substances (EPS) of the dissimilatory iron reducing bacteria isolated from high arsenic groundwater. Science of the Total Environment, 735, p.139501.

Liu, H., Yang, Y., Kang, J., Fan, M. and Qu, J., 2012. Removal of tetracycline from water by Fe-Mn binary oxide. Journal of environmental sciences, 24(2), pp.242-247.

Liu, J., Chen, Q., Yang, Y., Wei, H., Laipan, M., Zhu, R., He, H. and Hochella Jr, M.F., 2022. Coupled redox cycling of Fe and Mn in the environment: The complex interplay of solution species with Fe-and Mn-(oxyhydr) oxide crystallization and transformation. Earth-Science Reviews, 232, p.104105.

Lloyd, J.R. and Oremland, R.S., 2006. Microbial transformation of arsenic in the environment: from soda lakes to aquifers. Elements, 2, pp.85-90.

Lucchini, R.G., Aschner, M., Kim, Y. and Šarić, M., 2015. Manganese. Handbook on the Toxicology of Metals, 2, pp.975-1011.

Lv, C., Li, Z., Ding, J., Huang, X., Zhou, X., Zheng, Z., Cui, H., Huang, C., Xiang, L., Huang, Y. and Xu, H., 2024. Arsenate adsorption, desorption, and re-adsorption on Fe–Mn binary oxides: Impact of co-existing ions. Desalination and Water Treatment, 320, p.100678.

Madison, A.S., Tebo, B.M., Mucci, A., Sundby, B. & Luther, G.W., 2013. Abundant porewater Mn(III) is a major component of the sedimentary redox system. Science, 341, pp.875–878.

Mahto, K.U., Priyadarshanee, M., Samantaray, D.P. and Das, S., 2022. Bacterial biofilm and extracellular polymeric substances in the treatment of environmental pollutants: beyond the protective role in survivability. Journal of Cleaner Production, 379, p.134759.

Mamindy-Pajany, Y., Hurel, C., Marmier, N. and Roméo, M., 2011. Arsenic (V) adsorption from aqueous solution onto goethite, hematite, magnetite and zero-valent iron: Effects of pH, concentration and reversibility. Desalination, 281, pp.93-99.

Manceau, A., Kersten, M., Marcus, M.A., Geoffroy, N. and Granina, L., 2007. Ba and Ni speciation in a nodule of binary Mn oxide phase composition from Lake Baikal. Geochimica et Cosmochimica Acta, 71(8), pp.1967-1981.

Mandal, B.K. and Suzuki, K.T., 2002. Arsenic around the world: a review. Talanta, 58(1), pp.201-235.

Manning, B.A. and Goldberg, S., 1996. Modeling competitive adsorption of arsenate with phosphate and molybdate on oxide minerals. Soil Science Society of America Journal, 60(1), pp.121-131.

Manning, B.A., Fendorf, S.E. and Goldberg, S., 1998. Surface structures and stability of arsenic (III) on goethite: spectroscopic evidence for inner-sphere complexes. Environmental science & technology, 32(16), pp.2383-2388.

Manning, B.A., Hunt, M.L., Amrhein, C. and Yarmoff, J.A., 2002. Arsenic (III) and arsenic (V) reactions with zerovalent iron corrosion products. Environmental science & technology, 36(24), pp.5455-5461.

Mao, Y., Pham, A.N., Xin, Y. and Waite, T.D., 2012. Effects of pH, floc age and organic compounds on the removal of phosphate by pre-polymerized hydrous ferric oxides. Separation and purification technology, 91, pp.38-45.

Martin, J.E., Lisher, J.P., Winkler, M.E. and Giedroc, D.P., 2017. Perturbation of manganese metabolism disrupts cell division in Streptococcus pneumoniae. Molecular microbiology, 104(2), pp.334-348.

Masuda, H., 2018. Arsenic cycling in the Earth's crust and hydrosphere: Interaction between naturally occurring arsenic and human activities. Progress in Earth and Planetary Science, 5(1), pp.1-11.

Masue, Y., Loeppert, R.H. and Kramer, T.A., 2007. Arsenate and arsenite adsorption and desorption behavior on coprecipitated aluminum: iron hydroxides. Environmental science & technology, 41(3), pp.837-842.

McArthur, J.M., Banerjee, D.M., Hudson-Edwards, K.A., Mishra, R., Purohit, R., Ravenscroft, P., Cronin, A., Howarth, R.J., Chatterjee, A., Talukder, T. and Lowry, D., 2004. Natural organic matter in sedimentary basins and its relation to arsenic in anoxic ground water: the example of West Bengal and its worldwide implications. Applied geochemistry, 19(8), pp.1255-1293.

McArthur, J.M., Ravenscroft, P., Safiulla, S. and Thirlwall, M.F., 2001. Arsenic in groundwater: testing pollution mechanisms for sedimentary aquifers in Bangladesh. Water Resources Research, 37(1), pp.109-117.

McCann, C.M., Peacock, C.L., Hudson-Edwards, K.A., Shrimpton, T., Gray, N.D. and Johnson, K.L., 2018. In situ arsenic oxidation and sorption by a Fe-Mn binary oxide waste in soil. Journal of Hazardous Materials, 342, pp.724-731.

McCarty, K.M., Hanh, H.T. and Kim, K.W., 2011. Arsenic geochemistry and human health in South East Asia. Reviews on Environmental Health, 26(1), pp. 71-78.

Meharg, A.A. and Meharg, C., 2021. The pedosphere as a sink, source, and record of anthropogenic and natural arsenic atmospheric deposition. Environmental science & technology, 55(12), pp.7757-7769.

Melton, E.D., Swanner, E.D., Behrens, S., Schmidt, C. and Kappler, A., 2014. The interplay of microbially mediated and abiotic reactions in the biogeochemical Fe cycle. Nature Reviews Microbiology, 12(12), pp.797-808.

Mendez, J.C. and Hiemstra, T., 2020. Surface area of ferrihydrite consistently related to primary surface charge, ion pair formation, and specific ion adsorption. Chemical Geology, 532, p.119304.

Middleton, D.R., Watts, M.J., Beriro, D.J., Hamilton, E.M., Leonardi, G.S., Fletcher, T., Close, R.M. and Polya, D.A., 2017. Arsenic in residential soil and household dust in Cornwall, south west England: Potential human exposure and the influence of historical mining. Environmental Science: processes & impacts, 19(4), pp.517-527.

Miller, A.Z., Dionísio, A., Sequeira Braga, M.A., Hernández-Mariné, M., Afonso, M.J., Muralha, V.S.F., Herrera, L.K., Raabe, J., Fernandez-Cortes, A., Cuezva, S., Hermosin, B., Sanchez-Moral, S., Chaminé, H., Saiz-Jimenez, C., 2012. Biogenic Mn oxide minerals coating in a subsurface granite environment. Chemical Geology, 322–323, pp.181-191.

Miot, J., Benzerara, K., Morin, G., Kappler, A., Bernard, S., Obst, M., Férard, C., Skouri-Panet, F., Guigner, J.M., Posth, N. and Galvez, M., 2009. Iron biomineralization by anaerobic neutrophilic iron-oxidizing bacteria. Geochimica et Cosmochimica Acta, 73(3), pp.696-711.

Morales, E., Formanski, L.N., Shaner, S.E. and Stone, K.L., 2024. Characterizing Biogenic MnOx Produced by *Pseudomonas putida* MnB1 and Its Catalytic Activity towards Water Oxidation. Life, 14(2), p.171.

Morosini, C., Terzaghi, E., Raspa, G., Grotti, M., Armiraglio, S., Anelli, S. and Di Guardo, A., 2023. Arsenic movement and fractionation in agricultural soils which received wastewater from an adjacent industrial site for 50 years. Science of The total environment, 898, p.165422.

Muehe, E.M., Scheer, L., Daus, B. and Kappler, A., 2013. Fate of arsenic during microbial reduction of biogenic versus abiogenic As–Fe (III)–mineral coprecipitates. Environmental science & technology, 47(15), pp.8297-8307.

Mukherjee, A., Sengupta, M.K., Hossain, M.A., Ahamed, S., Das, B., Nayak, B., Lodh, D., Rahman, M.M. and Chakraborti, D., 2006. Arsenic contamination in groundwater: a global perspective with emphasis on the Asian scenario. Journal of Health, Population and Nutrition, pp.142-163.

Myers CR, Nealson KH (1988) Microbial reduction of manganese oxides: interactions with iron and sulfur. Geochimica et Cosmochimica Acta, 52, pp.2727-2732.

Nealson, K.H., Tebo, B.M. and Rosson, R.A., 1988. Occurrence and mechanisms of microbial oxidation of manganese. In Advances in applied microbiology, 33, pp.279-318. Academic Press.

Nelson, Y.M., Lion, L.W., Shuler, M.L. and Ghiorse, W.C., 2002. Effect of oxide formation mechanisms on lead adsorption by biogenic manganese (hydr) oxides, iron (hydr) oxides, and their mixtures. Environmental science & technology, 36(3), pp.421-425.

Nevo, Y. and Nelson, N., 2006. The NRAMP family of metal-ion transporters. Biochimica et Biophysica Acta (BBA)-Molecular Cell Research, 1763(7), pp.609-620.

Ng, J.C., Wang, J. and Shraim, A., 2003. A global health problem caused by arsenic from natural sources. Chemosphere, 52(9), pp.1353-1359.

Nickson, R., McArthur, J., Ravenscroft, P., Burgess, W., Ahmed, K., 2000. Mechanism of arsenic release to groundwater, Bangladesh and West Bengal. Applied Geochemistry, 15, pp. 403–413.

Nielsen, S.S., 2010. Phenol-sulfuric acid method for total carbohydrates. In Food analysis laboratory manual (pp. 47-53). Boston, MA: Springer US.

Nriagu, J.O., Bhattacharya, P., Mukherjee, A.B., Bundschuh, J., Zevenhoven, R. and Loeppert, R.H., 2007. Arsenic in soil and groundwater: an overview. Trace Metals and other Contaminants in the Environment, 9, pp.3-60.

Oldham, V.E., Jones, M.R., Tebo, B.M. and Luther III, G.W., 2017. Oxidative and reductive processes contributing to manganese cycling at oxic-anoxic interfaces. Marine Chemistry, 195, pp.122-128.

Ona-Nguema, G., Morin, G., Juillot, F., Calas, G. and Brown, G.E., 2005. EXAFS analysis of arsenite adsorption onto two-line ferrihydrite, hematite, goethite, and lepidocrocite. Environmental science & technology, 39(23), pp.9147-9155.

Ouyang, L., Wang, M., Zhu, L., Tang, H. and Shuai, Q., 2022. In situ speciation analysis and kinetic study of arsenic adsorption on ferrihydrite with surface-enhanced Raman spectroscopy. Nano Research, 16(2), pp.3046-3054.

Palermo, C. and Dittrich, M., 2016. Evidence for the biogenic origin of manganese-enriched layers in Lake Superior sediments. Environmental microbiology reports, 8(2), pp.179-186.

Pantsar-Kallio, M. and Manninen, P.K., 1997. Speciation of mobile arsenic in soil samples as a function of pH. Science of the Total Environment, 204(2), pp.193-200.

Parikh, S.J. and Chorover, J., 2005. FTIR spectroscopic study of biogenic Mn-oxide formation by *Pseudomonas putida* GB-1. Geomicrobiology Journal, 22(5), pp.207-218.

Parks, G.A. and Bruyn, P.D., 1962. The zero point of charge of oxides1. The Journal of Physical Chemistry, 66(6), pp.967-973.

Patel, K.S., Pandey, P.K., Martín-Ramos, P., Corns, W.T., Varol, S., Bhattacharya, P. and Zhu, Y., 2023. A review on arsenic in the environment: contamination, mobility, sources, and exposure. RSC Advances, 13(13), pp.8803-8821.

Payne, K.B. and Abdel-Fattah, T.M., 2005. Adsorption of arsenate and arsenite by iron-treated activated carbon and zeolites: effects of pH, temperature, and ionic strength. Journal of Environmental Science and Health, 40(4), pp.723-749.

Payne, T.E., Brendler, V., Ochs, M., Baeyens, B., Brown, P.L., Davis, J.A., Ekberg, C., Kulik, D.A., Lutzenkirchen, J., Missana, T. and Tachi, Y., 2013. Guidelines for thermodynamic sorption modelling in the context of radioactive waste disposal. Environmental modelling & software, 42, pp.143-156.

Pedersen, H.D., Postma, D. and Jakobsen, R., 2006. Release of arsenic associated with the reduction and transformation of iron oxides. Geochimica et Cosmochimica Acta, 70(16), pp.4116-4129.

Perez, J.P.H., Tobler, D.J., Thomas, A.N., Freeman, H.M., Dideriksen, K., Radnik, J. and Benning, L.G., 2019. Adsorption and reduction of arsenate during the Fe2+-induced transformation of ferrihydrite. ACS Earth and Space Chemistry, 3(6), pp.884-894.

Peryea, F.J. and Kammereck, R., 1997. Phosphate-enhanced movement of arsenic out of lead arsenate-contaminated topsoil and through uncontaminated subsoil. Water, Air, and Soil Pollution, 93, pp.243-254.

Piepenbrock, A., Schröder, C. & Kappler, A., 2014. Electron transfer from humic substances to biogenic and abiogenic Fe(III) oxyhydroxide minerals. Environmental Science and Technology, 48 (3), pp.1656-1664.

Poinern, G.E.J., Parsonage, D., Issa, T.B., Ghosh, M.K., Paling, E. and Singh, P., 2010. Preparation, characterization and As (V) adsorption behaviour of CNT-ferrihydrite composites. International Journal of Engineering, Science and Technology, 2(8).

Polizzotto, M.L., Harvey, C.F., Li, G., Badruzzman, B., Ali, A., Newville, M., Sutton, S. and Fendorf, S., 2006. Solid-phases and desorption processes of arsenic within Bangladesh sediments. Chemical Geology, 228(1-3), pp.97-111.

Post, J.E., 1999. Manganese oxide minerals: crystal structures and economic and environmental significance. Proceedings of the National Academy of Sciences, 96, pp.3447–3454.

Posth, N.R., Canfield, D.E., Kappler, A., 2014. Biogenic Fe(III) minerals: From formation to diagenesis and preservation in the rock record. Earth-Science Reviews, 135, pp.103-121.

Posth, N.R., Huelin, S., Konhauser, K.O. and Kappler, A., 2010. Size, density and composition of cell–mineral aggregates formed during anoxygenic phototrophic Fe (II) oxidation: Impact on modern and ancient environments. Geochimica et Cosmochimica Acta, 74(12), pp.3476-3493.

Powell, J.J., Bruggraber, S.F., Faria, N., Poots, L.K., Hondow, N., Pennycook, T.J., Latunde-Dada, G.O., Simpson, R.J., Brown, A.P. and Pereira, D.I., 2014. A nano-disperse ferritin-core mimetic that efficiently corrects anemia without luminal iron redox activity. Nanomedicine: Nanotechnology, Biology and Medicine, 10(7), pp.1529-1538.

Prieto, D.M., Devesa-Rey, R., Rubinos, D.A., Díaz-Fierros, F. and Barral, M.T., 2013. Arsenate retention by epipsammic biofilms developed on streambed sediments: influence of phosphate. BioMed Research International, 2013(1), p.591634.

Punshon, T., Jackson, B.P., Meharg, A.A., Warczack, T., Scheckel, K. and Guerinot, M.L., 2017. Understanding arsenic dynamics in agronomic systems to predict and prevent uptake by crop plants. Science of the Total Environment, 581, pp.209-220.

Quansah, R., Armah, F.A., Essumang, D.K., Luginaah, I., Clarke, E., Marfoh, K., Cobbina, S.J., Nketiah-Amponsah, E., Namujju, P.B., Obiri, S. and Dzodzomenyo, M., 2015. Association of arsenic with adverse pregnancy outcomes/infant mortality: a systematic review and meta-analysis. Environmental health perspectives, 123(5), pp.412-421.

Rahman, M.A., Hasegawa, H., Rahman, M.M., Miah, M.M. and Tasmin, A., 2008. Arsenic accumulation in rice (Oryza sativa L.): human exposure through food chain. Ecotoxicology and environmental safety, 69(2), pp.317-324.

Rahman, M.M., Naidu, R. and Bhattacharya, P., 2009. Arsenic contamination in groundwater in the Southeast Asia region. Environmental geochemistry and health, 31, pp.9-21.

Rajkumar, M. and Freitas, H., 2008. Influence of metal resistant-plant growth-promoting bacteria on the growth of Ricinus communis in soil contaminated with heavy metals. Chemosphere, 71(5), pp.834-842.

Ras, M., Girbal-Neuhauser, E., Etienne, P., Lefebvre, D., 2008. A high yield multimethod extraction protocol for protein quantification in activated sludge. Bioresource Technology, 99, pp.7464–7471.

Rashid, R., Shafiq, I., Akhter, P., Iqbal, M.J. and Hussain, M., 2021. A state-of-the-art review on wastewater treatment techniques: the effectiveness of adsorption method. Environmental Science and Pollution Research, 28, pp.9050-9066.

Rauf, M.A., Hakim, M.A., Hanafi, M.M., Islam, M.M., Rahman, G.K.M.M. and Panaullah, G.M., 2011. Bioaccumulation of arsenic (As) and phosphorous by transplanting Aman rice in arsenic-contaminated clay soils. Australian Journal of Crop Science, 5(12), pp.1678-1684.

Raven, K.P., Jain, A. and Loeppert, R.H., 1998. Arsenite and arsenate adsorption on ferrihydrite: kinetics, equilibrium, and adsorption envelopes. Environmental science & technology, 32(3), pp.344-349.

Rincón-Tomás, B., Khonsari, B., Mühlen, D., Wickbold, C., Schäfer, N., Hause-Reitner, D., Hoppert, M. and Reitner, J., 2016. Manganese carbonates as possible biogenic relics in Archean settings. International Journal of Astrobiology, 15(3), pp.219-229.

Rochex, A., Lecouturier, D., Pezron, I., & Lebeault, J. M., 2004. Adhesion of a Pseudomonas putida strain isolated from a paper machine to cellulose fibres. Applied microbiology and biotechnology, 65(6), pp.727–733.

Roden, E.E., 2004. Analysis of long-term bacterial vs. chemical Fe (III) oxide reduction kinetics. Geochimica et Cosmochimica Acta, 68(15), pp.3205-3216.

Ruthven, D.M., 1984. Principles of adsorption and adsorption processes. John Wiley & Sons.

Saleh, T.A., 2022. Kinetic models and thermodynamics of adsorption processes: Classification. In Interface science and technology, 34, pp.65-97, Elsevier.

Sander, M., Hofstetter, T.B. and Gorski, C.A., 2015. Electrochemical Analyses of Redox-Active Iron Minerals: A Review of Nonmediated and Mediated Approaches. Environmental Science & Technology, 49(10), pp.5862-5878.

Sassi, M., Chaka, A.M. and Rosso, K.M., 2021. Ab initio thermodynamics reveals the nanocomposite structure of ferrihydrite. Communications Chemistry, 4(1), p.134.

Saunders, J.A., Lee, M.K., Shamsudduha, M., Dhakal, P., Uddin, A., Chowdury, M.T. and Ahmed, K.M., 2008. Geochemistry and mineralogy of arsenic in (natural) anaerobic groundwaters. Applied Geochemistry, 23(11), pp.3205-3214.

Saunders, J.A., Lee, M.K., Uddin, A., Mohammad, S., Wilkin, R.T., Fayek, M. and Korte, N.E., 2005. Natural arsenic contamination of Holocene alluvial aquifers by linked tectonic, weathering, and microbial processes. Geochemistry, Geophysics, Geosystems, 6(4).

Saxe, J.K., Bowers, T.S., Kim Reynolds Reid, K. R., 1964. 13 - Arsenic, Editor(s): Robert D. Morrison, Brian L. Murphy, Environmental Forensics. Academic Press, pp.279-292, ISBN 9780125077514.

Schwertmann, U., 1991. Solubility and dissolution of iron oxides. Plant and soil, 130, pp.1-25.

Schwertmann, U., Friedl, J. & Stanjek, H., 1999. From Fe(III) ions to ferrihydrite and then to hematite. Journal of Colloid and Interface Science, 209, pp. 215–223.

Shaji, E., Santosh, M., Sarath, K.V., Prakash, P., Deepchand, V. and Divya, B.V., 2021. Arsenic contamination of groundwater: A global synopsis with focus on the Indian Peninsula. Geoscience frontiers, 12(3), p.101079.

Sharma, P., Ofner, J. and Kappler, A., 2010. Formation of binary and ternary colloids and dissolved complexes of organic matter, Fe and As. Environmental science & technology, 44(12), pp.4479-4485.

Sharma, V.K. and Sohn, M., 2009. Aquatic arsenic: toxicity, speciation, transformations, and remediation. Environment international, 35(4), pp.743-759.

Shen, S., Li, X.F., Cullen, W.R., Weinfeld, M. and Le, X.C., 2013. Arsenic binding to proteins. Chemical reviews, 113(10), pp.7769-7792.

Sherman, D.M. and Randall, S.R., 2003. Surface complexation of arsenic (V) to iron (III)(hydr) oxides: structural mechanism from ab initio molecular geometries and EXAFS spectroscopy. Geochimica et Cosmochimica Acta, 67(22), pp.4223-4230.

Shi, Y., Wang, C., Zhang, L. and Sun, S., 2024. Fe-Based Deep Eutectic Solvents for Amorphous Carbon-Encapsulated Fe_3O_4 Nanoparticles as Electrocatalysts for H_2O_2 Synthesis. ACS Applied Nano Materials, 7(11), pp.13328-13337.

Shipley, H.J., Yean, S., Kan, A.T. and Tomson, M.B., 2009. Adsorption of arsenic to magnetite nanoparticles: effect of particle concentration, pH, ionic strength, and temperature. Environmental Toxicology and Chemistry: An International Journal, 28(3), pp.509-515.

Si, M., Cao, W., Ou, C., Tu, G., Yang, W., Li, Q., Liao, Q. and Yang, Z., 2023. Simultaneous oxidization-adsorption for arsenic and antimony by biological Fe-Mn binary oxides (BFMO): The efficiencies and mechanism. Process Safety and Environmental Protection, 178, pp.65-73.

Siddiqui, S.I. and Chaudhry, S.A., 2017. Iron oxide and its modified forms as an adsorbent for arsenic removal: A comprehensive recent advancement. Process Safety and Environmental Protection, 111, pp.592-626.

Singh, N., Kumar, D. and Sahu, A.P., 2007. Arsenic in the environment: effects on human health and possible prevention. Journal of environmental biology, 28(2), p.359.

Singh, R., Singh, S., Parihar, P., Singh, V.P. and Prasad, S.M., 2015. Arsenic contamination, consequences and remediation techniques: a review. Ecotoxicology and environmental safety, 112, pp.247-270.

Sips, R., 1948. On the structure of a catalyst surface. The journal of chemical physics, 16(5), pp.490-495.

Smedley, P.L. and Kinniburgh, D.G., 2002. A review of the source, behaviour and distribution of arsenic in natural waters. Applied geochemistry, 17(5), pp.517-568.

Smith, A.H., Lingas, E.O. and Rahman, M., 2000. Contamination of drinking-water by arsenic in Bangladesh: a public health emergency. Bulletin of the world health organization, 78(9), pp.1093-1103.

Soldatova, A.V., Tao, L., Romano, C.A., Stich, T.A., Casey, W.H., Britt, R.D., Tebo, B.M. and Spiro, T.G., 2017. Mn (II) oxidation by the multicopper oxidase complex Mnx: a binuclear activation mechanism. Journal of the American Chemical Society, 139(33), pp.11369-11380.

Sowers, T.D., Harrington, J.M., Polizzotto, M.L. and Duckworth, O.W., 2017. Sorption of arsenic to biogenic iron (oxyhydr) oxides produced in circumneutral environments. Geochimica et Cosmochimica Acta, 198, pp.194-207.

Staicu, L.C., van Hullebusch, E.D. and Ackerson, C., 2021. Microbial Biominerals: Toward New Functions and Resource Recovery. Frontiers in Microbiology, 12, p.796374.

Stolarski, J., Coronado, I., Potocka, M., Janiszewska, K., Mazur, M., Baronnet, A., Cruz, J.A., Grauby, O. and Meibom, A., 2024. Post-mortem recrystallization of biogenic amorphous calcium carbonate guided by the inherited macromolecular framework. Scientific Reports, 14(1), p.17304.

Straub, K.L., Schönhuber, W.A., Buchholz-Cleven, B.E. and Schink, B., 2004. Diversity of ferrous iron-oxidizing, nitrate-reducing bacteria and their involvement in oxygen-independent iron cycling. Geomicrobiology Journal, 21(6), pp.371-378.

Straub, K.L. and Kappler, A., 2005. Formation of reactive Fe (III)-minerals by anaerobic oxidation of Fe (II) by phototrophs and nitrate-reducing bacteria.

Su, Q., He, Y., Pan, H., Liu, H., Mehmood, K., Tang, Z. and Hu, L., 2023. Toxicity of inorganic arsenic to animals and its treatment strategies. Comparative Biochemistry and Physiology Part C: Toxicology & Pharmacology, 271, p.109654.

Suda, A. and Makino, T., 2016. Functional effects of manganese and iron oxides on the dynamics of trace elements in soils with a special focus on arsenic and cadmium: a review. Geoderma, 270, pp.68-75.

Tan, K.L. and Hameed, B.H., 2017. Insight into the adsorption kinetics models for the removal of contaminants from aqueous solutions. Journal of the Taiwan Institute of Chemical Engineers, 74, pp.25-48.

Taylor, J.F., Robinson, A., Johnson, N., Marroquin-Cardona, A., Brattin, B., Taylor, R. and Phillips, T.D., 2009. In vitro evaluation of ferrihydrite as an enterosorbent for arsenic from contaminated drinking water. Environmental science & technology, 43(14), pp.5501-5506.

Tazaki, K., 2000. Formation of banded iron-manganese structures by natural microbial communities. Clays and Clay Minerals, 48(5), pp.511-520.

Tebo, B.M., Bargar, J.R., Clement, B.G., Dick, G.J., Murray, K.J., Parker, D., Verity, R. and Webb, S.M., 2004. Biogenic manganese oxides: properties and mechanisms of formation. Annu. Rev. Earth Planet. Sci., 32(1), pp.287-328.

Tebo, B.M., Johnson, H.A., McCarthy, J.K. and Templeton, A.S., 2005. Geomicrobiology of manganese (II) oxidation. TRENDS in Microbiology, 13(9), pp.421-428.

Temkin, M.I., 1940. Kinetics of ammonia synthesis on promoted iron catalysts. Acta physiochim. URSS, 12, pp.327-356.

Templeton, A.S., Trainor, T.P., Traina, S.J., Spormann, A.M. and Brown Jr, G.E., 2001. Pb (II) distributions at biofilm–metal oxide interfaces. Proceedings of the National Academy of Sciences, 98(21), pp.11897-11902.

Tian, H., Shi, Q. and Jing, C., 2015. Arsenic biotransformation in solid waste residue: comparison of contributions from bacteria with arsenate and iron reducing pathways. Environmental Science & Technology, 49(4), pp.2140-2146.

Tolins, M., Ruchirawat, M. and Landrigan, P., 2014. The developmental neurotoxicity of arsenic: cognitive and behavioral consequences of early life exposure. Annals of global health, 80(4), pp.303-314.

Toner, B., Fakra, S., Villalobos, M., Warwick, T. and Sposito, G., 2005. Spatially resolved characterization of biogenic manganese oxide production within a bacterial biofilm. Applied and environmental microbiology, 71(3), pp.1300-1310.

Toner, B., Manceau, A., Webb, S.M. and Sposito, G., 2006. Zinc sorption to biogenic hexagonal-birnessite particles within a hydrated bacterial biofilm. Geochimica et Cosmochimica Acta, 70(1), pp.27-43.

Tong, J., Li, R., Zhang, J., Ma, X., Wu, F., Suo, H. and Liu, C., 2020. Coupled dynamics of As-containing ferrihydrite transformation and As desorption/re-adsorption in presence of sulfide. Journal of hazardous materials, 384, p.121287.

Tong, M., Zhao, Y., Sun, Q., Li, P., Liu, H., Yuan, S., 2022. Fe(II) oxygenation inhibits bacterial Mn(II) oxidation by P. putida MnB1 in groundwater under O2-perturbed conditions. Journal of Hazardous Materials, 435, p.128972.

Tothero, G.K., Hoover, R.L., Farag, I.F., Kaplan, D.I., Weisenhorn, P., Emerson, D. and Chan, C.S., 2024. *Leptothrix ochracea* genomes reveal potential for mixotrophic growth on Fe (II) and organic carbon. Applied and environmental microbiology, 90(9), pp.e00599-24.

Tran, T.N., Kim, D.G. and Ko, S.O., 2018. Synergistic effects of biogenic manganese oxide and Mn (II)-oxidizing bacterium Pseudomonas putida strain MnB1 on the degradation of 17 α-ethinylestradiol. Journal of hazardous materials, 344, pp.350-359.

Tsuji, J.S., Chang, E.T., Gentry, P.R., Clewell, H.J., Boffetta, P. and Cohen, S.M., 2019. Dose-response for assessing the cancer risk of inorganic arsenic in drinking water: the scientific basis for use of a threshold approach. Critical reviews in toxicology, 49(1), pp.36-84.

Tufano, K.J. and Fendorf, S., 2008. Confounding impacts of iron reduction on arsenic retention. Environmental Science & Technology, 42(13), pp.4777-4783.

Tufano, K.J., Reyes, C., Saltikov, C.W. and Fendorf, S., 2008. Reductive processes controlling arsenic retention: revealing the relative importance of iron and arsenic reduction. Environmental Science & Technology, 42(22), pp.8283-8289.

Valášková, M., Leštinský, P., Matějová, L., Klemencová, K., Ritz, M., Schimpf, C., Motylenko, M., Rafaja, D., & Bělík, J., 2022. Hematites Precipitated in Alkaline Precursors: Comparison of Structural and Textural Properties for Methane Oxidation. International journal of molecular sciences, 23(15), p.8163.

Vareda, J.P., 2023. On validity, physical meaning, mechanism insights and regression of adsorption kinetic models. Journal of Molecular Liquids, 376, p.121416.

Vázquez-Sánchez, D. and Rodríguez-López, P., 2018. Biofilm formation of Staphylococcus aureus. In Staphylococcus aureus, pp. 87-103. Academic Press.

Villalobos, M., 2015. The role of surface edge sites in metal (loid) sorption to poorly-crystalline birnessites. In Advances in the environmental biogeochemistry of manganese oxides, pp. 65-87. American Chemical Society.

Villalobos, M., Escobar-Quiroz, I.N. and Salazar-Camacho, C., 2014. The influence of particle size and structure on the sorption and oxidation behavior of birnessite: I. Adsorption of As (V) and oxidation of As (III). Geochimica et Cosmochimica Acta, 125, pp.564-581.

Villalobos, M., Toner, B., Bargar, J., and Sposito, G., 2003. Characterization of the manganese oxide produced by *Pseudomonas putida* strain MnB1. Geochimica et Cosmochimica Acta, 67, pp.2649–2662.

Vincent, T., Taulemesse, J.M., Dauvergne, A., Chanut, T., Testa, F. and Guibal, E., 2014. Thallium (I) sorption using Prussian blue immobilized in alginate capsules. Carbohydrate polymers, 99, pp.517-526.

Violante, A. and Pigna, M., 2008. Sorption-desorption processes of metals and metalloids in soil environments. Revista de la ciencia del suelo y nutrición vegetal, 8(ESPECIAL), pp.95-101.

Vithanage, M., Mayakaduwa, S.S., Herath, I., Ok, Y.S. and Mohan, D., 2016. Kinetics, thermodynamics and mechanistic studies of carbofuran removal using biochars from tea waste and rice husks. Chemosphere, 150, pp.781-789.

Voegelin, A. and Hug, S.J., 2003. Catalyzed oxidation of arsenic (III) by hydrogen peroxide on the surface of ferrihydrite: an in situ ATR-FTIR study. Environmental science & technology, 37(5), pp.972-978.

Wang, C.H., Hsiao, C.K., Chen, C.L., Hsu, L.I., Chiou, H.Y., Chen, S.Y., Hsueh, Y.M., Wu, M.M. and Chen, C.J., 2007. A review of the epidemiologic literature on the role of environmental arsenic exposure and cardiovascular diseases. Toxicology and applied pharmacology, 222(3), pp.315-326.

Wang, H., Zhao, L. and Hou, W., 2024. Pseudo-Second-Order Kinetic Equation for Describing the Effect of Sorbent and Sorbate Concentrations. Langmuir, 40(7), pp.3559-3568.

Wang, J. and Guo, X., 2020. Adsorption isotherm models: Classification, physical meaning, application and solving method. Chemosphere, 258, p.127279.

Wang, J. and Guo, X., 2022. Rethinking of the intraparticle diffusion adsorption kinetics model: Interpretation, solving methods and applications. Chemosphere, 309, p.136732.

Wang, P., Tang, Y., Liu, Y., Wang, T., Wu, P. and Lu, X.Y., 2018. Halloysite nanotube@ carbon with rich carboxyl groups as a multifunctional adsorbent for the efficient removal of cationic Pb (II), anionic Cr (VI) and methylene blue (MB). Environmental Science: Nano, 5(10), pp.2257-2268.

Wang, S. and Mulligan, C.N., 2004, October. Arsenic in Canada. In Proceedings of the 57th Canadian Geotechnical Conference (pp. 1-18).

Wang, S. and Mulligan, C.N., 2006a. Occurrence of arsenic contamination in Canada: sources, behavior and distribution. Science of the total Environment, 366(2-3), pp.701-721.

Wang, S. and Mulligan, C.N., 2006b. Effect of natural organic matter on arsenic release from soils and sediments into groundwater. Environmental geochemistry and health, 28, pp.197-214.

Wang, S. and Mulligan, C.N., 2008. Speciation and surface structure of inorganic arsenic in solid phases: A review. Environment International, 34(6), pp.867-879.

Wang, X., Li, W., Harrington, R., Liu, F., Parise, J.B., Feng, X. and Sparks, D.L., 2013. Effect of ferrihydrite crystallite size on phosphate adsorption reactivity. Environmental science & technology, 47(18), pp.10322-10331.

Wang, Y., Zhang, L., Guo, C., Gao, Y., Pan, S., Liu, Y., Li, X. and Wang, Y., 2022. Arsenic removal performance and mechanism from water on iron hydroxide nanopetalines. Scientific Reports, 12(1), p.17264.

Waters, L.S., 2020. Bacterial manganese sensing and homeostasis. Current opinion in chemical biology, 55, pp.96-102.

Webb, S.M., Dick, G.J., Bargar, J.R., and Tebo, B.M., 2005. Evidence for the presence of Mn(III) intermediates in the bacterial oxidation of Mn(II). PNAS, 102(15), pp.5558 – 5563.

Weidler, P.G. and Stanjek, H., 1998. The effect of dry heating of synthetic 2-line and 6-line ferrihydrite: II. Surface area, porosity and fractal dimension. Clay minerals, 33(2), pp.277-284.

WHO and IARC, 2004. Some drinking-water disinfectants and contaminants, including arsenic (Vol. 84). IARC Working Group on the Evaluation of Carcinogenic Risks to Humans, World Health Organization and International Agency for Research on Cancer. Iarc.

WHO, 2003. Arsenicosis case-detection, management and surveillance. Report of a regional consultation. Regional Office for South-East Asia, WHO, New Delhi.

WHO, 2011. Arsenic in Drinking-water. Background document for preparation of WHO Guidelines for drinking-water quality.

WHO, 2022. Arsenic. Fact sheets, World Health Organization. Date accessed: 5 November 2024. Available from: https://www.who.int/news-room/fact-sheets/detail/arsenic.

Wingender, J., Neu, T.R., Flemming, H.C., 1999. Microbial Extracellular Polymeric Substances - Characterization, Structure and Function. first ed. Springer-Verlag, Berlin, Heidelberg, Germany.

Wu, H., Chen, W., Rong, X., Cai, P., Dai, K. and Huang, Q., 2014. Adhesion of Pseudomonas putida onto kaolinite at different growth phases. Chemical Geology, 390, pp.1-8.

Wu, Y., Li, W. and Sparks, D.L., 2015. Effect of Iron (II) on arsenic sequestration by δ-MnO2: Desorption studies using stirred-flow experiments and X-ray absorption fine-structure spectroscopy. Environmental Science & Technology, 49(22), pp.13360-13368.

Wu, Y., Zhou, X., Lei, M., Yang, J., Ma, J., Qiao, P., Chen, T., 2017. Migration and transformation of arsenic: contamination control and remediation in realgar mining areas. Applied Geochemistry, 77, pp. 44-51.

Xie, Z.M., Wang, J., Wei, X.F., Li, F., Chen, M.N., Wang, J., Gao, B., 2018. Interactions between arsenic adsorption/desorption and indigenous bacterial activity in shallow high arsenic aquifer sediments from the Jianghan Plain, Central China. Science of the Total Environment, 644, pp.382–388.

Xing, X., Alharbi, N.S., Ren, X. and Chen, C., 2022. A comprehensive review on emerging natural and tailored materials for chromium-contaminated water treatment and environmental remediation. Journal of Environmental Chemical Engineering, 10(2), p.107325.

Xu, L., Shu, Z., Sun, S., Wen, Y. and Zhou, J., 2024. Amorphous Fe–Mn binary oxides nanoparticles decorating waste bamboo biomass-based monolith for efficient arsenic removal with column adsorption. Separation and Purification Technology, 330, p.125426.

Xu, R., Li, Q., Nan, X., Jiang, G., Wang, L., Xiong, J., Yang, Y., Xu, B. and Jiang, T., 2022. Simultaneous removal of antimony (III/V) and arsenic (III/V) from aqueous solution by bacteria–mediated kaolin@ Fe–Mn binary (hydr) oxides composites. Applied Clay Science, 217, p.106392.

Xu, R., Li, Q., Nan, X., Yang, Y., Xu, B., Li, K., Wang, L., Zhang, Y. and Jiang, T., 2022. Synthesis of nano–silica and biogenic iron (oxyhydr) oxides composites mediated by iron oxidizing bacteria to remove antimonite and antimonate from aqueous solution: performance and mechanisms. Journal of Hazardous Materials, 422, p.126821.

Xu, W., Wang, H., Liu, R., Zhao, X. and Qu, J., 2011. The mechanism of antimony (III) removal and its reactions on the surfaces of Fe–Mn binary oxide. Journal of colloid and interface science, 363(1), pp.320-326.

Yan, X.P., Kerrich, R. and Hendry, M.J., 2000. Distribution of arsenic (III), arsenic (V) and total inorganic arsenic in porewaters from a thick till and clay-rich aquitard sequence, Saskatchewan, Canada. Geochimica et Cosmochimica Acta, 64(15), pp.2637-2648.

Yang, H., Yu, H., Zeng, M., Liang, H., Rong, H., Li, G. and Qu, F., 2023. Evolution of biogenic Fe-Mn binary oxide physicochemical properties during biofilter start-up for sustainable urban groundwater treatment. Sustainable Cities and Society, 98, p.104799.

Yang, K., Liu, Y., Li, Y., Cao, Z., Zhou, C., Wang, Z., Zhou, X., Baig, S.A. and Xu, X., 2019. Applications and characteristics of Fe-Mn binary oxides for Sb (V) removal in textile wastewater: selective adsorption and the fixed-bed column study. Chemosphere, 232, pp.254-263.

Yang, K., Zhou, J., Lou, Z., Zhou, X., Liu, Y., Li, Y., Baig, S.A. and Xu, X., 2018. Removal of Sb (V) from aqueous solutions using Fe-Mn binary oxides: The influence of iron oxides forms and the role of manganese oxides. Chemical Engineering Journal, 354, pp.577-588.

Yang, X., Peng, Q., Liu, L., Tan, W., Qiu, G., Liu, C. and Dang, Z., 2020. Synergistic adsorption of Cd (II) and As (V) on birnessite under electrochemical control. Chemosphere, 247, p.125822.

Yang, X., Zhang, H., Cheng, S. and Zhou, B., 2022. Optimization of the adsorption and removal of Sb (iii) by MIL-53 (Fe)/GO using response surface methodology. RSC advances, 12(7), pp.4101-4112.

Yoon, Y., Zheng, M., Ahn, Y.T., Park, W.K., Yang, W.S. and Kang, J.W., 2017. Synthesis of magnetite/non-oxidative graphene composites and their application for arsenic removal. Separation and Purification Technology, 178, pp.40-48.

Yu, H. and Leadbetter, J.R., 2020. Bacterial chemolithoautotrophy via manganese oxidation. Nature, 583(7816), pp.453-458.

Yudovich, Y.E. and Ketris, M.P., 2005. Arsenic in coal: a review. International Journal of Coal Geology, 61(3-4), pp.141-196.

Zaia, D.A., Coutinho, M.A., Mosca, D.H., da Costa, A.C. and Urbano, A., 2020. Study of the formation of ferrihydrite under prebiotic chemistry conditions: artificial seawater 4.0 Gy and ammonium thiocyanate. International Journal of Astrobiology, 19(6), pp.462-473.

Zhang, G., Liu, F., Liu, H., Qu, J. and Liu, R., 2014. Respective role of Fe and Mn oxide contents for arsenic sorption in iron and manganese binary oxide: an X-ray absorption spectroscopy investigation. Environmental science & technology, 48(17), pp.10316-10322.

Zhang, G., Qu, J., Liu, H., Liu, R. and Wu, R., 2007b. Preparation and evaluation of a novel Fe–Mn binary oxide adsorbent for effective arsenite removal. Water research, 41(9), pp.1921-1928.

Zhang, G.S., Liu, F.D., Liu, H.J., Qu, J.H., Liu, R.P., 2014. Respective role of Fe and Mn oxide contents for arsenic sorption in iron and manganese binary oxide: an X-ray absorption spectroscopy investigation. Environmental Science & Technology, 48 (17), pp.10316–10322.

Zhang, G.S., Qu, J.H., Liu, H.J., Liu, R.P. and Li, G.T., 2007a. Removal mechanism of As (III) by a novel Fe− Mn binary oxide adsorbent: oxidation and sorption. Environmental science & technology, 41(13), pp.4613-4619.

Zhang, Q., Crittenden, J., Hristovski, K., Hand, D. and Westerhoff, P., 2009. User-oriented batch reactor solutions to the homogeneous surface diffusion model for different activated carbon dosages. Water research, 43(7), pp.1859-1866.

Zhang, Y., Li, L., Su, H., Huang, W. and Dong, X., 2015. Binary metal oxide: advanced energy storage materials in supercapacitors. Journal of Materials Chemistry A, 3(1), pp.43-59.

Zhang, Y., Wang, C., Huang, G., Zhao, B., Wang, R. and Wang, C., 2023. Favorably adjusting the oxygen species over Fe-Mn binary oxide sorbent by directional etching for arsenic oxidation and adsorption. Chemical Engineering Science, 281, p.119170.

Zhao, A., Sun, J. and Liu, Y., 2023. Understanding bacterial biofilms: From definition to treatment strategies. Frontiers in cellular and infection microbiology, 13, p.1137947.

Zhao, X., Xie, Z., Li, P., Chen, M., & Zhong, Z., 2022. A newly isolated indigenous metal-reducing bacterium induced Fe and Mn oxides synergy for enhanced in situ As(III/V) immobilization in groundwater. Journal of Hydrology, 608, p.127635.

Zhao, X., Xie, Z., Li, Y., Liu, T. and Liu, D., 2022. Synergy of Fe and biogenic Mn oxide components mediated by a newly isolated indigenous bacterium to enhance As (III/V) immobilization in groundwater. Applied Geochemistry, 140, p.105266.

Zheng, J., Jiang, M., Li, Q. and Yang, W., 2024. The Formation and Stability of HA–Fe/Mn Colloids in Saturated Porous Media. Environments, 11(7), p.136.

Zheng, Q., Hou, J., Hartley, W., Ren, L., Wang, M., Tu, S. and Tan, W., 2020. As (III) adsorption on Fe-Mn binary oxides: are Fe and Mn oxides synergistic or antagonistic for arsenic removal?. Chemical Engineering Journal, 389, p.124470.

Zheng, Q., Tu, S., Chen, Y., Zhang, H., Hartley, W., Ye, B., Ren, L., Xiong, J., Tan, W., Kappler, A. and Hou, J., 2023. Micropore sites in ferrihydrite are responsible for its higher affinity towards As (III) relative to As (V). Geochimica et Cosmochimica Acta, 348, pp.27-40.

Zheng, Q., Tu, S., Hou, J., Ni, C., Wang, M., Ren, L., Wang, M., Cao, M., Xiong, S. and Tan, W., 2021. Insights into the underlying mechanisms of stability working for As (III) removal by Fe-Mn binary oxide as a highly efficient adsorbent. Water Research, 203, p.117558.

Zheng, Y., Li, Y., Long, H., Zhao, X., Jia, K., Li, J., Wang, L., Wang, R., Lu, X., Zhang, D., 2018. bifA Regulates Biofilm Development of *Pseudomonas putida* MnB1 as a Primary Response to H_2O_2 and Mn^{2+}. Frontiers in microbiology, 9, p.1490.

Zhou, D.H., Kim, D.G., Ko, S.O., 2015. Heavy metal adsorption with biogenic manganese oxides generated by Pseudomonas putida strain MnB1. Journal of Industrial and Engineering Chemistry, 24, pp.132–139.

Zhu, J., Pigna, M., Cozzolino, V., Caporale, A.G. and Violante, A., 2011. Sorption of arsenite and arsenate on ferrihydrite: Effect of organic and inorganic ligands. Journal of Hazardous Materials, 189(1-2), pp.564-571.